UNIVERSITY OF
Southampton

University of Southampton Research Repository

Copyright © and Moral Rights for this thesis and, where applicable, any accompanying data are retained by the author and/or other copyright owners. A copy can be downloaded for personal non-commercial research or study, without prior permission or charge. This thesis and the accompanying data cannot be reproduced or quoted extensively from without first obtaining permission in writing from the copyright holder/s. The content of the thesis and accompanying research data (where applicable) must not be changed in any way or sold commercially in any format or medium without the formal permission of the copyright holder/s.

When referring to this thesis and any accompanying data, full bibliographic details must be given, e.g.

Thesis: Author (Year of Submission) "Full thesis title", University of Southampton, name of the University Faculty or School or Department, PhD Thesis, pagination.

Data: Author (Year) Title. URI [dataset]

University of Southampton

Faculty of Engineering and Physical Sciences

School of Engineering

The Shaft Capacity of Small Displacement Piles in Chalk

by

Fernando Jesús Álvarez Borges

ORCID ID: 0000-0002-6940-9918

Thesis for the degree of Doctor of Philosophy in Engineering and the Environment

September 2019

University of Southampton

Abstract

Faculty of Engineering and Physical Sciences

School of Engineering

Thesis for the degree of Doctor of Philosophy in Engineering and the Environment

The Shaft Capacity of Small Displacement Piles in Chalk

by

Fernando Jesús Álvarez Borges

Multi-pile foundation systems are used to support offshore infrastructure in areas of Northern Europe underlain by Chalk. During installation, the tip of the tubular open-ended ‘small displacement’ pile crushes and destructures the Chalk forming a ‘putty’ interface or ‘annulus’ around it. Pile resistance to uplift (i.e. shaft capacity) results from sliding friction between the pile shaft and this putty chalk annulus. The limited knowledge of the characteristics of this interface is associated with pile design guidelines that may be overconservative, which could result in unnecessary increases in economic costs for the offshore renewable energy industry.

The present Thesis investigates the prospect of using soil mechanics to describe shaft friction in small displacement piles in Chalk as function of the critical state strength of the chalk putty that composes the annulus. To this end, oedometer and triaxial tests were conducted on low and medium density destructured White Chalk samples to determine the suitability of a critical state framework to characterise the mechanical behaviour of the material. Monotonic and cyclic simple shear tests were then used to simulate load transfer through the chalk-pile interface and examine the compatibility of interface performance with the prospective critical state framework. Thereafter, model piles of different geometries were installed in intact chalk cores and micro-focus X-ray computed tomography (XCT) was applied to measure the density of the chalk putty annulus. The piles were then tested in tension.

Oedometer and triaxial results demonstrate that a unique one-dimensional normal compression line and a unique critical state line (CSL) exist for the tested materials, regardless of their origin and the varied preparation methods used. This ‘uniqueness’ is associated with comparable grain shapes and size distributions, and to grain breakage processes that resemble those reported for sands. Simple shear experiments show that interface failure states comply with the CSL, although strain localisation precludes the attainment of critical state strengths when shearing initiates in significantly dense of critical conditions. A CSL-based framework defining interface strength as a function of void ratio was produced and found to compare well with the small number of early-life shaft capacity measurements of piles available in the literature. Yet, this framework could not predict the shaft capacity of the model pile experiments, due to heavily dense of critical states at the end of installation. XCT further revealed that pile penetration processes in chalk and sand are generally comparable, and that design approaches based on the cone penetration test might successfully estimate early-life shaft capacity. Though pile set-up was found to possibly result from annulus consolidation, its prediction may need to rely on empiricism for the foreseeable future.

Table of Contents

Table of Tables

Table of Figures

List of Accompanying Materials

Data supporting this Thesis are openly available from the University of Southampton repository at https://doi.org/10.5258/SOTON/D1208

Research Thesis: Declaration of Authorship

Print name:	Fernando Jesús Álvarez Borges
Title of thesis:	The Shaft Capacity of Small Displacement Piles in Chalk

I declare that this thesis and the work presented in it are my own and has been generated by me as the result of my own original research.

I confirm that:

1. This work was done wholly or mainly while in candidature for a research degree at this University;
2. Where any part of this thesis has previously been submitted for a degree or any other qualification at this University or any other institution, this has been clearly stated;
3. Where I have consulted the published work of others, this is always clearly attributed;
4. Where I have quoted from the work of others, the source is always given. With the exception of such quotations, this thesis is entirely my own work;
5. I have acknowledged all main sources of help;
6. Where the thesis is based on work done by myself jointly with others, I have made clear exactly what was done by others and what I have contributed myself;
7. Parts of this work have been published as:

Alvarez-Borges, F.J., Madhusudhan, B.N. and Richards, D.J. 2018. The 1D normal compression line and structure permitted space of low-medium density chalk. Géotechnique Letters, 8(4): 298-304. doi: 10.1680/jgele.18.00091

Alvarez-Borges, F.J., Madhusudhan, B.N. and Richards, D.J. 2018. Stiffness of Destructured Weak Rock. In Micro to MACRO Mathematical Modelling in Soil Mechanics. Springer Nature, pp. 1-9. doi: 10.1007/978-3-319-99474-1_1

Alvarez-Borges, F.J., Clayton, C.R.I., Richards, D.J. and Madhusudhan, B.N. 2018. The effect of the remoulded void ratio on unit shaft friction in small-displacement piles in chalk. Engineering in Chalk, Proceedings of the Chalk 2018 Conference. ICE Publishing, pp. 475-480. doi: 10.1680/eiccf.64072.475

Alvarez-Borges, F.J., Richards, D.J., Clayton, C.R.I. and Ahmed, S.I. 2018. Application of X-ray computed tomography to investigate pile penetration mechanisms in chalk. Engineering in Chalk, Proceedings of the Chalk 2018 Conference. ICE Publishing, pp. 565-570. doi: 10.1680/eiccf.64072.565

Signature: Date:

Acknowledgements

First and foremost, I extend my sincere gratitude to my supervisors Prof David Richards and Prof Chris Clayton, whose encouragement, guidance and support were fundamental to the execution of this research.

I am greatly indebted with Dr Madhu Murthy and Dr Sharif Ahmed, who have shown great interest in my research. This project would have been significantly less gratifying without their support in many day-to-day laboratory tasks and the frequent constructive commentary on my work. Their teachings in geotechnical laboratory testing and XCT scanning in geomechanics were crucial to the completion of this research. I also thank Prof David White for his comments, advice and support.

My appreciation goes to Harvey Skinner and Karl Scammell for their help in the laboratory. My sincere apologies for the ever-present chalk powder in the lab.

I also express my gratitude to the following people:

- Dr Mark Mavrogordato, Dr Orestis Katsamenis, Dr Kathryn Rankin and Dr Richard Boardman of the µ-Vis X-Ray Imaging Centre. Their help with the XCT scans and the advice on how to obtain the most out of them is sincerely appreciated.
- Dr Richard Pearce and Dr Charlie Thompson of the National Oceanography Centre, for their assistance with SEM imaging and particle size analysis.
- Peter Morgan from Geography and Environmental Science for training me in the use of the Mastersizer 3000 and for his help with particle size analysis.
- Dr Róisín Buckley of the University of Oxford (formerly Imperial College) for arranging the access to the St Nicholas-at-Wade test site to collect chalk samples.

I am very grateful for the support of my family and friends.

This research was financially sponsored by the National Council of Science and Technology (Consejo Nacional de Ciencia y Tecnología, CONACYT) and the Secretariat of Public Education (Secretaría de Educación Pública, SEP) of Mexico, and by the Faculty of Engineering and the Environment of the University of Southampton. Their support is much appreciated.

Chapter 1 Introduction

1.1 Introduction and rationale

Chalk is a weak biogenic calcareous rock, present over an extended area of Northern Europe, the North Sea, the Middle East and the Americas (Mortimore 1990; Bell et al. 1999; Mortimore 2012). Foundation engineering in chalk is often challenging, largely due to the high variability of its physical properties, which originates from diverse diagenetic processes and stress history (Clayton 1983, 1990; Clayton et al. 2003). Therefore, foundation design and works for major infrastructure projects in chalk have frequently coincided with investigations on poorly understood aspects of the mechanical performance of the material. For instance, regarding stability when used as fill material (Clayton 1978; Razoaki 2000), deformation behaviour in hydrocarbon reservoirs (Addis 1987; Leddra 1989), under shallow footings (Burland et al. 1983; Matthews 1993), and in tunnelling works (Millar 2000), and time-dependent behaviour (Katsaros 2008), to name a few. In this context, recent interest in expanding offshore wind-power infrastructure in the North Sea using jacket structures supported by small pile groups has highlighted the importance of the accurate estimation of the vertical capacity of driven piles in Chalk (Barbosa et al. 2015a, b).

Jacked or driven piles installed in chalk are designated as displacement piles (Hobbs and Healy 1979; Lord et al. 2002). These are classified into ‘large’ (PL) and ‘small’ (PS) displacement piles to differentiate closed-ended solid piles from H-section, cruciform and open-ended piles. Driven open-ended tubular steel piles are widely used in offshore multi-pile foundation systems (Gavin et al. 2011). These small pile groups rely on shaft friction to provide resistance against moment-induced uplift, which is the predominant loading case (Augustesen et al. 2015; Jardine et al. 2015).

Guidelines for PS pile design in chalk proposed by the Construction Industry Research and Information Association (CIRIA) originate from the analysis of a reduced number of pile tests (Lord et al. 2002). These guidelines suggest average ultimate unit shaft friction ($\bar{\tau}_{sf}$) design values of 20 and 120 kPa for sites in which low-medium density and high-very high density chalk is present, respectively. These shaft friction estimates are thought to be conservative and to introduce significant increases in cost, potentially making offshore wind a less attractive energy source in areas underlain by chalk (Carrington et al. 2011; Barbosa et al. 2015b; Jardine et al. 2018).

PS pile installation in chalk crushes the material, and in low and medium density chalk produces a ‘sleeve’ or annulus of ‘putty chalk’ around the pile (Hobbs and Atkinson 1993; Lord et al. 2002). Ultimate unit shaft friction and pile uplift resistance relies on the strength of this putty, but there is limited knowledge on this and other material properties. However, there is evidence that chalk putty is a principally silt- and clay-sized largely non-plastic granular material (Clayton 1983; Razoaki 2000; Bundy 2013). In other granular materials such as sands, the magnitude of ultimate unit shaft friction (τ_{sf}) is assumed to be described by a Mohr-Coulomb criterion (Lehane et al. 1993):

$$\tau_{sf} = \sigma'_{r} \tan \delta'_{ult} \tag{1}$$

where δ'_{ult} is the ultimate effective interface friction angle and σ'_{r} the radial (or horizontal) effective stress acting normally on the pile surface at failure. δ'_{ult} is expected to range between 29 and 33°, based on interface shear tests using smooth steel surfaces and a variety of chalk materials (Clayton 1990; Alvarez-Borges 2014; Ziogos et al. 2017; Chan et al. 2019). Variability in the magnitude of τ_{sf} is thus generally attributed to different σ'_{r} levels (Burland and French 1990; Lord et al. 2002; Jardine et al. 2018).

For silica sands, it has been shown that a correlation exists between the magnitude of the stresses developed at the pile tip during installation and σ'_{r} (e.g. Lehane et al. 1993, Chow 1997, Gavin & Lehane 2003, and others). This has led to the formulation of several popular PS pile design methods that estimate σ'_{r} based on penetration resistance measurements obtained from cone penetration tests (CPTs), and empirical correlations derived from an extensive collection of instrumented pile tests (e.g. Lehane et al. 2005b, Jardine et al. 2005, Kolk et al. 2005, Clausen et al. 2005). However, at the time of writing, CPT-based methods for chalk and calcareous soils in general are at an early stage of development and their use is uncommon. This is mainly due to the great variability in cone resistance measurements, the paucity of instrumented pile test data, the large reductions in σ'_{r} levels that occur whilst the material is crushed under the advancing pile or CPT tip during penetration, and particularities of the mechanical behaviour of calcareous sediments (Murff 1987; Le Tirant and Nauroy 1994; Thompson and Jardine 1998; Schneider et al. 2007). The crucial consequence of this is that there are currently no widely accepted methods by which to rationally estimate shaft friction in small displacement piles in Chalk, and further investigations are clearly urgent.

1.2 Thesis objectives

The present Thesis originates from the necessity to understand the factors that control shaft friction in small displacement piles installed in chalk. Improved knowledge of these factors is expected to allow for more cost-effective pile designs, which are particularly critical in the offshore renewable energy industry (Gavin et al. 2011; Kallehave et al. 2015).

The initial hypothesis of the present work is that the mobilisation of shaft friction in PS piles embedded in chalk is a soil mechanics process that can be assessed using critical state concepts (Schofield and Wroth 1968), as suggested by Burland (1990b) and Lord et al. (1994). Thus, the general aim is to examine the potential link between critical state chalk parameters and unit shaft friction. The specific objectives associated with this aim are:

1. The development of a critical state framework for the behaviour under compression and shear of chalk putty of different origins.
2. Evaluation of the applicability of a critical state framework in terms of effective stress and void ratio to predict the ultimate strength of steel-chalk putty interfaces.
3. Assessment of the link between the pile-chalk interface void ratio and shaft friction mobilisation during installation and tension loading, by way of a critical state framework.

1.3 Thesis organisation

Chapter 2 presents a review of the physical characteristics, classification and mechanical behaviour of Chalk.

Chapter 3 discourses on the current state of knowledge of the behaviour of displacement piles in Chalk during installation and axial loading. Previous extensive work regarding piles in sands is compared with the very limited research on piles in Chalk to identify resemblances and divergences.

Chapter 4 details the laboratory testing campaign of the Thesis. Oedometer and triaxial tests designed and performed to investigate the applicability of Critical State Soil Mechanics to the behaviour of chalk putty (Objective 1) are described. Monotonic and cyclic direct simple shear tests aimed at evaluating the applicability of this framework to interface friction are also included (Objective 2). Scaled physical models and micro-focus X-ray computed tomography employed to analyse how pile penetration processes affect the pile-chalk interface void ratio are presented. Tension testing of the model piles are used to examine a possible link between these void ratio measurements and shaft capacity via the prospective critical state framework (Objective 3).

Chapter 5 discusses the results presented in Chapter 4. Test data is used to propose a micro-mechanics basis for the critical state framework, and potential limitations are described, including the particularities of using said framework to characterise interface friction. This analysis is expanded to incorporate the outcomes of the testing of the scaled models and the available pile test data. Implications of this analysis are discussed in the context of CPT-based pile design.

Chapter 6 summarises major contributions of the investigation. Recommendations for future work are outlined.

Chapter 2 Chalk

2.1 Introduction

In broad terms, chalk is a porous and soft biomicrite, usually composed of more than 98% calcium carbonate ($CaCO_3$) and limited amounts of clay and silica minerals (Bell et al. 1999; Clayton et al. 2003). Chalk originated from the deposition of planktonic debris and foraminifera in a relatively warm and shallow marine environment during the late Cretaceous (Clayton 1983; Mortimore 1990). It is typically constituted of intact and broken coccoliths. Coccoliths are circular arrangements (5-20 μm in diameter) of fossilised micron-sized $CaCO_3$ platelets (Hancock, 1975, Clayton, 1983, Clayton et al., 2003; Figure 2.1).

While Middle-Upper Cretaceous chalks are usually composed almost entirely by $CaCO_3$, older materials are often present in the form of chalk marls with $CaCO_3$ contents as low as 30% (Mortimore 1990). This is attributed to the deposition of clays resulting from the erosion of emerged continental shelves. Clay deposition ceased as sea levels rose and land masses became submerged (Mortimore 1990; Bell et al. 1999). Thin marl seams may be found in younger White Chalk formations, which originated from the episodic deposition of volcanic ash (Bell et al. 1999; Lord et al. 2002).

Siliceous nodules, known as flints (Clayton 1986), are also commonly found in the Chalk. Flints were formed by the precipitation of silica from organic sediments, which filled the burrows made by organisms in freshly deposited chalk, and are far harder than the chalk that encloses them (Hancock 1975; Lord et al. 2002; Clayton et al. 2003).

Chalk variability extends beyond the presence of these silica and marl features. Natural variations of the macro- and micro-structure and fabric of Chalk, and changes to these characteristics caused by engineering activities such as pile driving result in distinct mechanical behaviours. This Chapter presents the current state of knowledge on the mechanical behaviour of intact and destructured chalk, with focus on low and medium density high $CaCO_3$-content chalk. A review of time-based changes in the mechanical performance of chalk is also provided.

2.1.1 A note on terminology

In this Thesis, 'chalk' refers to the weakly bonded calcareous rock described in the above paragraphs, while the geological group and formations in which chalk is present are referred to as

'Chalk' or 'the Chalk', following terminology usage found in Mortimore (1990) and Lord et al. (2002).

The term 'fabric' is used to refer to the arrangement of particles and pore spaces, including local and global porosity and particle characteristics such as size, shape, grouping, arrangement and contacts (Mitchell and Soga 2005). 'Structure' is employed as the combination of fabric and inter-particle forces originating from mechanisms such as electrostatic, electrochemical, and electromagnetic attractions, and cementation (Lambe and Whitman 1979; Mitchell and Soga 2005). As further discussed in this Chapter, cementation is of particular significance for the mechanical behaviour of intact chalk. Consequently, the term 'destructured' is employed to differentiate uncemented and thoroughly remoulded chalk from chalk that retains its natural fabric and widespread inter-particle cementation.

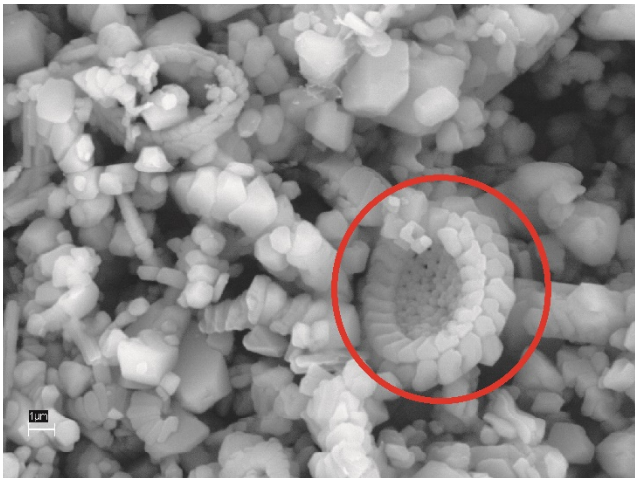

Figure 2.1. Microimage of high porosity chalk (Newhaven Chalk Formation; see Section 2.3). Coccolith structure shown inside red circle (Alvarez-Borges 2014).

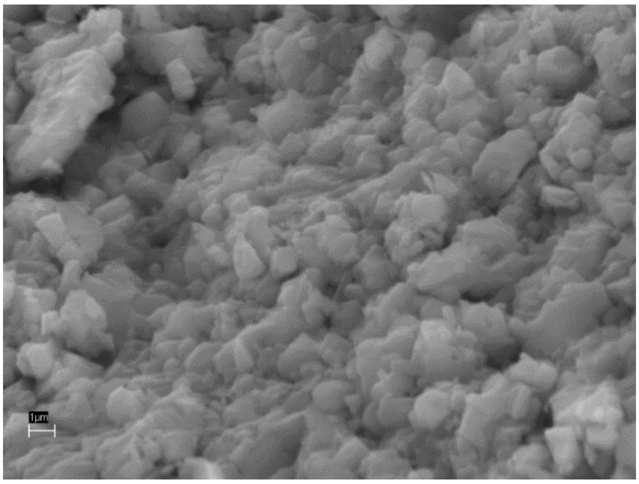

Figure 2.2. Microimage of low porosity Chalk Rock (Lewes Nodular Chalk Formation; see Section 2.3; Alvarez-Borges 2014).

2.2 Physical characteristics of chalk

Being often composed almost entirely by calcite, chalk is usually limited to a very narrow range of specific densities (≈2.70 Mg/m^3, Clayton, 1983). Accordingly, porosity, saturated moisture content and dry density are closely related. Extensive studies by Clayton (1978) have shown that the intact dry density (IDD) of chalk ranges from 1.25 Mg/m^3 to 2.50 Mg/m^3, with a corresponding porosity interval of 52 to 9% (Lord et al. 2002).

The degree of fragmentation of coccoliths and other fossil structures during the diagenetic evolution of Chalk had a direct impact on the porosity and density of the material. High porosity chalk is constituted of intact and moderately fragmented coccoliths, while low porosity chalks exhibit more extensive coccolith cataclasis, dissolution and calcite re-precipitation (Mortimore and Fielding 1990; Bell et al. 1999). Variations in the depositional rate of coccolithic debris was a major factor controlling the degree of fragmentation of these fossil assemblies and on the mass porosity of the Chalk (Kennedy and Garrison 1975; Clayton 1983; Clayton et al. 2003). Very high depositional rates meant that the sediment was quickly buried, limiting degradation of bioclasts and leading to very porous chalks (Figure 2.1). Slower depositional rates and interruptions allowed for widespread bioturbation, hardening and lithification, which led to denser chalks and hardgrounds (Figure 2.2).

Mechanical and chemical compaction associated with post-depositional burial were also key factors affecting the porosity of chalk (Clayton et al. 2003). The former occurred in the form of particle rearrangement and reshaping due to the overburden pressure exerted by the formation, while the latter took place as some of the biogenic calcite particles experienced dissolution and re-precipitation. Clayton et al. (2003) suggests that chemical compaction had a greater impact on the porosity of the material, as early cementation produced a porous yet competent structure capable of supporting large overburdens.

Chalk is generally found in a heavily jointed natural state (Lake 1990; Millar 2000). This is attributed principally to tectonic activity and weathering processes (Mortimore et al. 1990; Mortimore and Pomerol 1997). Some aspects of the mechanical behaviour of in-situ chalk are related to the presence of these discontinuities, as described in Section 2.4.1. Therefore, the frequency and aperture of these discontinuities are regarded as significant engineering parameters and are used for classification purposes (Lord et al. 2002; Section 2.3).

Weathering, particularly frost-thaw cycles, is known to significantly weaken the structure of Chalk, including the development of fissures and fractures and the general disaggregation of the material, often leading to variable forms of brecciation (Lautridou and Ozouf 1982; Matthews

1993; Murton 2018). Thus, porosity and other associated characteristics are in continuous evolution in surface Chalk because of weathering. As burial provides some protection against weathering in non-permafrost regions, a depth-based improvement in the structure of Chalk is often encountered (Clayton et al. 2003).

2.3 Stratigraphy and engineering classification of Chalk

The current lithostratigraphical classification of the Chalk of the Anglo-Paris basin makes use of the laterally continuous presence of hardgrounds (‘bulk rock mass character’, Aldiss et al. 2012) to identify nine recognised formations, presented in the fourth column of Figure 2.3 (Mortimore 1983, 1986; Bristow et al. 1997; Hopson 2005; Aldiss et al. 2012). This classification scheme substitutes the traditional Upper-Middle-Lower Chalk subdivision with White and Grey Chalk Subgroups, also shown in this Figure.

Classifying the Chalk for engineering purposes has been difficult due to its high variability and propensity to undergo changes in structure during sampling (e.g. opening or closure of discontinuities, crushing and remoulding, etc.), hence often precluding an accurate assessment of local in-situ characteristics (Lord et al. 2002). Attempts to develop an engineering classification based on visual inspection and plate loading tests were conducted in the 1960s (the ‘Munford grades’; Ward et al., 1968). However, this method was site-specific and not intended for general use, as it later occurred (Burland 1990b). Correlations between the Standard Penetration Test (SPT) blow count and the Munford grades or material properties were attempted (Wakeling 1966, 1970), but the reliability of these relationships was put in to question early on, despite widespread use of the method (as discussed by Hobbs & Healy 1979, Burland 1990b, Lord et al. 2002 and others).

The engineering classification for Chalk proposed by Lord et al. (2002) in CIRIA C574 has been increasingly accepted, particularly in the United Kingdom. The CIRIA C574 classification grades consider the following in-situ parameters: the intact dry density of chalk, the spacing and aperture of discontinuities, and whether the material is in a structured state or not. These three parameters are key to assess the mechanical behaviour of chalk, as discussed further throughout this Thesis. Clayton et al. (2003) proposed a useful conceptual flowchart for the application of the CIRIA engineering classification method, here presented as Figure 2.4. With exception of the intact dry density (IDD), which for chalk is often measured using the ‘modified gas jar method’ described by Clayton (1978, 1983), all CIRIA C574 classification parameters can be derived by visual inspection.

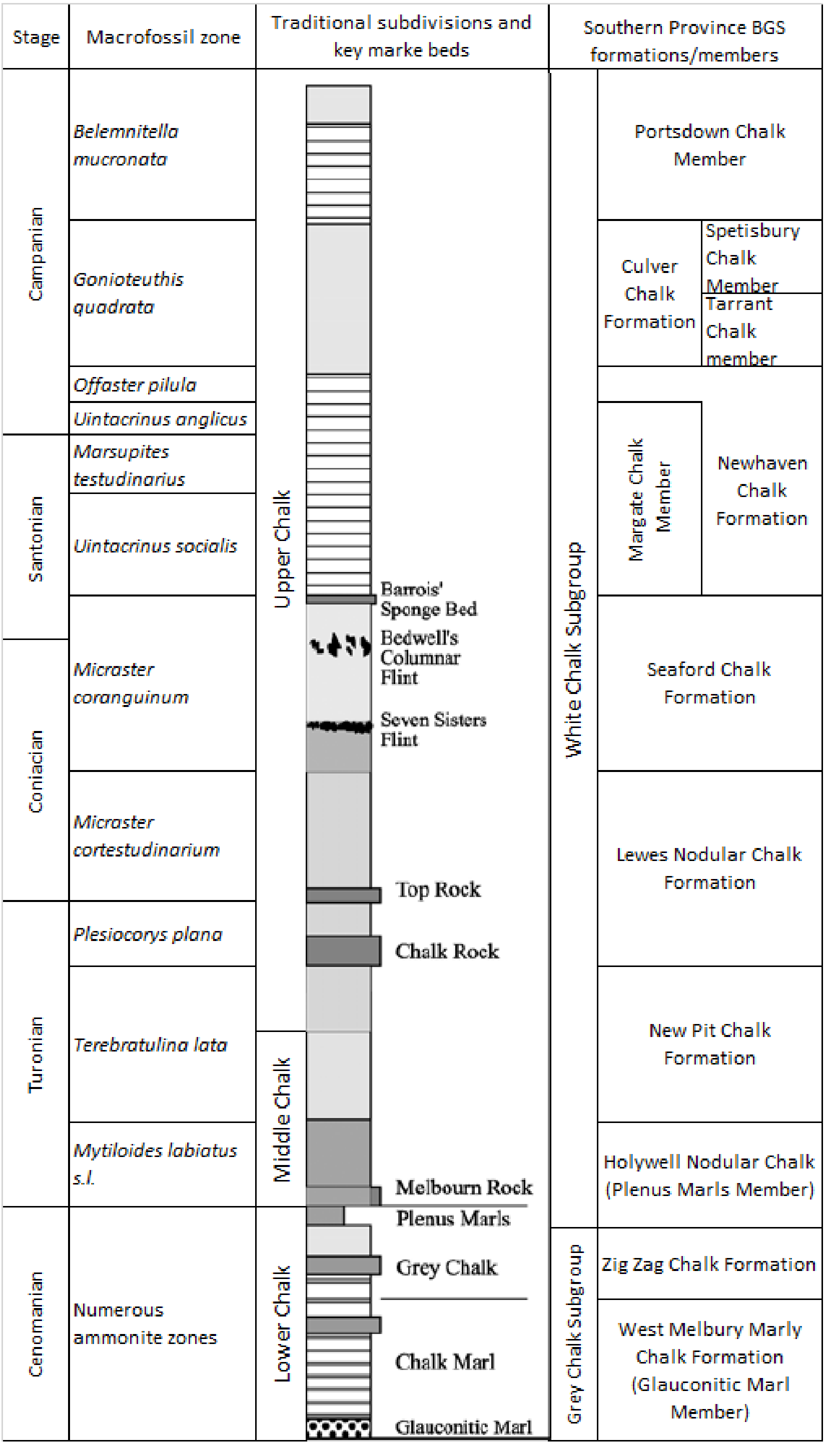

Figure 2.3. Modern lithostratigraphical units of the Southern Chalk Province, modified from Lord et al. (2002) and Aldiss et al. (2012).

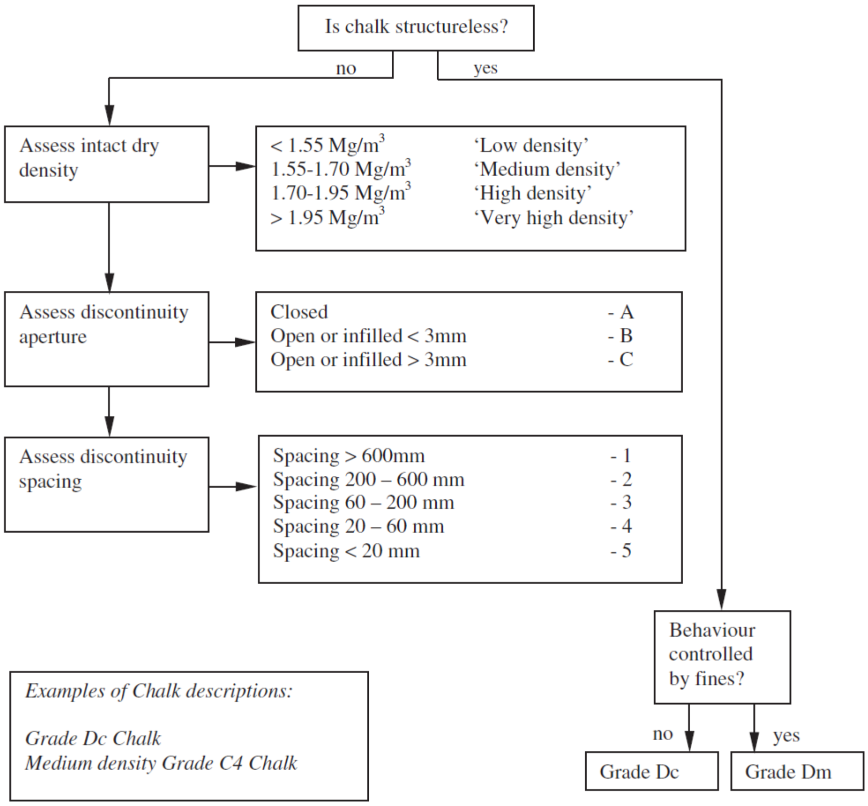

Figure 2.4. Engineering classification of Chalk, as proposed by Lord et al. (2002). From Clayton et al. (2003).

2.4 Mechanical characteristics of intact chalk

It is pertinent to approach the study of the mechanical characteristics of Chalk under the premise that it may exist as a variable arrangement of cemented units or blocks of sizes ranging from gravel to boulders, and as disaggregated soil-like material. This capricious macroscopic structure significantly affects its mechanical behaviour as a rock mass. The role of discontinuities in the rock mass in its behaviour in compression and shear has been addressed in substantial detail in the work of Matthews (1993), Holloway-Strong (1998) and Millar (2000). A key outcome of their investigations is that characterisation of the mechanical behaviour of discontinuity-bearing chalk formations using Critical State Soil Mechanics is unfeasible. Thus, the mechanical performance of the chalk rock mass will not be developed in detail in this Thesis. However, an overview of the research outcomes presented by these and other authors is offered in the succeeding Section. A more detailed study of the mechanical behaviour of intact and destructured chalk is presented thereafter. The 'intact' condition of chalk refers to structured material that contains no visible fractures, joints or discontinuities. This condition is only observed in specimens prepared in the laboratory from carefully selected blocks collected from the field.

2.4.1 Chalk mass behaviour: the role of discontinuities and macrostructure

The in-situ stiffness (‘mass stiffness’) and compressibility (‘mass compressibility’) of Chalk is significantly affected by the presence, spacing, aperture and infilling of discontinuities (Ward et al. 1968). The three main mechanisms that control stiffness and compressibility in the mass are (Barton 1986):

- The strength of the intact (discontinuity-free) rock composing each block of the rock mass.
- The closure of discontinuities due to the action of stresses acting perpendicularly (normal) to the discontinuity plane.
- Shearing and frictional dilation of the discontinuity due to stresses acting parallel to the discontinuity plane.

All of the above mechanisms are stress-dependent (Matthews 1993). Additionally, the discontinuity may be tightly closed or open, infilled with crushed rock or with clay, fresh and rough or smooth and polished (Hoek 2007). Each of these pairs of circumstances represent favourable and unfavourable conditions, respectively, from a mechanical performance perspective. Evidently, the accurate measurement of mass stiffness and compressibility in jointed rock, and in chalk, is not straight forward. Therefore, rock mass classification schemes are often used in conjunction with empirical correlations to derive very approximate values (Hoek and Diederichs 2006; Hoek 2007).

In Chalk, discontinuities are often either parallel or perpendicular to the horizontal ground surface, and therefore, closure resulting from normal loading is expected to be the dominant deformation mechanisms in most scenarios (Matthews and Clayton 1992). The particularities of discontinuity closure due to normal loading in Chalk have been described as follows (Matthews 1993; Holloway-Strong and Hughes 2001; Lord et al. 2002):

- Under a given load, the contact points (asperities) in the discontinuities bear with the applied stress (in compression, shear or both) until they yield (Figure 2.5).
- Once the asperities become crushed, they are likely to form a low strength putty if the intact material exhibits an elevated moisture content at saturation. Putty production appears to be directly correlated with an increase in compressibility (Holloway-Strong et al. 2007). Yield of the asperities and compression of the soft putty is generally observed as a ‘brittle yield’ during plate loading and shallow foundation tests (Burland and Bayliss 1990; Lord et al. 1994).

- High-density grade A Chalk (Figure 2.4) with widely spaced and closed discontinuities are predisposed to exhibit a much stiffer and less compressible response.
- Initially infilled discontinuities are likely to display low pre-yield stiffness before efficient contact is made between asperities. After the asperities break, the post-yield behaviour is expected to be affected by the propensity (or lack thereof) to strain harden of the infill material. However, discontinuities in Chalk are usually free of infill or partially filled with chalk fragments. Therefore, the role of infilling in the mass compressibility of Chalk is expected to be minor.

It is often found that the Chalk outcrop can sustain steep and tall cut faces and cliffs, probably associated with the parallel and normal preferential orientation of discontinuities, and the high stiffness and strength of intact Chalk (discussed in the forthcoming Sections). The minimal deformations occurring under these conditions led Longworth and Driscoll (1991) to propose that the in-situ horizontal stress levels may often be approximately zero. However, Lord et al. (2002) warn against assuming that zero horizontal stress conditions are widespread, and note that the 'tightness' of vertical discontinuities suggest the presence of considerable in-situ stresses.

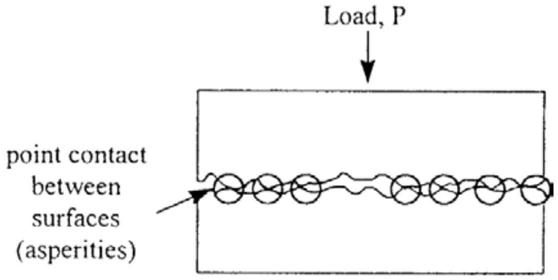

Figure 2.5. Asperity-based contact points within a discontinuity in chalk. From Holloway-Strong & Hughes (2001).

2.4.2 Behaviour in compression

Extensive research on the behaviour of intact chalk in drained compression has been carried out. Investigations have originated principally from the need to improve understanding of oilfield subsidence in Chalk reservoirs and have eventually sought to reveal the mechanisms that control the general behaviour of weakly cemented fine-grained carbonate formations. Key outcomes are:

- When intact chalk is subjected to stress, it progresses from a quasi-elastic behaviour before its yield limit to a particulate-frictional behaviour after the material yields, as depicted in Figure 2.6 (Addis 1987; Johnson et al. 1988; Leddra 1989). This occurs because, prior to yielding, the calcite cement bonds that hold together the constituting particles of chalk bear with most of the stress to which the material is subjected. As stresses increase, particle bonds rapidly break, and a brittle yield ensues. Effective stresses are expressed in this Figure (and in most instances in this Thesis) by invariants p' = $(\sigma'_1 + \sigma'_2 + \sigma'_3)/3$ (mean effective stress) and $q = \sigma'_1 - \sigma'_3$ (deviator stress in triaxial tests), where σ'_1, σ'_2 and σ'_3 are the major, intermediate and minor principal effective stresses.

- Loss of cementation due to stress increments is not instantaneous. Departure from quasi-elastic behaviour (Figure 2.6a,c) is associated with failure of the multi-particle structure forming the larger ovoid pore spaces in the matrix while the surrounding fabric remains largely intact (Kågeson-Loe et al. 1993). This process is termed ‘pore collapse’, which occurs immediately after ‘first yield’, and involves porosity reductions as low as 1% (Figure 2.6b; Kågeson-Loe et al. 1993, Schroeder 2002).
- With further stress increments, the overall bonding strength reduces as the newly broken bonds, which previously held together ovoid pore structures, shed their loads to the surrounding matrix, which is in turn brought to failure (Kågeson-Loe et al. 1993). This is observed as the rapid reduction of ovoid pore space followed by the collapse of ‘interstitial pores’ which originally delimited the larger ovoid pores. The initiation of these events constitutes the ‘second’ or ‘gross’ yield, regarded to be the onset of large volumetric strains, as shown in Figure 2.6.
- Continuing strain leads to extensive particle disaggregation and rearrangement, and substantial reductions in porosity (Figure 2.6b; Kågeson-Loe et al. 1993). The mechanical behaviour of the material is then controlled by the uncemented particles (Addis and Jones 1990; Leddra and Jones 1990).
- Dense chalk yields and exhibits plastic straining at larger stresses than more porous chalks (Matthews and Clayton 1993). This is associated with increased inter-particle contacts and bonding.

The above-described processes are qualitatively comparable in both isotropic and one-dimensional (zero radial strain) compression conditions (Kågeson-Loe et al. 1993). A relevant trait of the latter is the change in lateral to vertical stress ratio (or minor to major principal stress ratio), K_0, required to maintain zero radial strain conditions, depicted in Figure 2.6d. The increase in the K_0 ratio after first yield observed in this Figure indicates the progressive mobilisation of the frictional strength of the material (Jaky 1944; Michalowski 2005), and therefore, evidences that yielding and bond breakage leads to the transition to the particulate behaviour described previously.

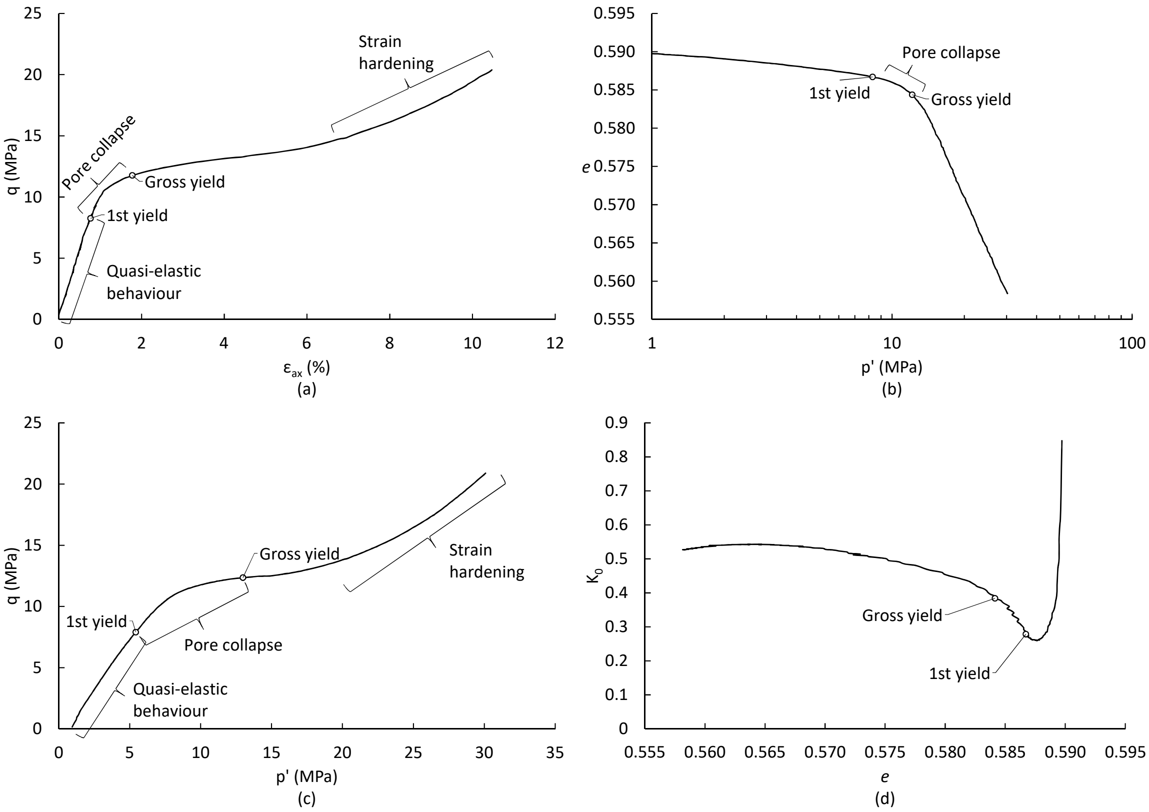

Figure 2.6. Mechanical performance of intact chalk under one-dimensional compression: (a) q vs axial strain (ε_{ax}); (b) p’ vs void ratio (*e*); (c) p’-q stress paths; (d) K_0 vs *e*. Based on Kågeson-Loe et al. (1993) and Schroeder (2002).

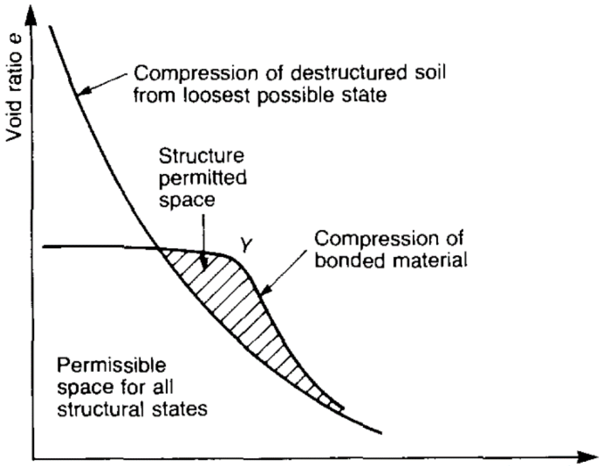

Figure 2.7. Definition of structure permitted space in volumetric space. ‘Y’ denotes yield. From Leroueil and Vaughan (1990).

As for other cemented geomaterials, the prevalence of inter-particle cementation in structured intact chalk allows it to withstand larger effective stresses without plastic deformations than destructured chalk at the same void ratio (Vaughan et al. 1988). These structure-supported effective stress – void ratio states constitute the ‘structure permitted space’, as defined by

Leroueil and Vaughan (1990), and shown in Figure 2.7. The properties of the structure permitted space are detailed in the following Section within the context of the shearing behaviour of intact chalk.

2.4.3 Behaviour in shear

The performance of intact chalk during shear is significantly affected by the presence of cementation. Absent cementation, Burland (1990b) predicted that chalk was liable to exhibit a mechanical behaviour compatible with critical state concepts, based on the work of Addis and Jones (1990) and Leddra and Jones (1990). Later investigations by e.g. Kågeson-Loe et al. (1993) and Heymann (1998), provided further evidence to support this view. Pertaining the effect of cementation, Homand and Shao (2000), Risnes (2001), Schroeder (2002) and others note that the mechanical performance of intact chalk during shear in triaxial experiments may be characterised into four effective stress-dependent modes:

- When chalk is sheared at an effective stress considerably above the gross yield limit and has experienced pore collapse and substantial compression-induced volumetric deformation, it behaves as a particulate material (dataset 1 in Figure 2.8). The material generally fails in a ductile manner and test stress paths denote strain hardening until reaching a Mohr-Coulomb critical state line (CSL; Figure 2.8a).
- When chalk is sheared at an effective stress below the first yield limit, the peak mobilised shear stress coincides with the yield strength (in shear) of the material because both parameters are controlled by bonding, and this stress value lies above the 'destructured' CSL in stress space (dataset 2 in Figure 2.8). The mode of failure is brittle and discrete diagonal shear bands develop. Disaggregated chalk is encountered in these shear bands and control the post-peak response (i.e. the 'residual' strength). This un-bonded material is expected to locally tend towards critical state conditions (Kågeson-Loe et al. 1993; Millar 2000).
- When chalk is sheared at an effective stress between the first and second yield limits, an intermediate behaviour is observed. Yield may be less brittle and may still coincide with the peak strength but may or not lie above the CSL (dataset 3 in Figure 2.8). Strain localisation in the form of 'ductile shear zones' (Petley et al. 1993) are often observed. These zones are composed by several putty-containing shear bands.

- Loading under tension is possible in cemented intact chalk. Tensile capacity is controlled by the cohesive strength of the cemented inter-particle contacts. Failure always occurs by the formation of fractures.

The above-described behaviours part from virgin isotropic compression scenarios (except the tension loading case), which are represented by the volumetric stress paths of Figure 2.8c. The pre-shear states for tests 1 and 3 shown in this Figure might be located inside the structure permitted space. Leroueil and Vaughan (1990) note that post-yield states within the structure permitted space and attained via compression are metastable. Their existence is only possible due to the partially uncemented fabric of the material being plastically hardened in the direction of the compression stress. This leads to high sensitivity upon shearing, exhibited as large positive pore pressure developments or substantial volumetric strains (Mitchell and Soga 2005). The strain levels required to eventually reach critical states during shearing inside the structure permitted space might not be achievable in triaxial test devices, and it is possible that the conditions depicted in Figure 2.8 do not correspond to such states. However, the application of sufficiently high pre-shear compressive stresses can theoretically lead to thoroughly destructured chalk fabrics and states no longer inside the structure-permitted space. In these cases, the material should cease exhibiting sensitive behaviour.

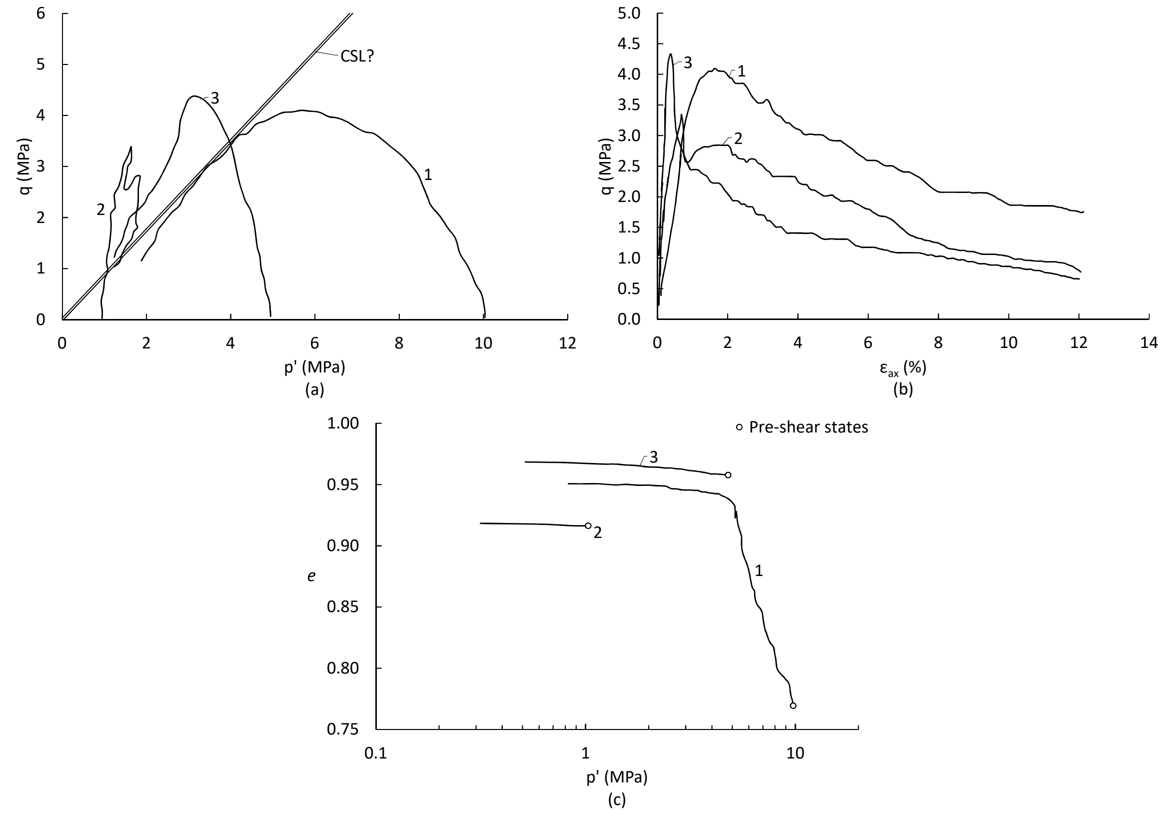

Figure 2.8. Undrained shearing behaviour of low density intact White Chalk: (a) stress paths; (b) stress-strain curves; (c) pre-shear compression paths. Re-drawn from Leddra (1989).

The stiffness of intact chalk is similarly controlled by cementation. At small strain levels (<0.01%) and at effective stresses below first yield, the effective stress-stiffness behaviour of chalk appears to be linear (Jardine et al. 1984; Clayton and Heymann 2001). This behaviour persists at various pre-yield stress levels until shear-induced yield occurs, as described above. Thereafter the stiffness-strain relationship becomes non-linear as in other uncemented soils.

2.4.4 Creep

Mitchell and Soga (2005) define creep in soils as the time-dependent deformations 'that develop at a rate controlled by the viscous resistance of the soil structure.' Soil structure deformation by creep results in (Ter-Stepanian 1992):

- Displacements at the molecular level.
- Displacements resulting from inter-particle bond rupture, particle displacement and rearrangement and particle crushing and/or breakage of angularities/asperities.
- Displacement and deformation of particle clusters or aggregations.

In broad terms, creep rates increase with increasing soil plasticity, water content, activity[1] and effective stress levels (Mitchell and Soga 2005). Creep rates tend to become reduced with time, except when stress levels have brought the soil close or past its yield limit.

The structure-changing nature of creep significantly affects weakly cemented and crushable soils, like many calcareous materials (Carter et al. 2000). Not surprisingly, creep is an important feature of the mechanical behaviour of chalk (Clayton and Heymann 2001; Matthews and Clayton 2004). Creep in chalk exhibits the following characteristics (based on Lord et al., 2002):

- Creep is directly related to in-situ Chalk grades (see Section 2.3), with Grade A showing insignificant creep rates whilst Grades B, C and D being progressively more prone to creep deformation. Clayton and Heymann (2001) and Matthews and Clayton (2004) suggest that this is because an important portion of time-dependent deformation is likely to occur by stress concentration along micro-fractures and discontinuities. This leads to localised strain by the closure of these micro-cracks. In chalk grades more susceptible to creep, and in chalk putty (Bialowas et al. 2018), creep rates appear to be log-scale linear in time.

---

[1] Ratio of plasticity index to the clay-sized content by dry weight; Skempton (1984).

- Creep rates increase with load intensity. It is generally thought that time-based structure deformation of intact chalk (i.e. assumed to be discontinuity-free) progresses from a mechanism that involves bond rupture and particle displacement at low and moderate stress levels, to a pore collapse-based process at higher stress levels (Dahou et al. 1995; Gennaro et al. 2003), which results in severe reductions in stiffness (Maranini and Brignoli 1999; Clayton and Heymann 2001). Katsaros (2008) notes that the pseudo-elastic limit can be regarded as a lower-limit stress boundary for observable creep to occur. Creep rates increase as the ratio of the stress applied to the yield stress increases and increases substantially as the material yields (Powell 1990; Clayton and Heymann 2001). A comparable performance has been reported for destructured chalk by Bialowas et al. (2018), but yield takes place at much smaller stress levels.
- Creep occurring at low and moderate stress levels that do not produce yield lead to gains in strength and stiffness, as observed in other granular materials (Katsaros 2008; Bialowas 2017). In uncemented materials, this is likely a result of increased ‘textural’ or surface-roughness (frictional) interlocking, and aggregation or clustering of particles. In cemented chalks, the closure of micro-fractures is speculated to be the dominant process. In both cases this leads to a less localised force-chain distribution and overall structural improvement of the material. This phenomenon is often described as ‘ageing’, which is addressed in more detail in Section 2.5.5.

2.5 Mechanical characteristics of destructured chalk

Several names are regularly used for chalk putty. Destructured chalk, remoulded chalk, chalk slurry, decomposed chalk and crushed chalk are common terms found in the literature (Clayton 1990; Bundy 2013). These terms are often used interchangeably. However, Bialowas (2017) points out an important distinction, based on definitions found in Leroueil et al. (1985) and Burland (1990a): a remoulded state is the condition in which sufficiently large mechanical disturbances have been imposed to the soil as to reduce its saturated strength to the minimum value, while reconstitution refers to thoroughly mixing a soil at a moisture content between the liquid limit and 1.5 times this value. Clearly, all reconstituted materials can be considered to be remoulded, but soils may also attain remoulded states outside the bounds of the definition for reconstitution. A generally agreed description for destructured chalk, independent from the method of creation, is that it is principally a ‘silt- and clay-sized’, largely non-plastic, carbonate granular material (Clayton 1990; Razoaki 2000; Lord et al. 2002; Bundy 2013).

2.5.1 Chalk putty preparation methods

Investigations into the mechanical behaviour of crushed low-medium density chalk have been largely an uncoordinated effort. The absence of an agreed upon method to prepare reconstituted or remoulded specimens and the high variability of the intact material hampers comparative analyses. Clayton (1978, 1983) crushed dry gravel-sized blocks in a TEMA mill or using a motorised mortar and pestle. In the former case, the material was sieved through the 425 µm sieve and the passing fraction was used. In the latter, either a <2 mm size limit was imposed by sieving or an unrestricted grading was used. Razoaki (2000) air-dried and crushed tunnelling by-product, and applied a 425 µm sieving treatment. Alvarez-Borges (2014) manually crushed blocks using a Proctor compactor, mortar and pestle, and pressing with a palette knife onto a glass plate, allowing the material to lose moisture during the process. Thereafter, the grading was restricted to <425 µm by sieving. An unrestricted grading was preferred by Bundy (2013), but the author used a TEMA mill on dry blocks as previously done by Clayton (1978). Doughty (2016) suspected that these methods did not accurately reproduce the material characteristics of the putty created during foundation works, in this case pile driving. Thus, this author proposed crushing the material by applying a specific number of blows using a light Proctor compactor whilst maintaining constant intact saturated moisture content. The grading of the resulting paste was not modified nor measured. Bialowas (2017) agreed that the dry-crushing procedures used by other researchers might not be adequate models of the remoulded chalk resulting from engineering activities. However, this author remarked that, to characterise material behaviour, it is necessary to ensure specimen repeatability, and a dry-crushing method seemed to be able to deliver this. Thus, Bialowas used a disc grinder and a jaw-crusher to destructure cobble-sized oven-dried chalk blocks, without restricting the grading of the resulting material. The effect of the application of these crushing procedures on the index characteristics of destructured chalk is discussed in the forthcoming Sections.

2.5.2 Particle size of chalk putty

Figure 2.9 shows the cumulative grading curves obtained for each of the methods described in the Section above for which particle size distribution (PSD) data is available. Table 2.1 summarises the intact and remoulded characteristics of these materials. It appears that the strongest PSD variability results from the application of additional crushing energy (Razoaki 2000), the use of an unrestricted grading (Clayton 1978; Bialowas 2017) and the use of very dense parent intact chalks largely composed by authigenic particles (Figure 2.2; Alvarez-Borges, 2014). For putties produced from low-medium density chalk and treated by sieving through the 425 µm mesh, the PSD variability seems to be low. This occurs because the PSD of putty chalk is controlled by the characteristics of the parent intact chalk (Clayton 1983; Lord et al. 2002; Clayton et al. 2003; Bundy 2013). When White Chalk from the low-medium density range is crushed, it tends to be reduced to the individual coccoliths, coccolith fragments and platelets of which it is largely composed. These putties are expected to exhibit lower void ratios than the parent material, and a poorly-sorted PSD. This is associated with the predominance of grain un-bonding over grain breakage that takes place during de-structuration (Katsaros 2008). In contrast, high and very high density chalk break down into better-graded larger, bulky and angular authigenic calcite blocks which result from the crushing of the heavily lithified structure of the material (Clayton 1983).

2.5.3 Atterberg Limits

Destructured White Chalk shows a limited plasticity range, with liquid limits within 18-32% and plasticity indexes within 4-9% moisture content (Clayton 1983; Lord et al. 2002). Uniformly graded putties created from crushing low-medium density generally exhibit higher liquid limit moisture contents (LL) and plasticity indexes (PI) than better graded materials resulting from the destructuration of higher density chalk. Clay minerals present in Grey Chalk (see Sections 2.2 and 2.3) can significantly affect the plasticity index range of chalk putties, effectively extending it to values between 4-30% with liquid limits ranging from 18 to 53% (Clayton 1983, 1990).

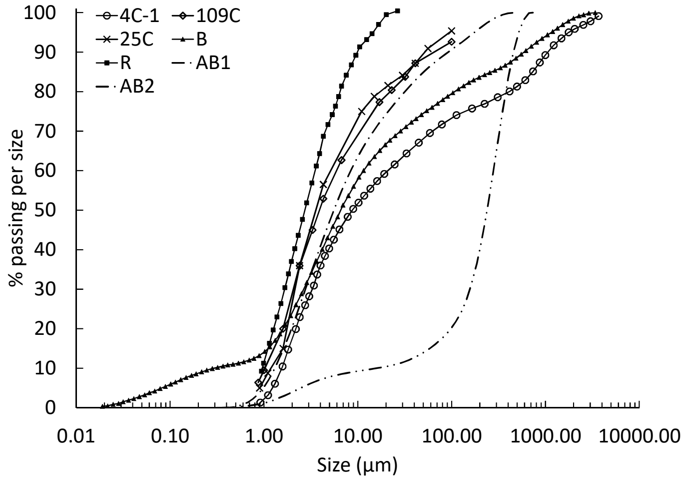

Figure 2.9. Cumulative particle size distributions of chalk putties prepared by various authors (legend key in Table 2.1).

Table 2.1. Chalk putty index properties according to various authors.

Author(s)	**Sample Abbrv.**	**Location**	**Formation**	**Mean IDD (Mg/m^3)**	**Prep. method**	**Grading range**	**LL (%)**	**PL (%)**
Clayton (1978)*	4C-1	Swanley	Seaford	1.43	Mortar/ pestle	Unrestr.	26	n/a
	4C-2					<2 mm	n/a	n/a
	25C	Thanet	Newhaven	1.47	Dry-milling	<420 µm	30	23
	109C	Lewes	Newpit	1.73			25	21
Razoaki (2000)	R	Brighton	Culver	1.65	Tunnelling waste + crushing(dry)	<425 µm	28	23
Bundy (2013)**	By-1	Longlands Quarry	Culver	1.78	Dry-milling (2 minutes)	Unrestr.	22	18
	By-2	Portsdown Quarry	Newhaven	1.65			27	23
Alvarez-Borges (2014)[†]	AB1	Somborne Quarry	Newhaven	1.47	Proctor crushing, mortar/ pestle and palette knife grinding (wet/dry)	<425 µm	28	22
	AB2	Mere	Lewes Nodular Chalk	2.49			18	n/a
Doughty (2016)[‡]	D	Wikinger	Maastrich-tian	1.50	Proctor crushing (wet)	Unrestr.	33.3 to 37.9	22.5 to 24.9
Bialowas (2017)	B	St. Nicholas-at-Wade	Margate	n/a	Dry-grinding + milling	Unrestr.	30	22

*Old lithostratigraphy used by original author. **Grading not provided in cumulative retained percentage per size. [†]Particle size analyses repeated using the same procedure as in present study. [‡]Grading not provided; some material data obtained from Doughty et al. (2018).

2.5.4 Behaviour in compression

Clayton (1978) and Razoaki (2000) have reported that when one-dimensional (1D) compression loads are applied to chalk putty, particles ‘stack’ upon each other and become locked due to their high angularity, without significant particle breakage taking place due to the very small particle size and abundant inter-particle contact points per unit volume (Mitchell and Soga 2005). Hence, they suggest that a unique effective compression stress-void ratio envelope (i.e., the one-dimensional normal compression line, 1D-NCL) cannot be produced at low-medium stress levels (<1000 kPa), because compression behaviour is dependent on the initial void ratio and stress history. However, as for sands, the application of sufficiently high compression stresses to some silts has been shown to produce convergent compression paths in void ratio-effective stress (e-σ') space, though whether this is associated with major particle damage is still subject to debate (Shipton et al. 2006; Carrera et al. 2011; Shipton and Coop 2012). Other researchers have found that the effect of the initial density, PSD and reconstitution method precludes compression path convergence (Nocilla et al. 2006; Grennan 2010). A small number of high-pressure (10 MPa) oedometer test on chalk putty specimens reconstituted at various initial void ratios recently presented by Bialowas et al. (2018) evidences convergent behaviour. The authors further suggest that the material performance is not different to that of typical carbonate sediments, though they do not comment on the possible micro-mechanics responsible for the observed behaviour.

2.5.5 Behaviour in shear

The angular and porous nature of the minute carbonate bioclasts of which low-medium density chalk putty is composed is associated with high void ratios that can often result in moisture contents close to the liquid limit (Clayton 1983; Lord et al. 2002; Clayton et al. 2003). Considering that the liquid limit represents the point at which particles are on the verge of losing contact due to water-saturation of pore space (Clayton 1983), an undrained shear load can rapidly lead to a reduction in effective stresses and a change in physical state (i.e. liquefaction; Youd et al. 2001). This renders the unconsolidated strength of chalk putty to near zero values, which is associated with a number of engineering problems including the low shaft capacities of PS piles pertaining this Thesis, as further discussed in Chapter 3 (Lake 1975; Clayton 1978; Razoaki 2000).

Investigations on the shearing behaviour of reconstituted or remoulded chalk specimens have been carried out by Clayton (1978), Razoaki (2000), Bundy (2013), Doughty (2016) and Bialowas (2017) by way of consolidated monotonic drained and undrained triaxial tests, and by Alvarez-Borges (2014) employing consolidated constant volume monotonic direct simple shear (DSS) tests. The shearing stages of these experiments were performed after various consolidation periods, lasting from less than two hours to over two months. The different consolidation timespans (often labelled 'ageing periods') were used to investigate the sometimes unexpected time-based gain in strength observed in crushed chalk, known as 'long-term' behaviour (Clayton 1978; Razoaki 2000; Katsaros 2008; Stone and Katsaros 2011). Following Bialowas et al. (2018), it is here assumed that the 'short-term' label applies to shear tests commenced within 24 h after the final change in effective confinement stress.

Figure 2.10 presents typical consolidated triaxial test results presented by two authors. Unfortunately, the amount of experimental data that complies with the above-defined short-term condition is sparse, and a dataset corresponding to a specimen that was consolidated for five days has been included in this Figure for comparison purposes. Material details for each dataset in Figure 2.10 are shown in Table 2.1. Specimens were reconstituted and tested using two methods and exhibited different pre-shear void ratios and stress histories. Razoaki (2000) placed several layers of chalk paste mixed at about the liquid limit inside a consolidometer, applying a vertical stress of 86.5 kPa thereafter. Bialowas (2017) poured a de-aired slurry mixed at about 2.2 times the liquid limit into a consolidometer, subsequently applied a vertical stress between 300 and 920 kPa. Test results are comparable in qualitative terms, despite the different chalk origins, reconstitution methods and test procedures. Data shows that a frictional Mohr-Coulomb criterion applies for destructured chalk in the short term. As for sands, shearing behaviour appears to be substantially affected by the pre-shear density. Specimens reconstituted using slurry-based methods exhibited pre-shear void ratios above 0.700 and seemed to predominantly contract upon shearing. In drained conditions, this was observed as increasing positive volumetric strains whilst in undrained conditions it was noted as an increase in pore water pressure (u) and a decrease in effective stress levels. In contrast, dilative behaviours observed as increases in effective stress (due to pore pressure reductions) or as volumetric expansion were noted in denser specimens, which were reconstituted using the 'layered' procedure and in one instance was in an overconsolidated state prior to shearing.

The shape of the undrained stress paths of material R in Figure 2.10a reveals a change from a highly contractive to a dilative response. This shift in stress path direction is termed phase transformation (Ishihara et al. 1975), and is often observed in sands. The transitory strain hardening (i.e. the initial increase in pore pressure) is sometimes named 'limited liquefaction' (Castro 1969; Ishihara 1993), and the momentary constant effective stress state before phase transformation is often termed 'quasi-steady state' (Alarcon-Guzman and Leonards 1988; Ishihara 1993). The reversal in volumetric strain occurring in drained conditions is called the 'characteristic state' (Luong 1980). For sands, there is evidence that these behavioural features may be associated with preparation-induced fabric (Ishihara 1993; Yoshimine and Ishihara 1998) and mode of shear (Yoshimine et al. 1999). In the case of destructured chalk, these trends appear to be predominant in specimens reconstituted using moisture contents lower than the liquid limit.

Clayton (1978), Razoaki (2000), Doughty (2016) and Bialowas (2017) also present results pertaining triaxial compression tests executed after consolidation periods in excess of 24 h, which are believed to exhibit various degrees of 'long-term' mechanical response. These authors identified two main aspects of ageing-induced mechanical behaviour in remoulded chalk:

- Ageing at constant volume (i.e., without change in volumetric strain) produced small (<8 kPa; Doughty et al., 2018) increments in fall cone-derived undrained strength, associated with thixotropic hardening. Additionally, specimens that were aged under drained constant load conditions that led to minimal changes in volume (due to low effective stresses and high reconstitution densities and/or high overconsolidation ratios) resulted in modest (≤5%) increments in small strain shear modulus (G_0) with time (Figure 2.11b; Bialowas et al. (2018)). Both ageing effects were believed to be aided by very weak contact-spot re-cementation, while Clayton (1978) further reported that the development of needle-shaped aragonite (a metastable form of $CaCO_3$) might strengthen the fabric of the material. However, ultimate states in large-strain shear were indistinguishable despite the different ageing conditions.
- Drained ageing at constant effective stress at high initial void ratios and/or high effective stress levels produced time-based reductions in void ratio (i.e. positive axial and volumetric strain; Figure 2.11a and Figure 2.12a). Therefore, specimens aged at a given effective pressure exhibited denser pre-shear states than unaged counterparts prepared at the same initial void ratio. This resulted in a broadly similar shearing performance to that expected for unaged overconsolidated specimens (compare Figure 2.12b with Figure 2.10a). Differences in shearing behaviour at similar void ratios and stress history after short and long ageing periods were uncommon and appeared to be limited to a modest increase in yield strength and (Figure 2.13). The very small strain shear modulus was also noted to increase considerably with ageing-induced strains (Figure 2.11b). Very minor increments in the cohesion intercept c', usually less than 10 kPa, have been reported as well, which are attributed to similar structure-developing processes as those occurring during constant volume ageing (thixotropic hardening, re-cementation, etc.).

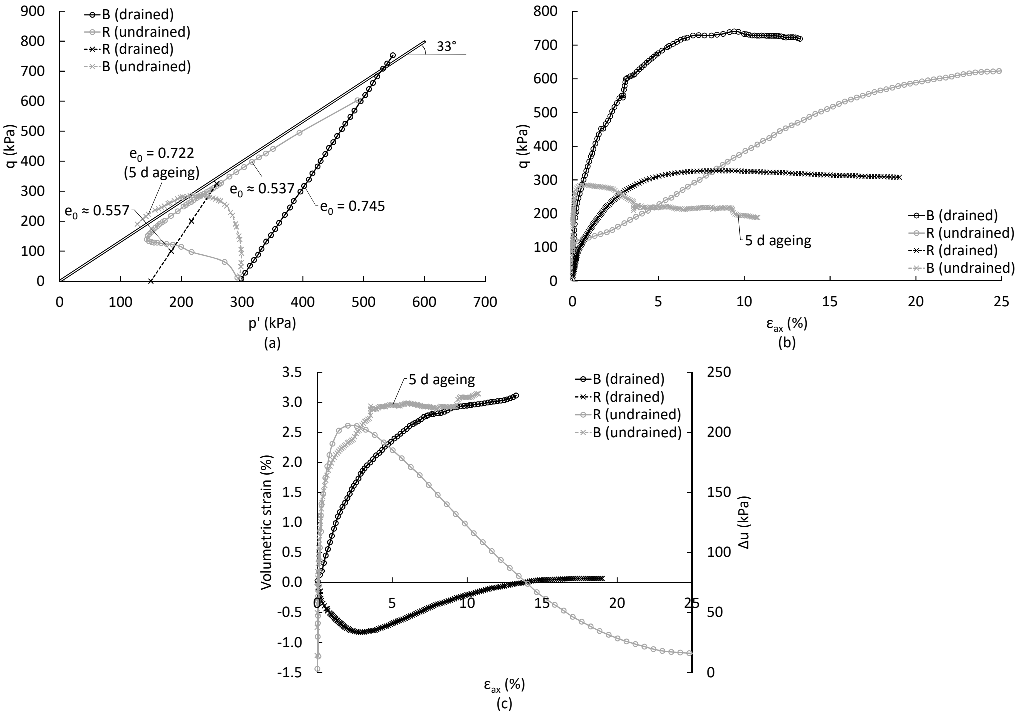

Figure 2.10. Shearing behaviour of two chalk putties: (a) stress paths; (b) stress-strain curves; (c) correlation between volumetric strain (ε_{vol}) or pore pressure change (Δu) with increasing ε_{ax}. OCR refers to the overconsolidation ratio. See Table 2.1 for legend key.

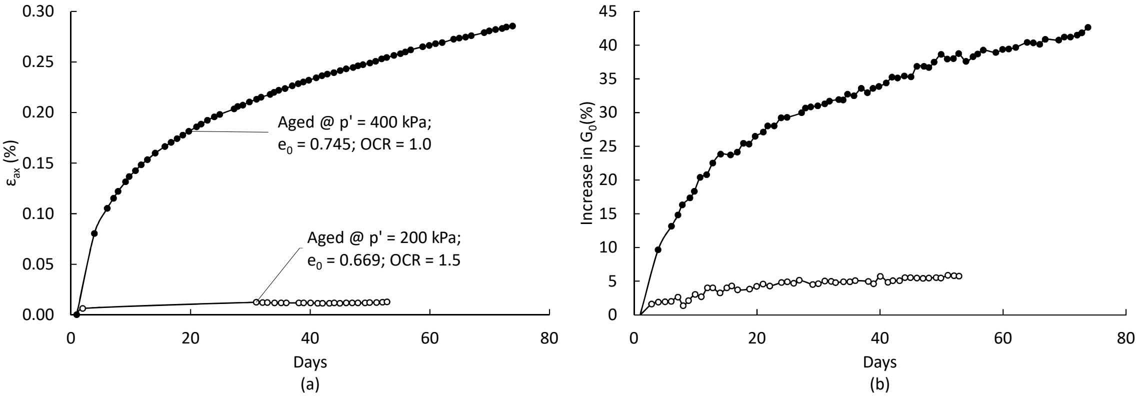

Figure 2.11. Comparison between time-based increases in ε_{ax} (a) and small strain shear modulus (b) during ageing of material B in Table 2.1. Re-drawn from Bialowas et al. (2018).

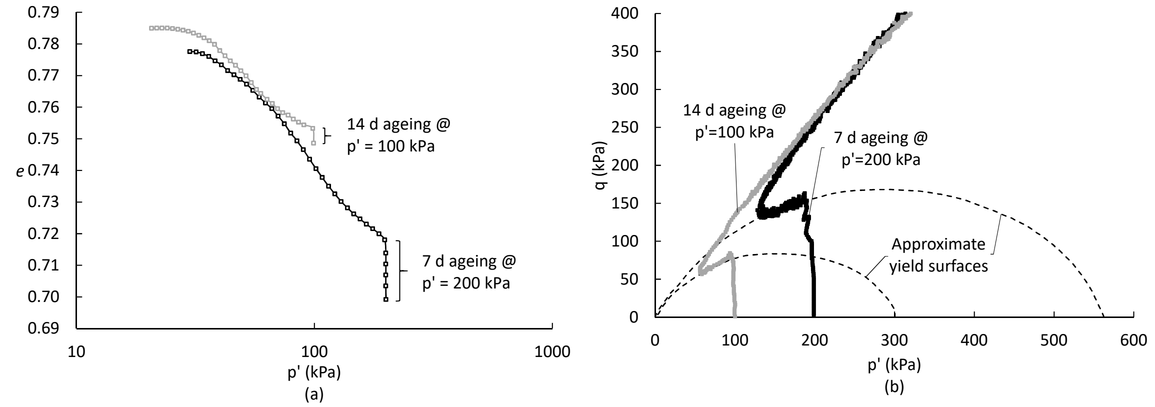

Figure 2.12. (a) Isotropic compression and (b) undrained shear paths in volumetric and stress space, respectively, of two normally consolidated triaxial specimens (material D in Table 2.1) reconstituted at a similar initial void ratio and aged under different effective isotropic pressures for 7 and 14 days. Re-drawn from Doughty (2016).

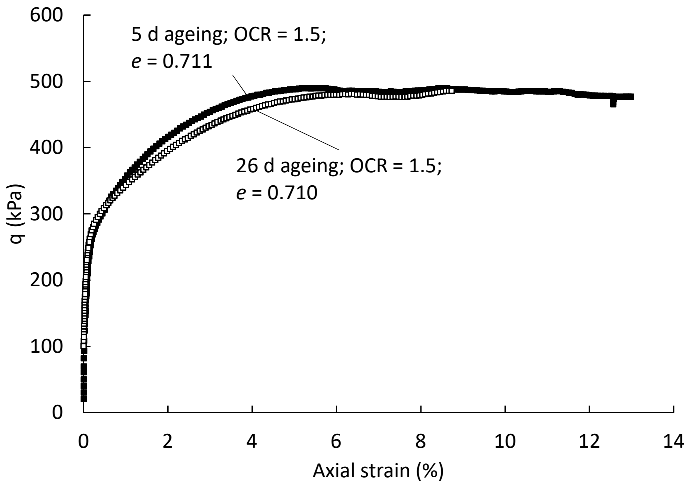

Figure 2.13. Drained shear stress-strain behaviour of specimens of similar characteristics (material B in Table 2.1) but aged for different time intervals. Re-drawn from Bialowas (2017).

2.5.5.1 Shearing behaviour and critical state concepts

The above-described density-based volumetric performance, in both aged and unaged conditions, is comparable to the mechanical behaviour reported for other non-plastic silts by e.g. Carrera et al. (2011) and Shipton and Coop (2012), and for sands by e.g. Been et al. (1991), Coop & Lee, (1993) and Verdugo & Ishihara (1996). These authors report that the mechanical performance of these granular materials can be characterised using Critical State Soil Mechanics (exposed in detail by Schofield and Wroth 1968, Atkinson 1993 and Muir Wood 1994). Therefore, it can be reasonably expected that critical state parameters can be also derived for destructured chalk.

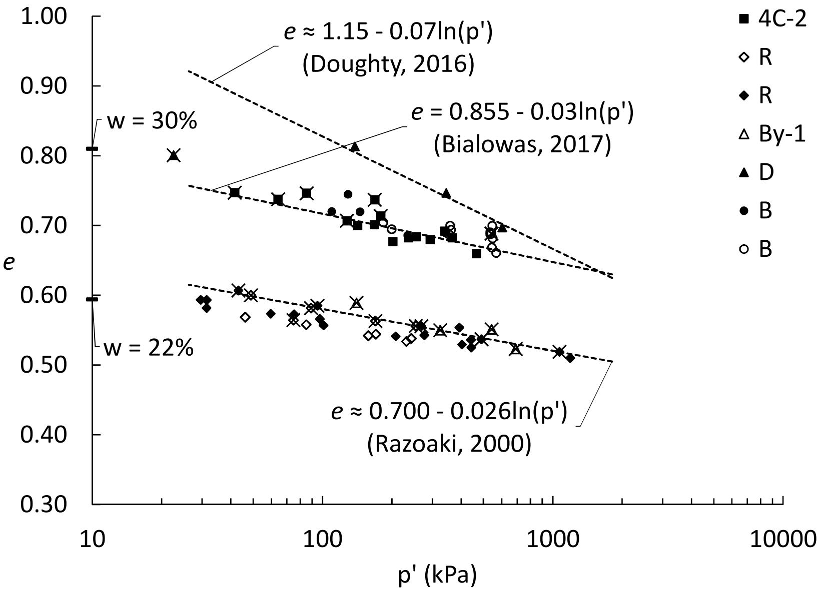

Figure 2.14. Ultimate states from triaxial experiments and CSLs by various authors (see Table 2.1). Open and filled markers denote drained and undrained test data, respectively; crossed markers refer to short-term conditions.

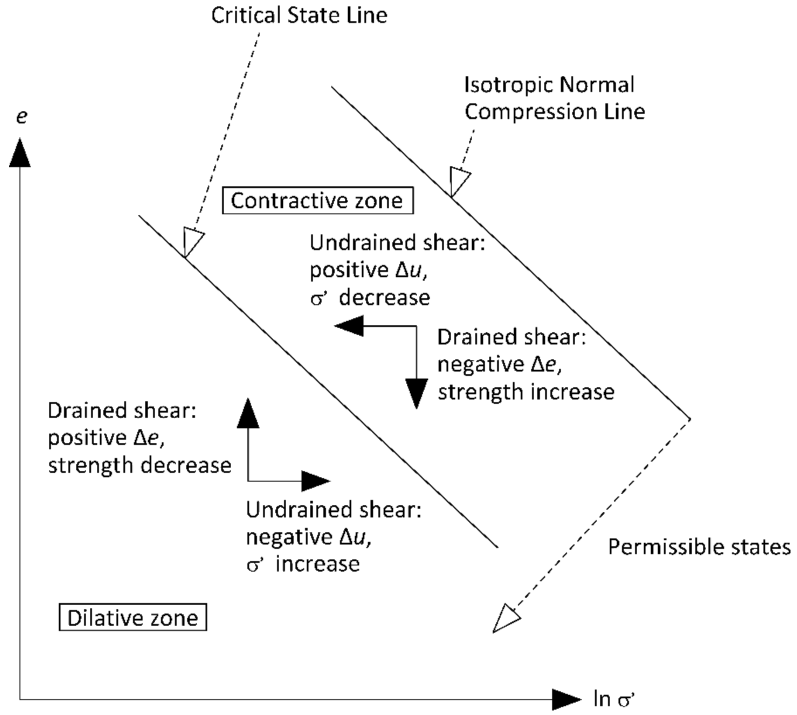

Figure 2.15. Influence of the initial state relative to the CSL on shearing behaviour, in terms of void ratio (e), effective stress (σ') and pore water pressure (u). Re-drawn from Mitchell and Soga (2005).

Critical state concepts have been applied to the behaviour of destructured chalk by Razoaki (2000), Doughty (2016) and Bialowas (2017). Figure 2.14 presents ultimate states in ln p'- *e* space, as presented by these authors. The term 'ultimate state' is in this case preferred over 'critical sate' because many tests initiated in conditions 'dry' or 'dense' of the critical state (i.e. in the 'dilative zone' below the CSL in Figure 2.15). This resulted in specimens exhibiting dilatant behaviour and, in many cases, strain localisation at approximate peak q, which prevented the attainment of the global theoretical critical state conditions (i.e., shearing at constant p', q and *e*; Casagrande 1936, Roscoe et al. 1958, Poulos 1981). Ultimate state data points are clustered in two linear patterns in Figure 2.14, in what would appear to be at least two distinct CSLs, proposed by Bialowas (2017) and Razoaki (2000). However, it should be noted that data points in the denser (or lowermost) group are in many cases dry of the plastic limit, and therefore, it would unrealistic to expect that uniform deformation occurred during these tests (see e.g. Barnes, 2013, Haigh et al., 2013). These low pre-shear void ratios were caused by the reconstitution method used. In contrast, most of the ultimate states in the looser (or uppermost) cluster are within the plastic range, delimited by moisture content (*w*) values of 30% and 22%, roughly corresponding to the average liquid and plastic limits of the materials, respectively (see Table 2.1). For both data groups it is notable to observe correspondence in ultimate states between chalk putties of different characteristics (prepared by different methods from different intact parent materials). It is apparent that the underlying phenomena that controls the ultimate strength of chalk putty are only substantially affected by strain localisation resulting from the specimen reconstitution method, and not by the procedure used to crush the chalk or the variability of the parent low-medium density rock.

2.5.5.2 Behaviour in cyclic shear

Experimental investigations on the behaviour of soils under cyclic loads are generally carried out by the application of a cyclic shear stress (τ_{cyc}) to a soil element using devices such as the triaxial, direct shear or direct simple shear apparatuses. τ_{cyc} is added or subtracted from a mean shear stress (τ_m), as schematically shown in Figure 2.16. As may be inferred from this Figure, cyclic loading may or may not involve stress reversal, i.e. a change in the direction of shearing that involves the application of 'positive' and 'negative' cyclic shear stresses and transition through the 'zero shear stress' condition during each cycle.

The application of τ_{cyc} generally results in the development of positive pore water pressures for soils that are wet of the CSL (i.e. in the 'contractive zone' in Figure 2.15; Robertson & Fear, 1997; Youd et al., 2001). Pore pressures steadily accumulate with each cycle, thus reducing effective stress levels and shear stiffness. As the volumetric state approaches the CSL, near-zero effective stress conditions may occur abruptly if cyclic shearing involves stress reversal, leading to an almost complete loss of shear strength and stiffness (Castro and Poulos 1977). Soil behaviour in these conditions resembles that of a fluid, and thus this type of failure is termed *cyclic liquefaction* (Robertson and Fear 1997). If cyclic loading does not comprise stress reversal, the material will still experience large pore pressure and shear strain accumulations, and shear stiffness reductions, but may retain some strength appropriate to its critical state void ratio and effective stress state (Yoshimi and Oh-Oka 1975; Castro and Poulos 1977). This failure mode is often called *cyclic mobility* (Castro and Poulos 1977; Youd et al. 2001; López-Querol 2009).

Cyclic shearing of soil at an initial state dry of the CSL (i.e. within the 'dilative zone' in Figure 2.15) will initially result in pore pressure accumulation, but subsequent dilatancy may prevent a total loss of shear strength (Castro and Poulos 1977; Robertson and Fear 1997; Hyde et al. 2006). However, strain accumulation and progressive softening may persist, to the point where such strains would be unacceptably high from an engineering perspective. This progressive straining without liquefaction is also commonly labelled cyclic mobility (Castro and Poulos 1977).

It is important to note that the above-described failure modes by cyclic loading do not necessarily take place every time a saturated granular soil is loaded in this manner. A key requirement for these failure processes to occur is the generation of excess pore pressures, which implies the disruption of soil structure (Mitchell and Soga 2005). This only occurs after (small-strain) yielding (Dobry et al. 1982; Jardine 1992; Vucetic 1994). Thus, a combination of τ_{cyc} and τ_m that does not cause the soil to yield should not result in pore pressure generation and the material will exhibit 'stable' behaviour (i.e. insignificant strain accumulation) under thousands of load cycles. It can be intuited that susceptibility to failure is closely linked to the proportion of the sum of τ_{cyc} and τ_m to the yield shear stress of the material (Sharma and Fahey 2003a, b). The latter is likely affected by current and previous effective stress levels and the volumetric state. Soil fabric is an additional factor per se that can significantly increase the shear strain and stress threshold after which instability may occur, but this parameter is seldom measurable (Peck 1979; Seed 1979).

In several engineering situations, particularly those involving offshore piled foundations, remoulded chalk may be subjected to cyclic stresses. However, there is a dearth of published work on the performance of remoulded chalk under these loading conditions. Carrington et al. (2011) presented a series of cyclic simple shear (CSS) tests on intact chalk specimens. In these tests, only a very thin film of remoulded chalk was probably present between the loading platen and the chalk specimen, essentially reducing the tests to direct shear conditions. A cyclic liquefaction-type failure was observed after the 1-3 cycles, probably because of the large cyclic strain amplitude applied (≈10%). Similar results were reported by Augustesen et al. (2015) and Dührkop et al. (2015) in constant normal stiffness (CNS) cyclic direct shear tests on remoulded chalk of unspecified characteristics. However, in-depth details of these tests and a thorough analysis of the results were not presented by these authors, as this was not the central objective of their studies. Coyne et al. (2015) report on a series of undrained cyclic triaxial and CSS tests on intact chalk samples. Grouted interfaces were used in some of the CSS tests to prevent failure through sliding of one of the test platens, as occurred in tests by Carrington et al. (2011). A low susceptibility to shear strength degradation due to cyclic loading was noted in the cyclic triaxial and grouted CSS tests, and it was attributed to the cemented nature of the specimens. As discussed in Section 2.4, cementation greatly increases the shear stress and strain threshold after which yield occurs and pore pressures are generated. Degradation was observed in non-grouted CSS tests in a similar fashion to what was reported by Carrington et al., probably due to specimen-platen sliding.

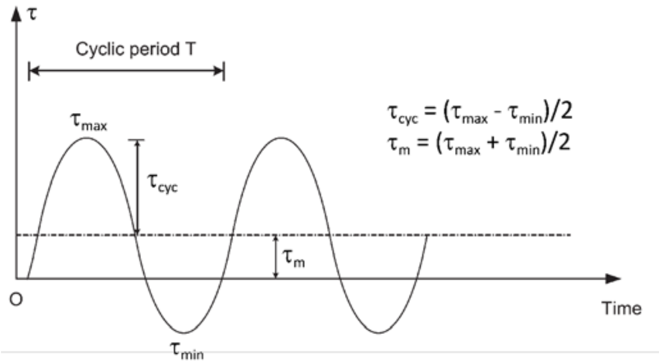

Figure 2.16. Time-domain stress parameters in cyclic shear tests. Edited from Tsuha et al. (2012).

Chapter 3 Small displacement piles

3.1 Introduction

Displacement piles, such as jacked or driven open- and closed-ended piles are installed without removing soil by excavating or boring. Instead, soil is displaced as the pile is pushed or driven (Fleming et al. 2009). The magnitude of the mechanical disturbances imposed on the soil due to this displacement depends significantly on the volume of the pile being installed (Gavin and Lehane 2003; White and Bolton 2004; Jardine et al. 2013b). Smaller disturbances occur in piles that displace relatively small volumes during installation, such as cruciform piles, open-ended tube piles and H-section piles. These piles are commonly referred to as ‘small displacement’ (PS) piles, as mentioned in Chapter 1 (Hobbs and Healy 1979). Conversely, piles which possess a geometry such that they displace larger volumes of soil when installed, like closed-ended steel tube piles, are referred to as ‘large displacement’ (PL) piles.

The total axial capacity of displacement piles results from the sum of the frictional resistance mobilised at the surface of the embedded pile shaft and the bearing capacity of the soil underneath the pile tip (Fleming et al. 2009). When a displacement pile is loaded in tension (uplift), the axial capacity is determined solely by the mobilised shaft friction.

This Chapter discusses the mechanics of displacement pile installation and shaft friction mobilisation, starting from the outcomes of previous research in sands, down to the particularities of piles in Chalk.

3.2 Small displacement piles in sands

Arguably, the fundamental difference between displacement pile installation in sands and clays is that in the former the process is assumed to be largely drained while in the latter it is expected to occur in undrained conditions (Fleming et al. 2009; Randolph and Gourvenec 2011). The implication of this is that the sand in the penetration path of a pile will experience large effective stresses that will locally alter the density of the material, and often induce changes in PSD due to crushing (Yang et al. 2010; Jardine et al. 2013a). The variability in sand properties, pre-installation in-situ sand states, pile geometries, amongst other parameters, results in great difficulties in deducing the post-installation state of the sand surrounding the pile, and therefore, the estimation of shaft friction and base bearing.

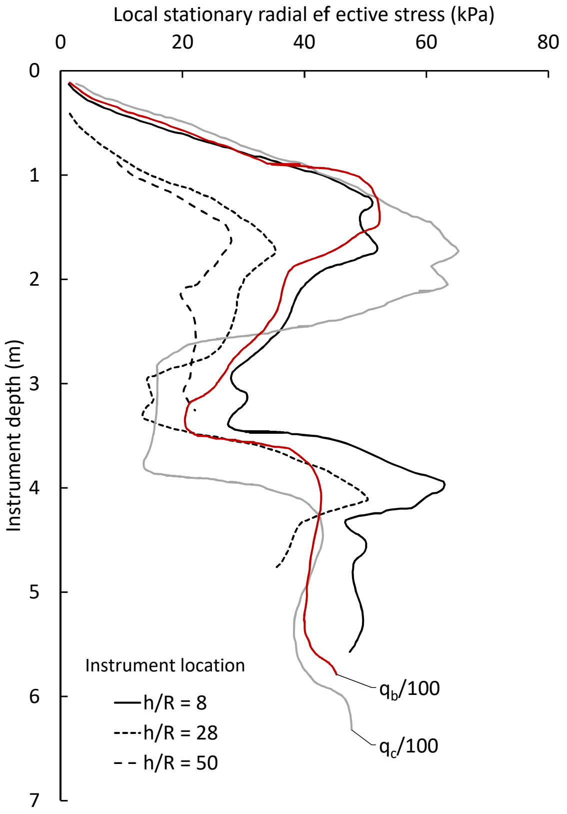

Figure 3.1. Profiles of local radial stationary effective stress measured at different distances (h) from the pile tip (normalised by pile radius R), and of q_c and q_b during jacking installation of a cone-tipped PL pile in silica sand. Redrawn from Lehane et al. (1993).

The work of Lehane et al. (1993) and Chow (1997) pertaining field tests using heavily instrumented piles have shed light on the stresses involved during pile penetration and loading. They provided evidence that local radial effective stresses and shaft friction are correlated with the stresses that occurred ahead of the pile tip during penetration (Figure 3.1). They suggested that the magnitude of these stresses are a measure of both the pre-installation intrinsic properties and state of the sand, and of the changes in these variables resulting from pile penetration. These observations and a large number of instrumented pile tests have led to a series of pile design methods based on simplified cone resistance (q_c) profiles from cone penetration tests (CPTs), which have been found to be broadly comparable with pile tip stresses (q_b) during installation, as evidenced by Figure 3.1 (e.g. Lehane et al., 2005b, Jardine et al., 2005, Kolk et al., 2005, Clausen et al., 2005).

Experiments using scaled physical models, CPT calibration chambers and geotechnical centrifuges have largely aimed at replicating the abovementioned results in a controlled environment, and to complement them by measuring stresses and strains in the sand during pile penetration and service loading. These investigations have made use of an array of innovative methods such as the use of photoelastic sand-like material (e.g. Dijkstra 2009), soil stress sensors (e.g. Jardine et al.

2013a), digital image correlation (DIC; e.g. White and Bolton 2004) and X-ray computed tomography (XCT; e.g. Ngan-Tillard et al. 2005), to name a few.

Analytical approaches have also been used to study pile behaviour. Perhaps the most notable outcomes of these are the cavity expansion model (Randolph et al. 1979; Yu and Houlsby 1991) and the strain path method (Baligh 1985; Baligh et al. 1987). The former comprises the idealisation of a cylindrical or spherical cavity representative of the pile tip being created in the soil mass. It is frequently used to model tip penetration and base bearing in solid piles (e.g. Randolph et al., 1994) and pile-sand interface dilation (e.g. Boulon & Foray, 1986). The strain path method models pile penetration as a continuous incompressible soil flow around a sphere- or cone-tipped rigid cylinder which provides a velocity field and displacement magnitudes that are amenable to local mathematical treatment along flow streamlines to determine strains.

The use of finite element analysis in displacement piles has had the advantage of allowing the study of states in which the sand around the pile is not at failure, e.g. during ‘safe’ service loading conditions (Dijkstra 2009). However, finite element modelling of pile penetration often encounters difficulties due to the very large mesh distortions associated with the severe straining of the sand around the pile (Einav and Randolph 2005; Sheng et al. 2005; Yang et al. 2014). Discrete element method (DEM) modelling has achieved some success in obtaining comparable quantitative and qualitative results to those derived from physical penetration studies, but such approaches are restricted by the number of individual particles that can be incorporated into the model and the use of unrealistically shaped particles (Lobo-Guerrero and Vallejo 2007; Arroyo et al. 2011).

Clearly, the volume of research on displacement piles in sand is vast. Therefore, the following Sections 3.2.1 and 3.2.2 are restricted to dealing with the mechanics of pile insertion and their relation with shaft capacity mobilisation, including common design approaches, based on key contributions mainly involving physical modelling, but also field testing and analytical models.

3.2.1 Installation

The most common installation procedures for small displacement piles in sands are:

- Driving, which involves striking the pile head repeatedly, pushing the pile down with each blow. Each strike involves bi-directional shearing of the pile-soil interface (White and Lehane 2004; Gavin and O'Kelly 2007). Many load cycles are expected to occur during installation. It is the most common installation procedure for offshore PS piles.

- Jacking, which involves pushing the pile downwards in a series of steps, at relatively constant rate. One load cycle is imposed in each jacking step, but a much reduced number of cycles takes place if compared with pile driving (White and Lehane 2004). It is usually impractical in offshore conditions, but preferred in urban environments were driving-induced noise and vibration would be unacceptable (White et al. 2002). It is also the method by which the penetrometer is inserted into the ground during the CPT.
- Vibro-driving, which involves the combined application of a vertical load and vertical vibration to the pile head to insert the element into sandy strata by fluidising the material close to the pile toe and shaft (Holeyman and Legrand 1997; Viking 2006). Though predominantly used in sheet pile installation, vibro-driving of tubular and H-section piles offers advantages over impact driving, such as higher installation rates and reduced noise levels (O'Neill et al. 1990; Wong et al. 1992). The use of vibro-driving methods for the development of offshore wind power infrastructure has gathered interest due to the latter, which reduces affectations to marine wildlife (Saleem 2011). However, detailed studies on the vibratory driving of piles in Chalk are not available, to the writer's knowledge, and the topic is therefore not discussed further in this Thesis.

Pile jacking has been generally favoured by researchers because its 'controlled' nature aids the process of studying penetration mechanisms. Thus, a rendering of key studies associated with pile jacking follows, organised by the research approach used by the authors. Thereafter, the effect of the installation method on penetration mechanisms is discussed in Section 3.2.1.4.

3.2.1.1 Physical modelling of large displacement jacked piles

Laboratory-based model tests involving PL piles jacked in sand have shown that a zone of highly compressed sand forms beneath the pile tip during installation (White and Bolton 2004; Yang et al. 2010). In tests involving flat-tipped prismatic piles installed in a plane-strain experimental set-up, White and Bolton (2004) found that this zone is cone-shaped, as previously reported by BCP (1971) and predicted by cavity expansion theory (Randolph et al. 1994; Salgado et al. 1997), and named it 'nose-cone' (Figure 3.2). For PL model piles installed in dry silica sand and biogenic calcareous sand, White and Bolton reported that the nose-cone material had experienced volumetric strains deemed to be too large to be attained by compression per se, and the authors proposed that a significant amount of drained shearing had to occur during pile installation. This intense shearing was found to produce substantial particle re-arrangement and comminution, as latter reported in more detail by Yang et al. (2010). The material constituting the central 'rigid' portion of the nose-cone was probably collected by the flat pile tip early during penetration and dragged down (and crushed) by it throughout the process (Randolph et al. 1994).

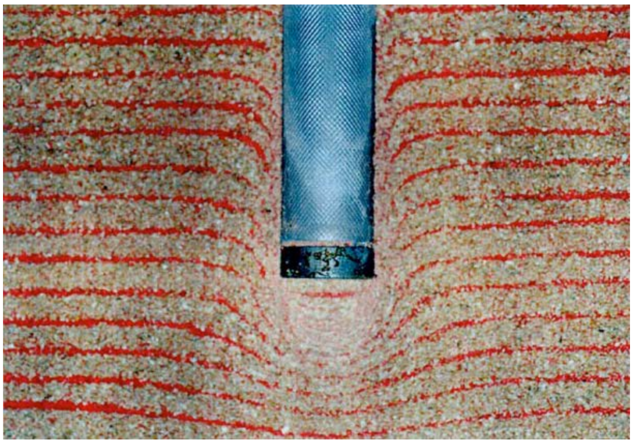

Figure 3.2. Heavily compressed ‘nose-cone’ zone underneath the tip of a model pile. From Kuwajima et al. (2009).

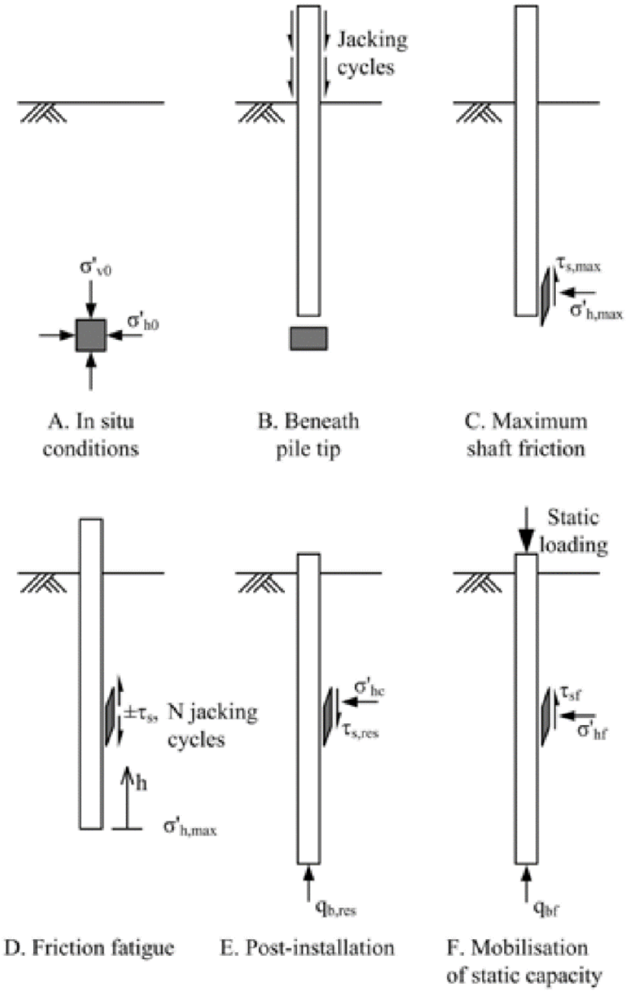

Figure 3.3. Schematic of stress and deformation history of a soil element initially collinear with the pile centre line at the start of installation (from White & Deeks 2007). $\sigma'_h = \sigma'_r$ (radial effective stress); q_b = pile tip stress (base bearing).

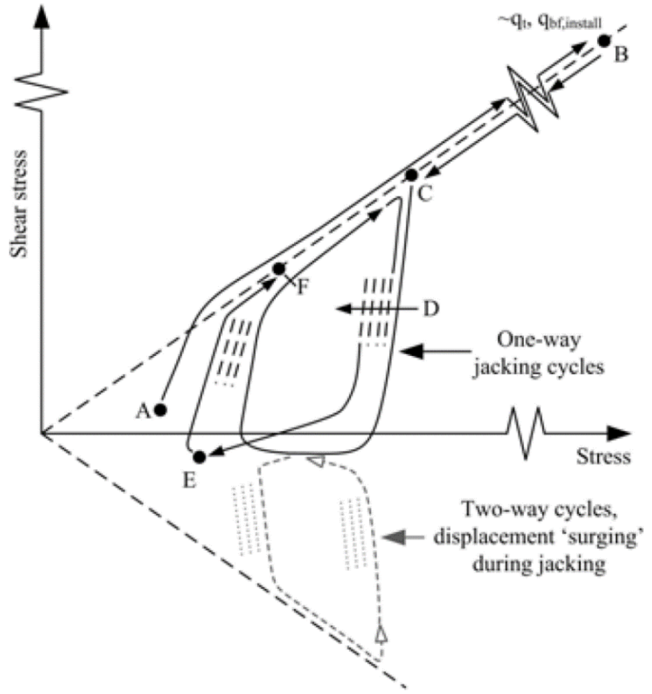

Figure 3.4. Representation of the stress paths corresponding to the stages shown in Figure 3.3 (White and Deeks 2007).

White and Bolton (2004) further reported that as the pile tip moved downwards during installation, strips (slivers or swaths) from the edge of the nose-cone moved radially from under the pile tip towards the pile shaft, effective forming a 'sleeve' or 'annulus' between the pile surface and the relatively undisturbed soil. The stress history associated with the creation of the crushed sand sleeve around a jacked pile may be schematically represented in a series of stages, as shown in Figure 3.3 and Figure 3.4, after White (2005) and White and Deeks (2007). These stages may be summarised as:

- Stage A: the element of sand is in undisturbed conditions under the action of in-situ stresses, i.e. K_0 conditions.
- Stage B: the pile tip and nose-cone approaches and the element of sand experiences very large increases in vertical and shear stress, and volumetric distortion accompanied by grain crushing (White and Bolton 2004; Lobo-Guerrero and Vallejo 2007; Kuwajima et al. 2009). Jardine et al. (2013b) suggests that stress conditions at this stage are equivalent to drained triaxial compression, with the vertical stress being the major principal stress. This behaviour is represented by the progression of the stress path from A to B in Figure 3.4 along the failure envelope of the material, though other authors believe that the soil state likely follows a K_0-path before curving towards the critical state envelope (e.g. Altuhafi & Jardine, 2011; Aghakouchak et al., 2015).

- Stage C: the nose-cone pushes the sand element radially producing further increments in stress levels, distortion and displacement until the pile tip passes (Randolph and Gourvenec 2011). The latter leads to significant stress reductions as the soil is removed from the action of the vertical stresses under the pile tip. The principal stress direction changes from a near vertical one (aligned with the pile axis) to a near horizontal one, aligned with the horizontal reaction of the sand (Salgado et al. 1997; White and Bolton 2004; Yang et al. 2010; Jardine et al. 2013a, b). This change in effective radial stress levels from a maximum at pile shoulder depth to a sharp reduction as the pile tip passess is shown in Figure 3.5 as measured by Jardine et al. (2013a) in model pile tests using an instrumented CPT calibration chamber, and has also been reported by Lehane et al. (1993), Chow (1997), and others, pertaining measurements using instrumented field-scale test piles. This unload path is proposed to follow the failure envelope from B to C in Figure 3.4.
- Stage D: the sand element, now at the side of the pile and forming part of the annulus, experiences cyclic shearing with each additional pile thrust. In addition to the contractive behaviour associated with principal stress rotation, particle rearrangement and far-field relaxation (Arthur et al. 1986; Iwashita and Oda 2000), cyclic shearing may also lead to particle comminution and migration towards the pile shaft (White and Bolton 2004; White and Lehane 2004; Yang et al. 2010; Doreau-Malioche et al. 2018). This contributes to an overall contractive performance and densification of the sand annulus and lower radial effective stress and shaft friction levels. These shaft friction reductions due to cyclic shearing are termed ‘friction degradation’ or ‘friction fatigue’, and are generally observed in all displacement piles installed in granular materials (Heerema 1980; Lehane et al. 1993; White and Lehane 2004; Gavin and O'Kelly 2007). Friction fatigue leads to lower effective radial stress levels with increasing relative distance to the pile tip, as evidenced in Figure 3.5, because this distance is directly correlated to the number of load cycles experienced by the sand element in question. Friction fatigue is represented in Figure 3.4 by the gradual progression of the cyclic shearing stress path loops towards lower stress levels with each cycle.
- Stage E: this stage depicts a state in which residual vertical stresses remain at the pile tip after installation has finalised. These are usually associated with stored energy in the soil under the pile tip resulting from shaft friction precluding the recovery of elastic deformations in the pile after the final installation thrust (Fellenius 2015).
- Stage F: representative of service loading conditions in which shaft friction and base bearing may oppose loads to the pile head. Shaft friction is discussed in deeper detail in Section 3.2.2.

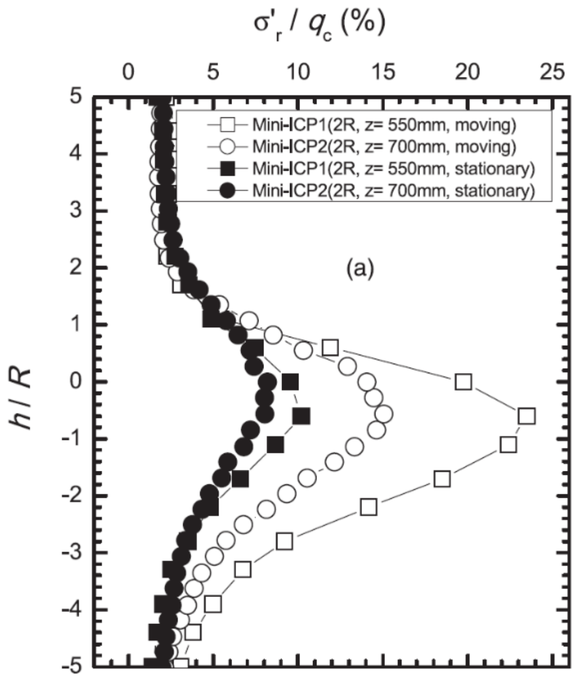

Figure 3.5. Normalised stationary and moving radial effective stress profiles at 2R from the shaft of a model pile, at depths z = 550 and 700 mm (h/R = normalised distance from the pile tip). Data from Jardine et al. (2013a), image from Yang et al. (2014).

3.2.1.2 Physical modelling of small displacement jacked piles

Lehane and Gavin (2001) and Gavin and Lehane (2003) carried out a series of tests using scaled open-ended steel tube piles installed in a CPT calibration chamber filled with dry siliceous sand. They were able to show that whether an open-ended pile becomes plugged or not during installation significantly affects stress and strain levels underneath the pile tip. When the pile penetrates the sand but becomes plugged, stress levels resemble those of a closed-ended pile. The volume of sand displaced and/or compressed becomes essentially the same as that occurring during the installation of a PL pile (Figure 3.6a). Conversely, if the pile penetrates without becoming plugged (‘full coring mode’), a much smaller volume of soil becomes disturbed and tip resistance and stress conditions across the tip during driving are significantly smaller (Figure 3.6b). Centrifuge-based tests on strain-gauged driven model piles by De Nicola and Randolph (1999) produced similar results, and the authors linked the lower stress levels resulting from smaller displaced volumes to reduced shaft friction.

White et al. (2005) considered that limiting pile the analysis of penetration behaviour to ‘plugged’ and ‘full-coring’ conditions is incomplete. They proposed that, for a given increment in penetration, the ‘net volume’ being pushed into the sand mass may be characterised by the effective area ratio, A_r:

$$A_r = 1 - \mathrm{IFR}\left(\frac{{D_i}^2}{{D_o}^2}\right) \tag{2}$$

where IFR (incremental filling ratio) is the ratio of the change in plug length to the increase in pile tip depth, and D_i and D_o are internal and external pile diameters, respectively. The authors then use A_r to relate the area enclosed by a full-coring open-ended pile to that of an equivalent closed-ended element of the same net pile volume. White et al. thereafter incorporate cavity expansion theory to estimate the ratio of radial stresses close to the tip that is adequate to the same A_r. To account for partial plugging (Figure 3.6c), White and colleagues use the IFR, which has been shown to decrease with:

- decreasing D_i to wall thickness ratio (D_i/t; Lehane & Gavin, 2001),
- decreasing D_o (Gavin and Lehane 2005), and
- decreasing penetration rates/velocities (e.g. the use of jacking instead of driving; Henke & Grabe, 2013).

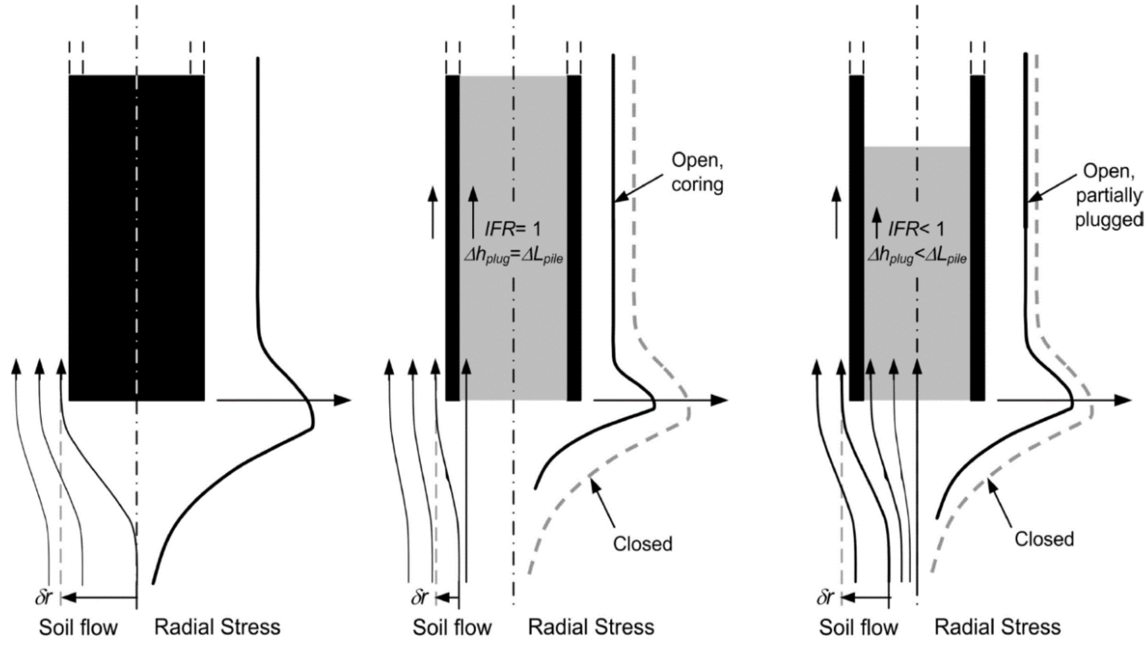

(a) Closed-ended pile. A_r= 1

(b) Coring (unplugged) open-ended pile. IFR= 1, A_r~ 0.1

(c) Partially plugged open-ended pile. IFR< 1, 0.1< A_r<1

Figure 3.6. Plugging of open-ended pipe piles and associated streamlines of soil flow during penetration. From White et al. (2005).

3.2.1.3 Field-scale investigation of small displacement piles

Though investigations based on scaled physical models are clearly a valuable tool to study pile penetration in sand, this research method rarely involves PS piles and almost exclusively uses jacking as method of installation. The preference for PL piles has been likely motivated by the more direct correlation with CPT, and by the reduced space available to install sensors within the wall of PS piles. Similarly, the use of pile jacking as opposed to pile driving reduces the probability of damaging the sensors during installation (see e.g. Chow, 1997 and Paik et al., 2003)

Yet, there is a growing database of tests involving strain gauged field-scale PS piles impact-driven in sands (see Yang et al., 2017). However, and in contrast with plane strain experiments and the post-test analyses performed on centrifuge or calibration chamber tests, field-scale tests cannot directly reveal pile penetration mechanisms.

As with the scaled laboratory experiments discussed in the preceding Sections, there is evidence that unplugged open-ended field-scaled piles mobilise smaller driving resistances at the tip (e.g. Brucy et al., 1991 and Byrne, 1994), and therefore, it is often assumed that lower radial effective stresses are present after the tip passes a given horizon (e.g. White & Deeks, 2007, and Lehane et al., 2008). This is in turn associated with lower shaft capacities. Field-scale compression tests by Paik et al. (2003) support this view.

Chow (1997) correlated observations from experiments involving open-ended piles driven into silica sand deposits with the strain path method (Baligh 1985; Baligh et al. 1987). From this assessment, Chow suggested that very high stresses and strains concentrate under the pile rim during penetration. These stresses and strains, however, were thought to be more localised and to decay more rapidly with increasing distance from the pile tip than in PL piles. Chow proposed several possible practical interpretations, of which the more promising were thought to be that (after Jardine & Chow, 2007):

- Penetration may occur in partially-plugged conditions, therefore, stresses and strains under the advancing tip are equal to those of a solid pile of the same diameter times a reduction factor that accounts for the degree of plugging.
- That the stresses under the pile rim were comparable to those of a solid pile of equivalent tip cross-section area, but the degradation rate with distance from the tip was higher.

The cavity expansion-based exposition of the penetration mechanics of open-ended piles proposed by White et al. (2005), and described in Section 3.2.1.2, draws on the first of Chow's interpretations exposed above. For both scenarios, Jardine and Chow (2007) point out that stresses immediately under the pile rim of full-coring piles are close to those observed in CPTs and under PL piles (≈0.7q_c), as fairly comparable mechanisms as those described in Figure 3.3 and Figure 3.4 are expected to occur locally.

The strain path method was originally formulated considering fully undrained conditions, and therefore, its correlation with pile penetration in sands is not universally agreed upon. However, both of the above propositions have been incorporated into the widely-used CPT-based pile design methods ICP-05 (Jardine et al. 2005) and UWA-05 (Lehane et al. 2005b). These two methods, which are described in greater detail in Section 3.2.2.2, are amongst the most reliable according to Lehane et al. (2005a), Jardine and Chow (2007), Schneider et al. (2008) and Yang et al. (2017).

3.2.1.4 The influence of installation method on penetration mechanisms

It is generally agreed that the main difference between impact-driving and jacking is an increase in the number of shearing cycles that the pile-sand interface experiences, whilst the pile tip stresses are comparable (White and Lehane 2004; Gavin and O'Kelly 2007). This might hold for PS piles if appropriate account is made for plugging, which is expected to occur principally during jacking. Field-scale plugging of driven piles is often assumed to be precluded by the inertial reaction of the sand inside the pile (Fleming et al. 2009; Randolph and Gourvenec 2011).

As previously discussed, a greater number of shearing cycles at the pile-sand annulus associated with pile driving is believed to augment the friction fatigue effect and lead to lower post-installation radial effective stresses and lower shaft frictions. Lehane et al. (2008) further comment that base-bearing behaviour of closed ended piles is expected to be stiffer for piles installed by jacking and presume that a similar effect may be observed in jacked open-ended piles.

3.2.2 Shaft friction

Shaft friction results from the resistance to rolling and sliding by the particles contained in the pile-sand interface or annulus (DeJong and Westgate 2009). The total shaft capacity ($\mathrm{Q_s}$) of a displacement pile installed in sand is calculated as (e.g. Lehane et al., 2005a):

$$\mathrm{Q_s} = \pi \mathrm{D} \int \tau_{\mathrm{sf}}\, \mathrm{dz} \tag{3}$$

where D and z are the pile diameter and embedded length, respectively.

As mentioned in Chapter 1, the pile-soil ultimate effective angle of interface friction (δ'_{ult}) and the radial effective stress (σ'_r) acting perpendicularly to the pile surface are considered to be the main factors controlling shaft friction in granular ('non-cohesive') soils (Figure 3.7; Boulon & Foray, 1986, Kraft, 1991, Lehane et al., 1993 and others). Local shaft friction (τ_{sf}) mobilisation can be described by the Mohr-Coulomb criterion stated in Chapter 1:

$$\tau_{sf} = \sigma'_r \tan\delta'_{ult} \qquad \text{(1 bis)}$$

Constant normal stiffness (CNS) simple shear conditions are believed to be locally representative of the deformation mechanism of the sand annulus sheathing a displacement pile, as depicted in Figure 3.7 (Randolph & Wroth, 1981, Boulon & Foray, 1986, Airey & Muir Wood, 1987, Kraft, 1991, Fakharian & Evgin, 1997, and others). After pile installation (i.e. the pile being stationary), the annulus rests at a dense and relatively low normal effective stress state (such radial stress is here designated as 'static' or 'stationary' radial effective stress, σ'_{rs}) resulting from the penetration mechanisms described in Section 3.2.1. In CNS simple shear conditions, σ'_r levels are expected to first become moderately reduced at the onset of pile axial loading and interface shearing due to principal stress rotation, and then increased with accumulating strain due to the dilative response associated with high densities and low effective stress levels. These σ'_r increases lead to an upsurge in shaft friction (Lehane et al. 1993; Chow 1997). Indeed, laboratory- and field-based instrumented pile experiments have shown that the dilative behaviour of the heavily compressed pile-sand interface might be an important factor in the mobilisation of shaft capacity (Lehane et al. 1993; Lehane and White 2005; Gavin and O'Kelly 2007; Lehane et al. 2012; Lim and Lehane 2015a). Therefore, effective radial stress increases associated with the dilative tendency of the constrained pile-sand interface ($\Delta\sigma'_{rd}$) is incorporated into Eq. (1) to derive local shaft friction values, producing the flowing expression (Figure 3.7; Lehane et al., 1993):

$$\tau_{sf} = \sigma'_r \tan\delta'_{ult} = (\sigma'_{rs} + \Delta\sigma'_r)\tan\delta'_{ult} \qquad (4)$$

δ'_{ult} is usually derived with relative ease by means of standard laboratory tests such as the direct shear test, the direct simple shear test and the ring shear test (e.g. Kishida & Uesugi, 1987, Jardine et al., 1993, Fakharian & Evgin, 1997). On the other hand, σ'_{rs} levels along the pile shaft and the magnitude of the potential increase in these magnitudes due to constrained dilation are more difficult to estimate. Boulon and Foray (1986) approximated the magnitude of $\Delta\sigma'_{rd}$ from cylindrical cavity expansion theory as:

$$\Delta\sigma'_r = \frac{4G\Delta y}{D} = k\Delta y \qquad (5)$$

where Δy is the radial longitude of the dilation of the slip surface, G is the operational horizontal shear modulus of the soil constraining the remoulded interface. The substitution k is regarded as the operational lateral stiffness of the soil, often expressed in kPa/mm (Johnston et al. 1987; Airey et al. 1992). While k can be approximated using in-situ tests which evaluate stiffness parameters (see e.g. Clayton, 2011), Δy is more elusive, principally due to the lack of knowledge of the in-situ conditions of the sand annulus. Hence, Δy is frequently assumed to be either equal to the average centreline surface roughness of the pile shaft when the average particle size in the interface is larger than this roughness value (Jardine and Chow 1996; Jardine et al. 2005; Altuhafi and Jardine 2011), or derived from interface shear tests at stress and density states assumed to be representative of in-situ conditions (Airey et al. 1992; Lehane et al. 2012). However, as the magnitude of $\Delta\sigma'_{rd}$ is limited by the pile diameter (as evident in Eq. (5)), authors often consider that any inaccuracies in the calculation of Δy has little impact on local σ'_r levels in large diameter piles (e.g. Lehane et al., 2008). It thus becomes clear that the objective of the majority of displacement pile design guidelines is the accurate estimation of σ'_{rs} along the embedded length.

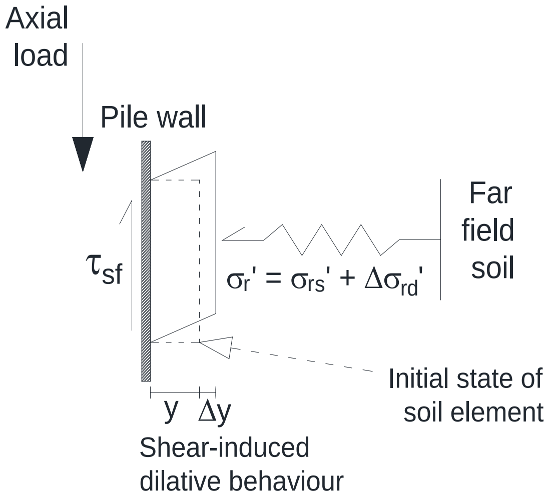

Figure 3.7. Representation of local shaft friction mobilisation. Re-drawn from Lehane and White (2005).

3.2.2.1 API local shaft friction estimation method

The 'main text' American Petroleum Institute Recommended Practice for Geotechnical and Foundation Design Considerations (API RP2 GEO) and for Planning, Designing, and Constructing Fixed Offshore Platforms – Working Stress Design (API RP2A-WSD) are perhaps the most widely used design guidelines for PS piles in sands (Iskander 2010). This 'main text' API method calculates the local τ_{sf} profile for PS piles in silica sands as:

$$\tau_{sf} = K_f\sigma'_{v0}\tan\delta'_{ult} = \beta\sigma'_{v0} \leq \tau_{sf\,lim} \tag{6}$$

where $\mathrm{K_f}$ is the lateral earth pressure coefficient, σ'_{v0} is the vertical effective overburden pressure adjacent to the pile at a given depth, and $\tau_{\mathrm{sf\,lim}}$ is a limiting value for shaft friction determined by the particle size and density of the deposit. $\mathrm{K_f}$ and $\tan\delta'_{\mathrm{ult}}$ are often assumed to be constants. It is largely due to these assumptions, and the use of $\tau_{\mathrm{sf\,lim}}$, that the 'main text' API method has been subjected to extensive criticism, as they are inconsistent with the pile penetration phenomena described in Section 3.2.1 and with physical mechanisms associated with shaft friction discussed previously (Randolph et al. 1994; De Nicola and Randolph 1999). It is thus unsurprising that API method designs perform poorly when compared with many CPT-based approaches, which indirectly incorporate pile-sand interaction (Lehane et al. 2005a; Schneider et al. 2008; Yang et al. 2017). However, the simplicity of the API-method and the scarcity of offshore foundation performance shortcomings associated with it have contributed to its popularity (Jardine and Chow 2007).

3.2.2.2 CPT-based local shaft friction estimation methods

API commentary to the RP2A-WSD guidelines have recognised the advantages of using CPT-based methods that account for penetration mechanisms and shaft-sand interaction, and proposed simplified versions of the ICP-05 (Jardine et al. 2005) and UWA-05 (Lehane et al. 2005a; Lehane et al. 2005b) methods, and the FUGRO-05 (Kolk et al. 2005) procedure. Schneider et al. (2008) and Yang et al. (2017) have evidenced that the full versions of these methods, plus the NGI-05 (Clausen et al. 2005), out-perform the simplified alternatives and the main-text API when estimated capacities are statistically compared against measured capacities (using high-quality site-investigation and instrumented pile test data). As previously mentioned, the ICP-05 and UWA-05 procedures appear to be the most accurate. The general formula to estimate local shaft friction values for cylindrical piles in both methods parts from eq. (4), and may be expressed as:

$$\tau_{\mathrm{sf}} = \mathrm{A_{ICP}}(\mathrm{B_{ICP}}\mathrm{d_{ICP}}\mathrm{q_c}{F_F}^{c} + \Delta\sigma'_{\mathrm{r}})\tan\delta'_{\mathrm{ult}} \tag{7a}$$

$$\tau_{\mathrm{sf}} = \mathrm{d_{UWA}}(\mathrm{A_{UWA}}\mathrm{B_{UWA}}\mathrm{q_c}{F_F}^{c} + \Delta\sigma'_{\mathrm{r}})\tan\delta'_{\mathrm{ult}} \tag{7b}$$

The A and B terms in eq. (7) are associated with the pile tip condition (e.g. closed-ended, open-ended full-coring, open-ended partially-plugged) and the change in effective stress levels from below the pile tip to immediately behind it, respectively. The d term includes a factor accounting for the direction of loading (i.e. tension or compression), as the Poisson effect of the pile and the stress reversal at the pile-sand interface may have an impact on the magnitude of τ_{sf} (De Nicola and Randolph 1999; Jardine and Chow 2007). The ${F_F}^{c}$ term typifies friction fatigue, but as specified in Table 3.1, may also invoke effects associated with the pile tip condition. The subscripts ICP and UWA define which terms are used in the ICP-05 (eq. 7a) and UWA-05 (eq. 7b) approaches, respectively. Table 3.1 evidences that both methods are quite similar, and statistical reviews by Schneider (2008), Yang et al. (2017) and others indicate comparable performances.

CPT-based methods have been shown to provide safe and relatively efficient shaft capacity design values for displacement piles in silica sands, but its applicability to piles in calcareous materials has not been definitively proven at the time of writing (Murff 1987; Thompson and Jardine 1998; Schneider et al. 2007; Mahanta et al. 2015).

Table 3.1. Parameter description for ICP-05 and UWA-05 shaft friction estimation methods described by eq. (7a) and eq. (7b).

Term	**Definition**	**Associated parameter**
$\mathrm{A_{ICP}}$	0.9 for open ended piles in tension, 1.0 for all other cases.	Tip condition and loading direction.
$\mathrm{B_{ICP}}$	$0.029\left(\frac{\sigma'_{v0}}{p_{ref}}\right)^{0.13}$ where σ'_{v0} is the effective vertical overburden and p_{ref} is a 100kPa reference stress.	Stress conditions immediately behind the pile tip and absolute depth.
$\mathrm{d_{ICP}}$	0.8 for tension and 1.0 for compression.	Loading direction.
${F_F}^c$	$\left[\max\left(\frac{h}{R^*},8\right)\right]^c$ where R^* is the equivalent radius which equals the pile radius R for closed-ended piles and $({R^2}_o - {R^2}_i)^{0.5}$ where R_o and R_i are the outside and inside pile radii, respectively, for open-ended piles; h is the relative distance to the pile tip; and c = -0.38.	Friction fatigue and pile tip condition.
$\mathrm{A_{UWA}}$	$(A_r)^{0.3}$ where A_r is the effective area ratio defined by eq. (2). When IFR is not measured, IFR ≈ $\min\left[1,\left(\frac{D_i}{1.5}\right)^{0.2}\right]$ where D_i is in metres.	Pile tip condition.
$\mathrm{B_{UWA}}$	0.3	Stress conditions immediately behind the pile tip
$\mathrm{d_{UWA}}$	0.75 for tension loading and 1.0 for compression.	Loading direction.
${F_F}^c$	$\left[\max\left(\frac{h}{D},2\right)\right]^c$ where c = -0.5 and D is the outside diameter	Friction fatigue.

3.3 Small displacement piles in Chalk

Displacement piles in Chalk are generally regarded to mobilise much lower shaft capacities than piles in sands (Lord et al. 2002). These differences are largely associated with the cemented nature of chalk, with its small and arguably relatively friable particles, and with the fact that it is often found in nearly saturated conditions close to the liquid limit.

Most of the current state of knowledge on the axial-loading behaviour of displacement piles in low-medium density chalk originates from the work of Ciavaglia et al. (2017a), Buckley et al. (2018a), Buckley et al. (2018b), Geduhn et al. (2018a), Geduhn et al. (2018b), and Jardine et al. (2018). Their investigations involved the installation and posterior cyclic and monotonic axial testing of instrumented onshore and offshore field-scale PL and PS piles. The onshore tests were carried out at the same site from which samples were collected for the present Thesis (Section 4.2).

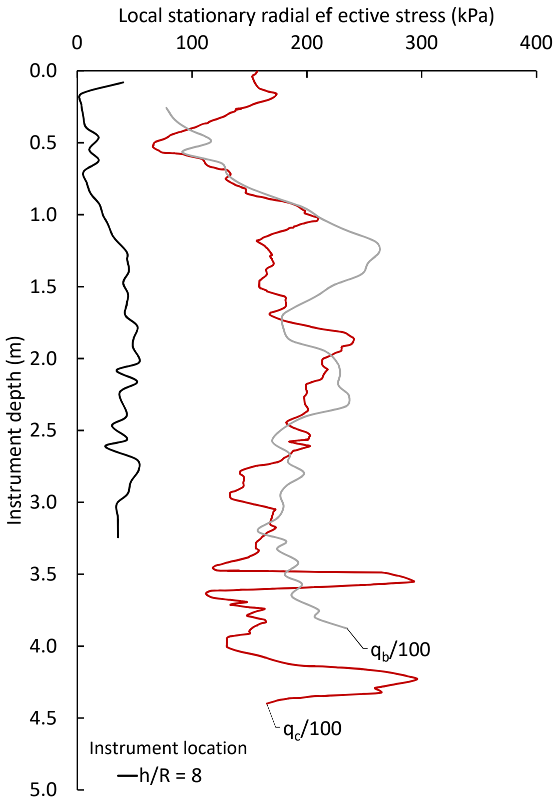

Figure 3.8. Profiles of local radial stationary effective stress measured at eight pile radii above the tip, and of q_c and q_b during jacking installation of a flat-tipped PL pile in low-medium IDD chalk. Redrawn from Buckley et al. (2018a).

Table 3.2. Short-term (unless otherwise noted) shaft capacity tests on small displacement (PS) and instrumented large displacement (PL) piles in Chalk.

Author(s)	**Site conditions**	**Installation details**	**Pile geometry**	**Average shaft friction, $\bar{\tau}_{sf}$ (kPa)**
Hobbs and Robins (1976)†	Woolwich – Upper Chalk	Driven; onshore; 8.5 m in chalk	H-pile (PS); UBP: 305 x 305 mm x 110 kg	41.7 (tension)
		Driven; onshore; 12.8 m in chalk		20.0 (tension)
		Driven; onshore; 12.0 m in chalk		8.3 (tension)
Lord and Davies (1979)	Brighton - Munford Grade II; $\overline{\text{IDD}}$ = 1.65 Mg/m^3	Driven; onshore; 4.0 m in chalk	Steel tube (PS); D_o = 800 mm; D_i = 760 mm	150.0 (tension)
Burland and French (1990)	Luton – Munford Grade VI	Driven; onshore; 4.9 m in chalk	Cruciform (PS); 140 x 140 mm	23.3 (tension)
Hobbs and Atkinson (1993)	Immingham – Grade A/B; $\overline{\text{IDD}}$ = 1.62 Mg/m^3	Driven; near-shore; 11.0 m in chalk	Steel tube (PS); D_o = 914 mm; D_i = 876 mm	125.0 (tension)
Ciavaglia et al. (2017a)	St Nicholas-at-Wade – CIRIA low-medium density grade A/B; $\overline{\text{IDD}}$ = 1.50 Mg/m^3	Driven; onshore; 4.0 m in chalk	Steel tube (PS); strain-gauged; D_o = 762 mm; D_i = 673 mm	11.0 (EOD, compression) 22.0 (7 d ageing, tension)
				23.0 (EOD, compression) 23.0 (6 d ageing, tension)
Buckley et al. (2018b)	St Nicholas-at-Wade – CIRIA low-medium density grade B3/B2; $\overline{\text{IDD}}$ = 1.49 Mg/m^3	Driven; onshore; 5.5 m in chalk	Steel tube (PS); strain-gauged; D_o = 136 mm; D_i = 119 mm	15.0-17.0 (EOD, compression); 39.0 (10 d ageing, tension)

Table 3.2 (concluded).

Author(s)	**Site conditions**	**Installation details**	**Pile geometry**	**Average shaft friction, $\bar{\tau}_{sf}$ (kPa)**
Buckley et al. (2018a)	St Nicholas-at-Wade – CIRIA low-medium density grade B3/B2; $\overline{\text{IDD}}$ = 1.49 Mg/m^3	Jacked; onshore; 4.10-4.30 m in chalk	Solid cylinder (PL); instrumented (ICP); 102 mm	50.0 (installation, compression); 20.0 (23-80 d ageing, tension)
Carotenuto et al. (2018)	Sheringham Shoal Offshore Windfarm – CIRIA low-medium density grade Dc/Dm to B5; $\overline{\text{IDD}}$ = 1.55 Mg/m^3	Driven; offshore; 9.5-23.40 m in chalk	Steel tube (PS); D_o = 4740-5700 mm; t_w = 50-75 mm	2.0-10.0 (EOD - compression)
Jardine et al. (2018); Geduhn et al. (2018b)	Wikinger Offshore Windfarm – CIRIA low-medium density grade A1/B2; $\overline{\text{IDD}}$ = 1.52 Mg/m^3	Driven; offshore; 20.4 m in chalk	Steel tube (PS); D_o = 1370 mm; D_i = 1290 mm	36.0 (EOD, compression) 158.0 (11-15 w ageing, tension - extrapolated)
		Driven; offshore; 24.2 m in chalk		35.0 (EOD, compression) 168.0 (11-15 w ageing, tension - extrapolated)
Nowak and Thijssen (2018)	Ipswich Tidal Barrier – CIRIA low-medium density grade D/C	Vibro-driving + impact driving; near-shore; 30.0 m in chalk	Steel tube (PS); D_o = n/a; D_i = n/a	≈15-40 (1-3d ageing, dynamic) ≈35-55 (≈100d ageing, dynamic)
Notes: EOD = end of driving. t_w = pipe pile wall thickness. $\overline{\text{IDD}}$ = average intact dry density. †Piles were observed to 'whip' (deflect) during driving, which possibly led to lower-than-expected $\bar{\tau}_{sf}$.				

Buckley et al. (2018a) evidenced that a comparable correlation may be found between pile tip stresses during installation and stationary radial effective stresses (σ'_{rs}), as reported for silica sands (Section 3.2), and shown in Figure 3.8. This led Buckley (2018)[2] and Jardine et al. (2018) to propose that, as for PS piles in silica sands, a CPT-based effective stress pile design approach may be adopted for piles in Chalk, i.e. the Chalk ICP-18 method. However, Jardine and co-authors recognised that there is currently limited pile test data to be able to definitively prove that the CPT is able to capture the high-sensitivity behaviour of high-porosity structured chalk described in Chapter 2. This behaviour is evidenced by the offset between the σ'_{rs} and q_c or q_b profiles in Figure 3.8, which is not present in Figure 3.5 using the same normalisation constant for q_c and q_b.

Previous to these recent works, Lord et al. (2002) presented the outcomes of six uncoordinated tests using uninstrumented PS piles from which they proposed current design guidelines. Details of these earlier and the more recent investigations are shown in Table 3.2.

In contrast with research on displacement pile behaviour in sands, scaled tests using geotechnical centrifuges, CPT calibration chambers or plane-strain arrangements are largely unsuitable for the investigation of penetration mechanisms in chalk. It is not feasible to prepare an intact specimen of the size needed in the majority of CPT calibration chamber and plane-strain tests, or to install stress gauges in the material without disturbing its structure. Furthermore, the vast majority of imaging techniques for DIC analysis cannot register most chalk grains due to their very small size. Therefore, the review of pile penetration mechanisms and shaft friction mobilisation in the subsequent Sections is based on the outcomes of the field-scale tests included in Table 3.2, and on analytical interpretations.

It is underscored that the average shaft friction values shown in Table 3.2, and the local stress measurements discussed in this Section correspond to early life ('short-term') capacities, unless otherwise indicated. There is evidence that some PS piles driven in chalk exhibit substantial gains in axial capacity with time, a phenomenon described as 'pile set-up' (Vijayvergiya et al. 1977). This effect is further discussed in Section 3.3.2.2.

---

[2] This publication was embargoed whilst preparing the present Thesis, but outcomes such as the Chalk ICP-18 method were presented by Jardine et al. (2018) at the Engineering in Chalk 2018 Conference in London, 16-18 September 2018.

3.3.1 Installation

PS piles in Chalk are mostly used in offshore and near-shore conditions and are largely installed by impact-driving (Jardine et al. 2018). Contrasting difficulties are sometimes encountered: piles may meet refusal before reaching the design depth or may ‘run’ several meters under self-weight or a single hammer blow (Dührkop et al. 2017; Jardine et al. 2018). This occurs because the variable sensitivity of the cemented soft rock results in performances that range from ‘strong’ and dilating to ‘toothpaste-like’ and contracting once cementation is removed during pile installation (Lord et al. 1994; Dührkop et al. 2017).

As mentioned in Chapter 1, it is widely agreed that pile penetration crushes the chalk and forms a chalk putty sleeve around the pile, commonly named annulus (Hobbs and Atkinson 1993; Lord et al. 2002). Thus, pile penetration mechanisms must accommodate the inserted pile volume plus the volume of crushed chalk. The latter quantity is dependent on the pile volume, on the density and grade of the Chalk mass, and potentially on the installation method. For example, a given pile volume installed at a rate compatible with the drainage characteristics of the formation is expected to shatter and displace a large amount of dense chalk and to crush and densify a fairly limited volume of porous chalk.

3.3.1.1 Penetration mechanisms from field-scale investigations

Though Hobbs and Atkinson (1993) and Lord et al. (2002) consider that chalk grades (Section 2.3) play a major role during penetration by allowing intact blocks to be pushed aside by the pile, Lord et al. (1994) and Dührkop et al. (2017) note that close to the pile and within the vertical path of the pile chalk crushing is expected to be the dominant penetration mechanism. Therefore, pile penetration was regarded by these authors to be essentially a granular interaction comparable to that of sands which should consider parameters such as pile shape (tip condition), lateral (radial) stress and friction fatigue.

Once the chalk becomes crushed under the tip, and therefore mobile, it becomes displaced from under the CPT or pile tip to the sides as observed for sands (Section 3.2.1), thus forming the annulus (Hobbs and Atkinson 1993; Lord et al. 2002). A key difference, however, is that the fully-drained penetration condition assumed for sands does not seem to apply for chalk. Diambra et al. (2014) and Buckley et al. (2018a) found that low-medium density chalk crushing during CPT leads to very high excess pore water pressure developments at the tip, and therefore, the crushed material is expected to exhibit low effective strengths in the short term (Dührkop et al. 2017). However, Buckley et al. (2018a) also noticed that pore pressures dissipate very rapidly. Pore pressure reduced by 40% between piezocone (CPTu) measurements at positions u_1 and u_2 (see Lunne et al. 1997) during continuous penetration, and 50% dissipation was achieved after 4 to 13 s during dissipation tests. Rapid pore pressure loss is associated with the high permeability of the material, and was proposed by Buckley et al. (2018b) to be related to major water content reductions and consolidation of the annulus, tentatively in the direction of the pile shaft. This suggestion was based on the partial exhumation of two driven open-ended tubular piles, and subsequent moisture content analyses performed at various depths and distances from the pile shaft, shown in Figure 3.9. Zones A, B and C refer to the completely puttified chalk annulus, partially shattered chalk blocks, and fairly undisturbed chalk with some fractures, in that order. Comparable but less detailed observations were made by Muir Wood et al. (2015) regarding the partial exhumation of driven steel sheets.

Ciavaglia et al. (2017a) and Buckley et al. (2018b) noted that the chalk crushed under the pile rim of open-ended PS piles may be preferentially displaced into the pile, leading to pile plug levels that rise above the ground level. This suggests a more favourable flow path towards the internal pile space than towards the periphery, where the chalk mass retains most of its cemented structure and might oppose the flow of chalk putty between it and the pile shaft.

Pile driving in high density chalk is recognised to mobilise much greater resistances to pile penetration (Lord et al. 2002; Dührkop et al. 2017). This is thought to originate from the higher stresses required to produce yield in the cemented material in compression (Section 2.4) and the dilatant performance of dense disaggregated chalk (Section 2.5; Hobbs and Atkinson 1993).

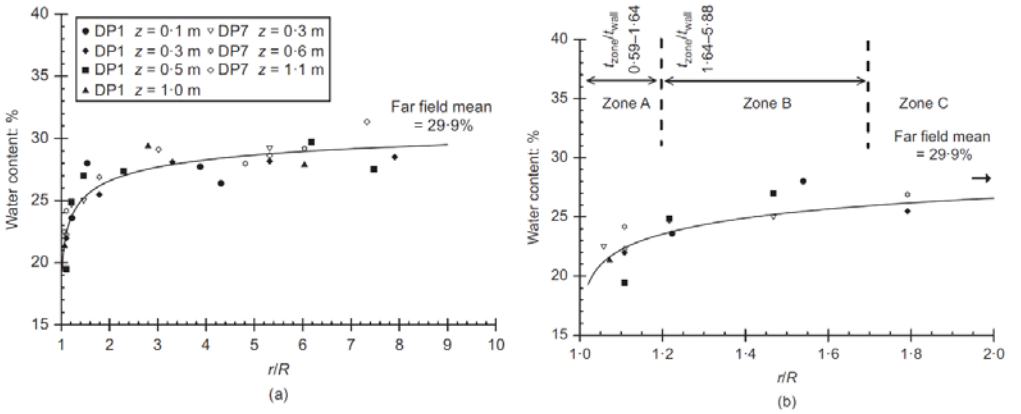

Figure 3.9. Moisture content profiles of the annulus and adjacent material (radial distances from the pile centreline r normalised by the pile radius R). From Buckley et al. (2018b).

3.3.1.2 Radial effective stress changes from field-scale investigations

As for sands, Ciavaglia et al. (2017a), Buckley et al. (2018a) and Buckley et al. (2018b) suggest that σ'_r levels are higher close to the pile tip, but dramatically reduce as the tip passes. These proposals were based on:

- The expected comparability with the observations from investigations in silica sands, discussed in Section 3.2.1. In particular, a similar stress history to that described in Figure 3.3 and Figure 3.4 is believed to be valid for a chalk element on the path of a displacement pile during installation, once its structure has yielded. This includes the effects of stress reversal and friction fatigue.
- The difference between the $\sigma'_r \approx 300$ kPa derived from sleeve friction measurements at 5.5 radii above the tip during CPT and the $\sigma'_r \approx 1500$ kPa speculated to be required to yield the chalk below the tip of the instrumented large displacement (PL) Imperial College Pile (ICP; equipment characteristics are given in Bond et al. 1991).
- The use of pile driving analysis (PDA) instrumentation (i.e. strain gauges) and IMPACT signal-matching technique (Randolph 2008), which suggested a non-linear shaft friction distribution at the end of driving (i.e. in compression), as shown in Figure 3.10.
- The possibility of liquefaction-like behaviour in the crushed chalk, associated with saturated conditions and high void ratios (Section 2.5.5.2).

Based on the above considerations and on the penetration processes described in Section 3.3.1.1, Buckley (2018) developed the CPT-based Chalk ICP-18. As for CPT-based pile design methods for silica sands, the premise of the Chalk ICP-18 procedure is that the stresses measured at the cone tip during CPT are indicative of the in-situ state and sensitivity of the chalk before and during pile installation. Jardine et al. (2018) proposed that the method is able to accurately estimate radial effective stresses and shaft friction during penetration and after pile set-up. Regarding the former, the Chalk ICP-18 specifies that:

$$\tau_{\mathrm{sf}} = (\mathrm{B} \mathrm{q}_{\mathrm{t}} F_F{}^{\mathrm{c}}) \tan \delta'_{\mathrm{ult}} \tag{8}$$

Where $\mathrm{q_t}$ is the cone resistance corrected for the ‘unequal area effect’ (Lunne et al. 1997), B = 0.031, F_F = max(h/R*, 6), c = $-0.481(D/t_w)^{0.145}$ and t_w is the wall thickness of the open-ended tube pile. Comparing with ICP-05, Chalk ICP-18 limits empirical corrections for the pile tip condition to the use of the equivalent radius R* in the friction fatigue term $F_F{}^{c}$.

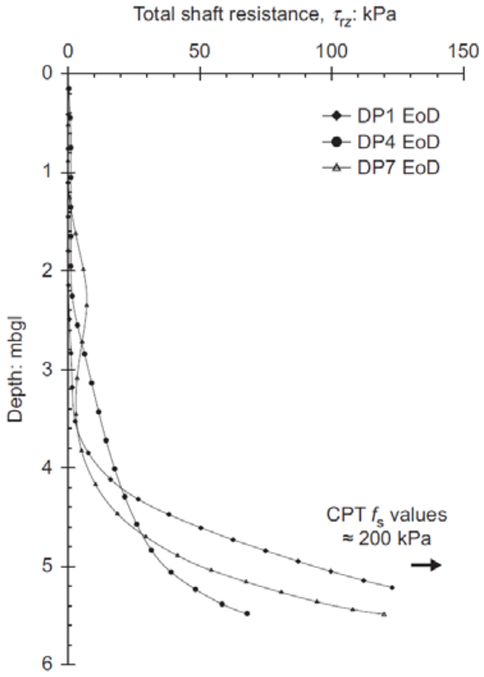

Figure 3.10. Average shaft friction profiles of 139 mm D_o piles (Table 3.2) at the EOD determined using PDA (Buckley et al. 2018b).

3.3.1.3 Critical state model for small displacement pile penetration in chalk

As discussed in Chapter 2, a critical state model for chalk was first outlined by Burland (1990b) based on the work of Leddra (1989) and Leddra and Jones (1990). Lord et al. (1994) extended the application of critical state concepts to pile penetration and shaft friction mobilisation, in terms of the in-situ void ratio (*e*), the local radial effective stress (σ'_r) and shaft friction (τ_{sf}), and broadly follows the stress history proposed by White (2005) and White and Deeks (2007), discussed in Section 3.2.1.1. This interpretation is depicted in Figure 3.11, where a chalk element in the path of the rim of a PS pile is initially at the natural in-situ effective stress state denoted by position 0. As the distance between the chalk element and the advancing pile reduces, effective stresses increase, and the state moves from 0 to 1. Once the element yields at 1, the material becomes 'mobile' due to de-bonding. The element is then displaced by the pile as the state transitions to position 2. Large pore pressures develop due to the element being looser than the critical state condition (i.e. 'wet of critical'), and because driving-induced shearing is expected to occur at a rate that is not compatible with free-drainage (Buckley et al. 2018b). Shearing continues once the element flows past the pile rim, but stress reversal and removal from the vertical action of the pile results in total and effective stress reductions, denoted by 3. At position 3, the element has become part of the remoulded annulus. The cemented, rigid, chalk enclosing the annulus and pile cannot re-impose in-situ σ'_r levels onto the annulus, and the process up to this point is thought to occur largely at constant volume (Geduhn et al. 2018b). This leads to very low shaft resistances during driving in low IDD chalks. Stress changes occurring after position 3 constitute part of the behaviour of the annulus associated with shaft friction and are therefore dealt with in the subsequent Section.

Lord et al. (1994) remark that, though the closure of discontinuities due to σ'_{r} increments during driving may contribute to lodge the remoulded chalk displaced by the pile, the fundamental process by which the pile and chalk putty annulus are accommodated is the reduction in volume and porosity associated with the creation of the putty. This volumetric straining in turn originates from the contractive behaviour of low-medium density chalk. It is therefore interesting to note that volumetric straining is not mentioned at any point during the process described above and does not feature in the paths traversed from positions 0 to 3 related to pile penetration.

3.3.2 Shaft friction

As for piles in silica sands, the shaft capacity of displacement piles in Chalk may be assumed to result from shearing of the pile-chalk putty interface under the action of an initial static radial effective stress σ'_{rs} which is complemented by the dilative or contractive component $\Delta\sigma'_{\mathrm{rd}}$, as defined by eq. (4) (Lord et al. 2002; Buckley et al. 2018a). While the ultimate angle of interface friction (δ'_{ult} in eq. (1) and (4)) has been found to range between 29 and 33° as mentioned in Section 1.1, the estimation of both σ'_{rs} and $\Delta\sigma'_{\mathrm{rd}}$ is not straightforward.

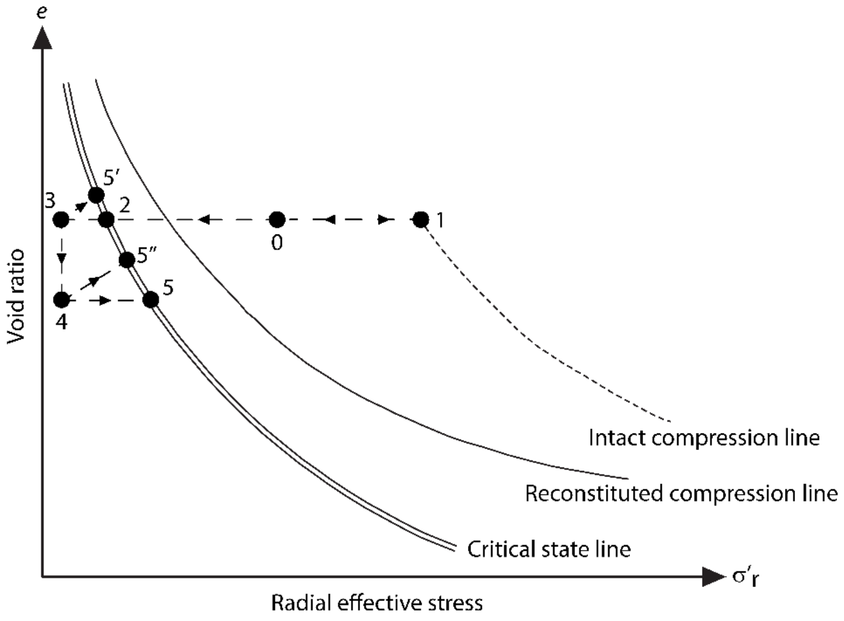

Figure 3.11. Assumed stress history of a chalk element in the remoulded annulus (based on Lord et al., 1994).

Based on the available case histories at the time, Lord et al. (2002) showed that σ'_{rs} could not be correlated to the effective overburden pressure, as proposed by API guidelines for sands, nor to the SPT blow count as suggested by Hobbs and Healy (1979). Therefore, they proposed to limit average ultimate unit shaft friction ($\bar{\tau}_{sf}$) design values for PS piles to 20 and 120 kPa for sites in which low-medium density and grade A high-very high density chalk was present, as discussed in Chapter 1. These design recommendations were within the failure envelopes deducted from the very limited collection of pile test data available to the authors. They further remarked that these values were predisposed to increase with time due to the pile set-up effect, and trial testing of a service pile was encouraged.

3.3.2.1 Short-term behaviour

The $\bar{\tau}_{sf}$ = 20 kPa and $\bar{\tau}_{sf}$ = 120 kPa guidelines proposed by Lord et al. (2002) imply an average radial effective stress at failure ($\bar{\sigma}'_r$) of approximately 35 kPa and 200 kPa in each case, using $\bar{\tau}_{sf}$ and $\bar{\sigma}'_r$ in place of τ_{sf} and σ'_r in eq. (1), and assuming $\delta'_{ult} \approx 30°$. The underlying mechanism for these differences in $\bar{\sigma}'_r$ levels were thought to be that the remoulded annulus sheathing a pile in dense chalk has a lower void ratio than the one around a pile in low density chalk, and that during shear the former displays dilatant behaviour while the latter exhibits contractive behaviour (Hobbs and Atkinson 1993; Lord et al. 1994). The rigid and largely structured chalk beyond the remoulded interface restricts straining of the annulus in the radial direction (perpendicular to the pile surface), and may enforce conditions resembling constant annulus thickness and constant volume; shearing therefore would entail constrained dilation and contraction which produces increases and decreases in $\bar{\sigma}'_r$, respectively, interpreted as $\overline{\Delta\sigma}'_{rd}$ (Lord et al. 1994; Carrington et al. 2011; Dührkop et al. 2015).

As exposed previously, Buckley et al. (2018a) and Jardine et al. (2018) remark that σ'_{rs} levels immediately after pile installation are approximately correlated with CPT q_c measurements (Figure 3.8), but much lower σ'_{rs}/q_c ratios than those obtained from tests in silica sands are observed. High q_c values are related to the cemented state of the material, whilst the low σ'_{rs} magnitudes result chiefly from the loss of cementation. In instrumented pile tests in carbonate sands (Lehane et al. 2012; Lim and Lehane 2015a) and chalk (Buckley et al. 2018a) using the large displacement ICP, σ'_{rs} levels were found to be close to zero along most of the pile shaft. Most of the shaft friction (τ_{sf}) mobilised in in subsequent tension tests originated from the dilatant behaviour of the interface material (i.e., it resulted from $\Delta\sigma'_{rd}$). The significance of constrained dilation is expected to be reduced with increasing pile diameter (Section 3.2.2) and with increasing σ'_{rs} levels, and to grow with higher annulus densities.

Buckley et al. (2018a) and Jardine et al. (2018) further observed that though very low σ'_{rs} values ($\sigma'_{rs}/q_c \approx 0.0025$) occur along most of the embedded length, these could be much higher in the vicinity of the pile tip, based on σ'_r values derived from dynamic analyses of driven piles during installation and re-strike data (Figure 3.10). In these tests, depth-based non-linearity in shaft capacity mobilisation was found to be much greater than for piles in sands, and was assumed to be largely associated with pore pressure dissipation and volumetric contraction of the annulus. In addition, these analyses suggested that 60-95% of the mobilised shaft capacity is related to shearing of the annulus at the bottom half of the embedded length in PS piles. In cases involving large embedment to diameter ratios, up to 40% of the shaft capacity was proposed to be mobilised in the bottom 10% of embedded pile.

Crucially, the end of driving (EOD) studies by Ciavaglia et al. (2017a) and Buckley et al. (2018b) strongly suggest that the average shaft friction of PS piles in low-medium density chalk immediately at the end of installation tends to be lower than the 20 kPa guideline. This draws attention to the central role played by the pile set-up effect, discussed below.

3.3.2.2 Long-term behaviour: the pile set-up effect

The critical state interpretation of shaft friction in chalk proposed by Lord et al. (1994) and introduced in Section 3.3.1.3 postulates a mechanism for long-term shaft capacity mobilisation. The completion of installation or pauses during driving may cause drainage in the putty material, and thus, increments in density and in shaft resistance, i.e. the set-up effect. These post-installation changes in density are denoted by the transition from 3 to 4 in Figure 3.11. The precise mechanisms responsible for this are not well understood, and the matter is discussed later in this Section. If post-installation pile loading and shearing of the annulus is assumed to take place in constant volume conditions, then progression from 4 to 5 or 3 to 2 would take place when post-driving annulus densification is present and absent, respectively. Some authors (e.g. Augustesen et al. 2015, Geduhn et al. 2018) believe that the changes in σ'_r during shaft friction mobilisation (i.e., $\Delta\sigma'_r$) are large enough to overcome the small strain mass stiffness of the surrounding formation and produce volume changes in the annulus. In such cases, paths 3 – 5' and 4 – 5'' would apply with and without post-installation hardening, respectively.

The definition of short- and long-term shaft friction behaviour is not straightforward. While the data reported in Table 3.2 mostly refers to pile testing after set-up periods of at least 10 days, Jardine et al. (2018) describe capacity increases of over 100% of the EOD value in less than 2 h after installation. However, they note that the rate of increment in shaft capacity evolves hyperbolically and eventually reaches equilibrium after about 80 days, with increases in capacity of over 400% in PS tubular piles. Figure 3.12 shows the application of the hyperbolic approach as presented by Buckley et al. (2018b) and includes data from other authors. It appears that different set-up behaviours might apply depending on unknown factors. In this regard, there are various conjectures regarding the mechanisms responsible for the pile set-up effect in chalk:

- Lord et al. (1994) state that lateral stresses cannot be re-imposed by the structured chalk mass adjacent to the annulus. Considering this implies an absence of radial consolidation, it may be assumed that increases in stiffness and/or density (and, therefore, strength) results from creep or secondary compression processes.
- Buckley et al. (2018b) propose that lateral stresses cannot be *immediately* re-imposed on the annulus because they become locked-in by an arching mechanism as orthoradial stresses through the structured chalk surrounding the annulus (as proposed for piles in sands by e.g. Jardine et al., 2006). Eventually, creep relaxation transfers the load onto the annulus, increasing radial stress levels, and producing densification.
- Buckley et al. (2018b) and Jardine et al. (2018) mention that oxidisation of the pile surface (as observed in tests on calcareous sands by Lehane et al. 2012) and/or re-cementation of the chalk putty annulus may contribute to the set-up effect.

Interestingly, tests performed by Buckley et al. (2018a) using the PL ICP did not result in increases in shaft capacity whatsoever. Furthermore, the authors monitored the changes in σ'_{rs} during ageing periods of up to 80 days and found that σ'_{rs} levels did not increase but reduced by almost 30% during this timeframe. Jardine et al. (2018) concede that set-up cannot be completely described by the above phenomena, and that it might be sensitive to pile end conditions and the installation method used, in a manner that is not yet comprehended. Furthermore, Ciavaglia et al. (2017a) and Buckley et al. (2018b) loaded test piles laterally and axially during the ageing period to assess the effect on set-up trends. They found that pre-tested or laterally-loaded piles mobilised smaller shaft capacities that virgin-aged piles. Moreover, Jardine et al. (2018) note that re-driving removes all set-up related gains in axial capacity in compression. On this matter, as discussed in Chapter 2, Razoaki (2000), Bialowas et al. (2018) and Bialowas and Diambra (2018) found evidence that reconstituted chalk does not experience any substantial increases in strength during ageing when compared to short-term capacities at comparable volumetric states. However, they noted that increments in stiffness may be encountered and are potentially related to structural changes in the material. These in turn may originate from re-cementation and creep. Such structural improvements are expected to be lost if substantial strains are applied to the material, such as those associated with re-driving and lateral loading.

Notwithstanding these uncertainties, Jardine et al. (2018) presented the aforementioned Chalk ICP-18 pile design method based on the CPT, which proposes means to predict long-term σ'_r, in the form:

$$\tau_{sf} = (Bq_t F_F{}^c + \Delta\sigma'_{rd}) \tan\delta'_{ult} \tag{9}$$

where B = 0.081, F_F = (h/R*) and c = -0.52. As with the short-term Chalk ICP-18 expression (eq. (8)), all effects related to pile end condition are invoked in the friction fatigue term $F_F{}^c$.

Jardine et al. (2018) further reported on the application of the Chalk ICP-18 method to four independent field-scale test datasets obtained by applying PDA-IMPACT signal matching and by tension and compression testing. Promisingly, Chalk ICP-18 predictions were reported to be close to the measured behaviour. This suggest that the method could perform much more efficiently than the current CIRIA guidelines. However, the need to increase the current pile test database to further assess the technique before implementing it in industry on a regular basis was stressed by Jardine and co-workers.

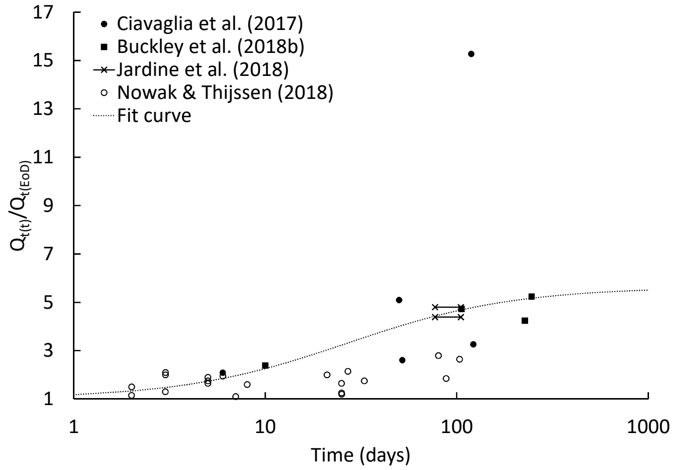

Figure 3.12. Relative increment in shaft capacity due to pile set-up. $Q_{t(t)}$ = shaft capacity at time of testing; $Q_{t(EoD)}$ = shaft capacity at end of driving. Based on Buckley et al. (2018b)[3].

---

[3] Best-fit curve numerically similar to the one proposed by Buckley et al. (2018b), but determined using: $Q_t/Q_{t(EoD)} = n\left\{m + (1-m)\left[\frac{t/T_{50}}{1+(t/T_{50})}\right]\right\}$ where n is the projected equilibrium set-up factor $Q_t/Q_{t(EoD)}$ = 5.625, m = 0.18; t = time; T_{50} = 27 days (time to reach 50% of the equilibrium shaft capacity, Q_{ult}).

Chapter 4 Laboratory investigation of shaft friction in displacement piles in Chalk

4.1 Introduction

The first specific objective of this Thesis pertains the assessment of the applicability of a Critical State Soil Mechanics framework to describe the mechanical behaviour of destructured chalk (Chapter 1). Previous investigations described in Section 2.5, though limited, suggest that the mechanical performance of intact and reconstituted chalk could be explained using critical state concepts. With reference to these preceding works, Section 4.3 of this Chapter presents a series of high-pressure oedometer and consolidated undrained triaxial experiments designed to:

- examine the possibility of a unique normal compression envelope,
- determine if the compression mechanisms of destructured chalk can be described using a similar behavioural framework as that of sands,
- assess the appropriateness of critical state concepts to describe the undrained shearing behaviour of destructured chalk, and
- investigate if a prospective critical state framework is limited by material variability.

As discussed in Section 3.3, the chalk putty annulus sheathing PS piles is expected to exhibit dilative or contractive behaviours during pile axial loading if the annulus is ‘dense’ or ‘loose’, respectively. The high lateral stiffness of the structured chalk may be assumed to restrict actual volumetric dilation or contraction. Substantial changes in radial effective stress are anticipated to occur instead, in conditions that may be representative of ‘constant annulus thickness’ and constant volume simple shear deformation. Changes in effective stress during constant volume shearing of the chalk putty annulus may be associated with the distance in effective stress – void ratio space between pre-shearing conditions and the CSL, as represented in Figure 3.11. This hypothesis corresponds to Objective 2 of the present Thesis and is scrutinised in Section 4.4 of this Chapter using monotonic and cyclic direct simple shear tests.

The review of the literature pertaining PS piles in Chalk set out in Section 3.3 evidences that most of the current state of knowledge regarding pile penetration is based on a limited number of field-scale pile tests. This has provided insight into pile behaviour, resulting in the formulation of a preliminary CPT-based design method for axially-loaded PS piles installed in chalk. However, the mechanisms occurring during pile penetration remain largely unknown, to the point that explanations for key processes such as the formation and characteristics of the remoulded annulus or the pile set-up effect are currently largely speculative. To understand the processes that disturb the chalk during pile penetration in such manner that leads to changes in density (void ratio), Section 4.5 presents an experimental approach using thermoplastic model piles of different geometries jacked in stages into low-medium density chalk specimens. Micro-focus X-ray computed tomography (XCT) has been performed before and after each installation stage, and the data used to retrieve interface void ratios. Interest in the void ratio of the material in contact with the pile shaft stems from the aforementioned hypothesis that, based on critical state concepts, this parameter is a key factor controlling ultimate shaft friction. Thus, after the final XCT scan, the piles have been tested in tension and average shaft friction values have been assessed considering the XCT-derived annulus void ratios.

4.2 Sample description

Given the variability in chalk characteristics (e.g. intact dry density, porosity, etc.), a careful selection of the sampling sites and materials had to be made, based on the objectives of the present Thesis. The main issue regarding the shaft capacity of displacement piles in chalk are the low average shaft friction values measured in piles installed in low and medium density materials, and it is believed that these low shaft friction magnitudes might be related to the characteristics of the puttified chalk in the annulus, as discussed in Chapter 3. Hence, it was decided that the putties to be tested should be produced by crushing intact chalk within the low-medium density range. They are also fairly easier to crush in the laboratory than denser chalks (Alvarez-Borges 2014). Therefore, intact samples were obtained from two sites in southern England, as further detailed in this Section.

4.2.1 Romsey samples

Somborne Chalk Quarry is located on the A3057 road, roughly half-way between Romsey and King’s Somborne, in Hampshire (51°2’41.13’’N, 1°31’11.30’’W). The quarry has been excavated into a geological fold; its cut wall was about 25 m in height at the time of sampling (February 2014) and exposed the White Chalk group. According to the British Geological Survey New Map Series (England and Wales Sheet 299 – Winchester), the Chalk formations present at the site are the Culver Chalk and the Newhaven Chalk.

The Culver Chalk Formation is characterised by being white, soft and lacking important marl seams (Mortimore et al. 1990; Aldiss et al. 2012). However, bands of flint of significant size are usually present. A well-developed marl band (Castle Hill Marl) serves as the lower boundary with the Newhaven Chalk Formation. The Newhaven Chalk is constituted by soft to medium hard chalk and contains significant marl seams (Mortimore 1986; Bristow et al. 1997; Aldiss et al. 2012). Bands of flint are often smaller in size than those found in the overlying Culver and underlying Seaford Formations.

Intact blocks were collected from the foot of the cut wall. The material exhibited an average intact dry density of 1.47 Mg/m^3 (see Table 4.1) and an average saturated moisture content of 30.8%. The samples were thus classified as low density according to CIRIA grades. The chalk lumps were white and soft and could be easily crushed to a putty with a geologist's hammer. Therefore, this material was appropriate for the study of shaft friction in low density chalk.

As the quarry is located at the surface geology boundary between the Culver and Newhaven formations, it was believed that the former, stratigraphically above the latter, would be of relatively small thickness. Considering that samples were collected at the foot of the excavated face, it has been assumed that the material corresponded to the Newhaven Chalk Formation. This is supported by the observation of horizontal patches of vegetation approximately at mid-height on the cut wall, possibly indicating the presence of marl seams, which are not present in the Culver Chalk (Mortimore, 1986; Figure 4.1).

The abbreviation SOM refers to chalk collected at Somborne quarry.

Figure 4.1. Somborne Chalk Quarry. Note possible location of marl seam.

4.2.2 St Nicholas-at-Wade samples

The St Nicholas Court Farm quarry is accessed via the Thanet Way (A299) and is located a few hundred meters from St Nicholas-at-Wade in east Kent (51°21'21.93"N, 1°14'10.98"E). The site has been excavated as an open pit. The Margate Chalk Member, a local lateral equivalent of the Newhaven Chalk Formation, overlies the Seaford Formation in the area (Bristow et al. 1997; Aldiss et al. 2004).

The Margate Chalk is characterised as a smooth white chalk, largely without marl seams or flint bands, but with some indurated iron-stained sponge beds (Mortimore et al. 1990; Bristow et al. 1997; Aldiss et al. 2004; Hopson 2005). Seaford Chalk is described as a soft white chalk containing numerous flint bands, which can be very large and are a contrasting feature with respect to the overlying Margate Member and underlying Lewes Formation (Bristow et al. 1997; Aldiss et al. 2004). Seaford Chalk also exhibits a grid of thin ‘grey-chalky’ veins a few millimetres in thickness, evidence of previous tectonic stress, as well as iron stains (Mortimore 1986).

The Margate Member is only present on the northeaster part of Kent (Aldiss et al. 2004; Hopson 2005). Aldiss et al. (2004) report that erosion has probably removed most of the Margate Chalk below the Paleogene strata on the western boundary of a Chalk inlier north of Chislet. This geological inlet is a mere 2 km west of the St Nicholas Court Farm quarry. It is therefore not surprising that the thickness of the Margate Chalk Member below ground level in the area surrounding the quarry has been reported to be of about 7 m in core samples (Ciavaglia et al. 2017b). As the quarry was excavated to approximately this depth at the time of the sample collection visit (May 2016), it is likely that the quarry floor material was representative of the Seaford Chalk, while the piles of machinery-worked boulders and lumps on site were probably produced from the overlying Margate Chalk. Indeed, very large flints were found at the bottom of the pit (Figure 4.2b), and intact chalk samples taken from the quarry floor exhibited the previously mentioned greyish chalk veins (Figure 4.2a).

The quarry-floor Seaford Chalk samples used in this investigation exhibited an average intact dry density of 1.57 Mg/m^3 (Table 4.1) and an average saturated moisture content of 25.5%. The material was thus classified as medium density using the CIRIA system. The difference in density and stratigraphy with respect to SOM samples was expected to allow for the assessment of potential diagenesis-based behavioural trends.

The abbreviation SNW refers to chalk material collected at the St Nicholas Court Farm quarry.

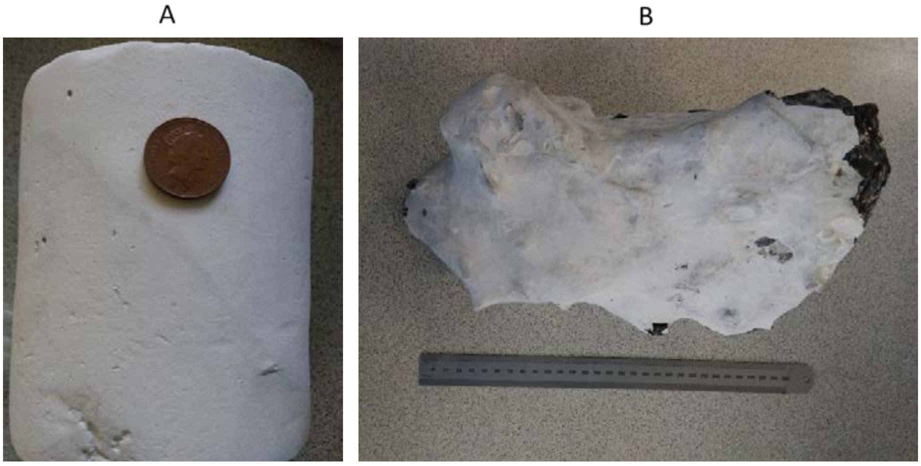

Figure 4.2. A – Grey chalky vein in SNW intact chalk specimen cut from a large boulder excavated from the quarry floor (1p coin used as size reference). B – Large flint collected from the quarry floor (300 mm ruler used as size reference).

4.2.3 Chalk putty preparation

Previous research on weakly cemented carbonate sands suggests that natural variability of the intact material and the potential alteration of the PSD during destructuration and reconstitution may hinder the production of suitable reference reconstituted specimens (Cuccovillo and Coop 1993; Vaughan 1997). To address reconstitution-based effects on PSD, two destructuring methods were employed.

Reconstitution method A comprised the use of a manual food (cheese) grater to destructure oven-dried chalk blocks no larger than 100 mm. Fossils and other hard particles were manually removed with a palette knife. The resulting powder was dry sieved through the 425 μm sieve. The passing material was reconstituted into putty by adding deionised water to the desired moisture content.

In reconstitution method B, immersion-saturated chalk lumps of approximately 100 mm in diameter were reduced in size by means of striking them with a geologist’s hammer until the resulting gravel did not exceed 25 mm in diameter. This stage of the crushing process entailed a relatively small amount of putty production, which was remixed with the chalk gravel. The gravel-putty mix was further crushed using a manual food processor (meat mincer) in a broadly similar procedure to the one used by Fearon and Coop (2000) on structured clays. Small amounts of deionised water were added during the process to promote the formation of a slurry. The slurry was then wet-sieved through the 425 µm sieve. The retained material was dried at room temperature and dry-sieved through the same mesh size. The passing fines were added to the wet-sieved slurry.

The procedures described in BS 1377-2:1990 and BS ISO 13320:2009 were employed to determine Atterberg limits and PSD data, respectively. A Malvern Mastersizer 3000 was used to measure the latter. PSD curves are shown in Figure 4.3, where it may be appreciated that the use of different destructuration methods did not result in significant grain size variability in the fraction passing the 425 µm sieve. Atterberg limits and average PSD data are presented in Table 4.1. Sample nomenclature denotes material origin (i.e. SNW or SOM) and preparation method (i.e. A or B).

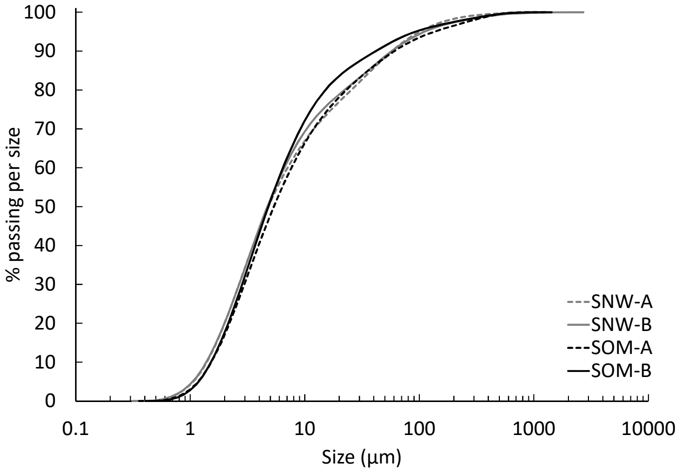

Figure 4.3. Particle size distribution of un-tested destructured chalks.

Table 4.1 Chalk putty index parameters (intact data shown in italics).

	SNW-A	**SNW-B**	**SOM-A**	**SOM-B**
Formation	*Seaford*	*Seaford*	*Newhaven*	*Newhaven*
Mean IDD (Mg/m^3)	*1.57 ±0.08*	*1.57 ±0.08*	*1.47 ±0.02*	*1.47 ±0.02*
Crushing method	A	B	A	B
LL (%)	29	28	30	31
PL (%)	22	22	23	22
d_{50} (µm)	4.9	4.9	5.7	4.8
d_{10} (µm)	1.4	1.4	1.5	1.5
d_{60}/d_{10}	5.1	4.7	5.0	4.2

4.3 Investigation of the mechanical behaviour of intact and reconstituted chalk

4.3.1 One-dimensional compression tests

Compression tests were performed using the oedometer consolidation apparatus. This device applies a vertical stress (σ'_V) on a radially confined cylindrical soil specimen. Thus, zero horizontal strain conditions are imposed and 1D compression takes place. Specimen height changes associated with σ'_V increments result in volumetric strains that are assumed to occur solely by void ratio decrements.

4.3.1.1 Apparatus set-up

The device used in this investigation was the 'Casagrande' type press described in BS 1377-5:1990 and diagrammatically shown in Figure 4.4, fitted with either the standard fixed-ring consolidation cell or a custom floating-ring cell. A 38 mm internal diameter oedometer ring was used with the fixed-ring arrangement, which allowed for maximum σ'_V values of 14.2 MPa. The floating-ring cell was equipped with a 20 mm internal diameter ring, allowing for maximum pressures of 52.5 MPa.

In both the fixed-ring and floating-ring devices the internal walls of the rings were lubricated with silicone grease to reduce friction between the ring and the specimen during testing (Leonards and Girault 1961). The purpose of using a floating-ring device was to further minimise wall friction (Lambe 1951).

The floating-ring oedometer cell consisted of a slightly taller (and reduced diameter) oedometer ring fitted into a custom ring restraint clamp, as shown in Figure 4.5 (parts G and D, respectively). This part was used to carry the weight of the ring during specimen preparation and during the initial stages of the test up to σ'_V levels of approximately 8.5 MPa. At this point the 'release screws' (E) shown in this Figure lowered the lateral ring restraint and the oedometer ring was thereafter supported solely by the internal wall friction between the ring and the specimen, thus limiting wall friction to the submerged weight of the ring. Though the clearance between the ring and the restraint fixture was just 0.05 mm, the 4 mm wall thickness of the former was expected to be able to bear with high lateral stresses with minimal radial deformation, therefore avoiding compression coupling between the two parts. That said, the interface between the ring restraint fixture and the external wall of the ring was lubricated with silicone grease to reduce any potential friction between the items and prevent the fixture from dragging down the ring during the release manoeuvre. For initially intact specimens, the ring restraint release had to be performed after substantial post-yield volumetric strains had taken place, as horizontal stresses and friction were feared to be too low to support the weight of the ring while the specimen remained structured.

Apparatus deformation was measured by carrying out tests on 38 and 20 mm steel dummies. These measurements were used to correct raw test data (see Appendix A).

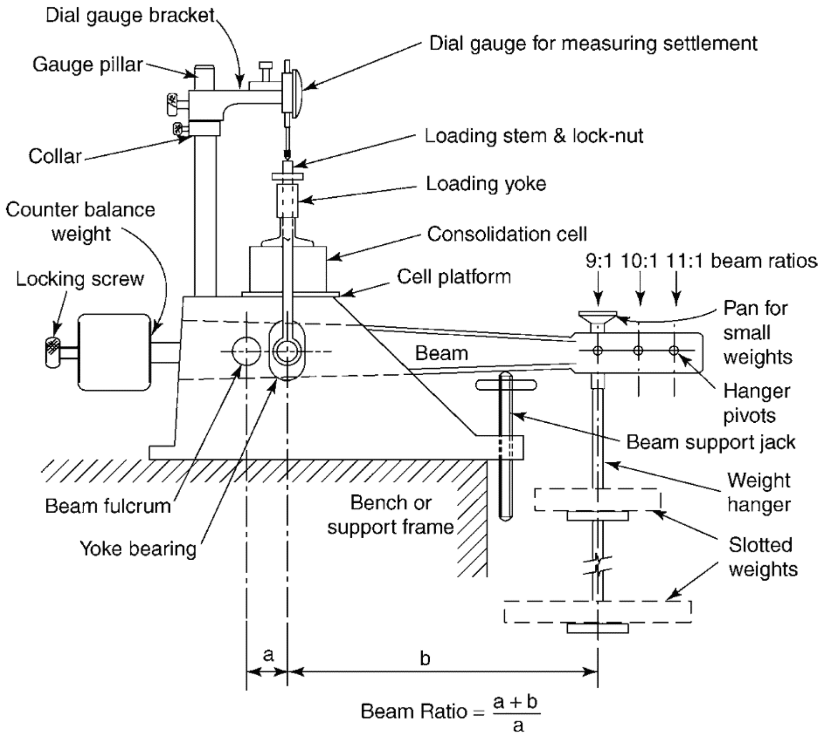

Figure 4.4. Casagrande-type consolidation apparatus (Head and Epps 2011).

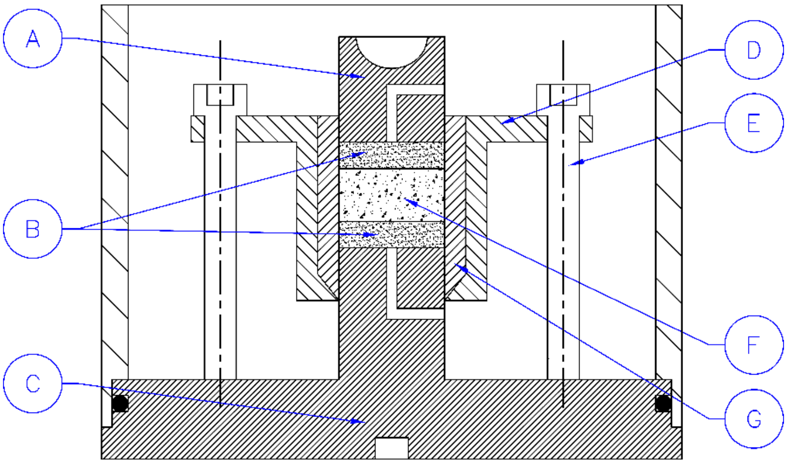

Figure 4.5. Schematic cross-section of the floating ring consolidation cell set-up: (a) loading cap; (b) porous discs; (c) base plate; (d) ring restraint clamp; (e) ring restraint clamp release screws; (f) soil specimen; (g) oedometer ring.

4.3.1.2 Specimen preparation and testing conditions

Reconstituted specimens were prepared by mixing chalk putty at moisture contents between 1 and 1.5 times the LL, as advised by Burland (1990a) for the reconstitution of natural clays, thus obtaining a slurry-like material. De-aired water was used during mixing, and the material was then transferred to a vacuum chamber for 2h. The slurry was thereafter gently remoulded and poured into the assembled oedometer consolidation cell. A small seating load of ≈5 kPa was applied directly on the device top-cap for a period of 24h. The ensuing height change was measured using a calliper before removing the seating load and docking the specimen by applying 4 kPa via the oedometer loading stem (Figure 4.4). Height after docking approximated 15 mm and 10 mm in 38 and 20 mm-diameter specimens, respectively.

Intact specimens were prepared from immersion-saturated block samples using a soil lathe and sand paper, avoiding material with visible heterogeneities. Fine-trimming was carried out using the cutting shoe of the oedometer ring whilst fitting the specimen into it, to minimise gaps between specimen and ring wall. Docking was carried out using the same procedure as in the reconstituted specimens, and the docked height amounted to ≈15 and ≈10 mm in 38 and 20 mm diameter specimens, respectively.

Table 4.2. One-dimensional compression test list and specimen details.

Test No.	**Material**	**Initial void ratio**	**Maximum σ'_V (MPa)**
1	SNW-B	0.736	14.2
2	SNW-A	0.717	14.2
3	SNW-B	0.789	14.2
4	SOM-B	0.776	14.2
5	SOM-A	0.827	14.2
6	SOM-B	0.786	14.2
7	SOM-B	0.734	52.5
8	SNW-Intact	0.763	14.2
9	SNW-Intact	0.799	52.5
10	SOM-Intact	0.910	14.2

Specimen weight, volume and moisture content were used to calculate average void ratios from pre- and post-test measurements as proposed by Madhusudhan and Baudet (2014), using a specific gravity for calcite of 2.70, after Clayton (1983). Post-test PSD analyses were conducted on both initially intact and reconstituted specimens. A summary of specimen and test details is presented in Table 4.2.

Stress increments, loading periods and settlement measurements were carried out as specified in BS-1377-5:1990. That is, each load increment approximately doubled previous stress conditions, stresses were commonly maintained during 24 h, and data logging was carried out either manually in square-root of time intervals, or in an automated fashion every two seconds (using a linear variable differential transformer [LVDT] and an ELE International data logger).

4.3.2 Consolidated undrained triaxial tests

4.3.2.1 Apparatus set-up

Consolidated undrained triaxial tests were conducted using an electromechanical displacement-controlled triaxial frame and a standard triaxial cell fitted with tubing and connections rated for pressures of up to 1.7 MPa. A diagram and photograph for this device is shown in Figure 4.6. Pore water pressure transducers were connected to the top and bottom specimen drainage lines. Cell and back pressure were applied via automated digital pressure controllers. Specimens were 38 mm in diameter and 76 mm high and were locally instrumented with a single submersible LVDT to measure radial strain. Global axial displacements were measured via an externally mounted LVDT, whereas loads were determined using a submersible load cell. All instruments were calibrated, and appropriate triaxial test corrections were applied (Appendix A).

4.3.2.2 Specimen preparation and testing conditions

Chalk putty was prepared using the intact samples described in Section 4.2 and the procedure defined in Section 4.2.3. Chalk slurry was reconstituted at moisture contents between 1 and 1.5 times the LL and de-aired as explained in Section 4.3.1.2. The slurry was then gently poured into a split-former assembled on the pedestal of the triaxial cell base plate and previously fitted with a set of saturated porous stones, filter paper discs and membrane. The water content range used did not produce a free-flowing slurry that could be poured using a glass tube or a funnel, as used by Bialowas (2017). Instead, the material was placed by using a small spatula and gently stirred with a glass rod to remove air bubbles, as similarly done by Doughty (2016). After sealing the specimen, a small vertical stress (≈4 kPa) and suction pressure (≈7 kPa) were applied via a 0.5 kg weight and burettes, respectively, and maintained for at least 2 h before removing the split-former. This pre-consolidation was carried out to prevent large pre-test distortions, and associated changes in water content were measured using the burettes. Once the triaxial cell was placed and filled, back pressures between 300 and 400 kPa were applied at low effective stress levels (≈7 kPa) to saturate the specimens, attaining B-values of 0.90-0.95 (as dictated in BS 1377-8:1990). Pre- and post-test specimen weight, water content and volume were used to derive in-test void ratio values, again following the recommendations by Madhusudhan and Baudet (2014), assuming a specific gravity of calcite of 2.70 as before.

Specimens were then subjected to consolidation in either 1D (K_0) or isotropic (ISO) conditions to targeted mean effective stress levels to attain a variety of pre-shear liquidity indexes qualitatively representative of 'loose' and 'dense' conditions, as reported in Table 4.3. 1D compression was achieved by maintaining constant specimen cross-section using feedback from radial strain measurements obtained via the strain belt. After consolidation, specimens were sheared in strain-controlled undrained conditions using strain rates of 0.1 or 0.2 %/h.

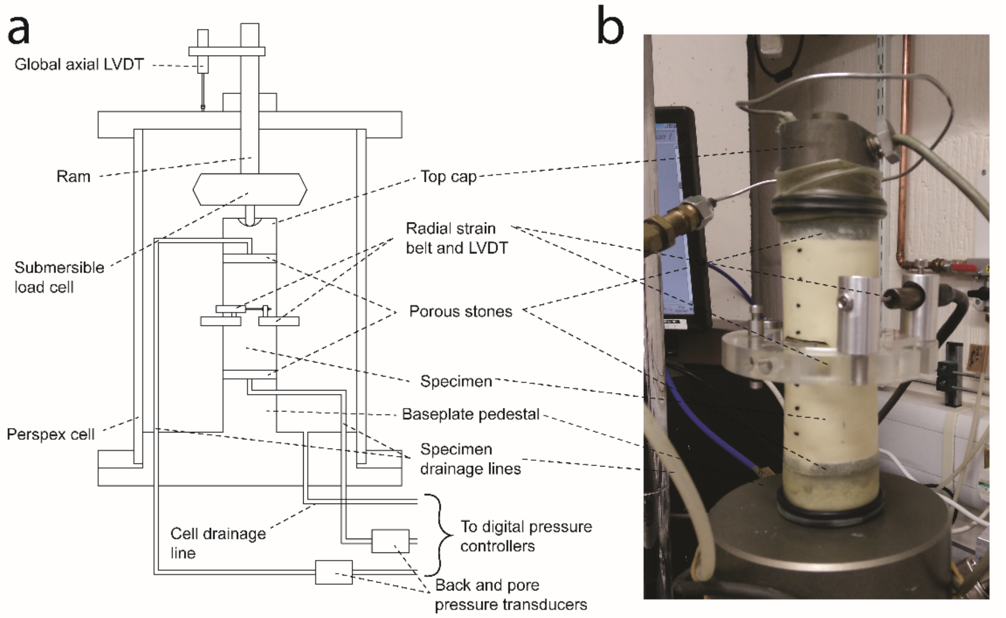

Figure 4.6. Diagram (a) and photograph (b) of the triaxial test device used.

Destructured chalk exhibits high creep rates, as previously commented in Section 2.4.4. To mitigate the influence of creep on shearing performance, the target pre-shear compression stresses were maintained constant during varied time periods until axial creep rates reduced to less than about 0.003 %/h (after Kuwano & Jardine 2002). For some tests, this led to consolidation periods that exceeded the 24 h threshold used to define short-term behaviour (Section 2.5.5), as shown in Table 4.3. To determine the effect of these varied but necessary ageing periods, Test 6 was aged at constant effective stress for a period of 13 days prior to shearing.

Table 4.3. Triaxial test list and specimen details.

Test No.	**Prep. method**	**Pre-shear conditions**			**Ageing (days)**	**Shear rate (%/h)**	**Ultimate state**			
		p' (kPa)	**q (kPa)**	**e**			**CS†**	**p' (kPa)**	**q (kPa)**	**ϕ' (°)**
1	SNW-B	1762	1396	0.571	<1	0.1	No	2894	4318	36.7
2	SNW-B	1879	1648	0.585	<1	0.2	No	2523	3696	36.1
3	SNW-B	52	1	0.743	1.7	0.2	Yes	61	85	34.4
4	SNW-B	268	16	0.674	<1	0.2	Yes	515	726	34.8
5	SNW-B	1301	2	0.630	1.1	0.2	No	1228	1644	33.2
6	SNW-B	1306	3	0.670	13	0.2	Yes	713	983	34.1
7	SNW-A	805	2	0.658	1.8	0.2	Yes	649	821	31.5
8	SOM-B	1904	1815	0.629	3.7	0.2	No	1502	2029	33.5
9	SOM-B	1299	2	0.659	3.6	0.2	Yes	685	914	33.1
10	SOM-A	1295	3	0.594	3.2	0.2	Yes	2057	2877	34.6

†Critical State: Yes = constant p' and q attained before visible strain localisation; No = constant p' and q not attained at end of test. Note that shearing was carried out in constant volume (undrained) conditions.

4.3.3 Results

4.3.3.1 One-dimensional compression test results

Measurement of primary consolidation in uncemented chalk was problematic due to its relatively high permeability and creep rates (Clayton 1978; Clayton and Matthews 1987). Data processing guidelines by Head and Epps (2011) for oedometer tests on silts and soils exhibiting large secondary compression, schematically shown in Figure 4.7, were employed to improve primary consolidation measurement accuracy. These primarily consist in the identification of the starting point of the time-domain log-linear secondary compression trend in the data (Mesri 1973), as indicated in this Figure.

Compression paths in σ'_V-e space for the reconstituted specimens are shown in Figure 4.8. These paths are non-coincident at σ'_V levels below 2 MPa and appear to be dependent on the reconstitution moisture content. However, all compression paths converge beyond σ'_V levels of about 2 MPa and a unique 1D-NCL can be derived. As for many sands and other granular materials that exhibit particle damage during compression, the 1D-NCL appears to be non-linear in ln σ'_V-e space (e.g. Pestana and Whittle 1995, Herle and Gudehus 1999 and others), and may expressed as (after Wang et al. 1990; Li and Wang 1998):

$$e = 0.928 - 0.065(\sigma'_V/\sigma'_{ref})^{0.186} \qquad (10)$$

where σ'_{ref} = 1 kPa for dimensional consistency.

One-dimensional compression paths in σ'_V-e space for the intact specimens are presented in Figure 4.9, which includes data by other authors. Yield occurs inside the structure-permitted space and is followed by volumetric strains associated with the loss of inter-particle bonds, pore collapse and rearrangement of the disaggregated grains until a stable fabric is achieved (Vaughan et al. 1988; Leroueil and Vaughan 1990).

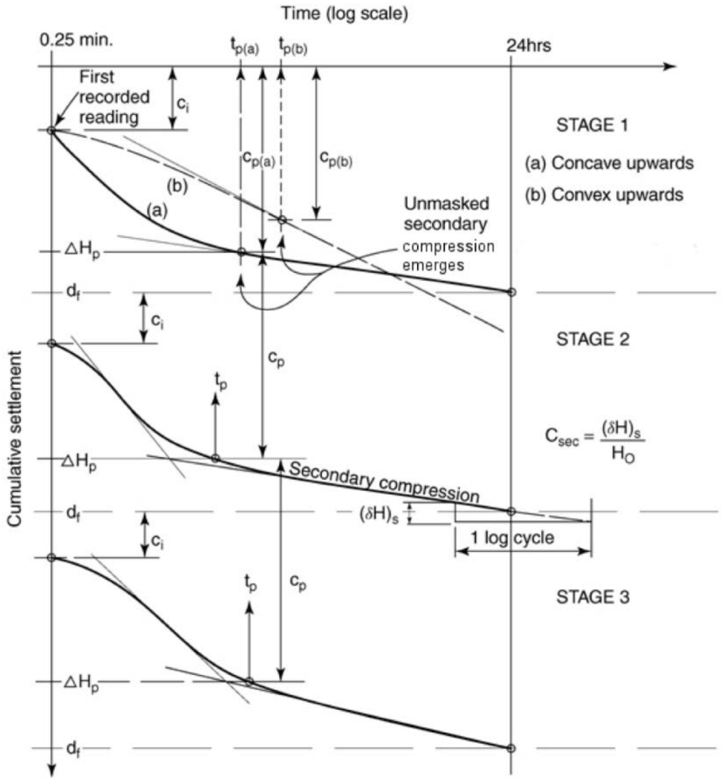

Figure 4.7. Graphic procedure to determine the time (t_p) and height change (H_p) at the end of primary compression during three loading stages (Head and Epps 2011). C refers to cumulative settlement, *i* and *sec* denote 'initial' and 'secondary compression'.

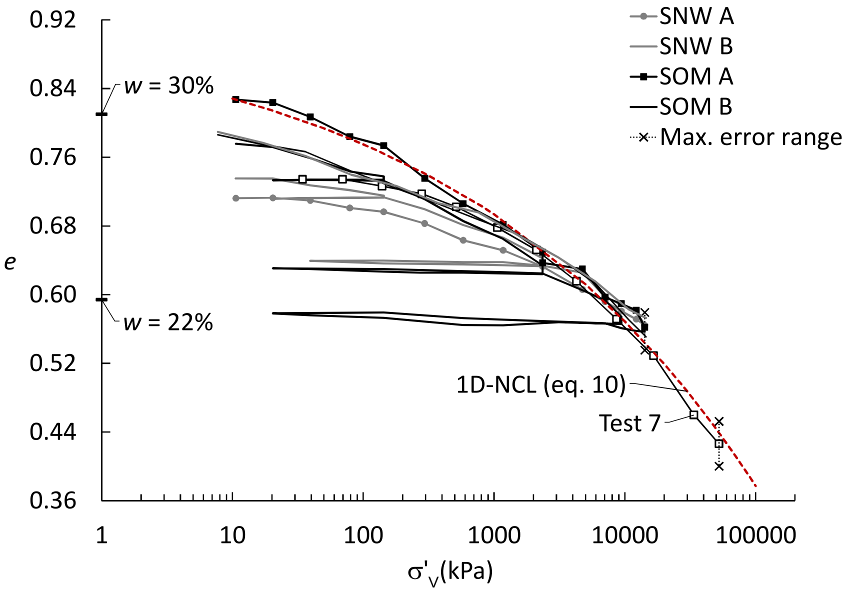

Figure 4.8. One-dimensional compression paths for reconstituted specimens.

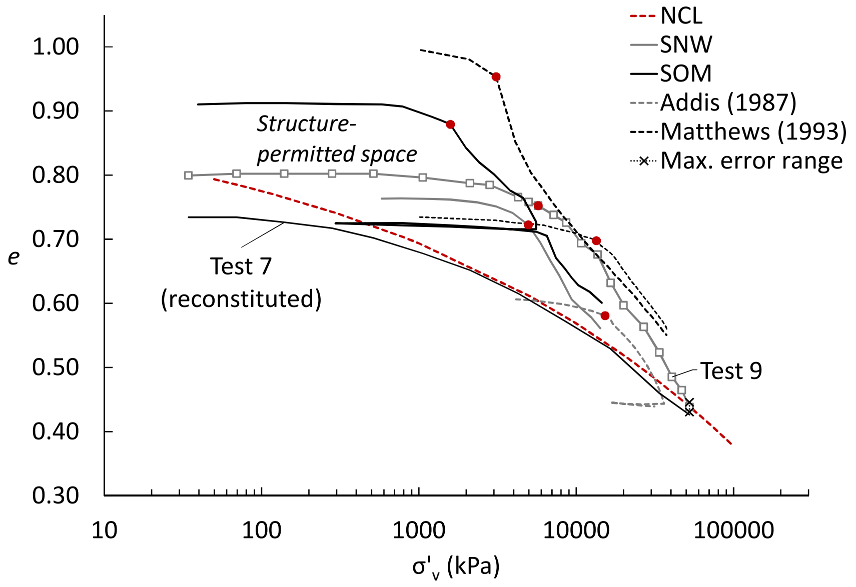

Figure 4.9. One-dimensional compression paths for intact specimens. Red markers denote yield states. The structure-permitted space are all states above the 1D NCL. Includes oedometer data by Addis (1987) and Matthews (1993).

4.3.3.2 Undrained triaxial test results

Figure 4.10 depicts stress paths in q – p’ space (a), stress – strain curves (b) and pore pressure evolution. For clarity, only selected results are presented but comparable patterns were observed in all tests. Most specimens exhibited contractive behaviour and effective stress reductions after yielding until reaching phase transformation, which was then followed by a dilative response. As is often the case during triaxial testing, strain localisation occurred at large strains (Viggiani et al. 1994; Finno et al. 1996). This was observed as multiple conjugate shear banding. The effect of strain localisation may be noted as a final reversal in stress paths from dilative to contractive in Figure 4.10a (Burland 1990a). ‘Ultimate states’ are denoted by markers before this reversal, which are also considered to be the ‘end of test’ conditions for these tests. As discussed in Section 2.5.5.1, the ‘ultimate state’ designation is used instead of ‘critical state’ because, in some cases, strain localisation prevented the attainment of global theoretical critical state conditions. This is indicated in Table 4.3 and using arrows in Figure 4.11. It is acknowledged that strain localisation may have commenced before being detectable from visual assessment or global stress/strain measurements.

Figure 4.11 presents ultimate states and stress paths in p’ – *e* space for all triaxial tests. Despite the limitations of strain localisation, a unique CSL may be proposed from the ultimate states, irrespective of the origin and method by which the destructured chalk was created. This CSL has been included in Figure 4.11 and, as for many sands (e.g. Been et al. 1991; Verdugo and Ishihara 1996) and silts (e.g. Carrera et al. 2011), may be proposed to be non-linear in Ln p' – *e* space. Thus, the CSL may be written as (after Wang et al. 1990; Li and Wang 1998):

$$e = 0.895 - 0.071\left(\mathrm{p}'/\mathrm{p}'_{\mathrm{ref}}\right)^{0.186} \tag{11}$$

where $\mathrm{p}'_{\mathrm{ref}}$ = 1 kPa for dimensional consistency.

Stress paths for all tests are presented in Figure 4.12 in terms of q/p' stress ratios and the state parameter ψ, defined by Been and Jefferies (1985) as the difference between the current void ratio and the void ratio at the critical state at current p', determined by way of the CSL equation (Eq. (11)). Convergence towards the critical state at approximately ψ = 0 is evident in this Figure. The average critical state stress ratio q/p' = M derived from tests that globally seemed to reach theoretical critical state conditions was 1.36, which amounts to a critical state angle of friction (ϕ'_c) of 33.7°.

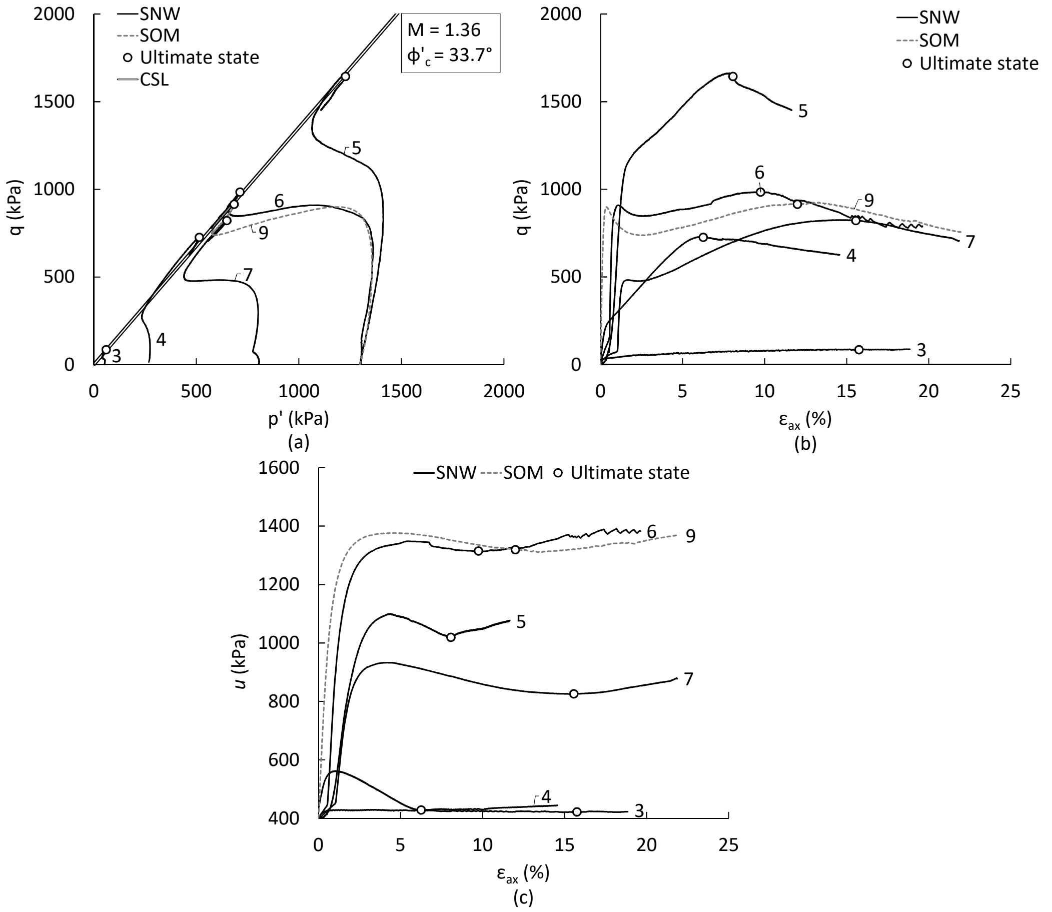

Figure 4.10. Selected triaxial test results: (a) stress paths; (b) stress-strain curves; (c) pore pressure evolution. Labels denote test number (Table 4.3).

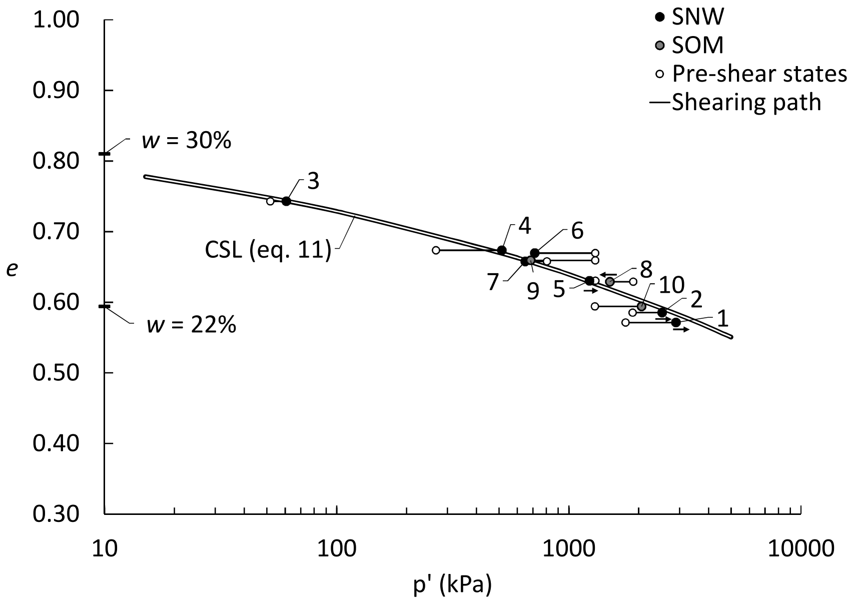

Figure 4.11. Undrained triaxial shearing paths and ultimate states in ln p' – *e* plane. Labels denote test number (Table 4.3).

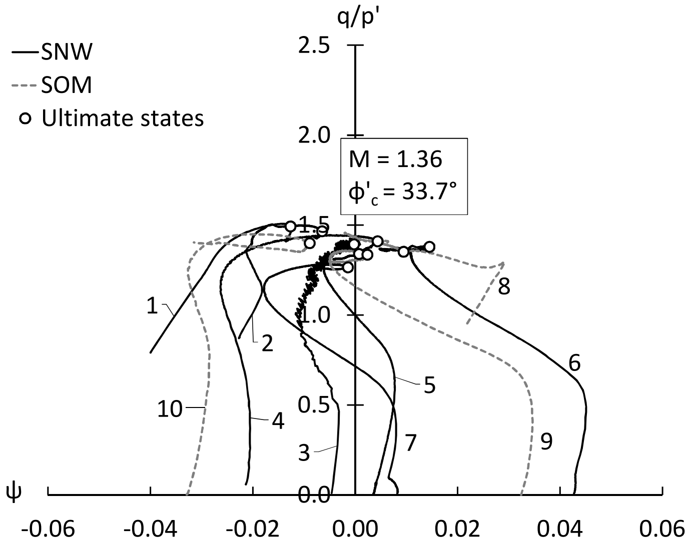

Figure 4.12. Undrained triaxial stress paths in terms of q/p' ratio and state parameter ψ. Labels denote test number (Table 4.3)

4.4 Investigation of the shear strength of steel-remoulded chalk interfaces

4.4.1 The direct simple shear test and apparatus set-up

Shearing of the putty chalk annulus in constant volume conditions may be approximately replicated in constant cross-section and constant height direct simple shear tests (Randolph and Wroth 1981; Dyvik et al. 1987), as depicted in Figure 4.13. Plane strain geometry and stress parameters for constant volume DSS are shown in Figure 4.14. After pile installation and before service loading, the remoulded annulus may be assumed to be in one-dimensional compression conditions with σ'_{rs} acting as major principal stress (Randolph and Wroth 1981), which is represented by σ'_{y0} in Figure 4.14a. Radial effective stress changes and gentle principal stress rotation occurring as the pile is vertically loaded and interface shearing takes place ($\sigma'_{\mathrm{rs}} + \Delta\sigma'_{\mathrm{r}}$ in Figure 4.13 and Eq. (4)) are represented in DSS testing by $\sigma'_{\mathrm{y0}} + \Delta\sigma'_{\mathrm{y}}$, as shown in Figure 4.14b.

Cylindrical chalk putty specimens measuring 100 mm in diameter and approximately 20 mm in height (H) were monotonically and cyclically sheared using a GDS Instruments automated electromechanical dynamic-cyclic simple shear apparatus (EMDCSS; GDS Instruments, 2014). Photographs and a diagram of the device are shown in Figure 4.15 and Figure 4.16, respectively. Specimens were radially confined by a latex membrane and a stack of Teflon-coated stainless steel rings, and vertical confinement was provided by two horizontal stainless steel porous discs, fitted to the base plate and top cap. Vertical loads were applied via the top cap and measured using a 10 kN compression load cell. Horizontal (shear) loads were imposed by the horizontal unidirectional sliding of the base plate mounted on two precision linear raceways equipped with lubricated contact ball bearings to minimise friction. Horizontal loads were measured at the bottom of the specimen by an in-line 10 kN compression-tension load cell fixed to the sliding base and at the top by a 10 kN shear load cell attached to the top loading cap. Both the base platen and top cap featured drainage lines connected to a digital pressure controller which measured the displaced pore water volume and maintained water bath pore pressure conditions (i.e. ≈1 kPa). Horizontal and vertical displacements were measured via LVDTs. The device was computer-operated using GDSLab software.

4.4.2 Specimen reconstitution

Specimens were reconstituted using chalk putty produced by the methods described in Section 4.2.3. Specimen reconstitution involved the preparation of a de-aired chalk slurry which was then gently placed in the assembled confinement rings and membrane, following a procedure similar to the one used in the oedometer tests (Section 4.3.1.2). The putty was gently stirred with a glass rod to remove air bubbles, as in the triaxial tests (Section 4.3.2.2). The bottom platen drainage path was closed before preparation to reduce moisture loss during the reconstitution procedure, and the internal surface of the membrane was lubricated using silicone grease to reduce wall friction during pre-shear consolidation (Section 4.4.3).

After specimen preparation, the bottom pedestal was attached to the sliding base and the top loading cap was slowly lowered onto the specimen until a target docking pressure of 5 kPa was applied. Top cap displacement was measured by an LVDT and computer-controlled using an encoder. The docking load was applied for a minimum of 8 hours and the top cap drainage line was opened during the process to promote the evacuation of water and air from the specimen. As for the oedometer tests (Section 4.3.1.2), specimen weight, volume and moisture content were used to determine the average void ratio during testing, assuming the specific gravity of calcite as 2.70. Specimen details are shown in Table 4.4 and Table 4.5.

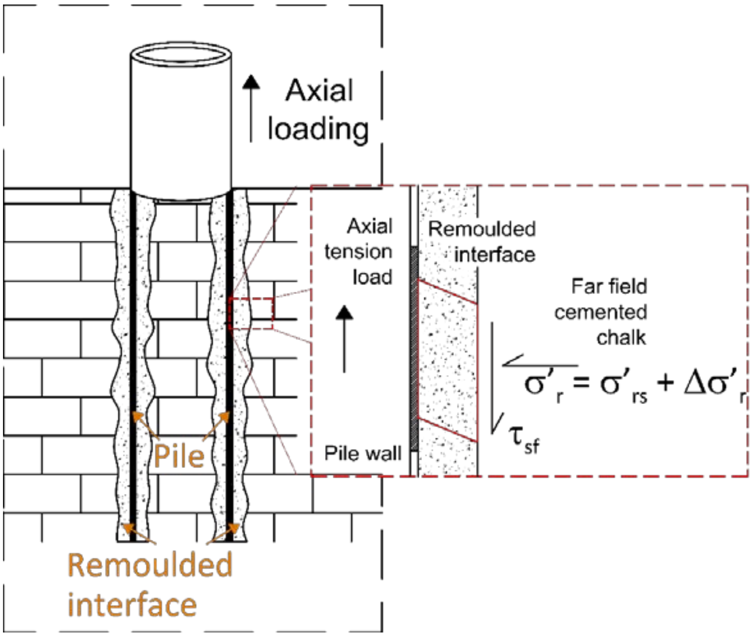

Figure 4.13. Simple shear deformation of the putty chalk annulus during axial pile loading.

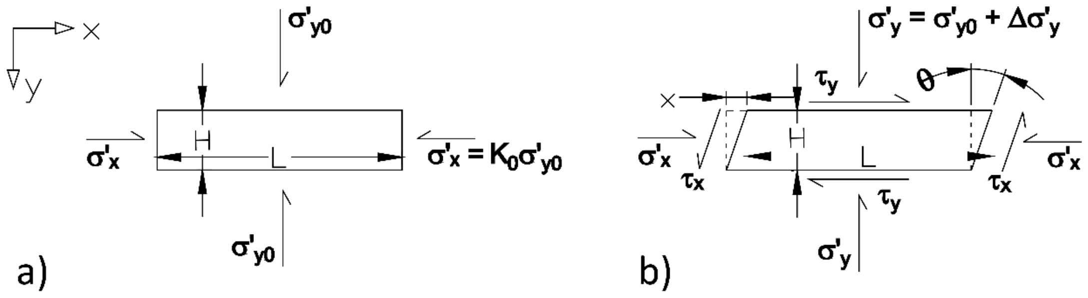

Figure 4.14. Plane strain constant volume simple shear (after Randolph & Wroth, 1981): a) pre-shear stress state; b) stress conditions during shear.

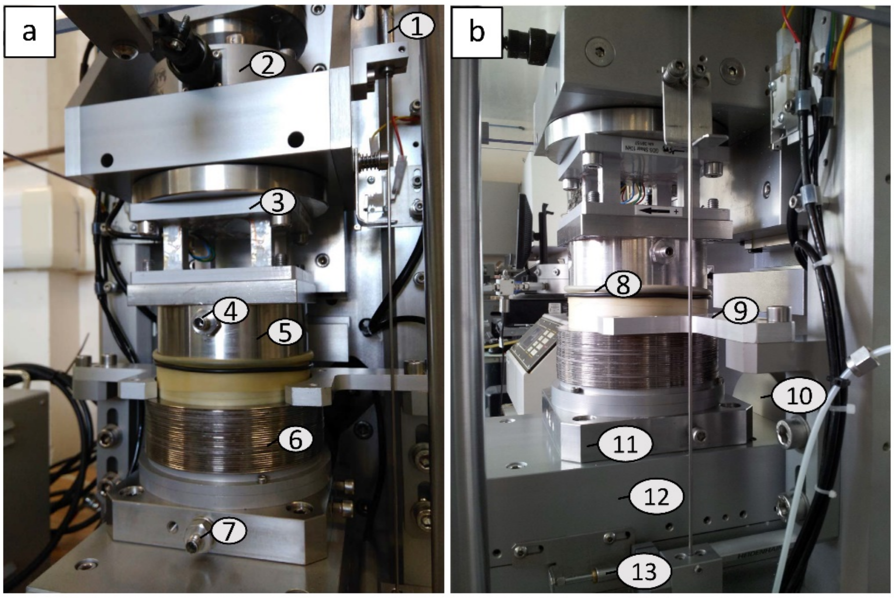

Figure 4.15. Photograph of EDMCSS device: 1. Vertical LVDT; 2. Compression load cell; 3. Shear load cell; 4. Top drainage line; 5. Loading cap; 6. Confinement rings; 7. Bottom drainage line; 8. Membrane and o-rings; 9. Anti-rotation clamps; 10. In-line compression-tension load cell; 11. Base pedestal; 12. Sliding base plate; 13. Horizontal LVDT.

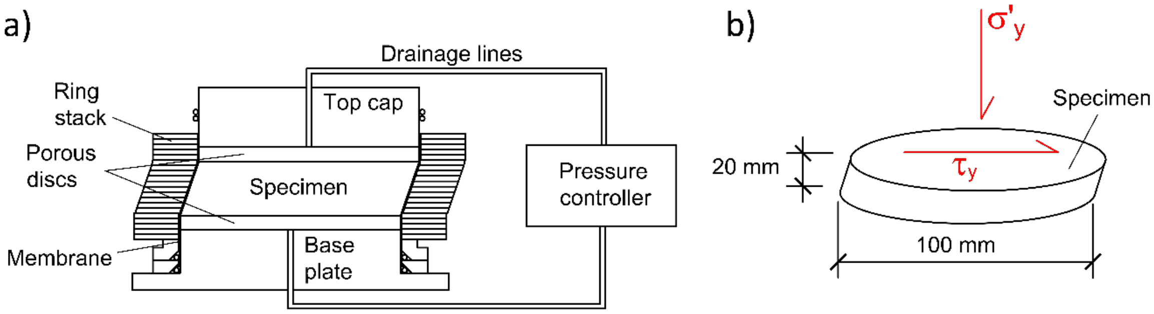

Figure 4.16. Schematic representation of EMDCSS apparatus.

4.4.3 Pre-shear consolidation

All tests consisted of at least one consolidation stage followed by either a monotonic or cyclic shearing stage. Effective vertical compressive stresses (σ'_y; Figure 4.14b and Figure 4.16b) were applied by increasing the top cap load in a series of steps. Drainage was allowed through both the top cap and bottom pedestal.

Consolidation stages were designed to evaluate the role of stress history on interface performance and to cover a range of densities and effective stresses within the plastic range of chalk putty. Specimen details are presented in Table 4.4 and Table 4.5. Monotonic Tests 3 and 5 and cyclic simple shear (CSS) Tests C4, C5, C8 and C9 were unloaded to lower σ'_y levels prior to shearing and were thus tested in overconsolidated conditions. CSS Test C7 was a multi-stage test. First, the specimen was subjected to one vertical load-unload cycle (from 5 to 1200 kPa and then unloaded to 25 kPa) to attain an overconsolidated state and was thereafter tested in CSS. Then, shear strain was reversed in constant volume until returning to the initial zero shear strain condition and vertically unloaded (i.e., σ'_y set to zero). Afterwards, the specimen was subjected to a second vertical load-unload cycle using the same stress range as in the first one, and a second cyclic shear phase followed. All other tests were single-stage and initiated at the maximum applied σ'_y.

4.4.4 Direct simple shear tests

Once the desired pre-shear consolidation state was achieved, simple shear deformation was applied by the horizontal displacement (x in Figure 4.14b) of the sliding base while the top cap remained static. This maintained the height of the specimen constant whilst the confinement rings preserved the specimen cross-section constant, thus enforcing approximate constant volume conditions. However, true undrained shear conditions in which pore pressure developments occur cannot be achieved in the EMDCSS, due to the open drainage lines and the clearance space between the ring stack confinement and the membrane-clad top cap. Still, equivalent pore pressure changes can be inferred from the decreases and increases in vertical stress required to maintain constant height (Dyvik et al. 1987). For test result interpretation purposes, discussed in Appendix C, an additional pair of constant normal load (CNL) tests were performed (Tests 11 and 12 in Table 4.4).

Horizontal (shear, τ_y; Figure 4.14b and Figure 4.16b) stresses were calculated by averaging the two force measurements obtained from the top and in-line load cells (Figure 4.15). Shear strains

(γ) were interpreted as $\gamma = x/H$ (Figure 4.14). A 5%/h strain rate was used for all tests (except CNL Tests 11 and 12,where ≈0.02%/min was used to ensure fully-drained conditions). Specimen and test details are presented in Table 4.4.

Table 4.4. DSS test list and specimen details.

Test No.	**Reconst. method**	**Consolidation max. σ'_y (kPa)**	**Pre-shear conditions**		**Conditions during shear**
			***e* (*w*)**	**σ'_{y0} (kPa)**	
1	SNW-B	400	0.756 (28.0%)	400	Const. Vol.
2	SNW-B	400	0.764 (28.3%)	400	Const. Vol.
3	SNW-B	900	0.656 (24.3%)	55	Const. Vol.
4	SNW-B	400	0.746 (27.6%)	400	Const. Vol.
5	SNW-B	1200	0.692 (25.6%)	62	Const. Vol.
6	SNW-A	600	0.740 (27.4%)	600	Const. Vol.
7	SOM-A	400	0.733 (27.2%)	400	Const. Vol.
8	SOM-B	400	0.757 (28.0%)	400	Const. Vol.
9	SOM-B	400	0.753 (27.9%)	400	Const. Vol.
10	SOM-A	600	0.731 (27.1%)	600	Const. Vol.
11	SNW-B	200	0.715 (26.5%)	200	CNL
12	SNW-B	50	0.767 (27.4%)	50	CNL

4.4.5 Cyclic simple shear tests

CSS tests were carried out in constant height (i.e., ≈constant volume) stress-controlled conditions by applying a cyclic shear stress (τ_{cyc}) around a mean shear stress (τ_{m}), as schematically depicted in Figure 2.16. The shape of the time-domain stress application path was approximately sinusoidal at 0.1 Hz. This testing frequency has been employed in previous chalk-related research (e.g. Carrington et al., 2011, Coyne et al., 2015), and is typical of wind and wave loading of the foundations of offshore structures (Andersen et al. 2013). Various pre-shear consolidation histories were used, as detailed in Table 4.5. Different combinations of τ_{cyc} and τ_{m} were applied such that cyclic loading could be symmetric ($\tau_{\mathrm{m}} = 0$) or exhibit static bias ($\tau_{\mathrm{m}} \neq 0$).

Stress control during CSS testing was performed by the EMDCSS software (GDSLab) based on an 'estimated stiffness' parameter input by the user. The stiffness estimate was used by the software to control the rate of loading. The estimated stiffness parameter was determined using a collection of constant height single-cycle low amplitude strain-controlled soundings at varying pre-shear vertical effective stress (σ'_{y0}) levels and consolidation history, as presented in Appendix B. However, stiffness degradation associated with cyclic instability (Section 2.5.5.2) caused the estimated stiffness value to eventually become higher than the actual response of the specimen. This resulted in large strains being applied during a given cycle, occasionally without being able to reach the target τ_{cyc}. To avoid accumulating a large number of cycles during which the prescribed τ_{cyc} was not attained, failure and the end of test condition was assumed to occur during the load cycle (N_f) when:

- 3.75% single-amplitude strain occurred, or
- when the accumulated strain amounted to 7.5%, or
- σ'_y reached zero and the reduced stiffness hampered the attainment of the target τ_{cyc}.

Similar failure criteria is found in the literature, e.g. Jefferies and Been (2016).

Table 4.5. CSS test list and specimen details.

Test No.	**Reconst. method**	**Consolidation max. σ'_y (kPa)**	**Pre-shear conditions**		**Shearing stage**		
			***e* (*w*)**	**σ'_{y0} (kPa)**	**τ_m (kPa)**	**τ_{cyc} (kPa)**	**$N_{failure}$**
C1	SNW-B	400	0.709 (26.3%)	400	0	25	77
C2	SNW-B	400	0.713 (26.4%)	400	0	20	255
C3	SNW-B	400	0.679 (25.2%)	400	16.5	10	Stable*
C4	SNW-B	1200	0.691 (25.6%)	50	0	5	Stable†
C5	SNW-B	800	0.678 (25.1%)	100	5	30	33
C6	SNW-B	400	0.682 (25.3%)	400	10	15	Stable‡
C7a	SNW-B	1200	0.676 (25.0%)	25	0	20	5
C7b	SNW-B	1200	0.634 (23.5%)	25	0	20	19
C8	SNW-B	1454	0.622 (23.0%)	200	10	30	2382
C9	SNW-B	1200	0.625 (23.1%)	25	0	20	56

* Stopped after 3478 cycles; † Stopped after 2170 cycles; ‡ Stopped after 2562 cycles.

4.4.6 Results

4.4.6.1 Direct simple shear tests

τ_y – γ and σ'_y – γ curves and stress paths in terms of τ_y and σ'_y are presented in Figure 4.17. Again, for simplicity, only selected results are shown in this Figure. Specimen sliding over the base plate porous disc was detected during the later stages of all DSS tests. For overconsolidated Tests 3 and 5, which experienced effective stress increments during shear, sliding occurred at about peak τ_y (Figure 4.17a). This was interpreted as a form of strain localisation prompted by a dilative response of the specimens, analogous to the behaviour of dense triaxial specimens (Section 4.3.2). A reversal in stress path direction was likewise observed (Figure 4.17c). For all other tests, specimen sliding occurred at large strains (approximately between 7 and 15%) after a period of steady state shearing (i.e. at constant τ_y and σ'_y; Figure 4.17a and Figure 4.17b). Thus, ultimate state conditions on the horizontal plane were interpreted as those occurring when shearing progressed without changes in τ_y and σ'_y in normally consolidated tests, or when visible strain localisation took place in overconsolidated Tests 3 and 5 (i.e. prior to the reversal in stress path; Figure 4.17c). The τ_y/σ'_y stress ratios measured at the ultimate states and Eq. (1) were used to derive δ'_{ult}, and the average δ'_{ult} for all tests is included in Figure 4.17c (29.0°). Whilst pinned or ridged porous discs could have been employed to attempt to restrict sliding, it was felt that their use would have resulted in test conditions that were unrepresentative of the pile-chalk interface.

Ultimate state conditions on the horizontal plane for all DSS tests are plotted in ln s' – *e* space in Figure 4.18, using the derivation for the principal stress invariant $s' = (\sigma'_1 + \sigma'_3)/2$ given in Appendix C. As in Figure 4.11 concerning the triaxial test data, arrows are used in Figure 4.18 to indicate that the attainment of constant τ_y and σ'_y conditions during shear was apparently curtailed by strain localisation in the form of specimen sliding in dense specimens (Tests 3 and 5). However, convergence to the same CSL (Eq. (11)) derived via triaxial testing is evident. In terms of s', the CSL is written as:

$$e = 0.895 - 0.068(\mathrm{s}'/s'_{\mathrm{ref}})^{0.186} \qquad (12)$$

where s'_{ref} = 1 kPa for dimensional consistency.

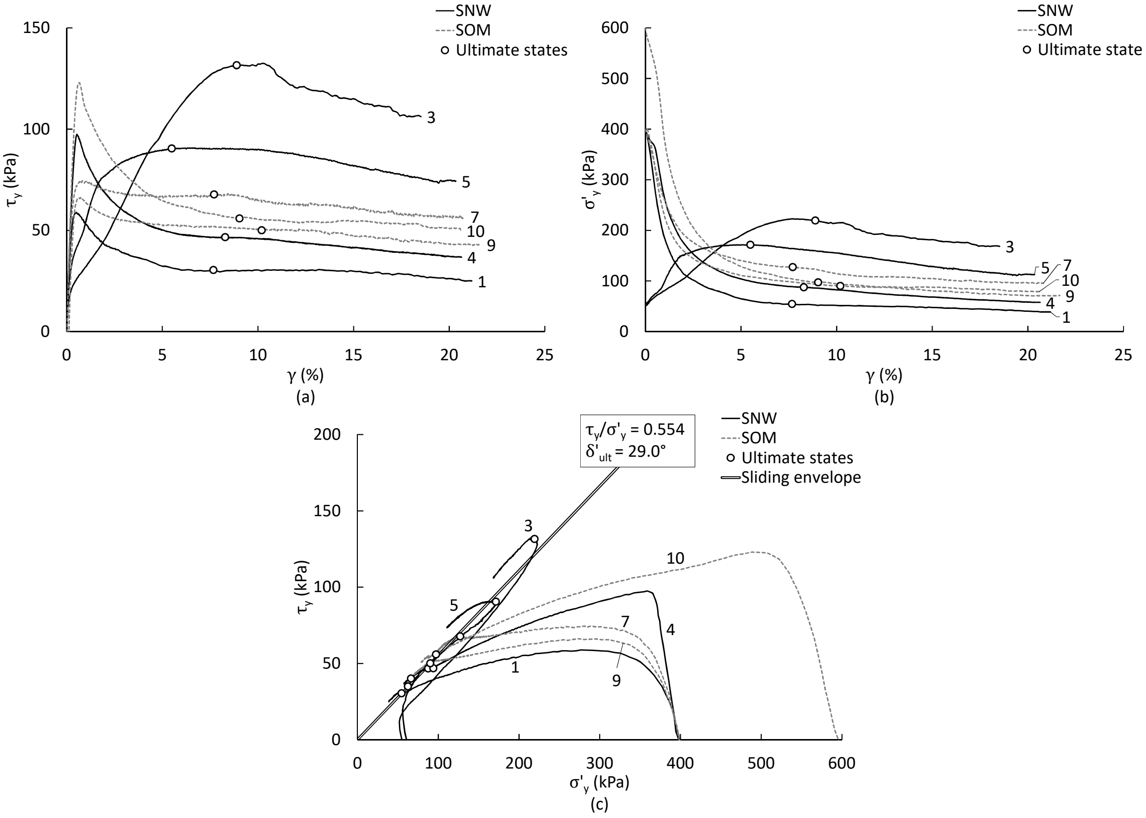

Figure 4.17. Selected DSS test results: (a) $\tau_y - \gamma$ curves; (b) $\sigma'_y - \gamma$ evolution; (c) $\tau_y - \sigma'_y$ stress paths (sliding envelope shown). Data labels denote test number (Table 4.4).

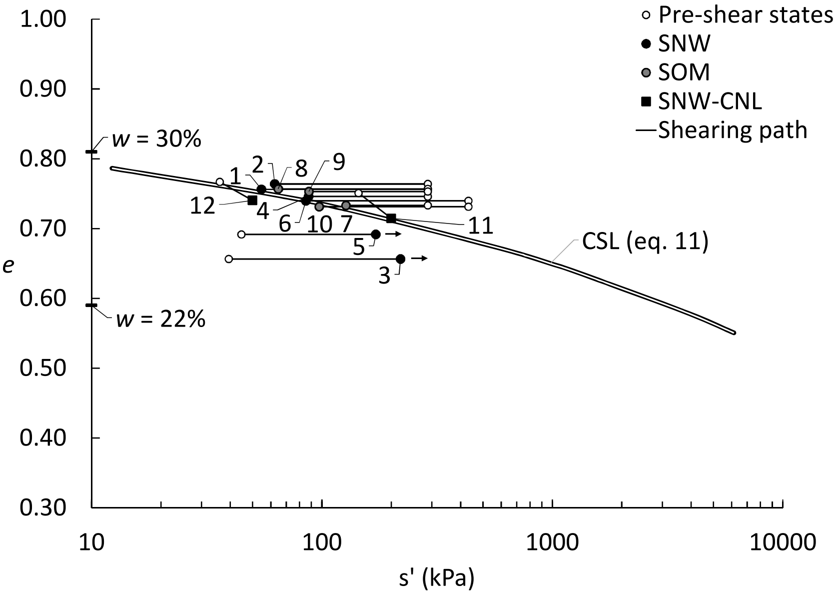

Figure 4.18. DSS shearing paths and ultimate states in ln s' – *e* space. Data labels denote test number (Table 4.4).

4.4.6.2 Cyclic simple shear tests

Cyclic liquefaction and cyclic mobility, as defined in Section 2.5.5.2, were encountered during CSS testing. Figure 4.19 and Figure 4.20 exemplify these two failure modes, corresponding to Tests C1 and C7b, respectively. In the former, the specimen exhibited gradual decrements in σ'_{y} at a fairly constant rate until a certain stress/strain threshold was reached after which stiffness reduced abruptly, shear strains accumulated rapidly (Figure 4.19c) and near-zero σ'_{y} levels were attained (Figure 4.19d). This behaviour is consistent with cyclic liquefaction. In contrast, in Test C7b, the specimen yielded during the first cycle but subsequently exhibited phase transformation and dilative behaviour (Figure 4.20b and d; Section 2.5.5). Shear strains steadily increased from cycle 1, and at a faster rate than Test C1 (Figure 4.20c). However, no abrupt increments in strain occurred, and the failure criterion was attained without the complete loss of σ'_{y} (Figure 4.20d), as expected during cyclic mobility.

Test C8, conducted in overconsolidated conditions and using a stress bias of 10 kPa (Table 4.5), exhibited a particular form of cyclic mobility that resembles low-cycle fatigue (Shajarati et al. 2012). Figure 4.21 denotes that negligible stiffness and σ'_{y} reductions occur for about 1700 cycles. Then, σ'_{y} and shear stiffness degraded at an increasing rate throughout a few hundred cycles without a complete loss of effective stress.

Table 4.5 shows that the τ_{cyc} and τ_{m} combinations used in Tests C3, C4 and C6 were insufficient to produce failure after prolonged cyclic loading. Figure 4.22, corresponding to Test C4, exemplifies this behaviour.

Specimen sliding on the base plate was not a relevant trait of the CSS tests because the cyclic failure criteria described in Section 4.4.5 resulted in tests ending short of the 7-15% strain range in which sliding tends to occur during monotonic tests. It is not known if sliding would have developed had cyclic shearing continued to larger strains.

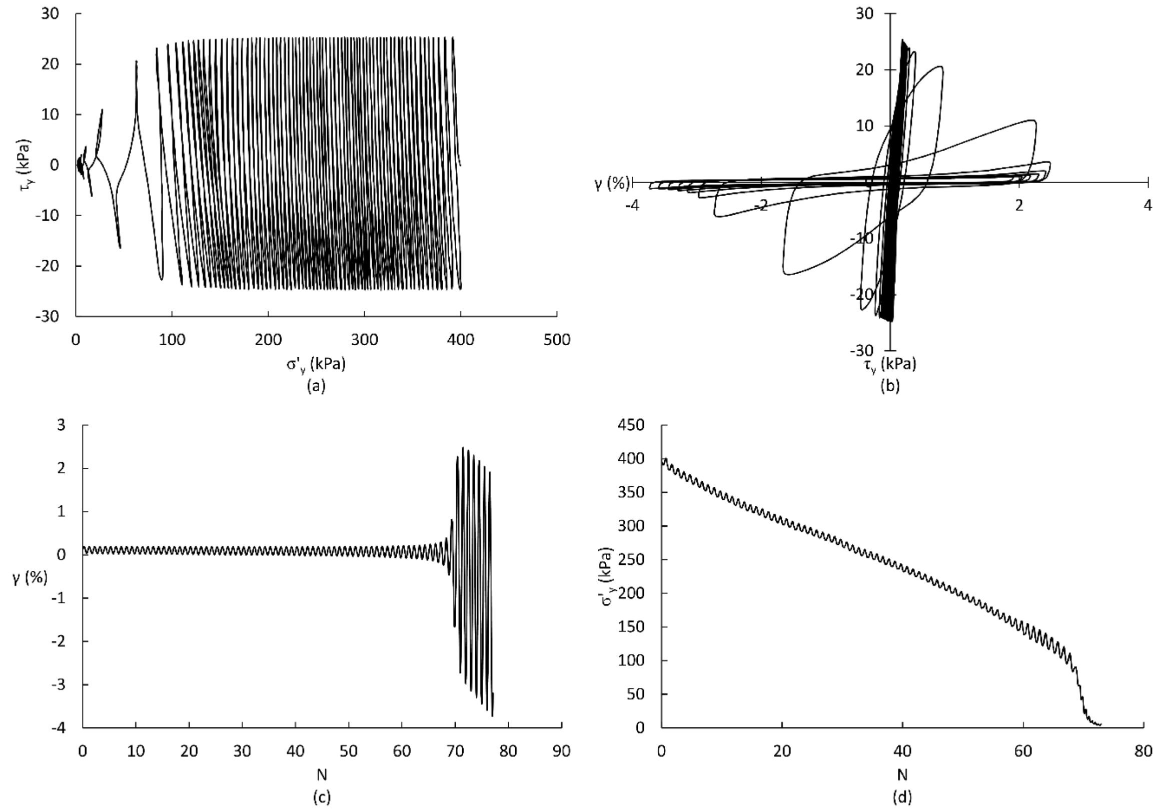

Figure 4.19. Results from Test C1 (Table 4.5): (a) stress paths; (b) stress-strain behaviour; (c) cyclic strain behaviour; (d) cyclic degradation of σ'$_y$.

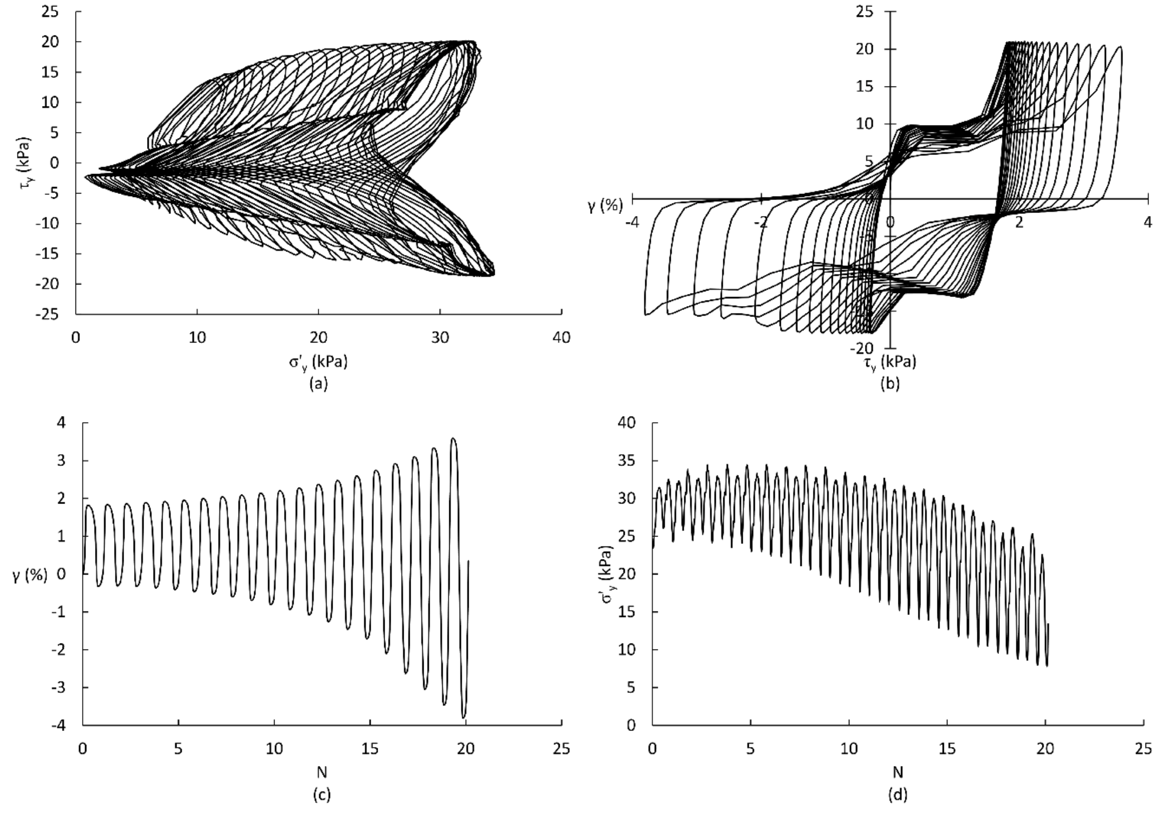

Figure 4.20. Results from Test C7b (Table 4.5): (a) stress paths; (b) stress-strain behaviour; (c) cyclic strain behaviour; (d) cyclic degradation of σ'$_y$.

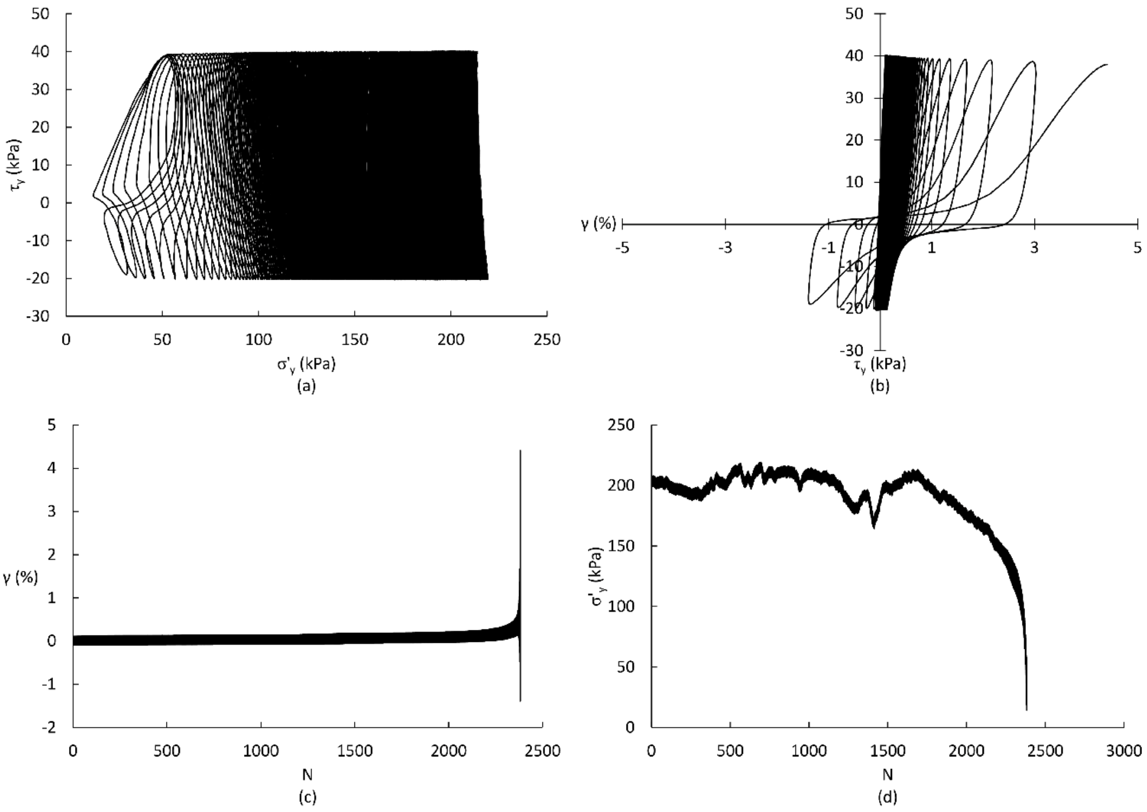

Figure 4.21. Results from Test C8 (Table 4.5): (a) stress paths; (b) stress-strain behaviour; (c) cyclic strain behaviour; (d) cyclic degradation of σ'$_y$.

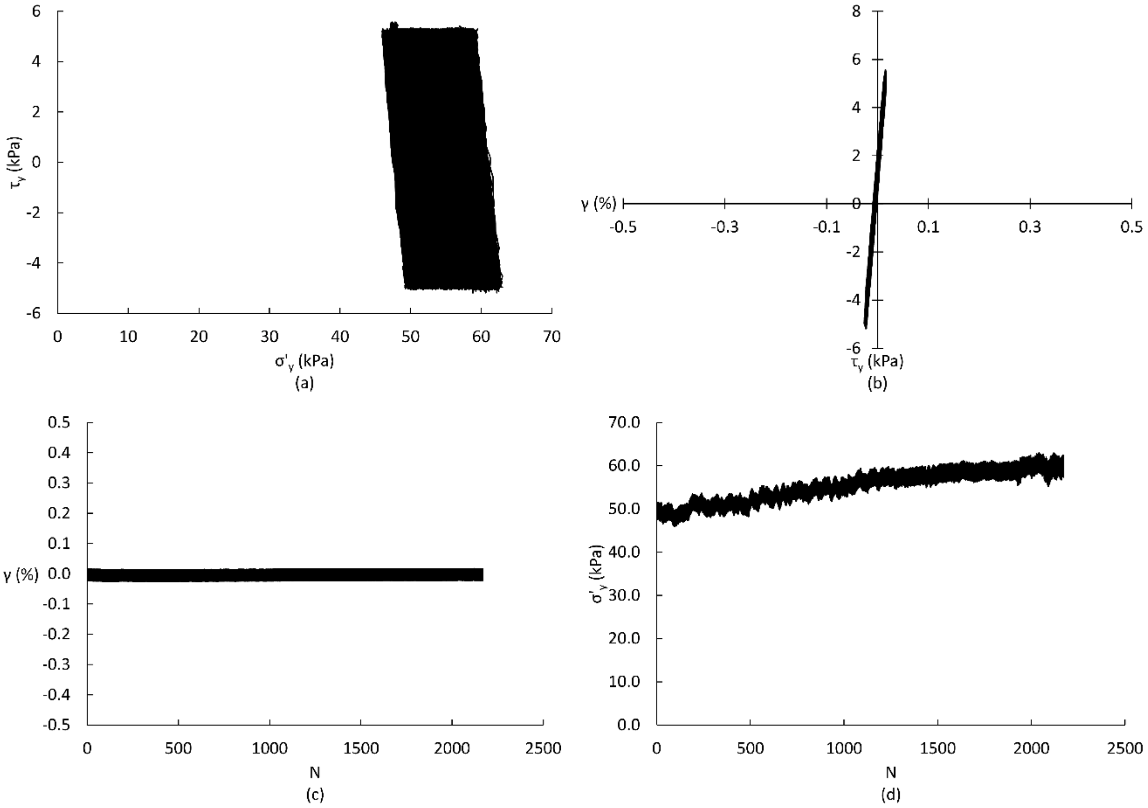

Figure 4.22. Results from Test C4 (Table 4.5): (a) stress paths; (b) stress-strain behaviour; (c) cyclic strain behaviour; (d) change in σ'$_y$ during cyclic loading.

4.5 Investigation of pile penetration mechanisms in chalk

4.5.1 Principles of X-ray micro-focus computed tomography

XCT involves the projection of X-ray images of a specimen from different directions, as shown in Figure 4.23. Most geomechanics research set-ups use a cone-beam scanner in which the X-ray source and detector remain stationary while the specimen rotates on an electromechanical stage at a predefined rate (Landis and Keane 2010; Cnudde and Boone 2013). A three-dimensional (3D) image is generated by reconstructing the X-ray projections around the axis of rotation of the specimen. Projection images result from the attenuation of the X-ray beam as it penetrates the specimen (Landis and Keane 2010). Attenuation is measured as the change in beam intensity (transmitted intensity, I) as it passes through the object. Assuming a monoenergetic X-ray beam, attenuation is dependent on the incident intensity of the beam (I_0) and the attenuation coefficient (μ) along the path of the ray (x). It is described by applying Beer's law in the form (Schulze et al. 2011; Cnudde and Boone 2013):

$$\ln\frac{I}{I_0} = -\int \mu(x)dx \tag{13}$$

Local μ values for each voxel in the 3D image can thus be assigned by using Eq. (13) in combination with an adequate reconstruction algorithm. Many cone beam flat panel XCT scanning systems use a proprietary reconstruction algorithm based on the Feldkamp solution for filtered backprojection (Feldkamp et al. 1984). As μ is approximately linearly correlated to density in materials of homogeneous mean atomic number (Mull 1984; Phillips and Lannutti 1997; du Plessis et al. 2013), variations in μ and, hence, in local density are recorded as the different greyscale intensities in each pixel of the two-dimensional (2D) projection images and in each voxel of the reconstructed 3D image (Desrues 2004; Otani et al. 2010). A more detailed description of the fundamentals of XCT scanning is given in Appendix D.

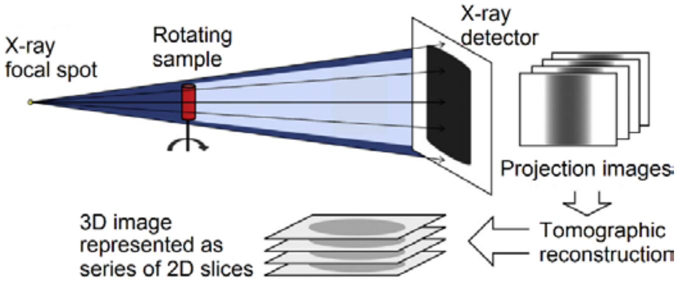

Figure 4.23. Schematic representation of XCT imaging process (edited from Landis and Keane, 2010, and Cnudde and Boone, 2013).

For data processing and quantification purposes, the reconstructed volume may be conceptualised as 3D array of cells (i.e., voxels), each of which contain four intrinsic and one explicit parameter. Three of the intrinsic parameters are the three cartesian coordinates (X, Y, Z) that describe the location of the centre of the voxel in 3D space, and are related to the position of the cell in the 3D array. The origin is often defined arbitrarily, as it depends on the orientation of the reconstructed volume. The fourth intrinsic parameter is the voxel geometry, which is typically assumed to be cubic, with a side length equal to the nominal scan resolution. Finally, the explicit parameter is the greyscale value (or voxel value) assigned to the voxel, which is a measure of the X-ray attenuation estimated for the portion of the sample represented by the voxel.

Table 4.6. XCT specimen and test details.

Specimen name	**CT02**	**CT03**	**CT04**
Mean height (mm)	119.77	135.96	131.86
Mean diameter (mm)	99.23	99.92	99.43
Mean bulk density (Mg/m^3)	1.974	1.973	2.010
Mean IDD (Mg/m^3)	1.545	1.546	1.604
Pile material	Polyether ether ketone (PEEK)	Polymethyl methacrylate (Perspex)	Polyether ether ketone (PEEK)
Pile OD (mm)	6.284±0.010	7.940±0.010	6.284±0.010
Pile ID (mm)	-	5.94±0.010	-
Tip condition	Flat, closed-ended	Flat, open-ended	40° cone-tipped
Embedded pile length at Step 1 (mm)*	18.166	15.503	18.531
Embedded pile length at Step 2 (mm)*	36.175	34.295	36.279
Embedded pile length at Step 3 (mm)*	-	38.680	
Total embedded pile length (mm)*	36.175	38.680	36.279
*XCT-derived.			

Figure 4.24. Filling of specimen-confinement pipe gap with epoxy resin using a small funnel.

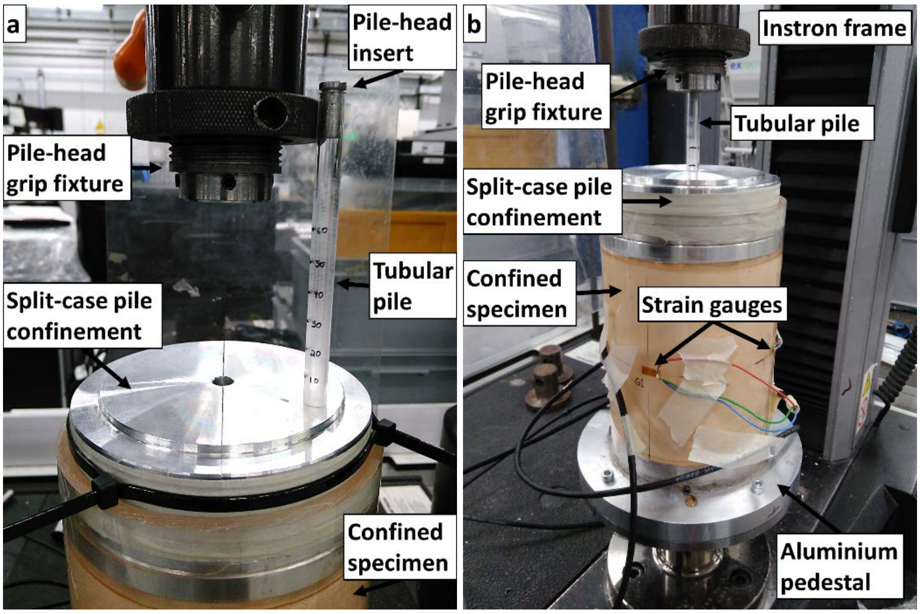

Figure 4.25. Model pile installation hardware.

4.5.2 Specimen preparation

Cylindrical chalk specimens were sculpted from intact block samples that had been submerged in de-aired water for a minimum of 10 days. The material was collected from St Nicholas-at-Wade as detailed in Section 4.2. Specimen geometry is presented in Table 4.6. After sculpting, the specimens were immersed again in de-aired water for at least 5 days before placing them on an aluminium test pedestal expressly designed and manufactured for the present experiments (see Appendix E for hardware details). Specimens were confined by a 5 mm-thick Perspex pipe bolted to the pedestal at its lower end (Figure 4.24). Gaps between the specimen and pipe confinement (≈5 mm wide) were filled using a high-strength, low-exotherm and low-viscosity epoxy resin (Robnor PX672H; Figure 4.24). The resin was left to cure for a minimum of 7 days before proceeding to install the model pile. A 5-10 mm head of de-aired water was kept at all times (including resin curing time, pile installation stages and XCT scanning sessions) to maintain a high saturation ratio.

4.5.3 Model pile installation

Three cylindrical model pile geometries (i.e., tip conditions) were used, one for each specimen/test. These were solid flat-tipped (Test CT02), tubular open-ended (Test CT03), and solid cone-tipped (Test CT04; 40° cone). Details are included in Table 4.6.

Pile installation was carried out ex-situ (i.e. outside the XCT scanning bay) using an Instron universal machine. The model pile head was gripped by a custom Instron fixture via grub screws (Figure 4.25). The head of the tubular pile was fitted with a cylindrical metal insert to prevent crushing of the element while fastening of these screws (Figure 4.25a). The aluminium pedestal on which the specimen rested was bolted to a custom-made Instron compression-tension plate. A split-case confinement device was fitted around the model pile to reduce pile deflection during installation (Figure 4.25). The device was centred on the pile and a 0.250 mm clearance between the pile and the device impeded friction between the elements before buckling. De-aired water was used as lubricant once buckling-induced contact between the pile and the device occurred. Further details of this test hardware are given in Appendix E.

The Instron machine controls were used to approach the model pile tip to the surface of the specimen, until applying a small docking load (0.002-0.050 kN). Pile penetration was displacement-controlled using Instron operating software Bluehill 2 at 0.174 mm/min, which is about 1000 times slower than the 20 mm/s standard penetration velocity of a CPT probe after discounting the difference in size. This slow installation rate was expected to favour fully drained pile penetration

Two installation stages were performed in CT02 and CT04 while CT03 consisted of three installation steps. Pile head load and displacement were recorded in all installation stages. The target pile head displacement in each stage was 20 mm. However, the third installation stage in CT03 was halted prematurely due to severe pile head damage. The pile head was unloaded at the end of each stage for all tests, and the elastic rebound of the element was measured to calculate the net head displacement.

The Perspex confinement pipe was externally instrumented with linear strain gauges placed at two mid-specimen height locations on diametrically opposite positions to measure circumferential strain (Figure 4.25b). Strain gauges were connected to a Micro-Measurements System 8000 StrainSmart data acquisition and signal conditioning unit.

4.5.4 Application of micro-focus X-ray computed tomography

4.5.4.1 Data acquisition

Specimens were scanned before the installation of the model pile and after each penetration stage, and scan sessions were labelled as numbers after the specimen name. All scans were 'local scans,' which means that the field of view excluded the Perspex casing tube and resin.

Scans were performed using a custom Nikon 450/225 kV Hutch system equipped with a temperature-controlled walk-in scanning bay. The following parameters were applied during scanning (see Appendix D for parameter definitions):

- Energy: 380-405 keV.
- Current: 229-275 µA.
- Magnification (scan resolution): ≈0.104 mm.
- Detector size: 2000x2000 pixels.

Additional acquisition parameters were the number of projections (3143), the number of frames per projection (fpp; 32), the exposure time per frame (0.125 s) and detector binning (2x2). These parameters are described as follows:

- Number of projections: the number of radiographic projections obtained during scanning and then used to perform the tomographic reconstruction.
- Number of frames per projection: the number of frames obtained from the same angular position and averaged thereafter to produce each radiographic projection.
- Exposure time per frame: time interval per frame during which X-rays are applied to the specimen at each angular position.
- Detector binning: method of operating the detector in which the signal recorded by an array of pixels, in this case a 2x2 array, is interpreted as being captured by a single, larger, pixel (Baek et al. 2013). Because electronic noise occurs at every signal recording pixel and

varies randomly within a given spectrum, a reduction in the number of pixel readings results in less noise and higher image contrast. The trade-off is that the scan resolution is reduced, in this case, halved (i.e. raw reconstructed volume dimensions equalled 1000x1000x1000 pixels [1000^3 voxels]).

Specimens were placed in the same position on the rotation stage of the XCT scanner as in the pre-installation scan session (labelled 00 for each test). The same scan settings were intended for each session, but slight differences in energy, current and focal spot location invariably occurred.

An aluminium bowtie filter was used to mitigate acquisition issues associated with variable beam-path lengths across the horizontal (XY) plane of the specimen. Most of these issues arose from the shorter beam-path lengths at the edges of the specimen, which resulted in much larger fluence being delivered to the detector, substantially increasing the dynamic range of the signal (Mail et al. 2009). The bowtie filter XY cross-section increased in thickness from the centre-line towards the edges, thus reducing the X-ray dose applied to the periphery of the specimen and mitigating this acquisition issue (Luck et al. 2013; Zhang et al. 2013).

Additionally, the aluminium bowtie device provided filtration of lower-energy X-rays in the cone beam, hence also reducing beam hardening artefacts during acquisition (Flay 2016). Beam hardening artefacts result from the lower energy X-rays in a polychromatic beam being preferentially attenuated or extinguished at small depths within the specimen (Hsieh 2015; Flay 2016). Consequently, the average energy of the X-ray beam increases as it passes through to the peripheral regions of the specimen, and therefore the ‘hardened’ beam becomes less attenuated at the inner regions of the sample. This artefact presents itself as brighter outer regions in cylindrical specimens, falsely suggesting a denser shell. ‘Cupping’ is also a common name for this effect.

4.5.4.2 Scan data reconstruction

CT Pro 3D software was used to reconstruct 3D images from the angular projections, employing a proprietary algorithm (see Section 4.5.1). Difficulties were encountered during reconstruction as the volumes often lacked edges and features that favoured the automatic detection of the centre of rotation (COR) of the volume. Visual assessments of the data were often required to adjust the coefficients of the COR location algorithm before the implementation of the in-built automatic calculation routine.

Though the COR varied in each dataset, all other reconstruction procedures were kept identical. These included the application of a beam-hardening correction algorithm and image masking, the latter used to reduce the number of peripheral voxels.

4.5.4.3 Post-reconstruction processing and artefact correction

As previously mentioned, bowtie filtering was used to mitigate beam hardening and XY-plane beam path-induced image artefacts. Further beam hardening corrections were applied during reconstruction. However, the heel effect and Z-direction beam path effect known as cone-beam or 'top-hat' artefact (Markins 2014) required post-reconstruction correction.

Figure 4.26 shows the Z-direction (vertical) profiles of mean grey values in a 30x30 pixel window of a peripheral region away from the centre where the pile was installed of each horizontal (XY) slice (region shown in Figure 4.27) for the three unprocessed reconstructed volumes of Test CT02. The abscissae axis indicates the XY slice number, where the origin corresponds to the lowermost vertical position in the 3D image (i.e. the bottom of the reconstructed volume). Difference in X-ray focal spot location along the vertical axis of the reconstructed volume results in a shift in profile features along the Slice No. axis in this Figure. These differences occur chiefly between CT02-00 and CT02-01/02 in this case. The top-hat effect is also observed as sharp changes in grey value towards the top and bottom regions of the volume. The top-hat effect results from the previously mentioned variable beam-path lengths, in this case along the Z axis of the specimen. These variable beam-paths occur from the 'diverging' directions of the X-rays in the cone-shaped beam originating at the focal spot (Figure 4.28), which produce 'chevron-shaped' artefacts in the vertical cross-section images (YZ or XZ plane) of the reconstructed volumes.

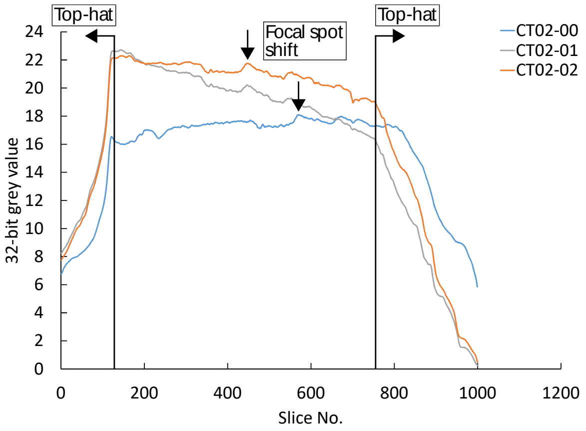

Figure 4.26. Mean grey value Z-profiles of sampling window shown in Figure 4.27 for the unprocessed reconstructed volumes of test CT02.

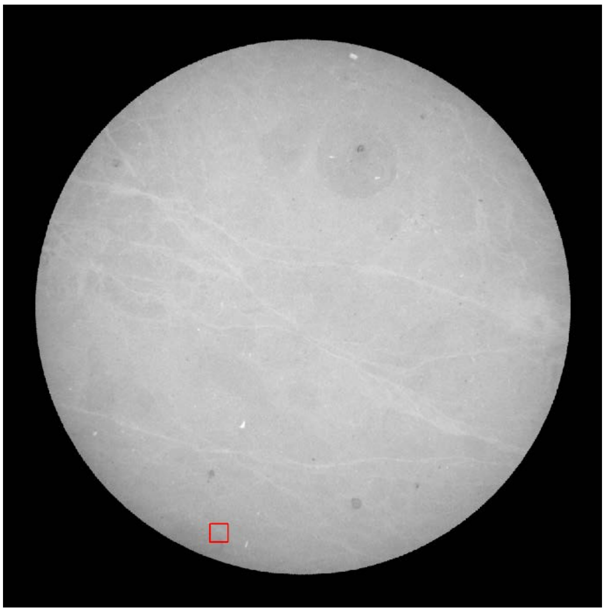

Figure 4.27. Central slice of CT02-00 and grey value sampling window.

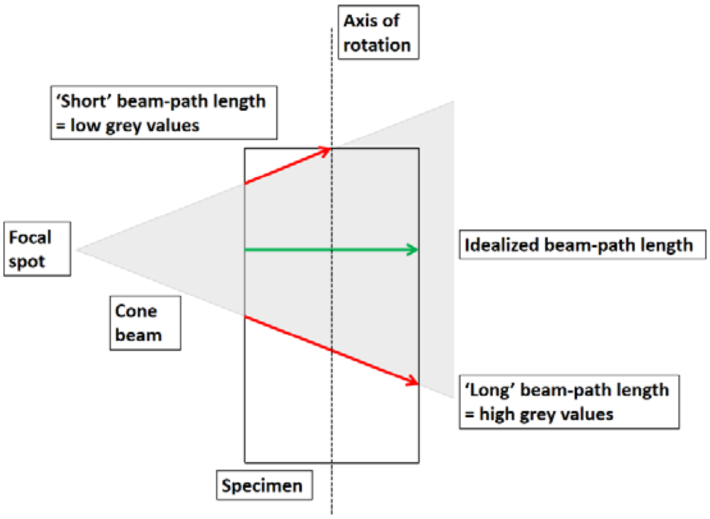

Figure 4.28. Schematic description of beam-path-induced 'top-hat' effect.

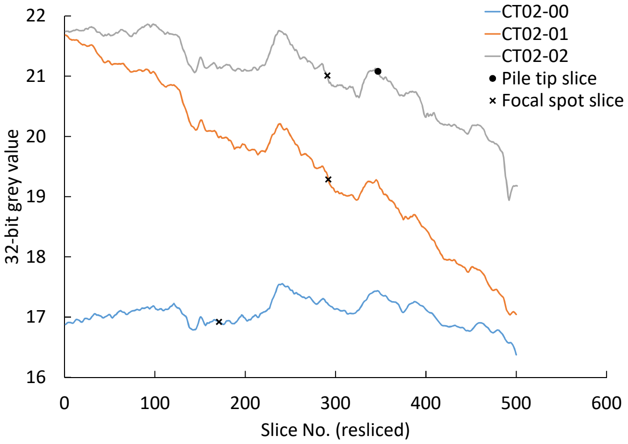

Figure 4.29. Mean grey value profiles of sampling window shown in Figure 4.27 of the cropped, re-aligned and re-sliced 3D images of test CT02.

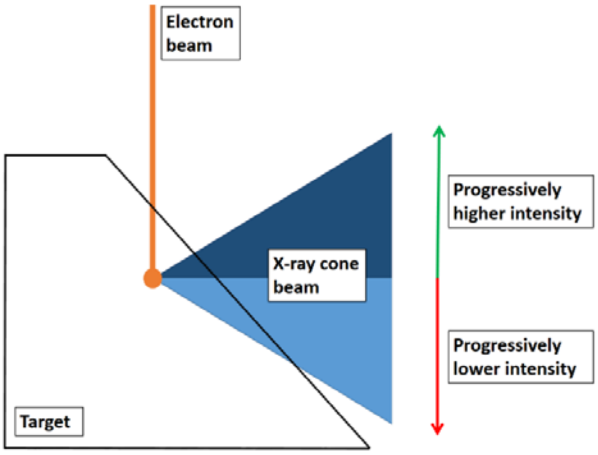

Figure 4.30. Schematic description of the heel effect.

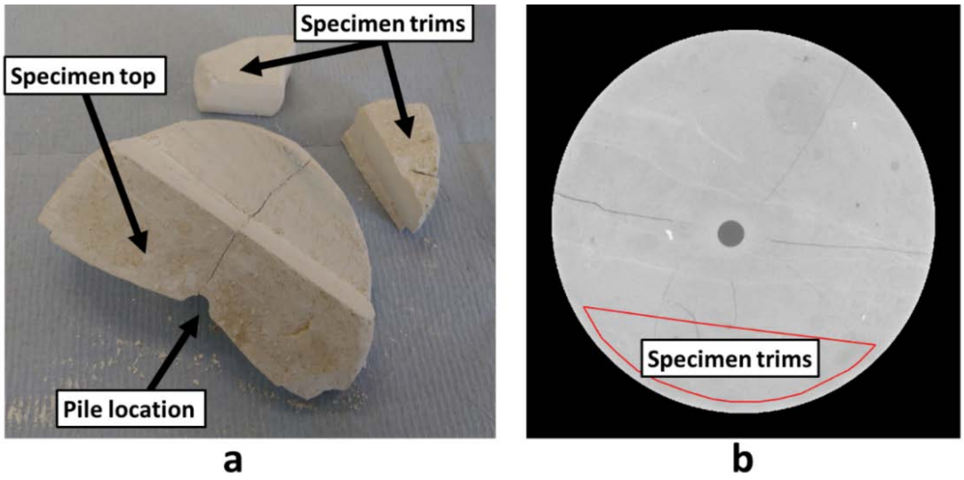

Figure 4.31. (a) Extraction of trims from specimen for post-test density measurements and (b) location of density sampling zone on XY slice of CT02-02.

The initial post-processing stage consisted in cropping-out the top and bottom regions of the reconstructed volumes to remove the top-hat effect, using Fiji-ImageJ software. The cropping boundary XY slices were varied in each volume such that the Z-direction misalignment of the focal spot was also removed. The Z-direction mean grey value profiles of the same ‘far-field’ sampling window of Figure 4.27 have been re-plotted for each of the cropped and re-aligned 3D images of CT02 in Figure 4.29.

The non-uniformity in grey value Z-profiles towards the top of the specimen (i.e. with increasing XY slice number) observed in Figure 4.29 was hypothesised to originate from chalk heterogeneity, or to be an image artefact associated with Z-direction cone-beam divergence and/or the heel effect. The latter is caused by the variable paths traversed by the X-ray beam *before exiting the target* (see Appendix D). Beam hardening associated with these variable in-target paths produces a Z-direction angular variability in X-ray intensity in the cone-beam (Figure 4.30), and an image artefact observed as progressively lower grey values in the regions above the cone-beam centre line (Braun et al. 2010; Hsieh 2015; Flay 2016).

Chalk heterogeneity was assessed by measuring the post-test intact bulk density of the specimen in the peripheral region where the 30x30 pixel grey value sampling window was located. Measurements were obtained by using the 'gas jar method' described by Clayton (1983) on intact samples cut from said part of the specimen (Figure 4.31a). Results showed limited top-bottom variability in bulk density values, with a standard deviation of less than 0.005 Mg/m^3. In Figure 4.32, the bulk density Z-profile of CT02-02 is shown alongside the mean grey value Z-profile of the same region (labelled 'acquired grey values'). Both parameters have been normalised by their overall mean value. Clearly, the top-bottom grey value variability is not associated with chalk heterogeneity, and it is therefore likely and image artefact. Artefact correction was carried out as follows, using a computer code written and compiled in MATLAB:

- A Z-direction mean grey value profile of the region where IDD was measured (Figure 4.31b) was determined from the cropped volumes. A moving average algorithm was applied to this Z-profile using a 10-voxel calculation window. Thus, a 'smoothened' version of the Z-direction mean grey value profile of the IDD region was obtained.
- The grey value in each pixel of each XY slice was divided by the mean grey value of the IDD-sample area of that slice obtained using the smoothened Z-profile. These 'normalised' grey values are a measure of the variability in tomodensity, referenced to the mean grey value in the intact (undisturbed) peripheral ('far-field') region of the specimen from where IDD samples were taken.
- The normalised pixels of each slice were multiplied by the average grey value of the whole un-smoothened Z-profile of the IDD sampling region. This removed the artefact-induced 'curving' of the original Z-profile (Figure 4.32). This correction reduced the dynamic range of the volume but maintained the original absolute dynamic range of each slice, thus preserving local grey value variability.
- A smoothening polynomial fit was determined for the normalised bulk density Z-profile of Figure 4.32, i.e., a function describing the vertically-distributed measurements of bulk density divided by the overall average of all measurements. Slice number was used as independent variable for this function. This normalised bulk density function was applied to each slice by multiplying the corrected grey values of the pixels in each slice by the function-derived normalised bulk density. This additional correction slightly increased the dynamic range of the volume by re-introducing the natural variability in bulk density across the specimen height but maintained the original absolute dynamic range of each slice.

The grey value profiles for the 30x30 sampling window of Figure 4.27 obtained after applying the above procedure to the data of test CT02 are shown Figure 4.33. Clearly, the method effectively removed the artefact-induced curving of the average mean grey value profile. However, it is also evident that there is a shift in the grey value range between volumes, which is associated with the slightly different scanning set-ups used. This impeded voxel-to-voxel comparisons of grey value changes caused by pile penetration. To remove this feature, further post-acquisition processing was carried out:

- An overall mean grey value of the top-bottom grey value profile of the footprint of the IDD sampling zone (Figure 4.31b) of each corrected reconstructed volume was calculated, thus obtaining a single far-field mean grey value for each volume.
- The far-field mean grey values of the three or four volumes pertaining each test were then averaged amongst them, thus obtaining an 'overall far-field mean grey value'.
- Every voxel of each reconstructed volume was divided by the far-field mean grey value calculated for that volume, and thereafter multiplied by the overall far-field mean grey value for the specimen.

Figure 4.34 shows the 30x30 far-field sampling-window profiles obtained after the application of this procedure to the cropped, re-aligned, re-sliced and corrected 3D images of test CT02. It is evident that the resulting 3D images now share a similar grey value range, though some inconsistencies persist. It is relevant to note that while this procedure successfully 'corrects' grey value data for the chalk phase of the reconstructed volumes, it may introduce false grey value variability in the voxels representing the naturally homogeneous thermoplastic pile. This is discussed further in Section 5.4.1.

Though the methods described above were exemplified using data from CT02, the same procedures were applied to the results from tests CT03 and CT04, which are provided in Appendix F.

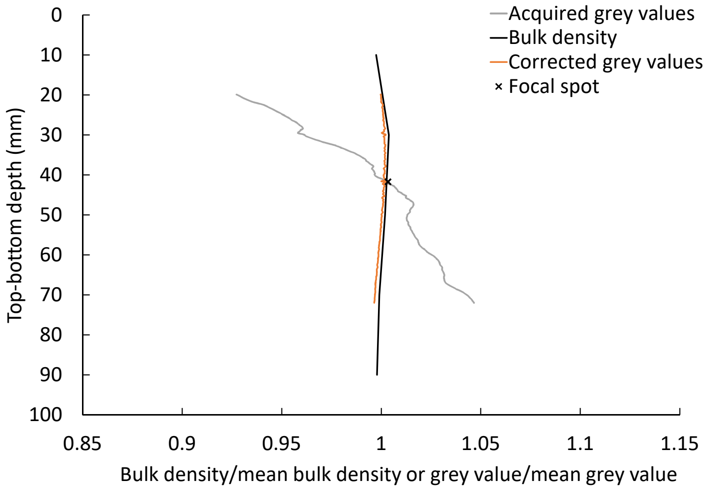

Figure 4.32. Top-bottom normalised intact bulk density and grey value profiles of the peripheral region of CT02-02 shown in Figure 4.31b.

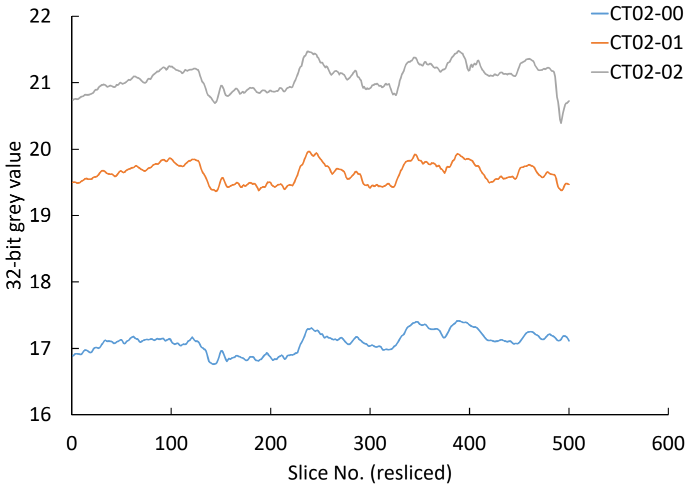

Figure 4.33. Mean grey value profiles of sampling window shown in Figure 4.27 of the cropped, re-aligned, re-sliced and corrected 3D images of test CT02.

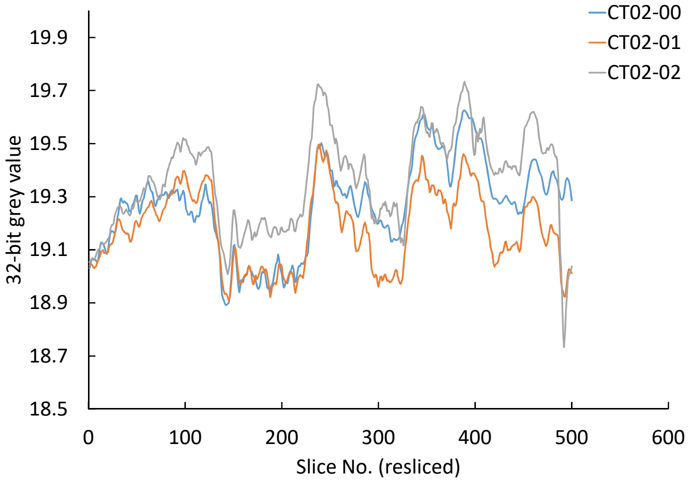

Figure 4.34. Corrected mean grey value profiles of Figure 4.33 after shifting grey value ranges.

4.5.4.4 Identification of chalk putty annulus

While the remoulded chalk annulus could be easily recognised in the reconstructed volumes by visual inspection, an unambiguous procedure was required to identify and examine the voxels in contact with the pile shaft. A script incorporating computer-vision was written and compiled in MATLAB to do this. The working principles of the code were:

- To reduce computing time, a region of interest (ROI) along the Z-axis was defined for the reconstructed volumes depicting the final pile installation stage. This ROI contained the central portion of the 3D image in which the pile and annulus were located (Figure 4.35a). Its XY coordinates were determined using Fiji-ImageJ.
- A Canny edge detector algorithm (Canny 1986) was applied to each slice in the ROI. The algorithm first used a one-dimensional gaussian filter of kernel size 4σ. Then, the algorithm employed an edge detection operator which calculated the image gradient (first derivative) and gradient direction and applied a non-maximum suppression edge thinning routine (i.e., by finding local maxima and supressing non-maxima values). Thereafter, local maxima were compared with user-input high and low threshold values and categorised as ‘strong edges’, ‘weak edges’ and ‘not an edge’, depending on whether the value was larger than the high threshold, or larger than the low threshold, or smaller than both thresholds, in each case. ‘Weak edge’ pixels were then compared via a hysteresis loop with neighbouring pixels in search for connections with ‘strong edge’ pixels; if none were encountered, the ‘weak edge’ pixel was re-categorised as ‘not an edge’. Finally, the algorithm returned a binary image containing the edges, which in this case corresponded approximately to the pile cross-section perimeter (Figure 4.35b). Weak threshold = 0.85, strong threshold = 0.99 and σ = 5 were used as input parameters.
- The edge coordinates obtained using the Canny detector did not correspond to the precise pile-chalk boundary due to ‘partial volume averaging’, where sub-voxel size detail is lost by the averaging of the different X-ray attenuations occurring within the voxel volume (Ketcham and Carlson 2001). To be able to collect grey value information of the actual destructured chalk annulus in close vicinity of the pile, edge coordinates in each slice were expanded by three pixels in the radial direction and the edge thickness was increased by one pixel (Figure 4.35c-d).

Coordinates for annulus voxels adjacent to the pile shaft were determined in this manner using the reconstructed volume corresponding to the final installation stage. These coordinates were then used to extract voxel values in other volumes, for example, before applying the mathematical adjustments described in the previous Section.

The thickness of the remoulded zone around the pile could not be readily measured with enough accuracy by using computer vision-aided automated routines as done in the near-field annulus identification procedure described above. Therefore, annulus thickness values had to be obtained through visual inspection.

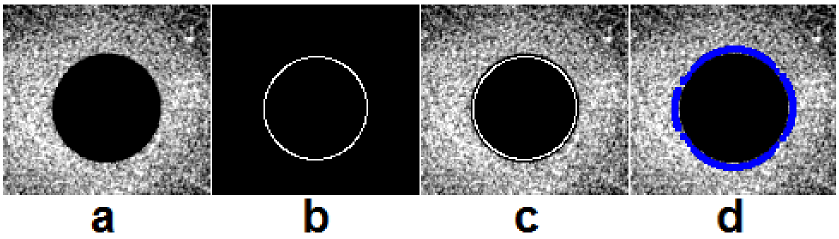

Figure 4.35. (a) XY slice of ROI of corrected CT-02-02 (the pile is the dark circle); (b) Canny edge detector output; (c) detected edge in (a); (d) pile-adjacent annulus pixels shown in blue.

4.5.5 Tension testing

After the final XCT scanning session, the same Instron universal machine and fixtures used for pile installation were employed for load-controlled tension testing. Loads were imposed in increments (or ramps), applying 12 N at a rate of 12 N/min in each ramp. This load magnitude was estimated to represent very approximately 10% of the failure load, using the upper-bound 120 kPa average ultimate shaft friction value proposed by Lord et al. (2002) for piles in high density, grade A Chalk. The rate was estimated by preliminarily calculating a time to failure as (after Gibson and Henkel 1954) $t_f = (12.7)[(d)^2/C_v]$, where d is the thickness of the chalk putty interface and C_v is the coefficient of consolidation of destructured chalk, and incrementing this value by 30%. d and C_v were taken a priori as 3 mm (about half the pile outside diameter) and 2.75×10^{-7} m^2/s (approximate value for a plasticity index of 0.5 based on oedometer data; further discussed in Section 5.5.2). Each loading increment was alternated with a two-minute constant load creep period, as often done during field-scale tests (e.g. Buckley et al. 2018b). The tests were halted when plunging failure took place.

Calibration and compliance tests were performed using the same tension loading conditions on model piles of the same length as those used in the XCT experiments. A standard tension testing Instron jaw-grip was used on the lower end of the piles and the custom grub-screw fixture at the top.

4.5.6 Model pile exhumation

After tension-testing each model pile, the Perspex casing and resin fill were carefully cut using a hacksaw. Specimens CT02 and CT04 developed longitudinal (Z-axis) fracturing during pile installation (Figure 4.36a; further discussed in Section 5.4). In these cases, the specimens were split along these discontinuities. For CT03, which did not fracture during pile penetration (Figure 4.36b), a shallow (≈10 mm) groove was longitudinally cut into the specimen using the hacksaw and a metal wedge was carefully pushed into the groove, thus inducing tensile failure and longitudinal splitting.

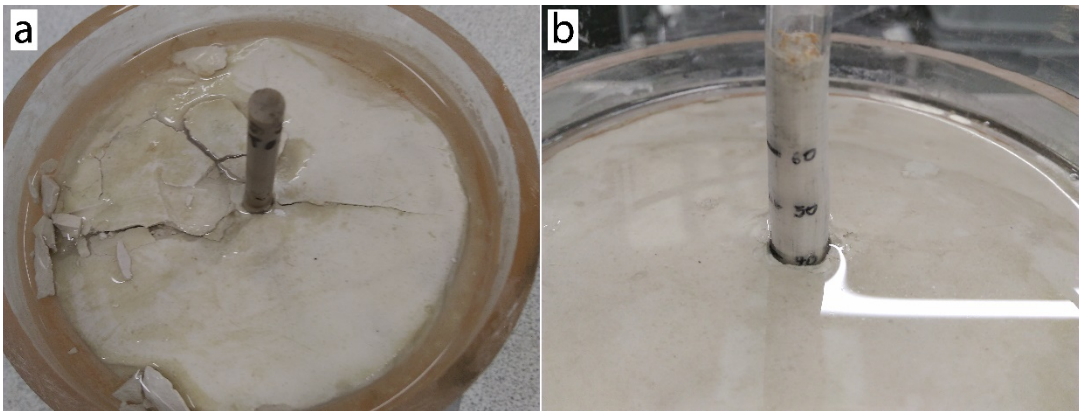

Figure 4.36. Top view of CT02 (a) and CT03 (b) after the final installation stage.

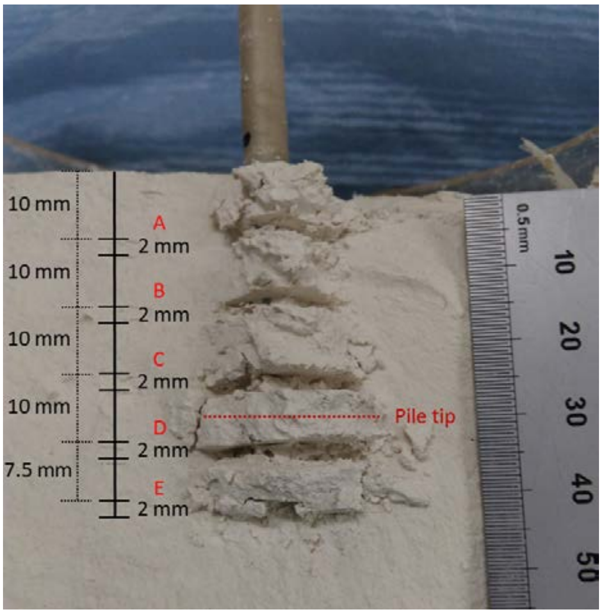

Figure 4.37. Detail of exhumation of CT02 and extraction of annulus samples.

The model pile and annulus were found to remain attached to one of the specimen halves in all three specimens. Small amounts (<1 g) of annulus material were sampled at every 10 mm of embedment depth using a scalpel. Figure 4.37 exemplifies this procedure. The following analyses were carried out on the annulus samples:

- Particle size analyses (PSAs): measurements were carried out using a laser-diffraction method (employing a Malvern Mastersizer 3000 device following guidance in BS ISO 13320:2009 as before; Section 4.2.3).
- Scanning electron microscopy (SEM): After extracting PSA samples, the split specimens were left to dry at room temperature in a covered container for a minimum of 4 weeks. Thereafter, small (less than 2 mm in maximum dimension) samples were carved out of the annulus feature using a scalpel and adhered to SEM stubs using carbon cement. As samples were not electrically conductive, they were sputter-coated in gold using magnetron deposition (see e.g. Newbury et al., 1986).

The very small volume of chalk putty forming the annulus of CT03 resulted insufficient to recover SEM samples or to obtain enough material to reach the optimal obscuration range of the PSA equipment, and therefore, micrographs and PSDs were not produced.

Due to the small size of the scaled experiment, and the even smaller size of the annulus feature, annulus samples could not be taken at varying radial distances from the pile axis whilst the material was moist and malleable. Therefore, PSAs could not produce a radial profile of annulus gradings. However, the SEM samples were obtained after the specimen had dried and become ‘stiffened’ and brittle. This allowed for the qualitative observation of the change in annulus fabric at different depths and at various comparative radial distances from the pile axis, as presented in greater detail in Section 4.5.7.4.

4.5.7 Results

4.5.7.1 Model pile installation

Figure 4.38a shows pile head stresses applied during installation vs measured pile head displacements. In stage 2 and thereafter, test data exhibits a clear ‘yield’ prior to a fairly linear increase in stress with pile head displacement, though this yield occurred at much smaller stresses in CT03 and CT04 than in CT02. Additionally, a notably serrated pile head vs displacement profile is observed in CT03.

Due to plastic deformation of the piles, it was only possible to accurately measure pile tip displacement using the XCT images. XCT-derived pile tip locations at the end of each installation stage are given in Table 4.6.

During the installation of the open ended pile in CT03, the pile plug level was observed to rise above the top surface of the specimen, as shown in Figure 4.36b, and as reported during field-scale pile testing in chalk (Ciavaglia et al. 2017a).

Circumferential strains measured during pile penetration are shown in Figure 4.38b. The wiring connecting the strain gauges to the StrainSmart signal acquisition unit had to be soldered off before each XCT scanning session, to avoid image artefacts induced by the presence of high-density metallic components, and then soldered back on prior to further pile jacking. This caused the strain gauge connection plates to degrade, to the point where one or more of the gauges ceased to produce useful data during the final installation step. Therefore, Figure 4.38b presents measurements from a single sensor that survived throughout the testing programme. However, it is important to note that circumferential strain measurements on the Perspex casing varied depending on fracture orientation in CT02 and CT04. This link between circumferential strain and the development and aperture of fractures during penetration is evident in the abrupt increase in strain at about 10 cm pile head displacement in CT02 (Figure 4.38a-b), which was approximately concurrent with the appearance of visible fractures. It may also be noted that larger strains were recorded in this experiment, which was attributed to the location of the strain gauge at an approximately transversal position to the major longitudinal fracture.

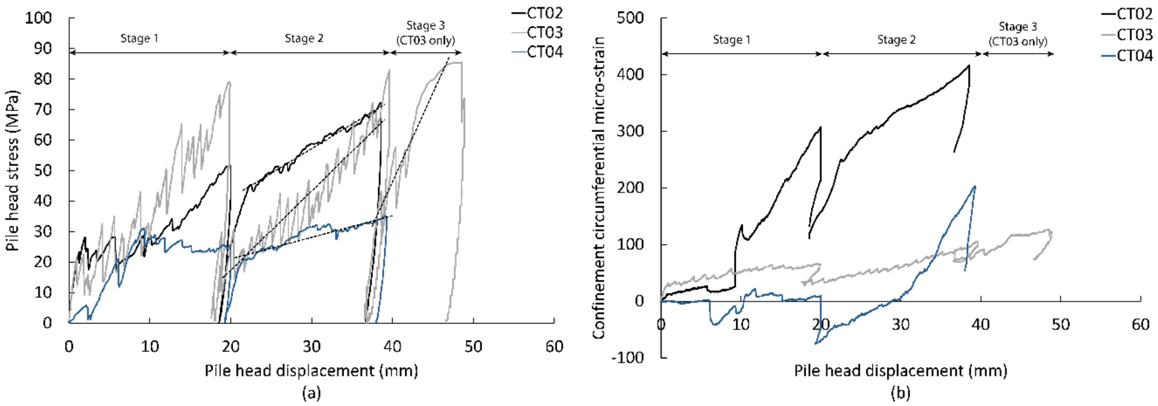

Figure 4.38. (a) Pile head stress (assuming constant pile cross-section area) and (b) circumferential strain.

4.5.7.2 Assessment of pile penetration and annulus density via XCT

Figure 4.39 depicts 3D vertical (YZ) cross-sections of the reconstructed and processed XCT volumes of the final installation step for all three specimens. Images were produced using VGStudio Max 2.1 software, and contrast and brightness has been adjusted to show more clearly the various features associated with pile penetration, chiefly amongst them the variations in greyscale. None of the processed volumes depict the top surface of the specimen, due to the cropping procedure performed to remove top-hat effects (Section 4.5.4.3).

All three piles lost verticality during installation, with the cone-tipped pile installed in CT04 exhibiting the most severe rotation from the vertical plane (about 16°) while the tubular pile of CT03 entered the chalk almost verticaly. However, key phenomena associated with pile penetration are revealed in this Figure, such as a densified zone around the pile in all three experiments and a network of fractures in CT02 and CT04. Gaps (macroscopic void space) were noted between the annulus and the enclosing structured chalk in regions away from the pile tips. These gaps extended to the vicinity of the cone-tip shoulder of the model pile used in CT04.

Top-bottom profiles of the average grey value (GV) of the annulus region in close contact with the pile shaft in each horizontal slice of the post-installation digital volumes are shown in Figure 4.40. These profiles are compared with grey value data extracted using the annulus coordinates in pre-installation 3D images, likewise averaged for each slice. Data has been normalised by the far-field average grey value of the region from which physical IDD measurements were obtained (Section 4.5.4.3; Figure 4.31). These profiles denote an increase in greyscale intensity of up to 10% from pre-installation conditions. Considering that X-ray attenuation in monomineralic geomaterials is approximately linearly correlated with bulk density (Section 4.5.1), the annulus to far-field greyscale ratio has been assumed to be equivalent to the bulk density ratio between these two regions. Thus, this ratio was multiplied by the physically measured bulk density of the IDD region (employing the depth-based regression curve for discrete density measurements described in Section 4.5.4.3) and used to determine average annulus void ratio profiles, assuming fully-saturated conditions and using (Madhusudhan and Baudet 2014):

$$e = \frac{\mathrm{G_s}\gamma_\mathrm{w} - \gamma_\mathrm{b}}{\gamma_\mathrm{w}(\gamma_\mathrm{b} - \gamma_\mathrm{w})} \tag{14}$$

where $\mathrm{G_s}$ is the specific gravity of calcite, assumed to be 2.70 (Clayton 1983), and γ_w and γ_b are the bulk density of water and chalk, respectively. Results are presented in Figure 4.41.

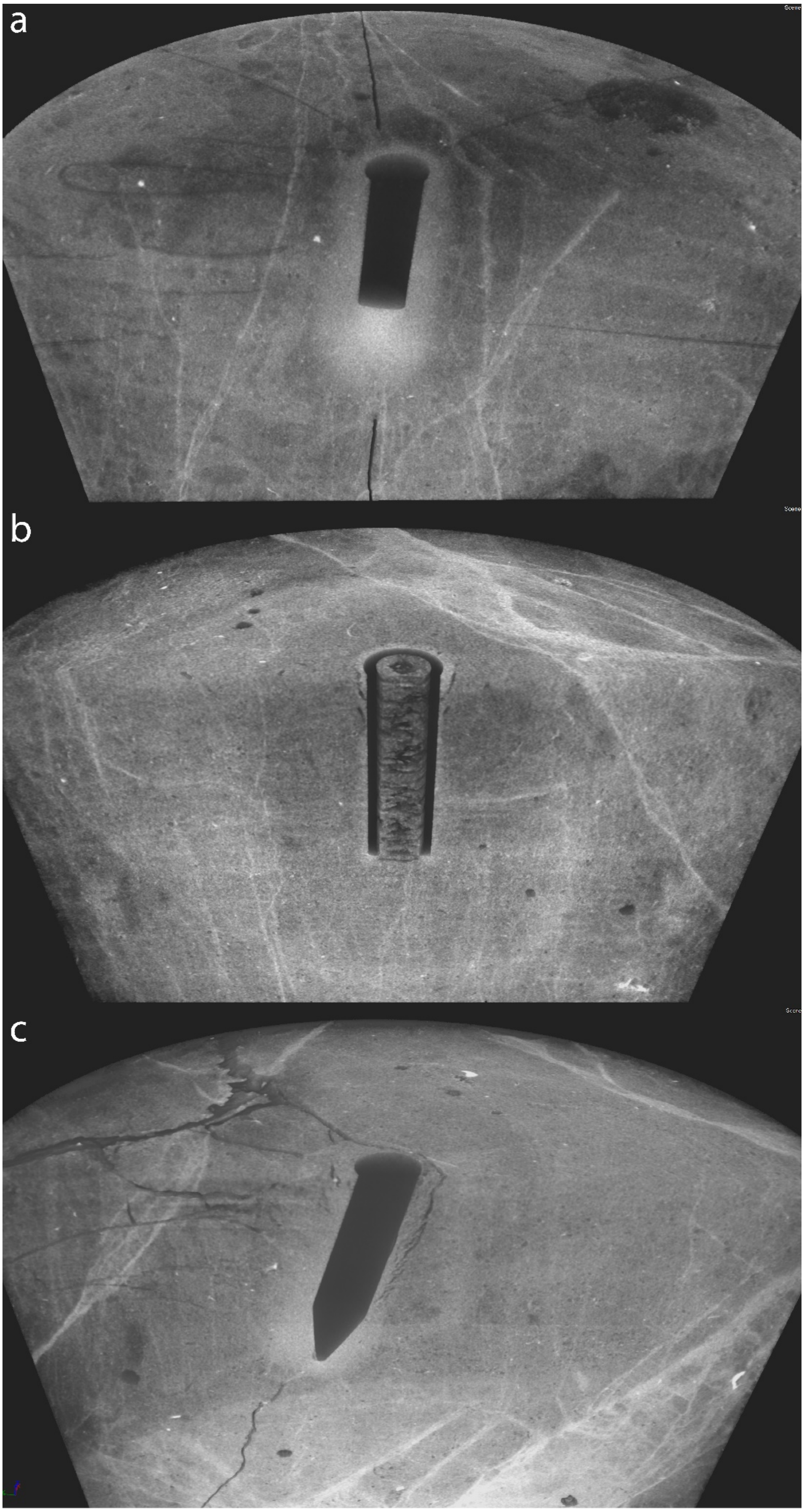

Figure 4.39. 3D vertical (YZ) cross-section of the processed XCT volumes after the final installation stage: (a) CT02; (b) CT03; (c) CT04.

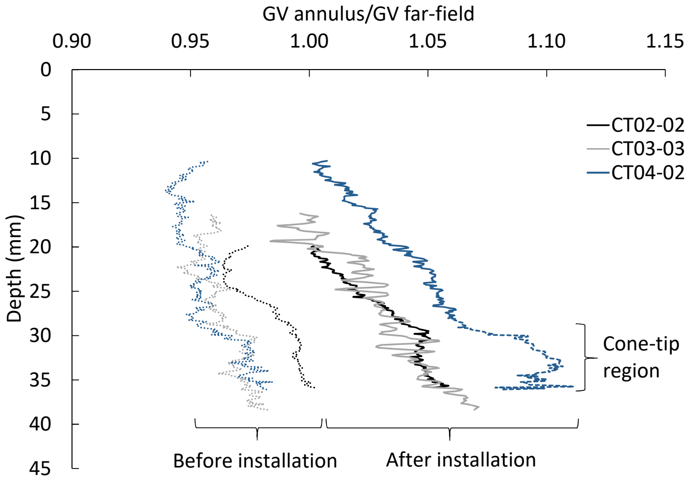

Figure 4.40. Grey value (GV) in chalk putty annulus coordinates normalised by the mean grey value in the far field IDD sampling region of the specimen.

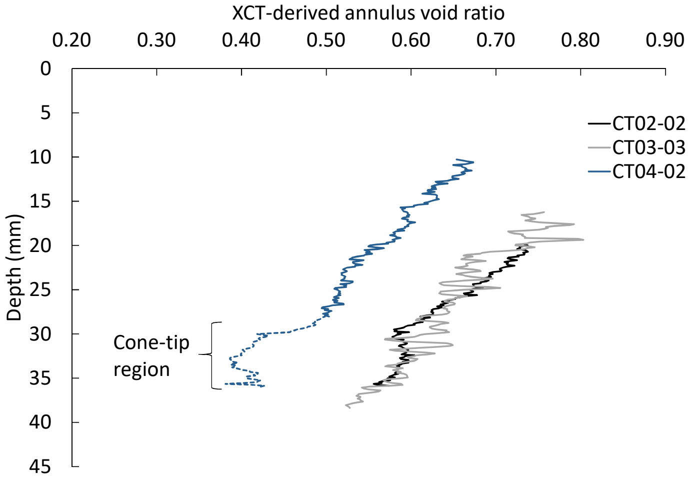

Figure 4.41. XCT-derived mean void ratio profiles of the remoulded annulus (values averaged for each slice).

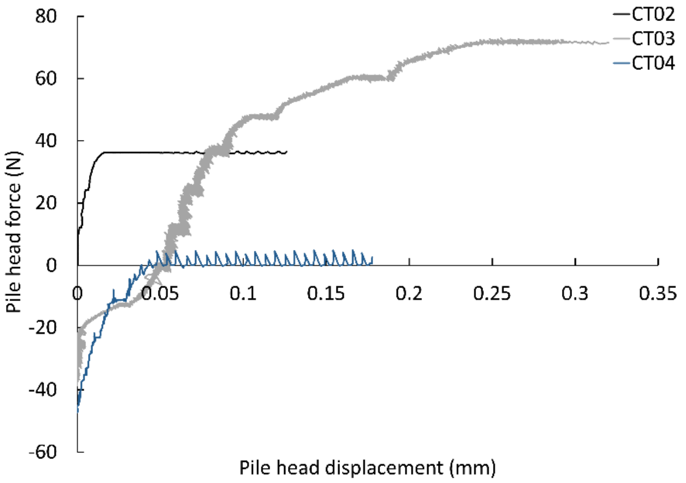

Figure 4.42. Pile head load during tension testing of model piles.

4.5.7.3 Model pile capacity in tension

Figure 4.42 presents the results of the post-scan tension tests on the model piles. Piles employed in CT03 and CT04 were docked using a compression load of approximately 40 N, expressed in this Figure as negative. All three piles failed after fairly small loads, with the cone-tipped pile used in CT04 mobilising near-zero vertical capacity in tension.

4.5.7.4 Pile exhumation

Annulus samples were taken as described in Section 4.5.6 and by Figure 4.37, i.e. at every 10 mm from the specimen surface until the lowermost region of the annulus was reached. Sampling locations are labelled A through E, as in this Figure. However, the acquisition of samples in all five locations was not always possible. PSA results are presented in Figure 4.43.

Figure 4.45 and Figure 4.46 show typical SEM images of the annulus at various depths and distances from the pile shaft. Very densely arranged grains are evident in the material in contact with the pile surface (i.e. from a field of view parallel to the pile axis), shown in Figure 4.45. Few fairly intact coccoliths seem to have survived the crushing and shearing processes that occurred in this region and there is evidence of edge-chipping or abrasion.

Micrographs of fields of view oriented perpendicularly to the pile axis are shown in Figure 4.46. These fields of view are schematically shown in Figure 4.44, using an XY slice of CT02-02. Figure 4.46 expose four qualitatively distinct structural conditions of the chalk in the vicinity of the pile. Figure 4.46a shows the same material depicted in Figure 4.45, i.e. chalk putty contiguous to the pile shaft and composed of closely packed grains with limited presence of coccoliths or other distinguishable fossil-based structures. The apparent greater presence of void space compared with Figure 4.45 is believed to stem from the disturbances produced during SEM sample preparation. Figure 4.46b corresponds to an observation point at a greater radial distance from the pile shaft than Figure 4.46a and depicts a melange of closely packed calcite platelets as well as some coccoliths, the majority of which appear to be broken. Intact coccoliths are more frequent in Figure 4.46c, which portrays a region at a greater radial distance from the shaft than Figure 4.46a and Figure 4.46b. In this micrograph, however, none of the larger ovoid pore space of intact chalk is discernible, and the material was found to be in a powdery state during SEM sample mounting, which suggests that de-cementation is likely to have taken place. Finally, Figure 4.46d shows fairly intact chalk in the far field region away from the pile, though some disturbances might have occurred during sampling.

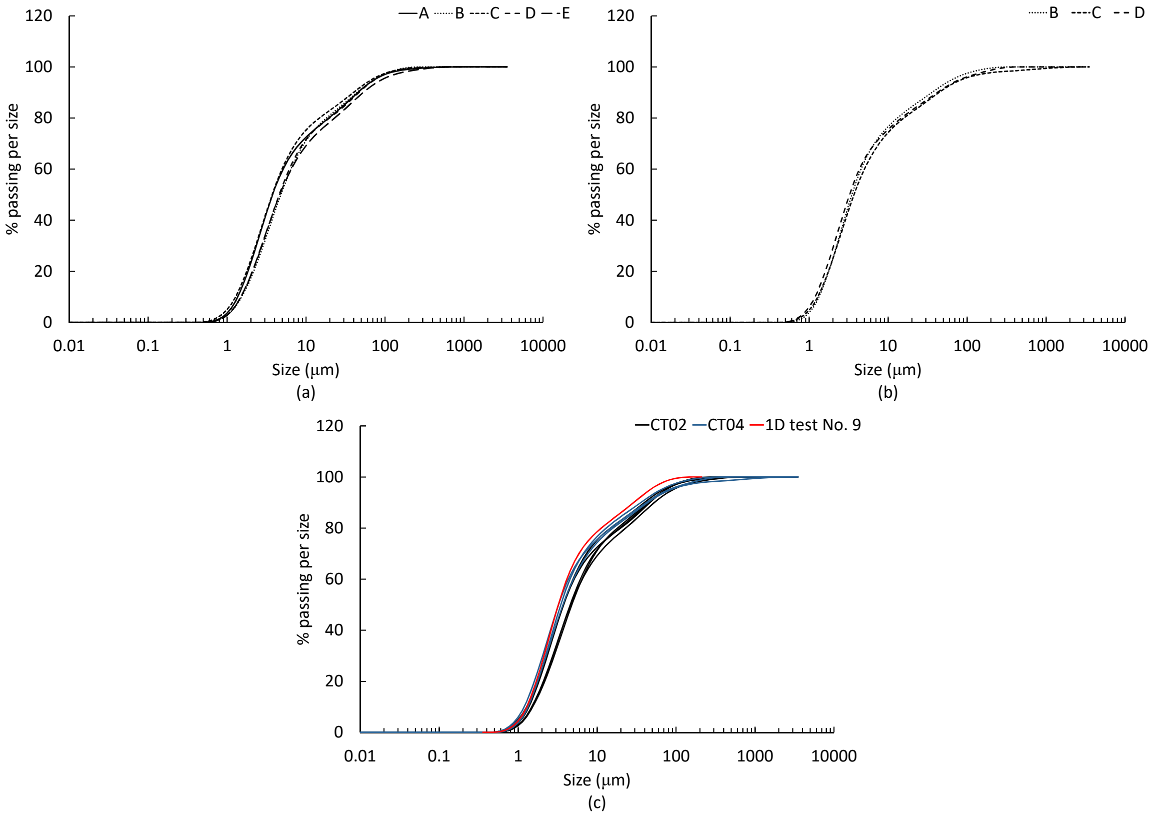

Figure 4.43. PSD of annulus material at different depths (see Figure 4.37): (a) CT02; (b) CT04; (c) all measurements plus data from Sections 4.2 and 4.3.

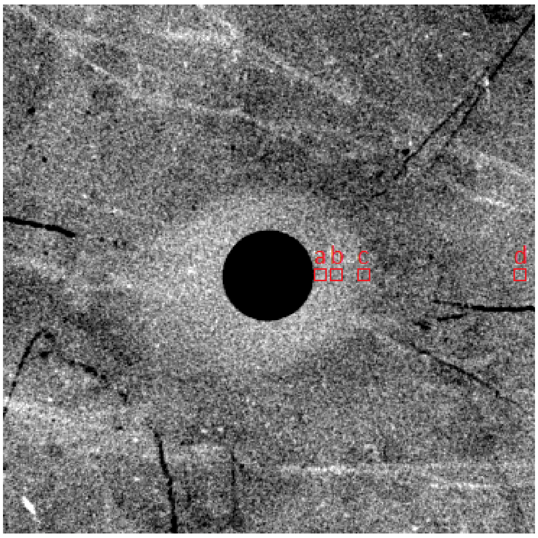

Figure 4.44. Schematic depiction of SEM fields of view of Figure 4.46.

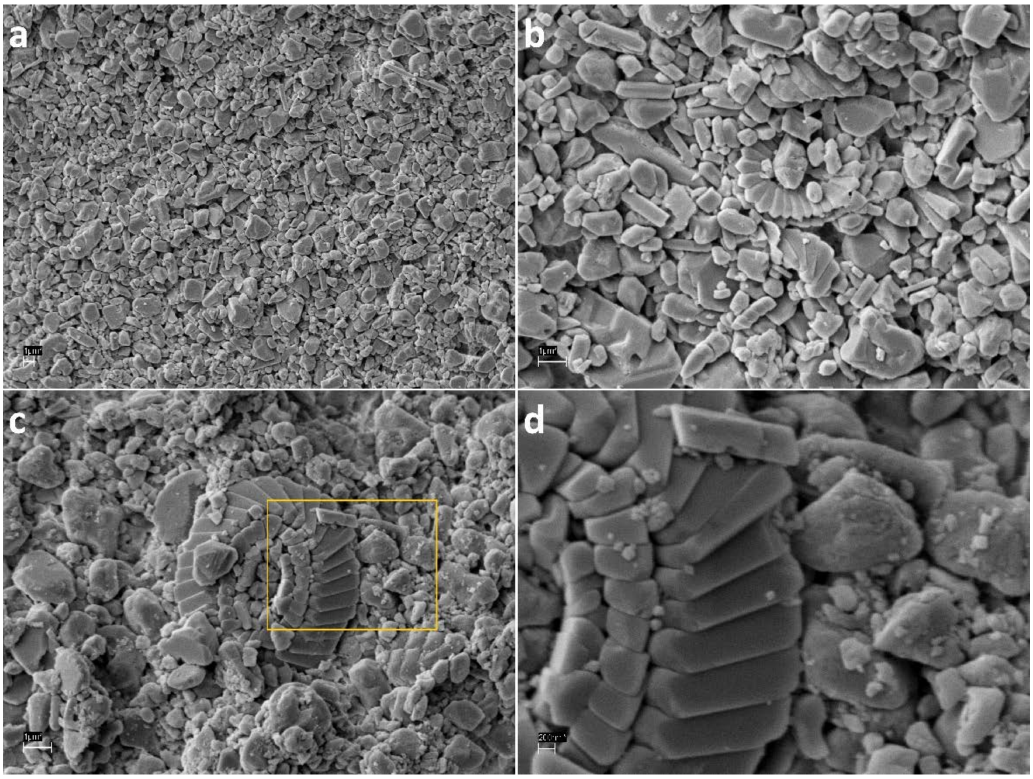

Figure 4.45. SEM images of annulus surface in contact with the pile shaft (CT02): at 4.2 mm depth, (a) 7500x and (b) 20000x; at 21.2 mm depth, (c) 20000x and (d) close-up to rectangle area in c, 60000x.

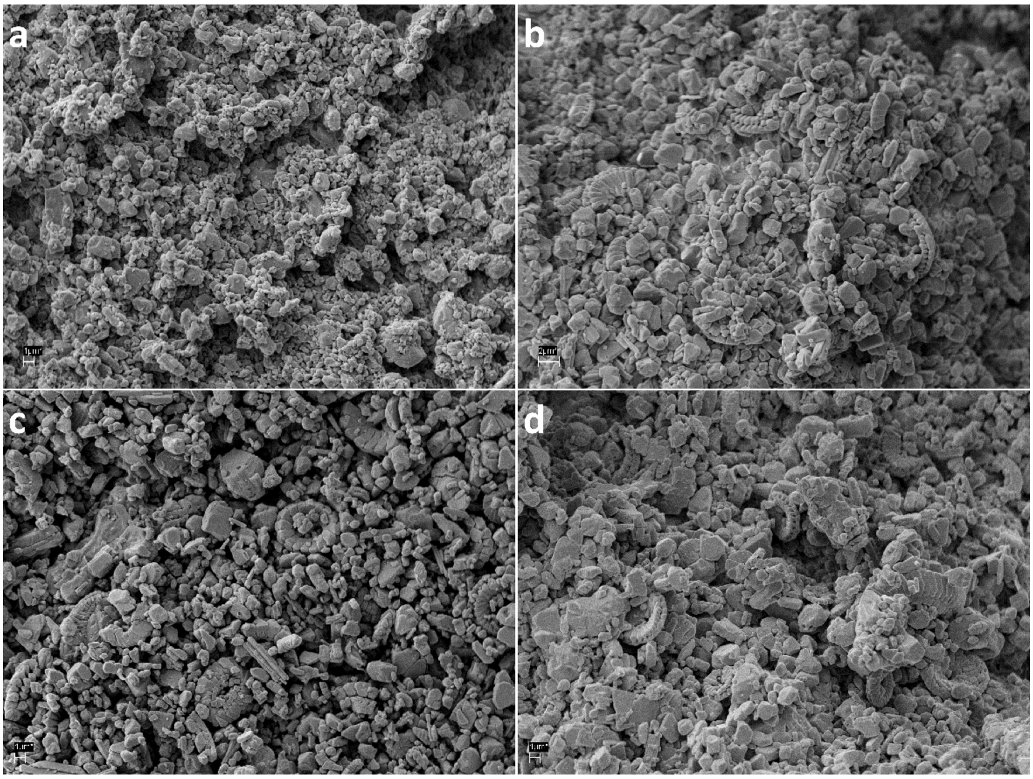

Figure 4.46. SEM images of annulus (CT02), views (schematically shown in Figure 4.44) are perpendicular to the pile shaft (all images at 7500x): (a), (b) and (d) at 36.1 mm depth; (c) at 5 mm depth.

4.6 Summary of laboratory investigation

The work presented throughout this Chapter aimed at producing the experimental data required to tackle the specific objectives of the Thesis, stated in Section 1.2. This work comprised:

1. The preparation of destructured chalk via different procedures and using intact samples of different origins within the low-medium density range. Such approach was not observed to produce significant variability in PSD or Atterberg limits.
2. Oedometer tests on intact chalk specimens and both oedometer and undrained triaxial experiments on the destructured chalk samples to examine the suitability of a critical state framework to describe the mechanical performance of the material. A potential critical state framework comprising unique 1D-NCL and CSL was identified from these tests.
3. Constant volume direct simple shear tests on destructured chalk specimens to evaluate the applicability of the critical state framework to predict the ultimate strength of chalk putty interfaces. For most tests, ultimate states were found to converge to the proposed CSL.
4. Model pile tests using intact chalk cores and XCT to analyse pile penetration mechanisms, determine the void ratio of the pile-chalk interface, and link these observations with the critical state framework derived from element testing. The tomography data showed that, as anticipated, an interface or ‘annulus’ of crushed chalk was present around the model piles after installation, and that this interface appeared to be significantly denser than the adjacent intact chalk.

These results are debated in detail in the following Chapter. There, the micromechanical justification for the behaviours observed during oedometer and triaxial testing is reviewed, the aptness and limitations of the resulting critical state framework with regards to interface strength prediction is analysed, the comparability of this framework with the stresses and void ratios inferred from the scaled experiments is examined, and the implications of these results and analyses for small displacement pile engineering in chalk is discussed using the pile test and CPT data available to the author.

Chapter 5 Discussion

5.1 Introduction

Results from the laboratory investigation detailed in the previous Chapter are assessed in the context of the current state of knowledge on the mechanical behaviour of chalk and on the performance of small displacement piles installed in this material, presented in Chapter 2 and Chapter 3, respectively. Aspects of the variability of destructured chalk, which may be associated with distinct mechanical behaviours, are first reviewed. Then, the micro-mechanical phenomena underpinning the existence of unique normal compression and critical state lines is examined and used to complement previous experiences reported in Chapter 2. This critical state framework is thereafter expanded to characterise the monotonic and cyclic behaviour of destructured chalk interfaces that mimic pile-chalk interaction. This method is subsequently applied to the performance of the scaled model piles, using the XCT-derived void ratio of the destructured chalk annulus as input parameter. Commentary pertaining the penetration mechanisms that control annulus density are also presented. Finally, results from this experimental campaign are used to re-interpret the available field-scale pile test data presented in Chapter 3 and implications for pile design are examined.

5.2 Critical state framework for destructured low-medium density White Chalk

5.2.1 Destructured chalk variability

PSD curves of Figure 2.9 pertaining previous investigations and Figure 4.3 corresponding to the present work are plotted together in Figure 5.1. The materials produced in this study are very similar amongst them in terms of PSD and are also very comparable to chalk putties produced by other authors using different methods but similar grading restriction (see Table 2.1).

The PSD similitudes are proposed to be partially responsible for the good comparability between the index properties of the four putties concerning this Thesis and that of previous works, as exhibited in Table 2.1 and Table 4.1. Additional relevant factors that affect these properties such as particle shape and form and mineralogy are estimated to be comparable in the four putties tested, and in the materials studied by other authors, as previously discussed in Section 2.5.2. As stated before, these similitudes stem from the equivalent biogenic origin of the chalk putty particles: White Chalks within the low-medium density range are largely composed of coccoliths and coccolith fragments, with limited presence of stronger block- or rod-shaped authigenic calcite grains and very small amounts of clay and silica minerals (Clayton 1983; Clayton et al. 2003). This suggests that grain size, shape and mineralogy, and therefore mechanical performance, are largely determined by the characteristics of the intact chalk and that the crushing method has relatively limited influence on these characteristics.

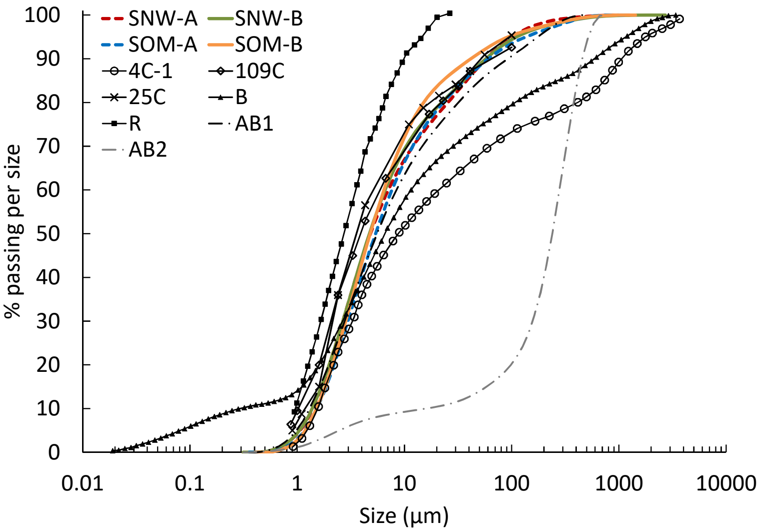

Figure 5.1. Comparison between the PSD of the putties produced in this Thesis and that of previous investigations (see Table 2.1).

5.2.2 Compression behaviour of destructured chalk

The congruence in 1D compression paths observed in Figure 4.8 is associated with the comparable characteristics of the reconstituted materials, such as grading, grain shape and mineralogy, as discussed above. Thus, compression behaviour is apparently uninfluenced by specimen size and reconstitution method. However, it is acknowledged that a diagenesis-independent change in the initial PSD of reconstituted chalk –for example, the inclusion of larger intact agglomerations into fine-sized slurries– may produce a different behaviour to that observed in Figure 4.8, as suggested by Clayton (1978). Naturally, diagenesis-dependent variability of the constituting particles of chalk, e.g. a generous presence of authigenic calcite grains and/or clay minerals, is also likely to eliminate the observed coherence in compression behaviour.

For sands, a progressive increase in the slope of one-dimensional compression paths while converging towards the NCL is associated with a progression from grain displacement and inter-particle grinding to breakage of angularities and particle splitting and fracturing as normally compressed states are attained (Mesri and Vardhanabhuti 2009). Near-elastic 1D unload-reload lines then result from permanent fabric strengthening induced by grain crushing and reorganistion during virgin loading (Coop 1990; Coop and Lee 1993). Compression path and NCL curving, and elastic unload-reload features are evident in Figure 4.8, where the average unload-reload slope was measured as 0.0026. Thus, it may be proposed that these traits are associated with the same grain fracture mechanics reported for sands.

To assess particle breakage during compression of the reconstituted specimens, an adapted version of the relative breakage factor proposed by Hardin (1985) has been used. This modified relative breakage factor, B_{rm}, is determined as (Figure 5.2):

$$B_{rm} = B_t/B_p \tag{15}$$

where B_p is the breakage potential, defined as the area between the pre-test cumulative PSD curve and the maximum and minimum grain diameters of 425 and 2 µm corresponding to the maximum and minimum nominal passing size and the size boundary between clays and silts, respectively; and B_t is the total breakage defined as the area between the pre- and post-test cumulative PSD curves.

Figure 5.3 shows that, at the same maximum σ'_v, B_{rm} is directly correlated with the initial void ratio, expressed as the liquidity index. This indicates that a high coordination number in initially 'dense' specimens entails less grain breakage during compression than in initially loose specimens, which is in agreement with the compression behaviour of sands (Altuhafi and Coop 2011).

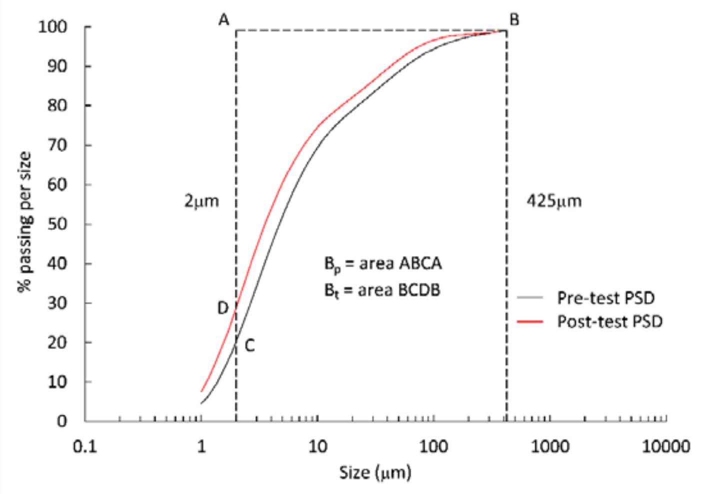

Figure 5.2. Parameter definition for the modified relative breakage factor B_{rm} (based on Hardin 1985; re-drawn and edited from Coop et al. 2004).

Further comparability is noted from the multiple compression paths below 2 MPa in Figure 4.8. These paths highlight the plausibility of infinite virgin compression curves circumscribed by the 1D-NCL, as documented for sands by e.g. Coop and Lee (1993), Pestana and Whittle (1995), Jefferies and Been (2000) and others. This characterisation of the compression response supports the use of critical state concepts to describe the compression behaviour of destructured low-medium density White Chalk.

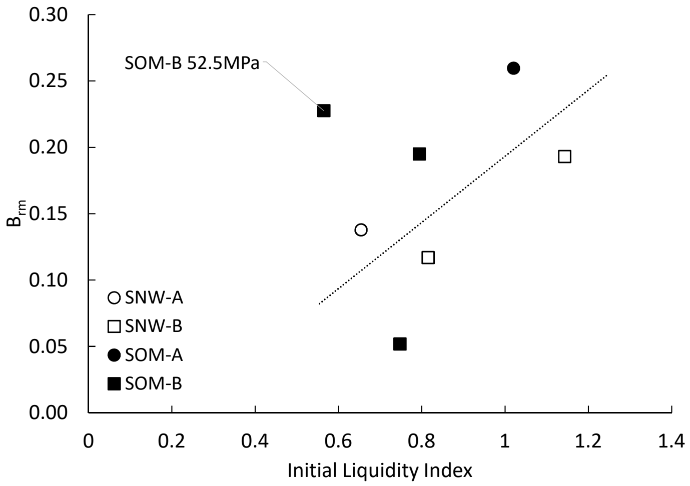

Figure 5.3. Correlation between the modified relative breakage factor B_{rm} and the initial liquidity index.

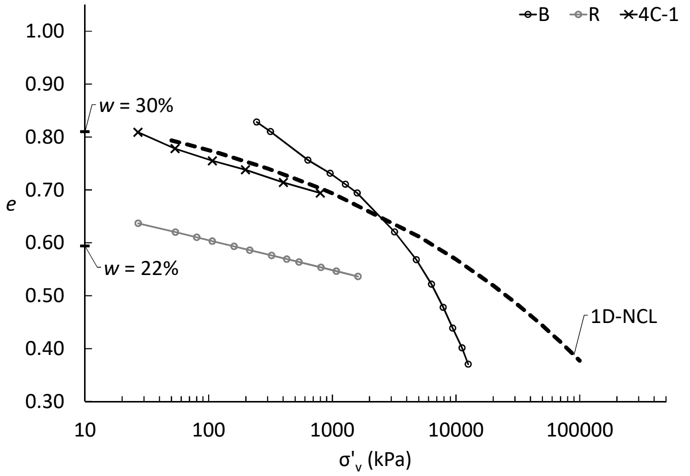

Figure 5.4. 1D compression paths from oedometer tests on reconstituted specimens as reported by various authors (see Table 2.1 for legend key).

Figure 5.4 presents oedometer compression paths for reconstituted specimens prepared from putties created by some of the methods summarised in Table 2.1, and the proposed 1D-NCL (Eq. (10)). A combination of factors may be speculated to lead to the contrasting behaviours shown by the materials tested by Razoaki (2000), ‘R’, and Bialowas (2017), ‘B’. In the former case, the tested putty exhibited a finer and more uniform grading than the materials prepared by the methods described in Section 4.2.3 (Figure 5.1), and the specimens were reconstituted at void ratios relatively close to the plastic limit. Both factors may have substantially affected the fabric of the material, resulting in a similar compressibility to that indicated by the 1D-NCL, but at much lower void ratios. Whether this compression path would have eventually converged with the proposed 1D-NCL is not known. The behaviour exhibited by the specimen tested by Bialowas (2017) is more intriguing. The evidently higher compressibility may be associated with the presence of larger intact grain agglomerations inherited from the parent material (Clayton 1978). However, this effect did not occur in the experiment by Clayton (1978), also shown in this Figure, which likewise involved chalk putty prepared using an unrestricted grading and exhibited a broadly comparable PSD to that of material ‘B’ (Figure 5.1). Additionally, it may be noted that the putty used by Bialowas (2017) was able to withstand vertical stresses in the order of 200 kPa at a void ratio close to the liquid limit, which is unexpected considering the very limited inter-particle contact at this moisture content. Reasons for this were not identified by the original author.

The compression paths for the 38 mm intact specimens in Figure 4.9 tend towards the reconstituted 1D-NCL, yet the majority remain within the structure permitted space. Vaughan et al. (1988), Clayton and Serratrice (1997) and others suggest that this is due to partial destructration, understood as incomplete bond breakage. However, post-test PSD of initially intact and reconstituted specimens tested at similar initial void ratios and to the same maximum σ'_V are compared in Figure 5.5, and only minor differences are noticeable. Yet, the unload-reload stress probe in Figure 4.9 crosses the 1D NCL and traverses the structure permitted space until merging (i.e. yielding) with the previous compression path. These observations suggest that:

- Bond breakage during post-yield compression of intact specimens is pervasive enough to cause the material to become effective uncemented.
- Regarding PSD, the reconstituted specimens used were a suitable reference material to investigate the compression behaviour of intact chalk.
- Slow convergence of compression paths with the reconstituted 1D NCL may be associated with the existence of fabric-controlled post-yield ‘intact 1D boundaries’, analogous to the ‘intact isotropic boundaries’ found for calcarenites by Cuccovillo and Coop (1999).

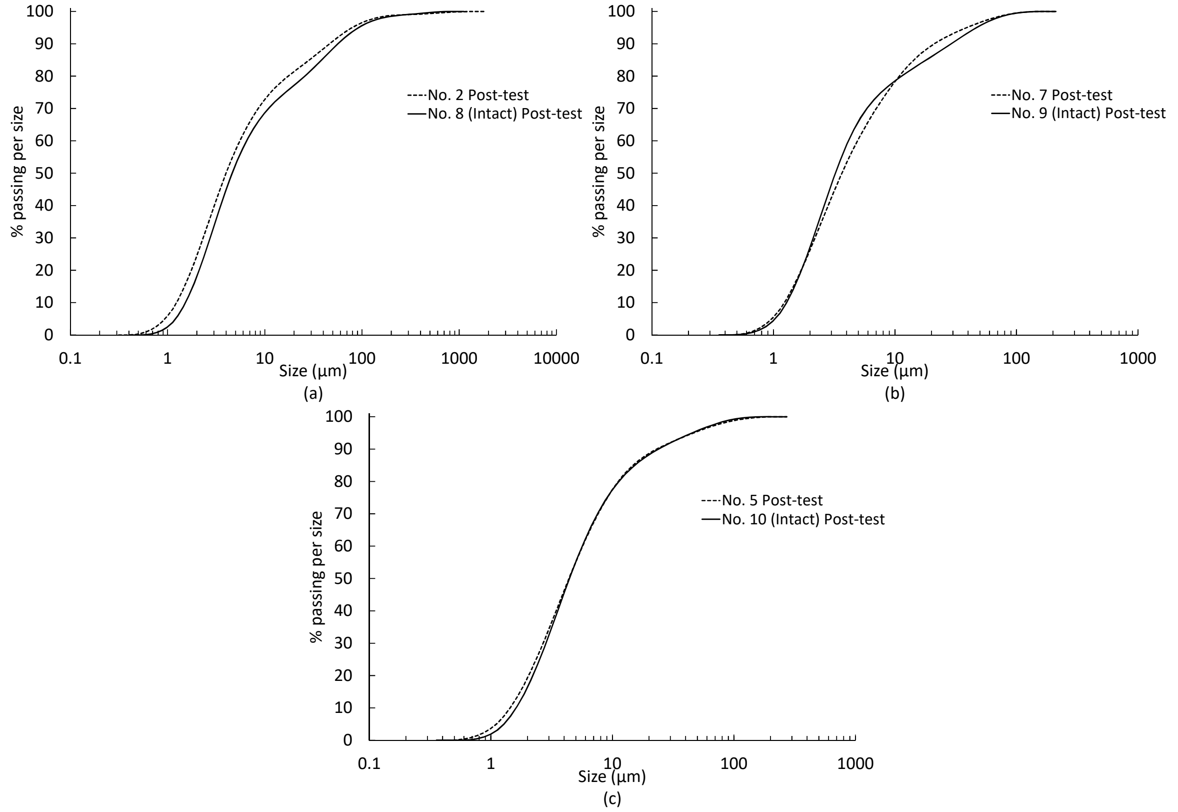

Figure 5.5. Comparison of post-test PSDs from intact and reconstituted specimens of comparable initial void ratio and tested to similar maximum effective stress levels.

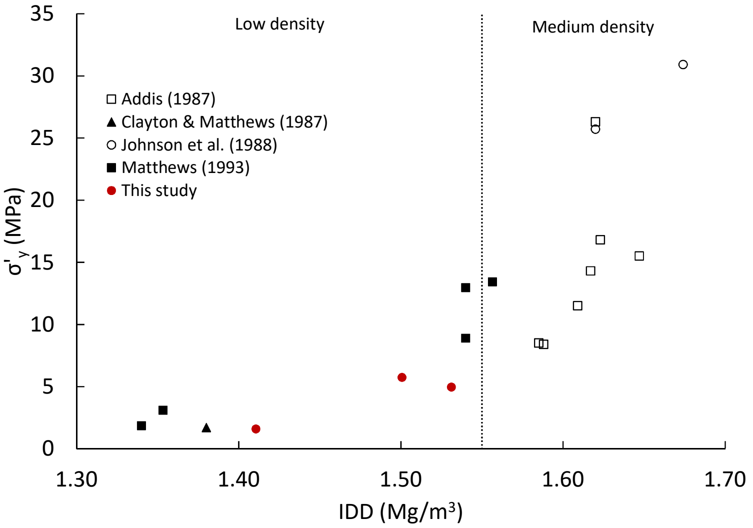

Figure 5.6. Correlation between 1D yield stress of high-$CaCO_3$ content, low-medium density intact chalk and IDD. Includes data from various authors; open and filled markers correspond to triaxial and oedometer test data, respectively.

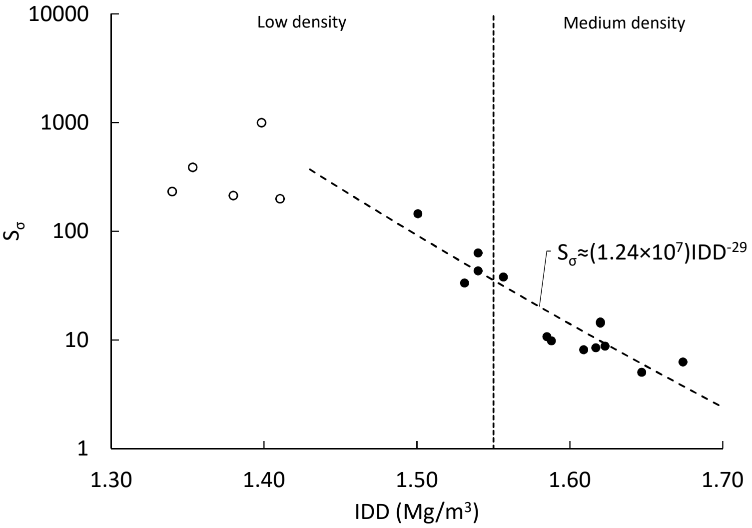

Figure 5.7. Correlation between stress sensitivity (S_σ) and IDD; based on data from Figure 5.6. Open markers refer to S_σ estimations using an equivalent yield stress (σ^*_e) of 8 kPa assuming liquid limit strength conditions.

As for calcarenites, the diversity in intact 1D boundaries is associated with variations in natural fabric characteristics such as local void ratio, particle arrangement and grouping, and inter-particle contacts (Lambe and Whitman 1979; Mitchell and Soga 2005). Based on the behaviour exhibited by Test 9 in Figure 4.9 and by the calcarenites investigated by Cuccovillo and Coop (1999), it is estimated that the compression curves of the 38 mm specimens would have eventually joined the proposed 1D-NCL if they had been subjected to larger stresses.

The macroscopic bond strength of structured chalk may be defined as the maximum capacity of cemented inter-particle contacts to oppose major plastic strains in 1D compression, which amounts to the 1D yield strength in excess to that of the reconstituted material at the same void ratio. 1D yield strengths (σ'_y) for low-medium IDD and high $CaCO_3$ content (>95%) intact chalk derived from data by a number of authors are shown in Figure 5.6, where σ'_y is evidently correlated with IDD, as reported by Leddra (1989). Using σ'_y-e states at yield from this Figure and Eq. (10), macroscopic bond strength can be parameterised as the ratio of the intact yield stress to the yield stress in reconstituted states at the same void ratio (σ'_y/σ^*_e), known as stress sensitivity, S_σ (Cotecchia and Chandler 1997, 2000). The correlation between IDD and S_σ corresponding to the data of Figure 5.6 is presented in Figure 5.7, where liquid limit σ^*_e values of 8 kPa have been used for intact void ratios above the 0.928 intercept of Eq. (10), after Muir Wood (1994). The very high S_σ observed for low IDD chalk indicates that the yield strength of this material is almost entirely accounted for by bond strength. Thus, breakage of cement bonds in low IDD chalk during yield leads to a post-yield fabric with very low 'frictional' strengths, which may be susceptible to collapse upon shearing (Leroueil and Vaughan 1990; Cuccovillo and Coop 1999). In contrast, S_σ

estimations shown in Figure 5.7 evidence that the 'intrinsic' yield strength σ^*_e logarithmically approaches σ'_y as IDD rises to ≈1.70 Mg/m^3. This indicates that the frictional strength of intact chalk rises more rapidly with increasing density than bond strength, as observed in cemented sands (Cuccovillo and Coop 1999).

5.2.3 Shearing behaviour of destructured chalk

The proposed ϕ'_c = 33.7° is well within the range of 30-35° quoted in the works of Clayton (1978), Razoaki (2000), Bundy (2013), Doughty (2016), Bialowas (2017) and others (e.g. Figure 2.10). As in these previous works and for many sands, shearing behaviour appears to be substantially affected by pre-shear density. Specimens reconstituted at states 'loose' of the proposed CSL (in ln p' - *e* space) predominantly exhibited contractive behaviours upon shearing (Tests 6, 8 and 9 in Figure 4.11 and Figure 4.12), developing positive pore water pressures (*u*). Conversely, dilative behaviours were encountered in dense-of-critical specimens (Tests 1, 2, 4 and 10 in Figure 4.11 and Figure 4.12), with negative *u* developments being predominant.

The suitability of the parallel 1D-NCL and CSL curves to characterise the compression and shear behaviour of chalk putty suggests that the mechanical performance of the material is not fundamentally different to that of monomineralic uniform sands (e.g. Been et al., 1991; Coop & Lee, 1993; Verdugo & Ishihara, 1996), as discussed previously in Section 5.2.2. Thus, as in compression, grain abrasion and breakage are expected to be important mechanisms during shear (Coop 1990; Coop and Lee 1993). However, these processes are associated with particle size and geometry (Altuhafi et al. 2016). Therefore, it is unlikely that crushed chalks produced from high-very high IDD rocks or from materials containing important amounts of non-calcite minerals will share the same CSL, because the particle shapes and size distribution of these materials are anticipated to be different to those of the tested putties (as discussed in Section 5.2.1 and in Section 5.2.2). Conversely, the similar grading, grain shapes and mineralogy that emerge from comparable diagenesis (Clayton 1983) suggests that chalk putties created from intact chalk in the low-medium IDD range should share the same CSL. To examine this, triaxial test data by Clayton (1978), Doughty (2016) and Bialowas (2017) (Section 2.5.5.1) have been plotted in Figure 5.8 alongside the results presented in Section 4.3.3.2. Data by Razoaki (2000) and Bundy (2013) have been omitted due to difficulties in interpreting their results, as it would be unrealistic to expect that globally uniform deformation occurred in tests performed from initial states close to or denser than the plastic limit. Additionally, ultimate state void ratios in the dataset by Doughty (2016) in Figure 5.8 correspond to those recorded upon specimen removal by the same author, which was felt to better reflect the global void ratio during shear. Sample details are given in Table 2.1.

Correspondence between the proposed CSL with ultimate states in p' – *e* space from the independent data is evident in Figure 5.8. The proposed CSL seems to better describe the data than the alternatives proposed by other authors (compare with Figure 2.14). It is apparent that the underlying phenomena that controls the ultimate strength-volumetric state relationship of chalk putty are not substantially affected by the procedure used to crush the chalk or the natural variability of the parent low-medium density rock. This is probably because, as discussed above, low-medium density White Chalk fines exhibit very limited differences in particle shapes and size distribution, and this fine fraction controls the mechanical performance of crushed chalk when it accounts for at least 20% of its dry weight according to Puig (1973) and Rat and Schaeffner (1990). Nonetheless, it must be underscored that high-$CaCO_3$ content partially destructured low-medium density White Chalk containing mostly coarse particles, which differ in size and shape from the coccoliths and calcite plates constituting chalk putty, might exhibit different critical state behaviour.

With regards to the role of time-based changes in mechanical performance, Figure 4.10 and Figure 4.11 present results for Tests 6 and 9 which were sheared at broadly similar void ratios, but aged for 13 and 3.6 days, respectively. Comparable ultimate strengths consistent with the CSL are evident, regardless of whether the pre-shear volumetric states were attained by prolonged ageing or by subjecting an initially denser specimen to a shorter consolidation stage under the same effective stress. These Figures also include results from Tests 4 and 7 which experienced much shorter ageing periods. These tests were conducted at broadly similar void ratios as Tests 6 and 9, but experienced different pre-shear effective stresses, resulting in distinct ψ values at the commencement of shear. Test 4, initially exhibiting $\psi = -0.027$, predominantly dilated after yielding. In contrast, Test 7 with initial $\psi = 0.003$ generated substantial positive *u* before undergoing phase transformation and softening towards the CSL, in a comparable manner to Tests 6 and 9. Again, differences in stress history have no noticeable effect on ultimate conditions in volumetric space, as these are chiefly dependent on the pre-shear void ratio. Similar behaviour is observed using independent data from Doughty (2016) and Bialowas (2017), shown in Figure 5.9. This Figure denotes once more that ultimate states are not affected even by several weeks of drained ageing and considerably different pre-shear p' levels and are instead dependent on the pre-shear void ratio of the material. It is also evident from Figure 4.10a and Figure 5.9 that ageing does not alter the critical state angle of friction.

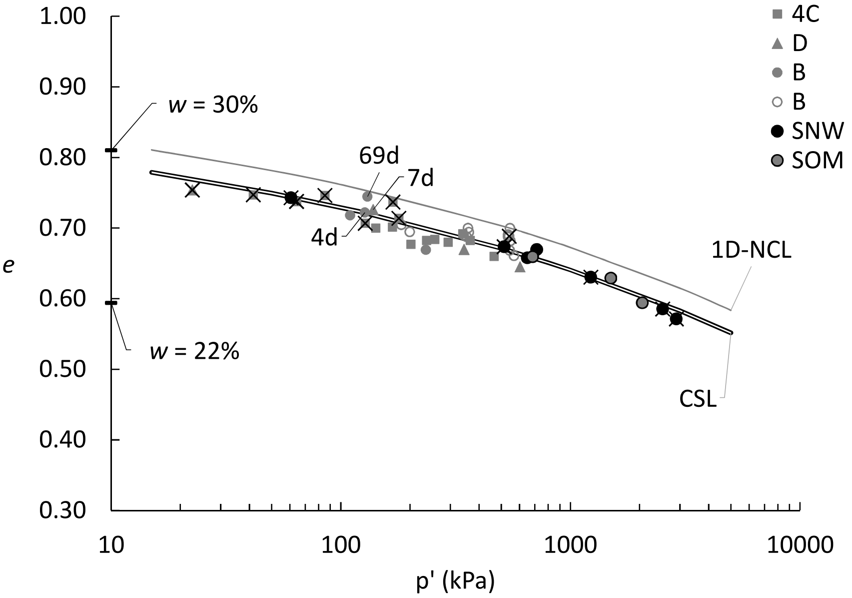

Figure 5.8. Comparison of ultimate states from triaxial experiments by various authors (Table 2.1) and the results presented in Section 4.3.3.2. Open and filled markers denote drained and undrained test data, respectively; crossed markers refer to short-term conditions.

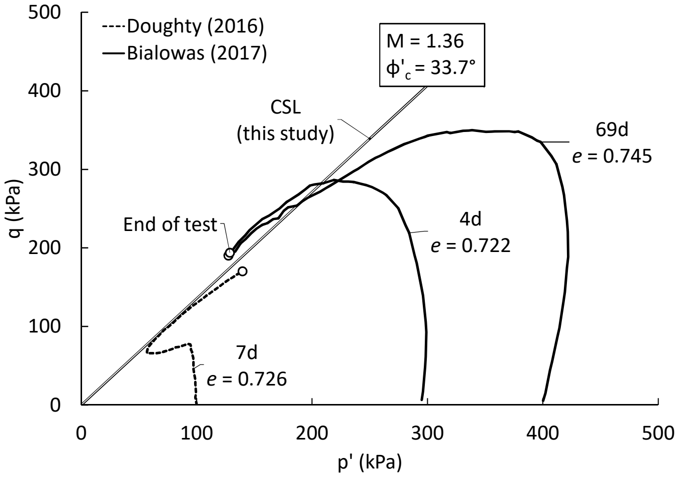

Figure 5.9. Undrained triaxial test data from Doughty (2016) and Bialowas (2017) after various ageing periods.

These observations are congruent with Figure 5.8, which includes results from drained and undrained triaxial experiments involving various ageing periods and does not support the notion that ageing changes the location of the CSL and, therefore, the intrinsic strength of destructured chalk at large strains. To explain improvements in chalk putty strength associated with ageing, Figure 5.10a presents the volumetric compression path of Test 6, where reductions in void ratio whilst ageing at constant p’ are evident. These void ratio reductions can be associated with an increment of the equivalent p’ on the CSL at current void ratio (p'_c) of over 100%, which may be linked with a similar increase in strength. Figure 5.10b (secondary axis) shows that a significant portion of p'$_c$ increments in the time domain occur when the reduction in void ratio becomes approximately linear with the logarithm of time, interpreted as secondary compression (Mesri 1973). Secondary compression is not associated with pore pressure dissipation and is therefore compatible with the zero-pore pressure change conditions applied to the specimen during and after the ramping of p' in the pre-shear consolidation stage. It may be thus proposed that volumetric strains occurring during and after the end of primary compression result in an increment in ultimate strength compatible with the increase in density and that these strains are potentially the fundamental cause of the ageing or long-term behaviour of destructured chalk.

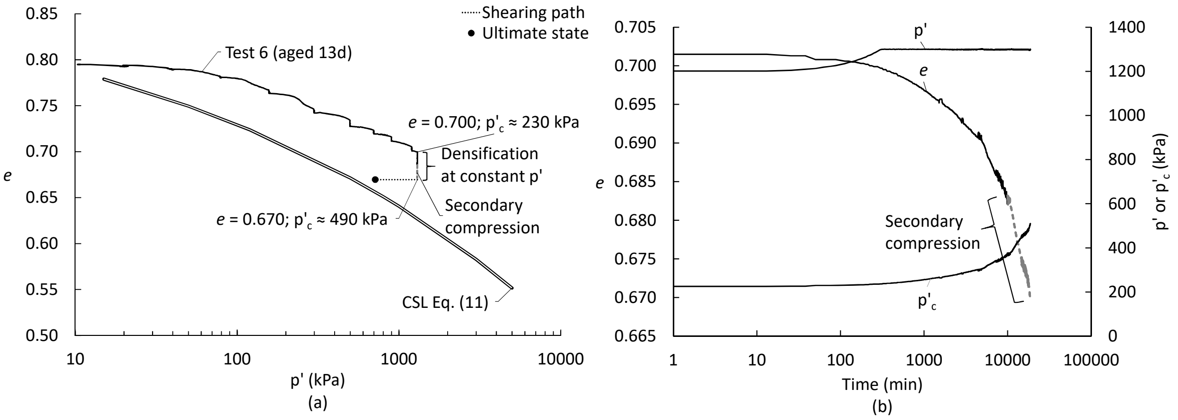

Figure 5.10. (a) Volumetric compression path for Test 6; (b) Time-based decrease in *e* and increase in p'$_c$ during final p' ramp and ageing period (see text).

5.3 Critical state framework for interface friction

5.3.1 Destructured chalk interface performance in monotonic shear

The role of the pre-shear s' – *e* state relative to the CSL in the mobilisation of ultimate τ_y during DSS testing is evident in both Figure 4.17 and Figure 4.18. As mentioned previously, overconsolidated Tests 4 and 5, which were dense of critical before shearing, exhibited notable increases in σ'_y and mobilised large post-yield peak τ_y values just as interface failure by sliding took place before reaching the CSL. All other tests, which were normally consolidated and loose of critical, exhibited substantial effective stress reductions and mobilised τ_y values that were smaller than those attained at yield. Additional evidence of state-controlled interface strength is given by Tests 1 and 7, which were normally consolidated to the same maximum σ'_y but were prepared at different initial void ratios, and Tests 7 and 10, which were normally consolidated to different maximum σ'_y but exhibited similar pre-shear void ratios. It may be noted that, specimen 7 mobilised larger τ_y than looser specimen 1, whereas specimens 7 and 10 developed broadly similar ultimate τ_y magnitudes. This is consistent with the critical state framework presented in Section 4.3 and discussed in Section 5.2. Thus, DSS results convey that denser chalk putty interfaces mobilise larger interface strengths and that this tendency may be quantified using the CSL. The magnitude of τ_y appears to be linked to σ'_y and consolidation history only to the degree that volumetric strains are associated with current and past σ'_y levels.

Test results show that $\tan\delta'_{ult} \approx \sin\phi'_c$ (0.554 ≈ 0.555), which satisfies eq. (31) in Appendix C. Therefore, it can be proposed that τ_y and MIT invariant t(=[σ'_1-σ'_3]/2) are numerically similar at critical state conditions, which entails that $\tau_y \approx s'(\sin\phi'_c)$ during such conditions and that mode of failure b in Figure C1 of Appendix C may be adequate for the present case. The magnitude of s' at the critical state may be derived from the CSL (Eq. (12)), thus obtaining a general expression to estimate the ultimate strength of chalk putty interfaces in simple shear:

$$\tau_y \approx (s'_{ref}\sin\phi'_c)\left(\frac{e-0.895}{-0.068}\right)^{1/0.186} \tag{16}$$

where τ_y may also be found to be numerically equivalent to the undrained shear strength (τ_u).

Eq. (16) provides means to estimate the shear strength of chalk putty interfaces based on the fundamental mechanical behaviour of chalk and delivers scientific underpinning to the notion that density is the key parameter controlling ultimate chalk putty interface friction, as hypothesised by Hobbs and Atkinson (1993) and Lord et al. (1994) regarding the pile-chalk annulus (Section 3.3.2.1).

However, it is important to recognise the greater scatter between ultimate states and the CSL in Figure 4.18 compared with the triaxial test results presented in Figure 4.11. Though there are previous experiences in the use of the DSS test to determine the CSL in volumetric space (e.g. Stroud, 1971) the estimation of the in-test void ratio is less straightforward than in the triaxial test. This is because the precise specimen saturation levels are unknown, volume change is difficult to track with mm^3-accuracy and apparatus disassembly might entail considerable specimen disturbance (which could lead to variability in post-test moisture content measurements and, thus, void ratio calculations). Considering the relatively shallow slope of the CSL in volumetric space, small errors in void ratio may result in significant inaccuracies in the estimated τ_y. Additionally, monotonic shearing is unlikely to realistically represent loading conditions of the chalk putty annulus, either during installation or service loading.

5.3.2 Destructured chalk interface performance in cyclic shear

The performance of chalk putty in CSS testing is in some ways comparable with the behaviour often described for sands, exhibiting cyclic liquefaction or cyclic mobility during failure as detailed in Section 2.5.5.2. In the latter, phase transformation precedes the dilative response of the specimen that prevents a complete loss of strength. This is exhibited as a kink on the stress path graphs of Figure 4.20a and Figure 4.21a, and is congruent with the performance observed during DSS testing (observe, for example, the stress path and $\tau_y - \gamma$ curve for Test 3 in Figure 4.17).

It was stated in Section 2.5.5.2 that effective stress reductions during cyclic loading were associated with plastic straining. Thus, the ratio of the shear stress imposed during cyclic shearing ($\tau_{\mathrm{cyc}} + \tau_{\mathrm{m}}$) to the yield shear stress is thought to be directly related to the rate at which pore pressure develops during shearing. It was also stated that the magnitude of the yield stress is related to the volumetric state (and thus compression history) and fabric of the material, but that the latter was difficult to quantify. Therefore, and in contrast with monotonic behaviour, the cyclic stability of chalk putty interfaces may not be uniquely dependent on material density. This is evident in Figure 5.11, which presents the pre-shear states of all CSS tests. Stable Tests C3, C4 and C6 are not those exhibiting the lowest void ratio or the most negative value of state parameter (which is a measure of how dense of critical the pre-shear state was). This also means that the use of the undrained shear strength as sole reference parameter for cyclic stability assessment, as sometimes done for clays (e.g. Andersen 2009), would be ill-conditioned.

Considering that stiffness and yield strength are correlated with both void ratio and effective stress levels, a common method for the assessment of the undrained cyclic behaviour of sands from element tests is to graphically correlate the cyclic resistance stress ratio ($\tau_{\mathrm{cyc}} + \tau_{\mathrm{m}}$)/ σ'_{y0} with the number of cycles to failure (N_f) for each experiment, while indicating the density or state parameter of the specimens (see e.g. De Alba et al. 1978), as presented in in Figure 5.12a. Though the dataset is small, cyclic resistance stress ratios (CRRs) for a determined number of cycles to failure may be determined from this Figure, as proposed by e.g. Jefferies and Been (2016). The CRRs corresponding to 1000 cycles (CRR_{1000}) have been highlighted in Figure 5.12a. This number of load cycles represents the boundary between ‘metastable’ and ‘stable’ performance of piles under cyclic axial loads, as defined by Tsuha et al. (2012). Thus, a CRR_{1000} vs ψ chart that correlates cyclic stability of the chalk putty interface with the stresses imposed and state of the material may be produced, as presented in Figure 5.12b. The same CRR analysis has been applied to CSS test data on Fraser River Sand (FRS; alluvial sand) and Quiou Sand (QS; carbonate sand), as reported by Jefferies and Been (2016) and Porcino et al. (2008), respectively. For the latter, the CSL for QS proposed by Golightly (1988) has been used. This analysis reveals two notable aspects of the performance of chalk putty interfaces in CSS:

- Chalk putty interfaces are susceptible to cyclic instability in conditions wet of the CSL, even under very low CRRs (<0.05). Thus, it may be proposed that the chalk putty annulus around a pile might exhibit cyclic instability during driving-induced cyclic loading, when the putty forming the annulus is anticipated to be at high void ratios close to or wet of the CSL in low-medium density Chalk formations. This would explain the very low shaft frictions during pile driving in chalk reported by e.g. Ciavaglia et al. (2017a) and Buckley et al. (2018b).
- Chalk putty interfaces seem to remain stable at larger CRR and looser conditions than interfaces formed by the two sands with which they were compared. This may be associated with the fine-grained and low plasticity characteristics of chalk putty (Boulanger and Idriss 2006). Thus, though chalk putty interfaces are clearly susceptible to cyclic instability, this susceptibility may be inferior to that of some sands.

An important limitation of this characterisation approach, in addition to the relatively small number of experiments involved, is that it disregards the role of fabric. As discussed by Coop (1990) concerning carbonate sands, virgin compression or unloading from a higher stress (i.e., overconsolidation) state may deliver the exact same effective stress-void ratio state for specimens reconstituted at different initial void ratios. However, this results in differences in fabric and a significantly larger shear stiffness in the overconsolidated case (Coop and Jovičić 1999). In turn, this may be associated with the capacity to withstand larger cyclic stress ratios without developing pore pressures than in virgin compressed conditions at the same state parameter ψ. Further investigations may be required to fully assess the influence of stress history-induced fabric on the cyclic shearing performance of chalk putty.

As a final note on the topic of the role of fabric on CSS performance of chalk putty, overconsolidated stable Test C4 (Figure 4.22) is especially noteworthy because σ'_{y} levels are observed to increase with the number of loading cycles, suggesting negative pore pressure developments. However, cyclic loading did not produce significant shear strains, and it is uncertain that dilatancy resulting from plastic deformation was responsible for these gains in σ'_{y}. A similar response has been reported in overconsolidated undrained cyclic triaxial tests on sand (Aghakouchak et al. 2015) and in calibration chamber instrumented pile tests in which stable behaviour was observed (Tsuha et al. 2012; Rimoy 2013)[4]. Tsuha et al. (2012) attributes this

---

[4] These tests were not performed whilst enforcing constant volume conditions.

behaviour to the development of an “optimal soil fabric that enhances dilation during cyclic loading”, which may be interpreted as a form of small strain (non-linear elastic) kinematic hardening (Jardine 1992).

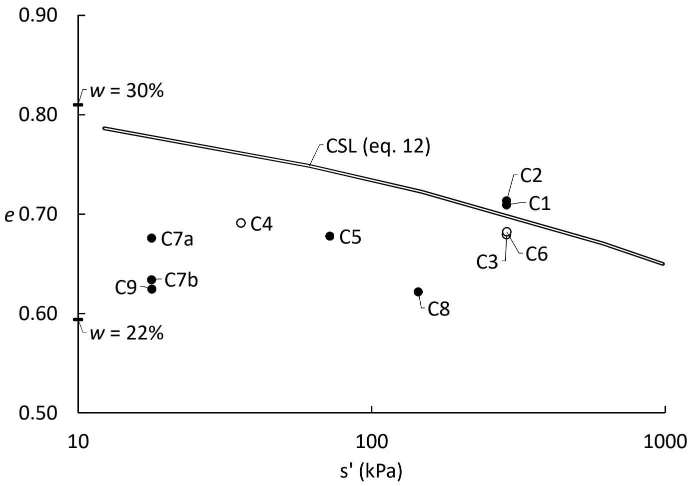

Figure 5.11. Initial states in volumetric space for CSS tests (Table 4.5). Filled markers correspond to tests that exhibited cyclic instability.

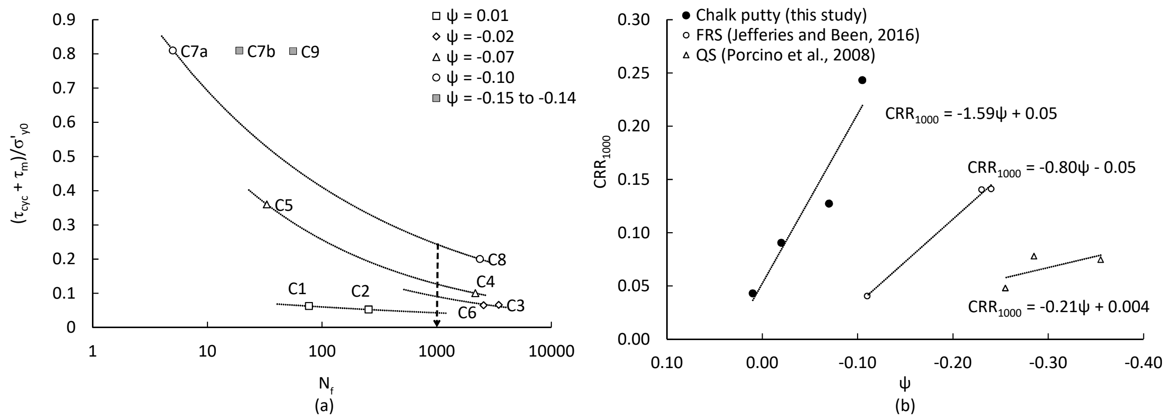

Figure 5.12. (a) Cyclic stress ratio and number of cycles to failure from CSS tests on chalk putty (Table 4.5); (b) cyclic stress ratio to produce failure before 1000 cycles and state parameter.

5.4 Application of critical state framework to scaled experiments

5.4.1 Commentary on XCT-derived void ratios

It has been proposed in Section 4.5.7.2 that void ratio values may be retrieved from the XCT data. Such quantification approach for the density of the remoulded annulus region in contact with the pile surface suggests very low void ratios, as shown in Figure 4.41. This is qualitatively supported by SEM images (Figure 4.45). However, whether these void ratio values reflect true physical conditions is difficult to corroborate with absolute certainty. An important consequence of the polychromatic nature of the cone beam used during XCT is that the assumption of a linear correlation between x-ray attenuation and bulk density may not be fully accurate (Section 4.5.1). Given the relatively gentle slope in ln p' – *e* space of the proposed CSL for destructured chalk, small errors in void ratio may involve significant inaccuracies in the estimated critical strength of the material. Therefore, alternative methods to derive annulus void ratios from XCT data are proposed in this Section to explore potential divergences from the results obtained using the procedure described in Section 4.5.7.2 (labelled hereafter as the 'original' method):

- Alternative 1 (A1). Average annulus grey values of each XY slice in the cropped but uncorrected 3D images are normalised by the average value in the IDD sampling region of the same slice. Then, as in Section 4.5.7.2, these grey value proportions are assumed to be bulk density ratios, and Eq. (14) is applied to estimate annulus void ratios.
- Alternative 2 (A2). Average annulus grey values of each XY slice in the cropped but uncorrected digital volumes are normalised by the average grey value of the mini pile in the same slice. Annulus void ratios are derived by applying Eq. (14) and using the average measured pile bulk density (1.22 and 1.30 Mg/m^3 for Perspex and PEEK, respectively), assuming that grey value proportions approximate bulk density ratios as before.
- Alternative 3 (A3). The average bulk density of water in fractures and macropores (1.0 Mg/m^3), thermoplastic pile, undisturbed chalk (Table 4.6) and crystallised fossils (2.7 Mg/m^3) were paired with the average grey scale values for these materials in the corrected digital volumes. A regression line was fitted to this data to obtain a grey scale-bulk density function (Figure 5.13) to interpolate density data from specimen regions for which only the grey scale was known (e.g. the annulus). A similar approach was first explored by Mull (1984) and has been used in geomechanics research by e.g. Desrues (2004), Louis et al. (2007), Otter (2011) and others.

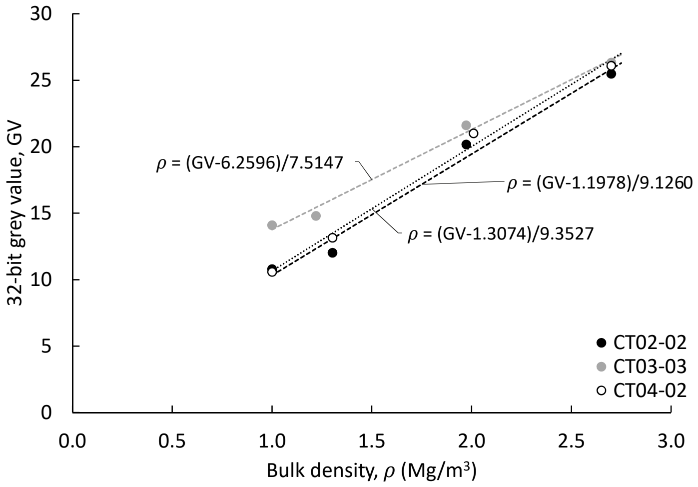

Figure 5.13. Grey value-bulk density calibration functions using voxels containing water, Perspex or PEEK, intact chalk and crystallised fossils (calcite).

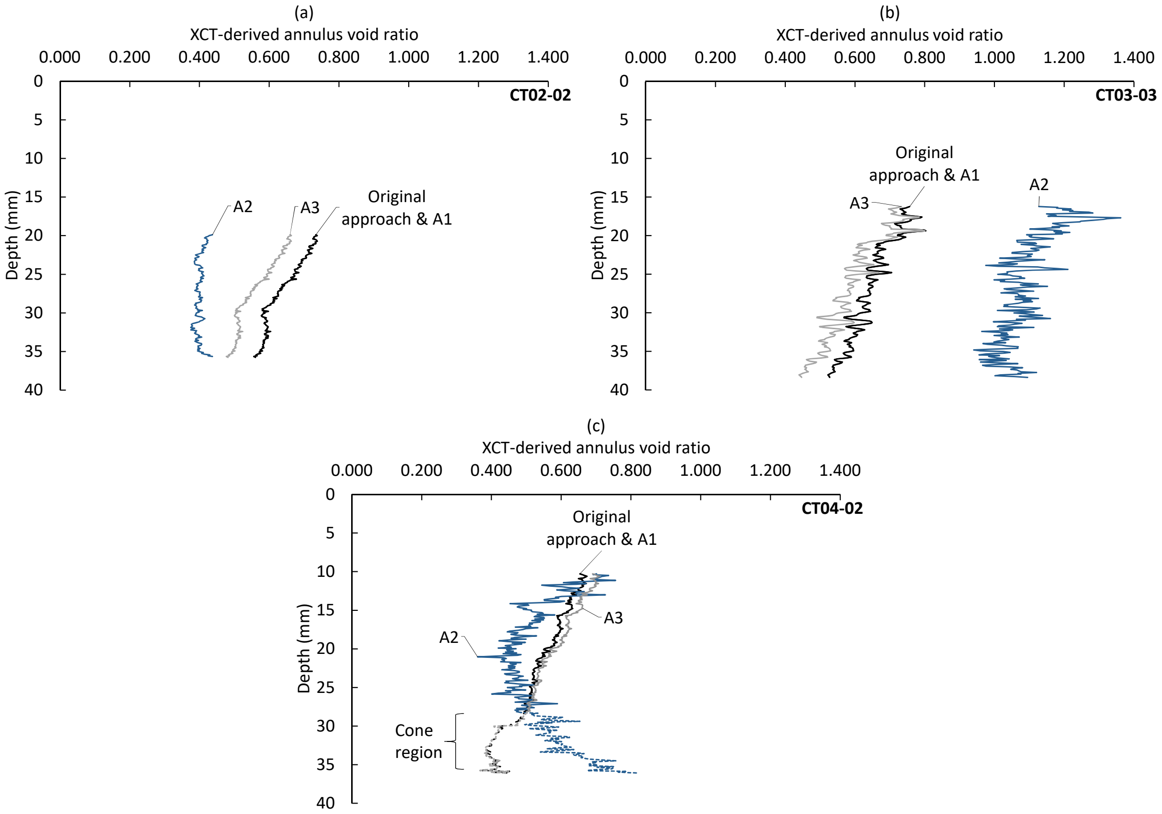

Figure 5.14. XCT-derived average annulus void ratios in voxels adjacent to the pile shaft using four data processing techniques (see text).

Figure 5.14 reports the outcome of this exercise. No differences between method A1 and the original approach are observed, indicating that that the data conditioning procedures described in Section 4.5.4.3 did not introduce any relevant variability in the XCT-derived annulus void ratio. Void ratios estimated using A2 can be considerably different than the those derived by the original and the other alternative methods. This results from the low total mass attenuation coefficients (μ/ρ) of PEEK and Perspex resulting from their low effective atomic numbers. At effective photon energies above 50 keV, the μ/ρ of PEEK and Perspex are approximately 0.25 cm^2/g and 0.26 cm^2/g (Birnbacher et al. 2018). For comparison, water exhibits $\mu/\rho \approx 0.31$ cm^2/g despite being considerably less dense than both thermoplastics. Such characteristics affect the assumption of a linear correlation between grey values and density, as noted in the slight disparity in the thermoplastic material datapoints of Figure 5.13. In other words, due to the high x-ray transparency of Perspex and PEEK at high energies, grey value data for the thermoplastic phase suggest densities that are lower than the physical value, which alters XCT-derived void ratio magnitudes using method A2. This effect is also present for method A3, because the calibration function is affected by it. Such issues are not expected to occur with A1 and the original procedure, because both destructured and intact chalk exhibit the same effective atomic number. Therefore, variations in μ/ρ and in grey value should correspond to physical differences in bulk density (ρ).

Considering the above and to be able to proceed with the present analysis, XCT-derived void ratios by the method described in Section 4.5.7.2 have been preliminarily assumed to reflect physical conditions to acceptable accuracy.

5.4.2 Model pile penetration mechanisms and compatibility with critical state framework

Figure 4.39a and Figure 4.39c convey that the PL piles used in CT02 and CT04 crushed and densified the chalk producing a bulb of dense putty ahead of the tip and the annulus feature behind it. The densified chalk putty bulb is analogous to the nose-cone feature described by White and Bolton (2002, 2004) pertaining model piles installed in sand and discussed in Section 3.2.1. This feature seemed to increase in size during penetration, which is evidenced by annulus thickness measurements (t_a) shown in Figure 5.15. In this Figure, distances from the pile tip (h) and t_a have been normalised by the equivalent pile radius R* defined in Table 3.1. The underlying cause for this depth-based increase in annulus density and thickness is postulated to be that the rigid chalk neighbouring the crushing zone constrained flow and displacement of chalk putty. Therefore, greater volumes of chalk were crushed and densified as penetration progressed, to be able to accommodate both the pile and the crushed chalk, as hypothesised by Hobbs and Atkinson (1993) (Section 3.3).

Chalk crushing and densification was accompanied by fracturing of both specimens involving PL piles (Figure 4.39a and Figure 4.39c). The longest fracture was approximately aligned with the pile axis, forming a sub-vertical discontinuity along the height of the chalk cylinder. This promoted lateral movement of intact chalk blocks, evidenced by the large circumferential strains reported in Figure 4.38b (compared with the smaller strains of fracture-free CT03). Additional cracks were created at an approximately perpendicular direction from the pile shaft. These fractures were believed to be prompted by the inclined penetration of the pile tip whilst the pile head remained horizontally fixed, thus producing a lever-arm mechanism, schematically shown in Figure 5.16a. The lateral action of the deflected pile and the Perspex confinement might have produced tensile failure in the upward direction as represented in this Figure. To further examine this, a preliminary test performed whilst tuning the XCT methodology was re-assessed. In this experiment (labelled CT01), a flat-tipped closed-ended cylindrical Duralumin pile was inserted in an intact chalk core of similar characteristics as those described in Table 4.6. The substantially stiffer nature of Duralumin resulted in the pile entering the chalk almost vertically. Though the scan settings had not yet been refined to produce images of sufficient quality to be able to quantify local grey value variability, the reconstructed volumes clearly depict the fracture network resulting from pile insertion, shown in Figure 5.16b. Sub-horizontal fractures are largely absent in this Figure, supporting the proposition that pile buckling was likely responsible for their origin in CT02 and CT04.

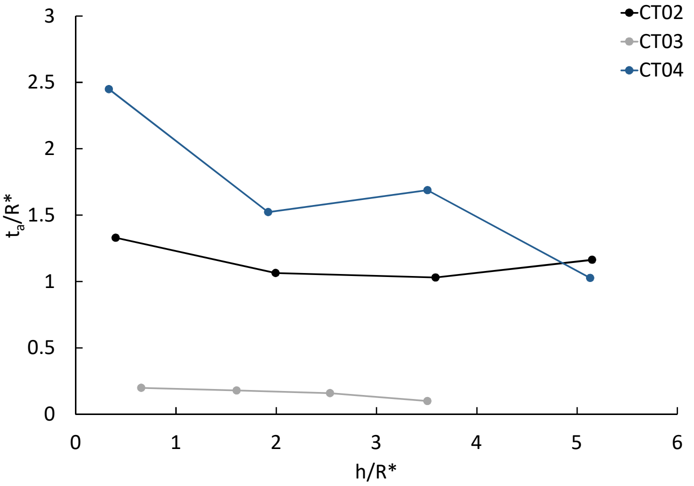

Figure 5.15. Correlation between annulus thickness (t_a) and distance from the pile tip (h).

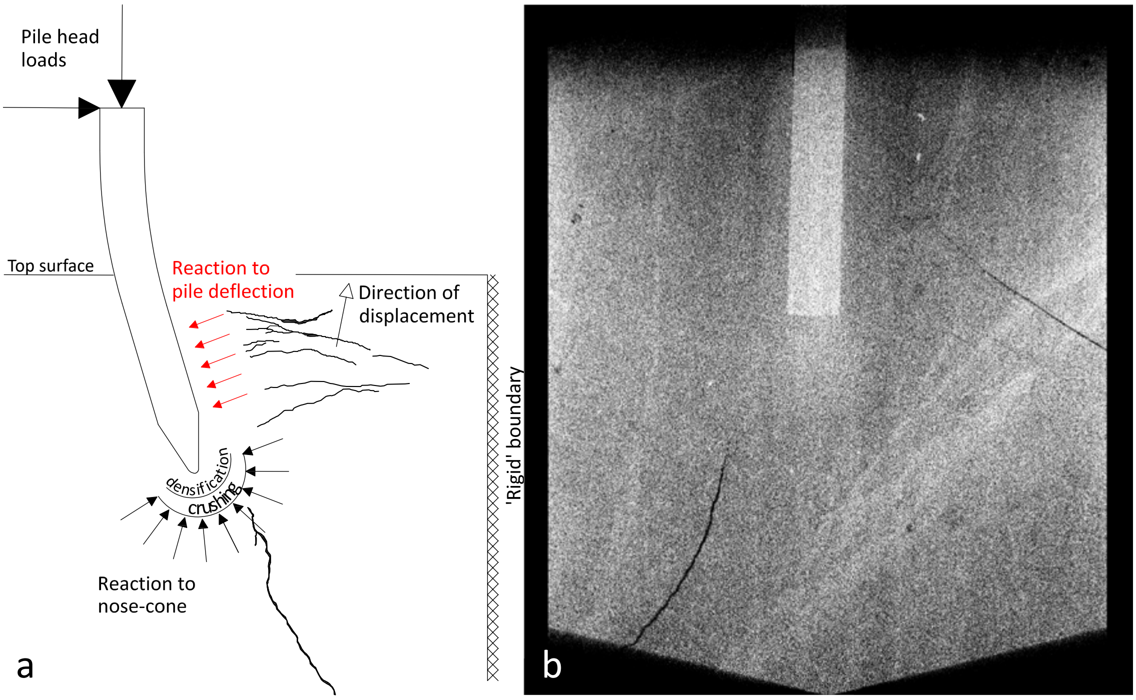

Figure 5.16. (a) Schematic of pile deflection during penetration (based on Figure 4.39c); (b) YZ slice of preliminary test CT01 (see text).

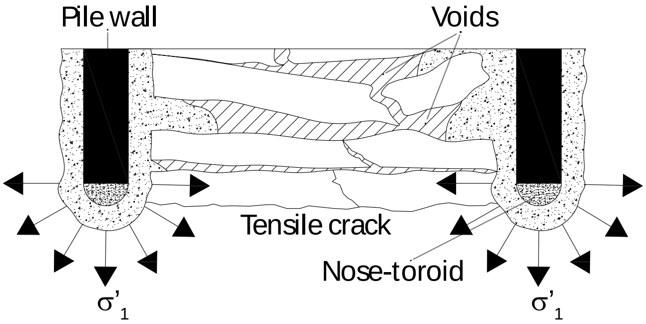

Figure 5.17. Schematic vertical cross-section view of the radial compression of chalk entering the PS pile.

With regards to CT03 (Figure 4.39b), the model PS pile puttified the chalk under the flat rim, partially displaced part of the putty into the pile aperture and cored into the specimen. This may have prevented specimen-wide fracturing. However, chalk became fragmented as it entered the tube pile inner volume, creating a plug composed by a mixture of chalk putty and elongated cemented chalk fragments. Substantial gaps may be noted between the chalk splinters in Figure 4.39b, though the zones closest to the internal pile wall are seen to be mostly infilled with chalk putty. It is conjectured that the half-toroid-shaped region of densified chalk ('nose-toroid') beneath the pile rim laterally compressed the cemented chalk enclosed by this feature, eventually leading to tensile failure in the vertical direction, as schematically shown in Figure 5.17. This behaviour agrees with the reversal from compressive to extensive loading condition imposed on soil entering a thin-walled sampling tube reported by Baligh (1985). Unequal displacement of some of the chalk fragments caused them to tilt as they entered the pile, eventually experiencing flexural loading and breaking up. Both tensile and flexural fracturing led to stress relaxation, facilitating the displacement of plug material as penetration progressed. These fracture-induced stress reductions are evidenced by the serrated pile head stress-displacement and circumferential strain profiles recorded during the installation of this pile (Figure 4.38). The displacement of chalk putty and intact fragments through the PS pile resulted in the restriction of all structural changes in the chalk to the outer boundaries of the annulus (Figure 4.39b), which was proportionally thinner than that of the PL piles and did not substantially change in thickness with penetration depth (Figure 5.15)

Changes in interface density with penetration depth can be assessed using grey value data sampled across horizontal paths perpendicular to the pile shaft at varying depths, as shown in Figure 5.18. These values have been calibrated to void ratios as described in Section 4.5.7.2, smoothened using a moving average algorithm of kernel size 5 and normalised by the average void ratio in the intact chalk portion of the profile. Distinction is made in this Figure between the intact (dotted lines) and annulus (continuous lines) regions of the sampled profiles. This Figure suggests a moderate predisposition towards lower void ratios with proximity to the pile tip, as qualitatively denoted by SEM micrographs (Figure 4.46).

From the above observations and the results presented in Section 4.5.7, it may be proposed that the penetration mechanisms of the model piles share some similitudes with the processes described for sands and discussed in Section 3.2.1. Specifically:

- A densified chalk putty region equivalent to the ‘nose-cone’ formed ahead of the piles.
- Figure 4.43 does not suggest any significant changes in annulus PSD with embedment depth, which indicates that crushing ceased once the putty moved from the under the tip to the annulus and denotes significant effective stress reductions.
- A densified interface formed around the pile shaft.

Unfortunately, establishing a link between pile head stresses (Figure 4.38a) and XCT-derived pile tip depths and annulus void ratios is not straightforward because the measured pile head displacements include the elastic compression of the pile, pile deflection and localised pile head damage (in the case of CT03). A rudimentary approach may be drawn by assuming for stages 2 and 3 that penetration occurred solely after the end of the ‘reloading’ (or ‘yield limit’) portion of the pile head stress-displacement curves of Figure 4.38a. That is, during the ‘post-yield’ broadly linear increase in pile head stress marked by dotted straight lines in this Figure. It may be also assumed that pile deformation was significant at large stresses but fairly small below a threshold stress of 50% of the compressive strength of the pile material (≈100 MPa for PMMA, Blumenthal et al. 2002; ≈130 MPa for PEEK, Rae et al. 2007). Thus, pile head stresses and displacements below this threshold but above the 'yield limit' of the curves of Figure 4.38a can be approximately linked with pile tip depths. With some additional considerations, detailed below, the pile head stress data of Figure 4.38a within this range may be used to very preliminarily compare applied stresses with XCT-void ratio measurements using cavity expansion theory (Randolph et al. 1979; Yu and Houlsby 1991).

Cylindrical cavity expansion theory applied to piles proposes that σ'_{r} levels experienced by a soil element in the path of the pile during penetration increases as the vertical distance to the tip reduces (Salgado et al. 1997). Maximum levels ($\sigma'_{\mathrm{r\,max}}$) are attained when the element reaches the pile tip shoulder (i.e. when the relative distance to the tip shoulder equals zero; Salgado et al., 1997), and such values are related to the vertical soil resistance to penetration under the tip (σ'_{z}) by (after Jardine et al., 2013b):

$$\sigma'_{\mathrm{r\,max}} = \sigma'_{\mathrm{z}}[\tan(45 - {}^{\phi'}\!/_{2})]^2 \tag{17}$$

σ'_{z} values were not measured during the scaled experiments. However, pile head loads recorded during tension testing (Figure 4.42) arguably suggest that the contribution of shaft friction to the total penetration resistance during jacking might have been relatively small. Assuming that σ'_{z} is broadly similar to the measured pile head stress and that $\phi' = \phi'_c$, local XCT-derived void ratios in the immediate vicinity of the shaft may be plotted versus $\sigma'_{\mathrm{r\,max}}$ as shown in Figure 5.19 for CT02 and CT03. To account for the open-ended condition in the latter, the right-hand side of Eq. (17) has been factored by $\mathrm{A_r}^{\mathrm{b}}$, where $\mathrm{A_r}$ is the effective area ratio described in Section 3.2.1.2 and b is the 'end condition index' for cavity expansion theory defined by White et al. (2005) as:

$$\mathrm{b} = -\frac{1 - \mathrm{K_P}}{2\mathrm{K_P}} \tag{18}$$

where $\mathrm{K_p}$ is the passive earth pressure coefficient calculated as $(1 + \sin\phi')/(1 - \sin\phi')$ and here assumed to equal 3.49 by taking $\phi' = \phi'_c$ as before. Test CT04 has not been assessed in this manner because the severe deflection of the pile during penetration significantly reduces the appropriateness of the pile head stress $\sim\sigma'_{\mathrm{z}}$ assumption.

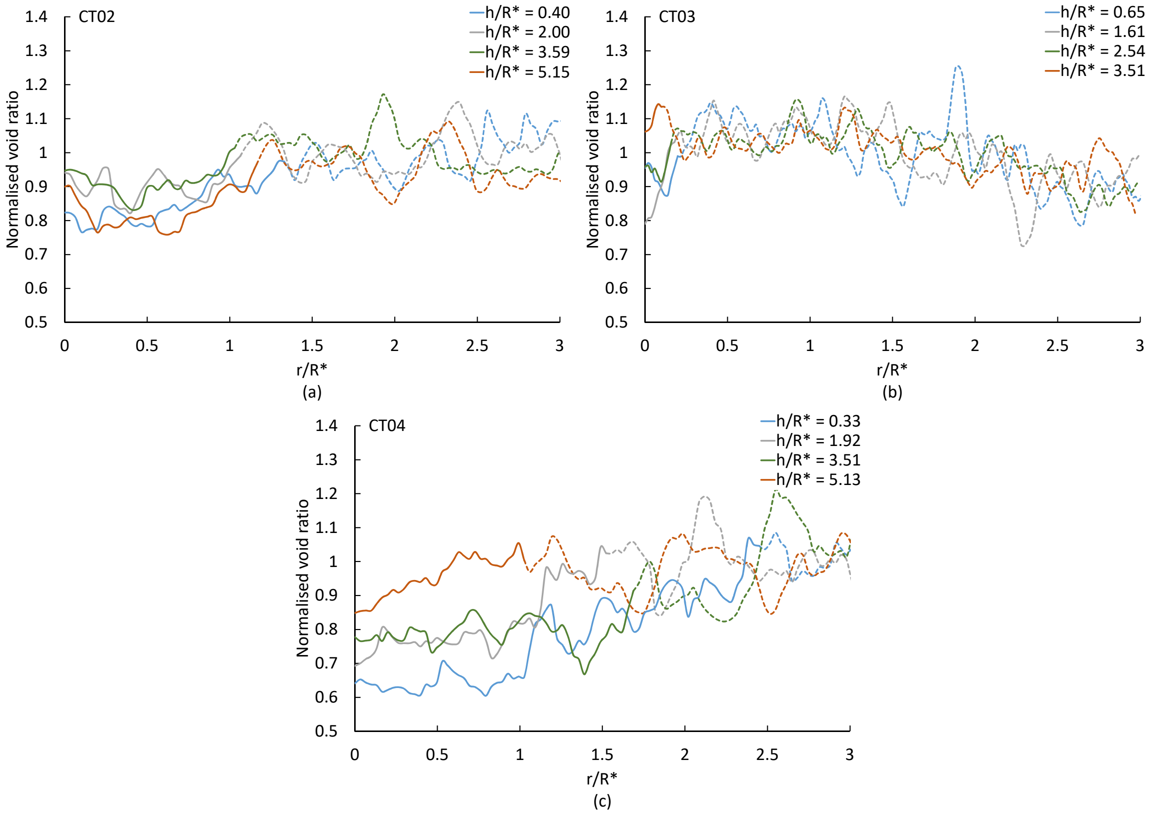

Figure 5.18. XCT-derived normalised void ratios of horizontal sampling paths (perpendicular to the pile shaft) at various depths. Horizontal distances to the pile shaft (r) and vertical distances (h) between the sampling paths and the pile tip shoulder have been normalised by the equivalent pile radius R* (Table 3.1).

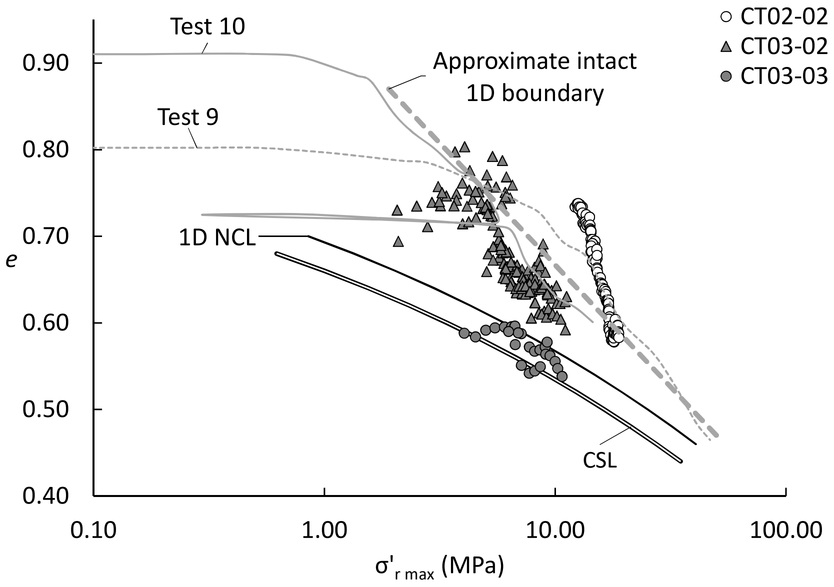

Figure 5.19. Estimated effective radial stress at pile tip depth from cylindrical cavity expansion theory ($\sigma'_{r\,max}$) vs XCT-derived void ratios at said depths (*e*).

$\sigma'_{\mathrm{r\,max}}$ corresponds to σ'_1 during cavity expansion (Salgado et al. 1997) and the limit condition at the cavity wall is the critical state (Collins et al. 1992). Therefore, the CSL (eq. (11)) in terms of σ'_1 is included in Figure 5.19. In this Figure, XCT-derived void ratios and estimated $\sigma'_{\mathrm{r\,max}}$ magnitudes suggest that the annulus material did not reach the CSL in the looser, shallower regions of the feature, but approximately did so for CT03-03 as stresses increased and void ratios reduced. As for cylindrical cavities expanded in other geomaterials (Russell and Khalili 2002; Jiang and Sun 2012), crushing is more limited when the cavity is expanded from high void ratios and relatively low effective stress conditions, like those present at shallow depths. Incomplete destructuration associated with limited crushing restricts the suitability of the CSL of thoroughly destructured chalk (Vaughan 1997), as discussed in Section 5.2. Crushing and volumetric strains increase at higher effective stresses like those occurring at greater depths, and more thorough destructuration apparently results in greater compatibility with the CSL. Such destructuration is probably aided by the unload-reload cycle between stages 2 and 3 of CT03 and the cyclic loading produced by the build-up and relaxation of stresses during fracturing of the material entering the pile.

That said, very modest differences are found between the PSDs along the shaft of CT02 and those of the reference destructured chalks SNW-A and SNW-B (Figure 4.43c), suggesting overall uniform de-cementation. On the other hand, PSD measurements correspond to the entire thickness of the annulus and local variability in grading is a distinct possibility supported by SEM images. In Figure 4.45, a greater presence of sub-micron sized particles may be noted at greater depths (b vs c). Likewise, Figure 4.46 qualitatively exhibits changes in fabric and density with distance from the pile surface (in agreement with XCT-based measurements shown in Figure 5.18). Thus, it is proposed that:

- Pile penetration largely de-cemented the chalk even at shallow depths and low stress levels, but the persistence of the original fabric might have led to incomplete convergence of the effective stress-void ratio state of the annulus material with the CSL for destructured chalk.
- Increments in stress levels with penetration depth (and cyclic loading in CT03) reduced the void ratio while possibly producing local changes in PSD and eliminating remnants of the original fabric, which may be associated with improved convergence of the effective stress-void ratio state of the annulus material with the CSL.

The presence of remnants of the original fabric in the chalk putty as it reaches the pile tip shoulder is proposed to be qualitatively comparable with the persistence of fabric-based post-yield intact boundaries discussed in Section 5.2.2 (Figure 4.9). To exemplify this, the compression paths for initially intact oedometer specimens 9 and 10 and the 1D-NCL have been included in Figure 5.19, where it may be noted that XCT datapoints are inside the structure-permitted space and fairly close to the intact 1D boundary.

Though limited by the very small number of tests, these results preliminarily support the critical state model for pile penetration described in Section 3.3.1.3, where penetration resistance is correlated with Chalk density, its cemented condition, and volumetric compression and/or pore pressure developments. The latter are associated with the rate of penetration. In the present case, it was assumed that these rates were sufficiently low (0.174 mm/min; Section 4.5.3) to achieve fully-drained penetration, which allowed for the pile head stress $\sim\sigma'_{\mathrm{z}}$ assumption required to calculate $\sigma'_{\mathrm{r\,max}}$. However, fully drained conditions are unlikely during pile driving and CPT testing. Drainage, field-scale geometries and the influence of the mass-behaviour of Chalk on pile penetration and the critical state model are further discussed in Section 5.5.

5.4.3 Application of critical state framework to model pile shaft capacity

The application of the critical state framework for interface friction described in Section 5.3 to forecast shaft friction requires knowledge of the void ratio of the chalk putty interface. In the case of the scaled experiments concerning this Thesis, void ratios were derived using the XCT data as detailed in Section 4.5.4, but minding the limitations exposed in Section 5.4.1.

Figure 5.18 shows that annulus void ratios at a given depth are lower than the values for intact chalk, but the former increase with radial distance from the shaft until matching the latter. This tendency is depicted by the micrographs presented in Figure 4.45 and Figure 4.46, where notable differences in particle packing can be observed between parts a and c-d of the latter (see Section 4.5.7.4). This denotes progressively lower disturbances in the chalk structure with increasing distance from the pile centreline. A similar trend has been previously reported at a macroscopic scale by Buckley et al. (2018b) regarding field-sized piles (Figure 3.9; Section 3.3.2). The precise density within these variable radial profiles potentially correlated with unit skin friction is anticipated to correspond to the location where failure occurs within the annulus. Unfortunately, time-constraints impeded the application of XCT scanning after tension testing, but it is possible that the scan resolution would not have permitted the observation of the shear bands associated with interface failure anyway.

Table 5.1. Maximum depths of annulus macroscopic void space in the XCT experiments.

	CT02	CT03	CT04
Step 01	10.388 mm	11.745 mm	11.119 mm
Step 02	15.086 mm	19.575 mm	26.700 mm
Step 03	-	23.437 mm	-

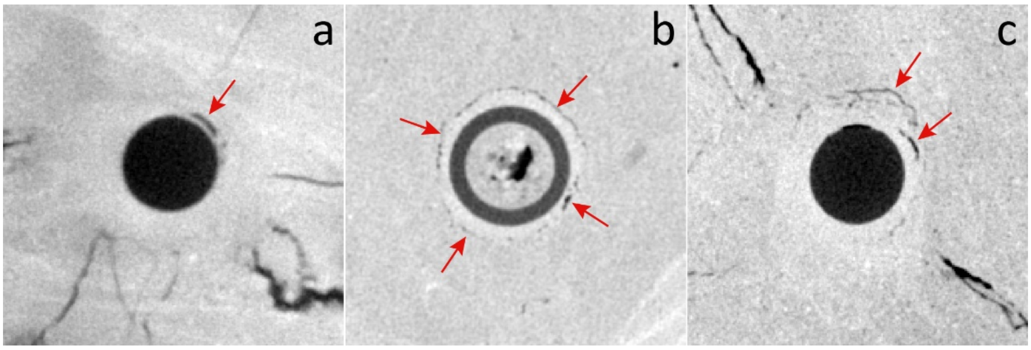

Figure 5.20. XY slices of the XCT volumes showing gaps in the putty chalk interface (marked by arrows): (a) CT02, (b) CT03, (c) CT04.

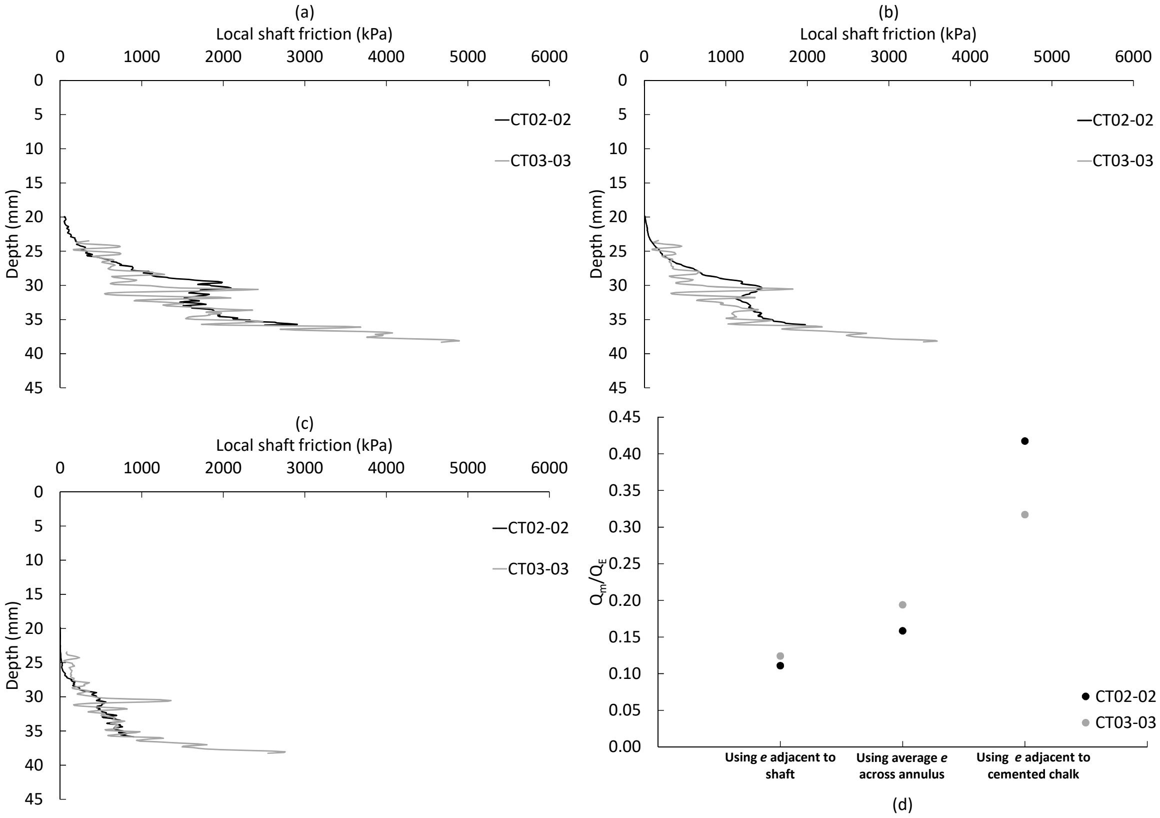

Figure 5.21. Local shaft friction profiles estimated using Eq. (16) and different assumptions for the interface void ratio (a through c; see text), and the comparison between these calculations and measured values (d).

Another notable feature of pile-chalk interface of the scaled tests that hampers the direct application of the critical state framework is the aforementioned development of gaps between the chalk putty annulus and the pile and/or the enclosing cemented chalk (Section 4.5.7.2). Skin friction cannot be transferred through gaps and gaps are anticipated to hamper the development of effective stress increments associated with constrained dilation. Examples of these macroscopic void spaces are shown in Figure 5.20. The mechanisms behind their origin are not well understood. They occur in discontinuous fashion from the specimen top down to variable depths, being present along a generous portion of the embedded shaft. However, gaps are absent in the deeper annulus regions of CT02 and CT03, as presented in Table 5.1. A plausible explanation is that accidental disturbance of the pile between penetration stages might have produced these features. Pile deflection during installation may have contributed to the presence of these gaps as well, in a manner analogous to how the whipping of H-section piles during driving resulted in visible gaps developing between the shaft and the chalk in field tests by Hobbs and Robins (1976). The elastic decompression of the pile whilst unloading from the final installation stage resulted in a decrement in pile cross-section area from the maximum values attained during installation and may have been a further minor contributor to these gaps.

Evidently, the selection of an appropriate void ratio to apply the critical state framework is not straightforward. Three approaches have been explored to obtain a void ratio input for Eq. (16):

- The void ratio profiles shown in Figure 4.41, corresponding to the annulus region in contact with the pile shaft, which is also the densest portion of the annulus (Figure 5.21a).
- Void ratio profiles corresponding to the mean value for each depth across the thickness of the annulus (Figure 5.21b).
- Void ratio profiles corresponding to values adjacent to the cemented chalk enclosing the annulus (Figure 5.21c), which tends to be the loosest region of the feature.

Each of these approaches have been used to estimate total shaft capacities. In all cases it was assumed that no significant shaft friction developed in annulus regions were gaps were present. Figure 5.21a through Figure 5.21c presents the depth-based local shaft friction mobilisation profiles resulting from these calculations. Figure 5.21d compares the total shaft capacity derived for each of these approaches (Q_E) using Eq. (3), normalised by the measured value (Q_m). Clearly, the direct application of the critical state framework (Eq. (16)) overestimates shaft capacity by up to an order of magnitude, depending on the annulus void ratios used in each case. The less inaccurate solution, corresponding to assuming failure along the loosest annulus region (i.e., adjacent to the cemented chalk), predicted capacities that were over 100% larger than the measured values. The analysis concerning CT04 has been omitted due to gaps being present along most of the embedded shaft (down to the cone-tip shoulder) and the model pile being unable to mobilise any resistance to uplift (Figure 4.42).

Three explanations for the apparent incompatibility between the critical state framework for interface friction and the prediction of shaft capacity may be drawn:

1. Considering the low XCT-void ratio measurements and the proposed large effective stress reductions after the passing of the pile tip shoulder (Section 5.4.2), it is possible that the annulus material was considerably dense of critical at the onset of the tension testing stages. This may have precluded the mobilisation of critical state strengths due to strain localisation. A similar performance was observed in heavily overconsolidated DSS Tests 4 and 5 examined in Section 5.3.1. In essence, it is unrealistic to expect that a very dense particle arrangement at initially low effective stress levels will deform homogeneously to large strains during shear whilst exhibiting dilation-induced increases in effective stress of several megapascals until reaching the CSL (see e.g. Desrues and Viggiani 2004 or Desrues and Ando 2015).
2. The estimated shaft friction and shaft capacity values presented in Figure 5.21 were derived assuming constant volume conditions in the annulus during shear, i.e. constant void ratio. Such conditions are possible, in theory, only if the horizontal stiffnesses of the cemented chalk enclosing the annulus and that of the pile are very high. It is unclear if such high stiffness conditions can be provided by Perspex PS pile of CT03 or the intact chalk enclosing it, but they are unlikely in CT02 where the cemented material became fractured during pile installation.
3. The XCT-derived void ratios might not be sufficiently accurate to be used with the highly void ratio-sensitive Eq. (16), as explained in Section 5.4.1.

Furthermore, though the model piles may behave as rigid elements due to their short lengths and the small tension loads involved, ultimate strengths are not expected to be mobilised simultaneously along the entire embedded shaft as assumed whilst generating Figure 5.21d. This is due to the different annulus thicknesses, stiffnesses and strengths involved at each depth. A load-transfer analysis, using the procedures described by e.g. Fleming et al. (2009) and Randolph and Gourvenec (2011), may provide a more adequate comparison between estimated and measured values. However, knowledge of the post-rupture (i.e., residual) strength of the chalk putty interface is needed. Unfortunately, the large strain CNS and/or constant volume tests on dense chalk putty required to characterise residual strengths representative of pile-chalk interaction were not performed in this investigation and were not available in the literature at the time of writing.

5.5 Small displacement pile engineering in Chalk

5.5.1 Pile installation and short-term shaft capacity

Though the scaled models were not meant to faithfully replicate field-scale piling, some of the pile penetration processes revealed by XCT and discussed in Section 5.4 as well as the material and interface mechanical behaviours analysed in Sections 5.2 and 5.3 may be preliminarily extrapolated to the installation and early-life shaft capacity of full-size piles. These processes may be described by adapting the critical state model presented in Section 3.3.1.3 using Figure 3.11. Thus, Figure 5.22 depicts the stress history in volumetric space of an intact chalk element in the path of a pile during (a) fully drained and (b) partially drained penetration, as well as the 1D-NCL and CSL for destructured chalk proposed previously (Section 4.3).

In Figure 5.22a, representing fully drained penetration as in the XCT experiments, an element of intact chalk first experiences large increases in effective stress with negligible changes in void ratio, due to its cemented state (path A-B). Cementation breaks down as the material yields at B and void ratio rapidly reduces (path B-C). Effective stress levels continue to increase as the relative distance to the approaching pile tip reduces until reaching maximum levels when this distance becomes zero (i.e., when the chalk element and pile tip shoulder become horizontally aligned). Thereafter, the element ceases to be under the action of the pile tip and stress levels reduce dramatically, as denoted by path C-D. Unloading is not necessarily restricted to the process of flowing past the pile tip shoulder. A jacking cycle may end before the pile tip reaches the chalk element, and thus the material would become temporarily unloaded, as denoted by path E-F. Reloading during the following cycle follows a path closer to the 1D-NCL or CSL (path F-G), as in CT03-03 (Section 5.4.2; Figure 5.19), because cementation is removed during earlier yielding and volumetric straining, and the metastable fabric inside the structure-permitted space (Section 5.2) becomes damaged by the shearing component of penetration and unloading in the previous cycle. Unloading immediately after the element becomes definitively positioned behind the pile tip during a subsequent jacking stroke (path G-H) leaves the material at a much denser state than without unload-reload cycles. Thus, slow, cyclic penetration promotes the densification of the putty chalk annulus, which may lead to significant shaft friction developments during the process, as shearing from either D or H leads to effective stress increases while the state moves towards the CSL.

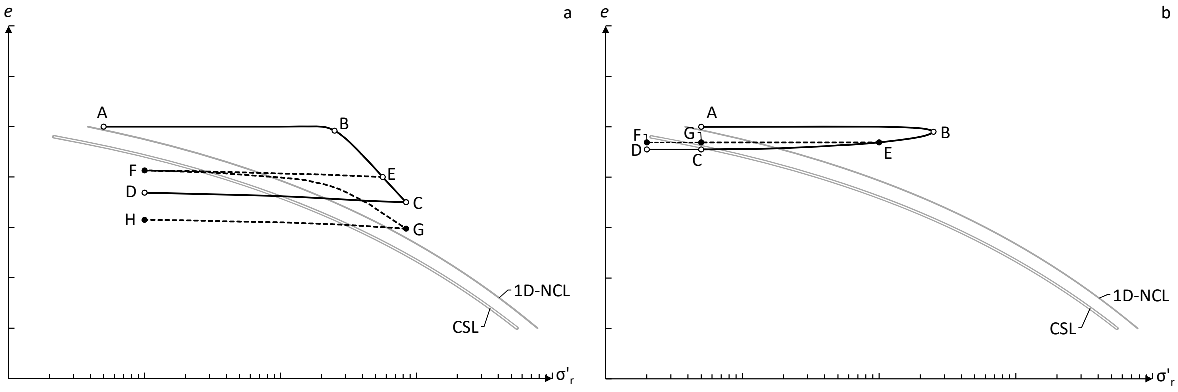

Figure 5.22. Model for drained (a) and undrained (b) effective radial stress history during penetration based on the results of the scaled models (see text).

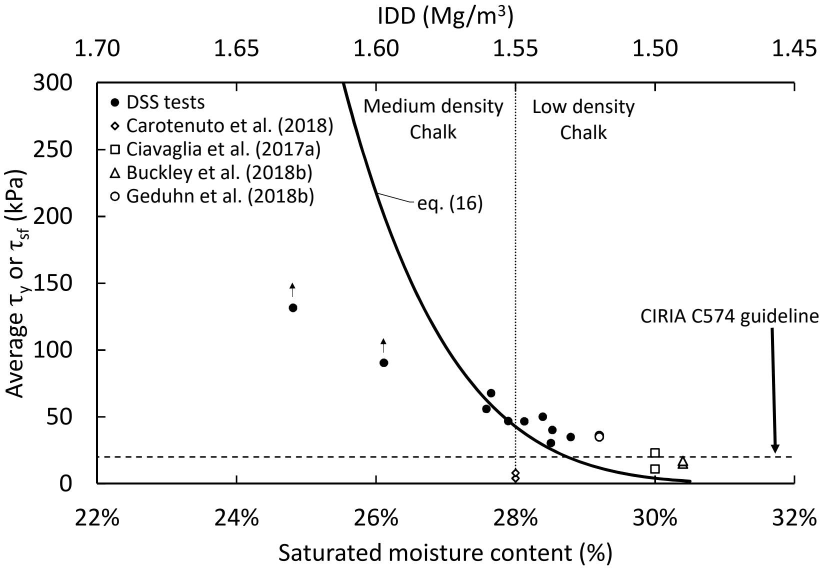

Figure 5.23. Comparison between estimated average shaft friction values during PS pile driving according to various authors and Eq. (16). DSS test results (Section 4.4.6) included for reference.

In Figure 5.22b, corresponding to penetration with very limited drainage, the chalk element experiences sharp increments in effective stress levels as the pile tip approaches (path A-B). As during drained penetration, no plastic volumetric strains or significant pore pressure developments occur because the applied load is entirely supported by the cemented microstructure of the material. However, pore pressures rise dramatically as yielding ensues and stresses are transferred to the pore water. Limited drainage allows for modest volumetric straining, but effective stresses do not recover. The volumetric state tends towards the CSL (path B-C), though CSL convergence might be hindered by fabric as discussed in Section 5.4.3. The passing of the pile tip shoulder produces large total stress reductions, but unloading occurs primarily on the pore water and only moderate effective stress changes take place (path C-D). As during drained penetration, unload-reload cycles may take place before the chalk element is displaced past the pile tip shoulder (path E-F). Instead of substantial volumetric straining, the collapse of the metastable fabric of uncemented chalk during unload-reloading produces pore pressure increments, but the effective stress state is not anticipated to increase significantly (path F-G). Therefore, rapid cyclic penetration with limited drainage, like pile driving, promotes the creation of a loose putty chalk annulus, which is expected to mobilise very low shaft frictions. Such low interface strengths were found during CSS testing of high-void ratio chalk putty as discussed in Section 4.4.6.2 and Section 5.3.2, and are also often reported during PS pile driving in low-medium density chalk, as discussed in Section 3.3 and inferred via back-analysis of driving records by e.g. Anusic (2018), Carotenuto et al. (2018) and others.

Based on the above model, it may be conservatively and preliminarily proposed that the average shaft friction mobilised during pile driving with no or very limited drainage may be broadly comparable to the critical strength of the interface derived by applying Eq. (16) and using the void ratio corresponding to the average intact density of the material (that is, assuming that no void ratio reductions occurred during driving-induced crushing). Thus, Figure 5.23 compares independent intact void ratios derived from average IDD measurements paired with EOD average shaft friction values estimated using dynamic methods with Eq. (16), as well as the results from DSS testing. Though the application of dynamic methods to determine the contribution of shaft friction to the total resistance to driving involves considerable uncertainties (see e.g. Randolph 2003 and Svinkin 2004), results show broad compatibility with the stated assumptions and the interface tests. This suggests that:

- Unloading after the passing of the pile tip leaves the annulus material in a volumetric state sufficiently close to the CSL to attain conditions close to or at the critical state. This indicates that shearing at heavily dry of critical states inferred for the XCT experiments and the associated strain localisation that precludes the mobilisation of critical strengths may not take place during pile driving in low-medium density chalk.
- $\Delta\sigma'_{\mathrm{r}}$ levels along the shaft are small compared with the horizontal stiffness of the structured chalk enclosing the annulus. Therefore, conditions resembling constant volume shearing of the chalk putty annulus take place during early-life shaft friction mobilisation.
- The effect of asynchronous load transfer along the pile-chalk interface as described in Section 5.4.3 is small. This is likely due to the rigidity of full-scale steel piles, the small local shaft frictions mobilised during driving, and moderate depth-based differences in interface thickness (as in CT03) and strength.

- Friction fatigue might be manifested as a cyclic mobility failure condition encompassing a substantially reduced stiffness combined with the attainment of critical state strength (Section 5.3.2).

However, the approach has some important limitations, particularly:

- It does not account for the variability of the ground profile nor the effect of Chalk grades. Notably, data by Carotenuto et al. (2018) corresponds to EOD average shaft capacities that do not distinguish between contributions by Chalk (grade D) and overlying Paleogenic strata, which accounts for more than half of the total embedment depth. These datapoints evidently outlie Eq. (16).
- Eq. (16) predicts average EOD shaft friction values greater than 100 kPa for piles driven into chalk with IDD ≥ 1.57 Mg/m^3. Such magnitudes are not reported in the limited number of case histories available. Large average τ_{sf} values could also imply large average $\Delta\sigma'_r$ magnitudes which may limit the validity of the constant interface thickness assumption.
- The proposed approach is not a significant improvement to the CIRIA C574 design guideline for PS piles in materials exhibiting an IDD below about 1.525 Mg/m^3.

For practical purposes and based on the above analysis, it may be proposed that Eq. (16) and the intact void ratio can be used to preliminarily estimate short-term (EOD) shaft capacities of small displacement piles driven in Chalk exhibiting an average IDD ≤ 1.57 Mg/m^3. However, for conditions where IDD ≤ 1.52 Mg/m^3, the very low average shaft friction values predicted by Eq. (16) and the likelihood of modest void ratio reductions during driving-induced crushing of such a porous material could justify the application of CIRIA C574 recommendations of an average shaft friction of 20 kPa. For sites where IDD > 1.57 Mg/m^3, the use of intact void ratios and Eq. (16) to estimate early-life shaft capacities is not supported by the small number of available case histories and further investigations are required.

5.5.2 Pile set-up and long-term shaft capacity

Though the results of the present investigation cannot indisputably demonstrate the underlying mechanisms responsible for pile set-up, they can be used to analyse some of the current hypotheses on the matter (described in Section 3.3.2.2).

The broad correlation between average shaft friction estimates at the end of installation and the critical state framework for chalk putty discussed in the previous Section suggests that the assumption that pile driving occurs with very limited drainage is adequate. Considering the relatively fast draining nature of chalk, pore pressures in the chalk putty annulus are expected to start dissipating almost immediately after the last installation strike or during installation pauses. Pore water pressure dissipation involves stress transfer onto the chalk putty grains (i.e. an increase in effective stress) and/or unloading (i.e. a reduction in total stress). The void ratio reductions related to the former might be relatively small, though they could theoretically originate substantial gains in shaft friction. For example, the two-fold increment in average shaft friction from the ≈35 kPa measured at EOD ($\tau_{sf\,(EOD)}$) to 75 kPa after about 120 minutes reported by Jardine et al. (2018) for the PS pile tests of Geduhn et al. (2018b) (Section 3.3.2.2) would imply a mean reduction in void ratio from 0.748 to 0.728 on the CSL as per Eq. (16) (i.e. a change in saturated moisture content of about 0.75%). If the thickness of the chalk putty annulus is known, the timeframe during which this change in void ratio occurs may be estimated by using 1D consolidation theory, assuming that drainage occurs in the radial direction away from the pile shaft (Randolph et al. 1979; Teh and Houlsby 1991). Thus:

$$\mathrm{T} = \frac{t\mathrm{C_h}}{d^2} \tag{19}$$

where T is a time factor (see e.g. Powrie 2014), t is time, $\mathrm{C_h}$ is the coefficient of consolidation in the horizontal direction and d is the length of the drainage path (i.e. the thickness of the remoulded annulus). Figure 5.15 and field observations by Muir Wood et al. (2015) and Buckley et al. (2018b) suggest that the thickness of the chalk putty annulus ranges between 0.40 and 1.6 times the wall thickness of a tubular PS pile. Supposing that a 40 mm-thick putty chalk annulus encased the PS piles tested by Geduhn et al. (2018b) (i.e. a 1:1 wall to annulus thickness ratio) and using the coefficients of consolidation for chalk putty derived from the oedometer tests (shown in Figure 5.24a) and assuming that vertical and horizontal directions exhibit the same coefficients (i.e. $\mathrm{C_v} = \mathrm{C_h}$), the time required for the 0.748 to 0.728 change in void ratio to be 99% complete would be of 117 minutes. This is very close to the 120 minute timeframe reported by Jardine et al. (2018). Figure 5.24b compares the set-up trends for this example with those derived from using different average annulus thicknesses at EOD (d_{EOD}), where $\tau_{sf\,(t)}$ is the average shaft friction at time t.

Of the alternative conjectures presented in Section 3.3.2.2 on the mechanics of the potential time-based σ'_r increments, the transfer of orthoradial (or hoop) stresses onto the annulus and pile shaft as radial stresses due to creep-induced collapse of an arching structure of grains around the annulus has been supported by Jardine et al. (2018). It also has some theoretical underpinning according to the cavity expansion and collapse analysis presented by White et al. (2005). However, the premise of an interlocked arching feature implies that the cemented material adjacent to the annulus is continuous, which might not be the case in certain Chalk grades (Section 2.2). Ultimately, and regardless of the cause, it might be reasonable to suppose that that potential increments in σ'_r are linked to a small radial movement of the chalk rock mass towards the annulus. According to the consolidation analogy used before, the average magnitude of this relaxation would be of less than 0.5 mm for the change in average shaft friction of 35 to 70 kPa used in the previous example and d_{EOD} values below about 45 mm. However, the elastic cavity contraction or 'relaxation' of the rigid chalk mass onto the shaft may lead to effective stress reductions, which could decrease the rate and magnitude of pore pressure-dependent densification of the annulus.

Secondary compression and creep may further reduce the annulus void ratio in the medium and long term, as in the 'ageing effect' examined via triaxial tests in Section 5.2.3. However, this densification process is dependent on effective stress levels as well. As for primary compression, the reduction of σ'_r levels by densification-induced chalk rock mass relaxation might limit the rate of further densification in the long term.

Significantly, the origin and even the existence of stationary σ'_r increments remains open to debate, as they have not been recorded in field or laboratory conditions involving chalk (though research on the matter is very scarce). Past experiences pertaining piles in sand have been somewhat contradictory, but evidence apparently favours the hypothesis that time-based increments in shaft capacity are not solely related to increments in σ'_{rs} (which for sands are associated with the hoop stress relaxation theory), but may also result from ageing and creep-induced dilatancy (Lim and Lehane 2015b; Zhang and Wang 2015). However, in the case of piles in Chalk, if ageing/creep does not encompass void ratio reductions, then any set-up effect will only be apparent. As described in Section 2.5.5, constant volume ageing/creep in destructured chalk may lead to increments in stiffness, but no substantial gains in ultimate strength. Thus, the destruction of ageing- or creep-induced fabric/structure in the chalk putty annulus may remove any time-based (apparent) gains in strength. This has been reported by Jardine et al. (2018) for a small number of field tests, as mentioned in Section 3.3.2.2.

Annulus consolidation at the end of installation is expected to be much less significant, or even negligible, when the pile is inserted at slow rates. Much of the dissipation processes would occur during installation in these cases, as per the drained penetration model described in Section 5.5.1. Increments in effective stress at the end of installation would therefore be small and would not induce significant reductions in void ratio due to the substantially dense of critical conditions at the end of installation. Furthermore, creep and secondary compression rates are very slow in very dense of critical and highly overconsolidated states (Bialowas 2017), which further impairs time-based reductions in void ratio of the chalk putty annulus and associated increases in ultimate interface strength. Hence, it is proposed that jacked piles would not exhibit a strong set-up effect. Such appears to be the case of the PL piles tested by Buckley et al. (2018a), which did not exhibit set-up whatsoever (Section 3.3.2.2).

Whatever the magnitude of the annulus densification events taking place after pile installation, it should be remembered that the mobilisation of critical interface strength may be curtailed by strain localisation when shearing commences at heavily dense of critical conditions, as observed in the DSS tests (Section 5.3) and inferred for the scaled experiments (Section 5.4).

Finally, it is important to note that the example calculations presented throughout this Section correspond to very simplified and idealised average values and are specific for the case history presented by Geduhn et al. (2018b) and Jardine et al. (2018). The actual profile of the protracted time-based decrease in void ratio and thickness of the chalk putty annulus is expected to vary with depth, being more acute in the vicinity of the pile tip were effective stresses and pore pressures are largest at EOD. More importantly, considering the very significant uncertainties on the processes involved in pile set-up and the impossibility to measure in-situ annulus characteristics (e.g. thickness and void ratio) and their evolution with time, it is likely that pile design for long-term capacities will rely on empiricism for the foreseeable future.

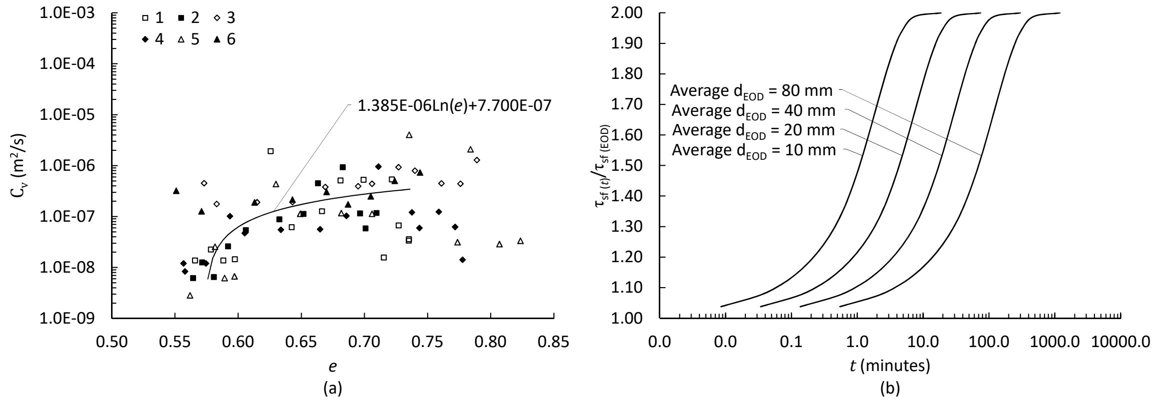

Figure 5.24. (a) Correlation between C_v and *e* (legend corresponds to oedometer test number, see Table 4.2); (b) CSL-based 20 to 40 kPa average shaft friction set-up trends for various EOD annulus thicknesses (see text).

5.5.3 Correlations with the CPT to predict short term shaft capacity

The CPT in many ways resembles pile installation. Therefore, and as widely documented for sands and as proposed by Buckley (2018) and Jardine et al. (2018) (Chapter 3), CPT-derived measurements in chalk may provide insight into the shaft friction performance of displacement piles and the prospective correlation of this performance with the critical state framework for the material.

Anusic (2018) offers CPT data for locations in the North Sea underlain by Chalk. This data is complemented by site-specific material characteristics. Unconfined compressive strength (UCS) data is given with considerable meticulousness. Matthews and Clayton (1993) showed that a direct correlation between UCS and IDD exists (Figure 5.25a) and this property has been used to derive IDD profiles to pair with the CPT data given by Anusic.

CPT cone resistance q_c is related to τ_u in fine-sized soils (Lunne et al. 1997). However, cementation provides excess strength to that of the intrinsic (destructured) condition. This additional strength becomes reduced as S_σ approaches 1 (Section 5.2.2). Therefore, the ratio $(q_c-\sigma_{v0})/\tau_u$ plotted against IDD in Figure 5.25b[5] denotes a similar trend to that of S_σ (Figure 5.7). $(q_c-\sigma_{v0})/\tau_u$, also known as the 'cone factor' N_{kt} (Lunne et al. 1997), was calculated using q_c and IDD data from Anusic (2018) (IDD obtained from Figure 5.25a) and τ_u derived using the intact void ratio and Eq. (16). This link between N_{kt} and S_σ is further evidenced by Figure 5.25c, which directly compares both parameters by using the trendline proposed in Figure 5.7 to estimate S_σ from IDD. Both Figure 5.25b and Figure 5.25c suggest that penetration resistance q_c is decreasingly related to bond strength and increasingly associated with (granular) frictional strength with increasing IDD. This evidences that the CPT may be able to capture Chalk sensitivity when used in conjunction with the critical state framework proposed in Sections 5.2 and 5.3, which supports its use to study and forecast pile behaviour.

Associations between sleeve friction (f_s) and τ_u derived using Eq. (16) and the intact void ratio are difficult because cone penetration may not be fully undrained (Buckley et al. 2018a) and the void ratio of the putty chalk adjacent to the friction sleeve is unknown. However, if f_s is assumed to be broadly equal to τ_u as proposed by e.g. Drnevich et al. (1974), Cancelli et al. (1982), Lunne et al. (1997) and others for clays, then Eq. (16) can be used to estimate the volumetric strain (ε_{vol}) associated with the transition from the intact void ratio prior to installation to the critical state void ratio attained whilst shearing at the friction sleeve after destructuration ahead of the cone

---

[5] σ_{v0} corresponds to the total overburden pressure. Ideally, q_c should be corrected by the 'unequal area effect' described by Lunne et al. (1997). This correction cannot be implemented using the available data.

tip. Such volumetric strains are shown in Figure 5.25d. Naturally, chalks of lower IDD seem to predominantly contract while those of higher IDD apparently tend to dilate. But these observations are insufficient to quantitatively assess, at least preliminarily, the short-term shaft capacity of displacement piles.

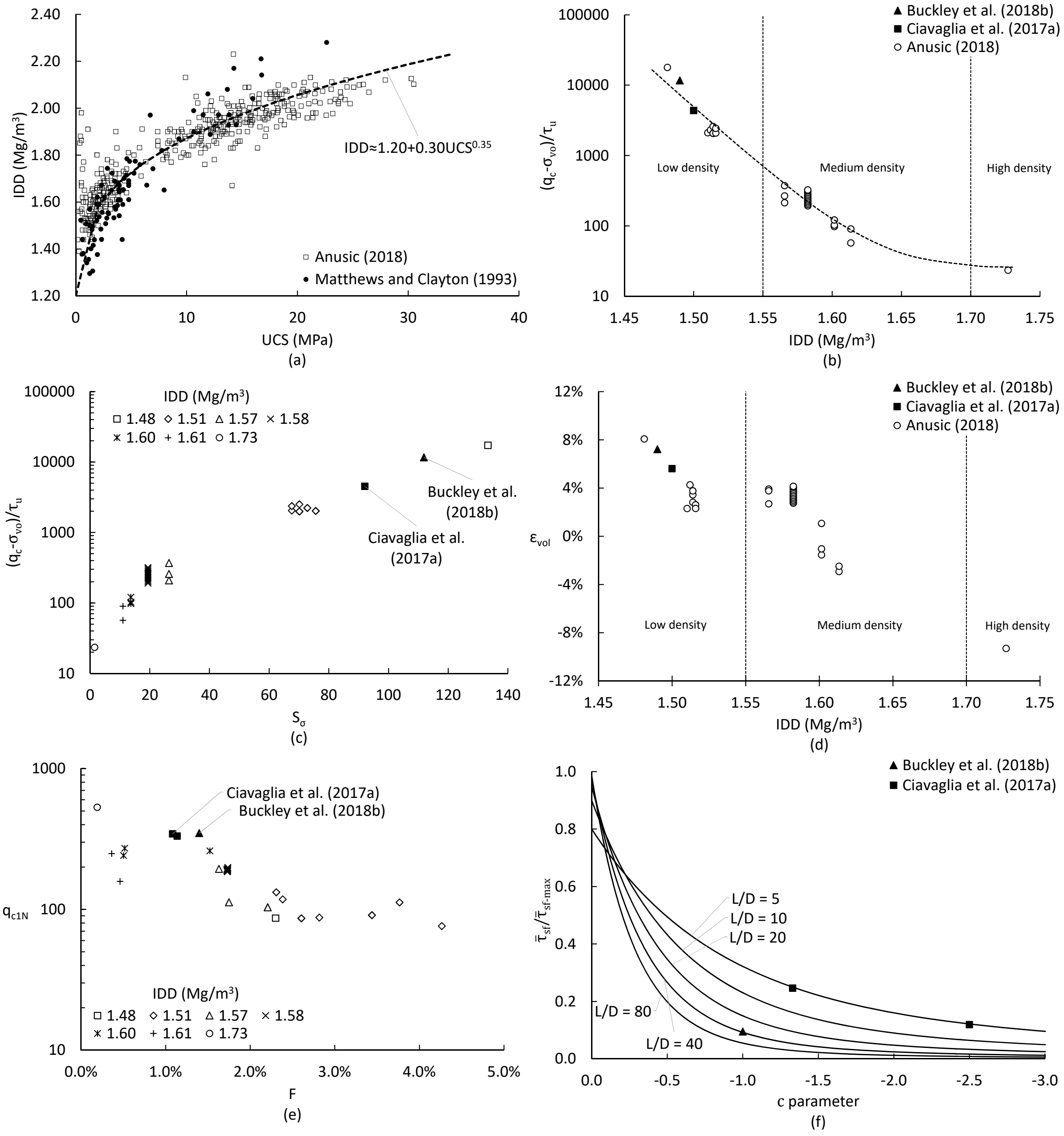

Figure 5.25. (a) Correlation between IDD and UCS; (b) Correlation between cone factor N_{kt} and IDD; (c) Correlation between N_{kt} and S_σ; (d) Estimated penetration-induced volumetric strain associated with the $f_s = \tau_u$ assumption (see text); (e) Correlation between q_{c1N} and F; c parameter trends according to Eq. (23).

CPT-based pile design methods discussed in Sections 3.2 and 3.3 may be a useful starting point to carry out a preliminary quantitative assessment of initial shaft friction, given their success in sands. As exposed in these previous Sections, key parameters required are a factor accounting for the influence of the pile tip geometry (A), a parameter quantifying the change in stress levels from immediately ahead of the pile tip shoulder to immediately behind it (B), and the reduction in σ'_r levels due to friction fatigue characterised as a power function of the relative distance from the pile tip (FF^c).

Following the UWA method, parameter A may be assumed to amount to $\mathrm{A_r}^{\mathrm{b}}$, which is defined in Section 5.4.2. Maximum shaft friction ($\tau_{\mathrm{sf-max}}$) is mobilised immediately above the pile tip shoulder just after the stress drop represented by B has taken place (Section 3.2.1.1). $\tau_{\mathrm{sf-max}}$ may be expressed in terms of q_c following Eq. (1):

$$\tau_{\mathrm{sf-max}} = \sigma'_{\mathrm{r}} \tan \delta'_{\mathrm{ult}} = \mathrm{B} q_{\mathrm{c}} \mathrm{A_r}^{\mathrm{b}} \tan \delta'_{\mathrm{cs}} \tag{20}$$

where q_c is assumed to be approximately equivalent to the stress levels under the pile tip, and therefore, B has been introduced as the ratio of σ'_r at $\tau_{\mathrm{sf-max}}$ to q_c. In the CPT, $\mathrm{A_r}^{\mathrm{b}}$ = 1 (closed-ended condition) and $\tau_{\mathrm{sf-max}}$ may be taken as roughly equal to sleeve friction (f_s), as suggested by White (2005), White and Deeks (2007) and others. Thus:

$$\mathrm{B} = \frac{\mathrm{f_s}}{\mathrm{q_c} \tan \delta'_{\mathrm{ult}}} = \mathrm{R_F} \left(\frac{1}{\tan \delta'_{\mathrm{ult}}}\right) \tag{21}$$

where $\mathrm{R_F}$ is the CPT friction ratio. According to Anusic's dataset, the normalised friction ratio F = $f_s/(q_c-\sigma_{v0})$, which is similar to $\mathrm{R_F}$, ranges from 0.01 to 0.03 for low-medium IDD materials, as shown in Figure 5.25e. This Figure uses the normalised cone penetration resistance corrected for overburden stress $q_{c1N} = (q_c/P_a)/(\sigma'_{v0}/P_a)^{0.5}$ where P_a is the atmospheric pressure, as proposed by Robertson and Wride (1998). Such F range indicates B values between about 0.02 and 0.05 using $\tan \delta'_{\mathrm{ult}}$ = 0.554 from the DSS tests. This interval compares well with the 0.02-0.04 range recommended for piles driven in silica sands (Schneider et al. 2007), which suggests that there is limited difference in the unloading processes associated with the displacement of material past the pile tip in piles in Chalk and siliceous sands.

Assuming that shaft friction degradation due to friction fatigue is a power function of the relative distance to the pile tip as in the UWA and ICP methods (Section 3.2 and Section 3.3), shaft friction at any point along the shaft may be estimated as:

$$\tau_{\mathrm{sf}} = \tau_{\mathrm{sf-max}} \left(\frac{\mathrm{h}}{\mathrm{D}}\right)^{\mathrm{c}} \tag{22}$$

where h is the distance to the pile tip, D is the pile outside diameter and 'c' is a reduction factor. The integration of Eq. (22) from $h = D$ to h = the total embedment length (L) provides an estimate of the ratio of average shaft friction to average maximum shaft friction $\bar{\tau}_{sf}/\bar{\tau}_{sf-max}$, such that:

$$\bar{\tau}_{sf}/\bar{\tau}_{sf-max} = \frac{1}{(c+1)}\left[\left(\frac{L}{D}\right)^{c} - \frac{D}{L}\right] \quad (23)$$

which is amenable to numerical solution.

Figure 5.25f plots Eq. (23) for various L/D values, as done by White (2005), as well as the results from Buckley et al. (2018b) and Ciavaglia et al. (2017a). While reduction factor c is expected to approximate -0.5 in siliceous sands, it appears that this figure may be lower than -1 for low IDD chalk (though the dataset is evidently sparse). Schneider et al. (2007) proposed that c = -1 for calcareous and micaceous sands, arguing that the effect of friction fatigue was greater in these materials. Such appears to be the case for chalk as well. This is qualitatively compatible with the results from CSS testing as discussed previously in Section 5.5.1.

Thus, considering a compression loading scenario (d = 1; Table 3.1) for the installation of the full-scale and full-coring piles tested by Geduhn et al. (2018b) assessed in the previous Section ($A = A_r^{b}$ = 0.46; Section 5.4.2), an average estimate of B = 0.035, c = -1 as advised by Schneider et al. (2007), critical state conditions at the pile-chalk interface (i.e. $\Delta\sigma'_r$ = 0) and $\tan \delta'_{ult}$ = 0.554 as determined from DSS testing, the particular expression originating from Eq. (7b) for short-term shaft friction during penetration may take the form $\tau_{sf} = 0.0051 q_c (h/D)^{-1}$. A comparison is made in Figure 5.26a for the first two diameters above the pile tip between this equation and the Chalk ICP-18 method presented by Jardine et al. (2018) using the same pile geometry (Eq. (8)). Results show that the use of the adapted UWA-05 method produce moderately lower EOD shaft friction estimates. This is principally due to the effect of B, as the h-based degradation patterns are approximately similar. In fact, the use of a high-estimate B = 0.05 produces a similar profile as that of Chalk ICP-18, as presented in Figure 5.26b. This denotes role of the interpretation of the stress changes that occur as the chalk putty is displaced behind the pile tip. As with Chalk ICP-18, extensive instrumented pile testing is needed to corroborate the applicability of the modified UWA-05 approach.

The set-up effect is more difficult to relate to the CPT, as the test does not directly reveal the local thickness and void ratio of the chalk putty annulus, nor the effective stress changes that take place as pore pressures equalise. Additionally, the pore pressure developments occurring during the CPT are likely quite different from those that develop during pile driving, which is carried out at a much faster rate, as exposed in Section 5.5.2. Furthermore, strain localisation during shearing at highly dense of critical conditions could preclude the mobilisation of theoretical ultimate interface strengths derived from the critical state framework, as discussed throughout this Chapter. Therefore, long term small displacement pile design for Chalk may have to resort to empirical correlations like the ageing characteristic curve of Figure 3.12, as currently done for silica sands (Gavin et al. 2015).

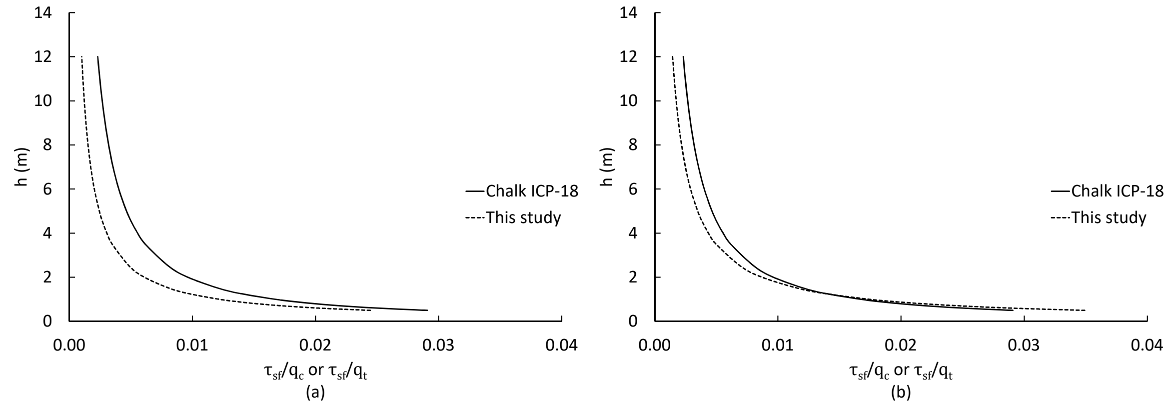

Figure 5.26. Example of the application of the analysis of this Section and the Chalk ICP-18 method using full-scale pile geometry data from Geduhn et al. (2018b): (a) using B = 0.035; (b) using B = 0.05.

Chapter 6 Conclusions

6.1 Introduction

Pile driving in low and medium density chalk crushes the material and produces a destructured 'putty' chalk interface between the shaft and the Chalk formation. This Thesis investigated the characteristics of this interface (or 'annulus') and the processes involved in its creation, with the aim of rationally describing the mechanisms associated with shaft friction mobilisation, and therefore, shaft capacity. This research was motivated by the need to optimise current design guidelines and reduce the cost of deploying offshore renewable energy infrastructure in regions underlain by Chalk.

The scarce previous research on the topic suggested that piles driven into high density chalk mobilise larger shaft capacities than those installed in low-medium density materials. These works proposed that this could be explained by the former producing denser annuli than the latter. Based on these observations, the parting hypothesis of the present Thesis was that unit shaft friction could be computed as a function of the void ratio, or density, of the destructured chalk interface using Critical State Soil Mechanics.

The study was organised in three main tasks. First, the suitability of a critical state framework to characterise the mechanical performance of destructured low-medium density chalk was assessed via triaxial and oedometer experiments. Secondly, the applicability of the critical state framework to characterise the role of interface density on ultimate unit interface friction was evaluated using monotonic and cyclic simple shear tests that qualitatively replicated the pile-annulus interface. Thirdly, pile penetration was studied by applying micro-focus computed tomography (XCT) to physical models to observe the processes by which the annulus is created and the link between these processes and interface density in the context of Critical State Soil Mechanics.

Major contributions resulting from this work are summarised in this Chapter.

6.2 A critical state framework for destructured White Chalk

Oedometer experiments on destructured specimens revealed that (Section 5.2):

- Compression paths in effective stress-void ratio space are dependent on the depositional density of chalk putty (Section 4.3). This behaviour is typical of sands and non-plastic silts.
- As for many sands and non-plastic silts, the compression paths of chalk putty merge in effective stress-void ratio space at large stresses (>2 MPa) into a unique one-dimensional normal compression line (1D-NCL; Eq. (10)).
- Particle breakage is a key mechanism associated with compression path convergence into the 1D-NCL, in good resemblance to the mechanical performance of other granular geomaterials.

Oedometer tests on intact specimens showed that (Section 5.2):

- The excess strength supplied by cementation creates a structure-permitted effective stress-void ratio space above the destructured 1D-NCL.
- The structure-permitted space persists after yield, signalling the existence of intact 1D boundaries supported by the metastable fabric of the material, as similarly reported for calcarenites and other weak rocks.
- The bond strength at yield can be defined using the stress sensitivity concept. This characterisation shows that denser grain arrangements contribute to a substantial portion of the 1D yield strength of chalk in the upper-bound limit of the medium density range, rather than cementation. Conversely, low density chalks are almost entirely reliant on cementation to support loading.

Undrained triaxial tests on destructured chalk (Section 4.3) and the analysis of previous investigations showed that (Section 5.2):

- A unique critical state line (CSL) exists for the chalk putties studied in this Thesis (Eq. (11)).
- The use two destructuration methods applied to low and medium density intact White Chalk samples collected from two sites of different lithostratigraphy did not alter the location of the CSL.
- Shearing after prolonged consolidation periods under constant effective stress, often interpreted as ‘ageing’ in the literature, does not affect the location of the CSL.
- Independent test data by various authors involving putties produced from low-medium density White Chalk is appropriately described by the proposed CSL. Thus, the CSL

appears to be suitable for all chalk putties produced from rocks of the same characteristics.

- The underlying reason for 1D-NCL and CSL-uniqueness may be that most chalk putties produced from low-medium density intact White Chalk have comparable gradings and particle shapes because they are all composed by the coccoliths and coccolith platelets that form the parent rocks. This was supported by very limited pre-test variability in particle size distribution (PSD) and Atterberg limits between samples.
- The effect of ageing can be explained by consolidation and secondary compression, which lead to densification (void ratio reductions) and increments in ultimate strength. This strength was demonstrated to be compatible with the CSL.

The CSL and 1D-NCL constitute the critical state framework of destructured low-medium density White Chalk. It was anticipated that this framework would be unsuitable for chalk putties produced from rocks of different mineralogy (e.g. containing important amounts of clay or silica) and/or higher density, because the grains that compose these materials would be different to those of the putties tested in this study. Similarly, the proposed framework may be inappropriate for coarsely crushed low-medium density White Chalk mostly containing cemented grain agglomerations of different size and shape to the coccolithic debris that formed the investigated putties.

6.3 Performance of chalk putty interfaces during shear

Constant volume monotonic direct simple shear (DSS) tests performed using the same putties as in the oedometer and triaxial tests showed that:

- The CSL was suitable to describe the behaviour and ultimate shear strength of destructured chalk interfaces (Section 4.4). This corroborated the link between the density or void ratio of destructured chalk and interface shear strength, as anecdotally proposed in previous studies.
- An expression to estimate ultimate interface strength as a function of void ratio was formulated (Eq. (16); Section 5.3), based on the CSL equation.
- A highly dilative response during shear at heavily dense of critical states led to interface failure by strain localisation before mobilising the ultimate strength predicted by the CSL.

Instability during constant volume cyclic simple shear (CSS) testing was found to depend on the generation of plastic strains resulting from the shearing-induced disruption of the chalk putty fabric (Section 4.4). This led to the reduction of effective stress levels and stiffness, which produced cyclic instability in a comparable manner to saturated sands and non-plastic silts (i.e. cyclic liquefaction and cyclic mobility). As for sands, the stress threshold leading to unstable behaviour was proposed to be related to the small strain yield strength of the interface, which was in turn associated with density, effective stress levels and previous stress history (Section 5.3). A state parameter approach was used to quantitatively assess this. The technique was found to adequately relate the cyclic stress ratios that produce instability with interface density and pre-shear effective stress conditions. The suitability of this approach also proved that the critical state framework could be used to characterise the performance of chalk putty during cyclic loading, but that density or void ratio alone were insufficient to do so.

Additionally, destructured chalk was found to perform better under similar cyclic loading conditions than two sands, based on independent CSS test data. This was suggested to originate from the mildly plastic nature of chalk putty and showed that the material is not intrinsically more susceptible to cyclic instability than other granular geomaterials.

6.4 Model pile penetration mechanisms in chalk

Physical models and XCT revealed that jacked piles penetrated the chalk by crushing and densifying it under the tip (Section 4.5). This process led to the creation of the chalk putty annulus. In particular:

- Solid cylindrical piles created a bulb (‘nose-cone’) of highly compressed material under the tip. The surrounding cemented chalk hampered the displacement of chalk putty, leading to a larger and denser nose-cone and annulus with penetration depth. The increment in effective stresses with tip depth fractured the neighbouring intact chalk, which aided pile insertion.
- Open-ended tubular piles also crushed and densified the chalk, producing a half-toroid-shaped region (‘nose-toroid’) beneath the pile rim. The annulus exhibited greater density with proximity to the pile, but neither annulus thickness nor nose-toroid volume changed significantly in size with penetration depth because the putty was partially displaced through the pile opening. This prevented the generation of the large radial stresses required to fracture intact chalk.

These observations and post-test exhumation and analysis of the destructured chalk interface suggested that pile penetration processes around the tip region were qualitatively compatible with those of model pile experiments in uniform sands (Section 5.4). The high-compression and large volumetric strain zone formed ahead of the pile tip indicated high stresses, while the cessation of changes in particle size distribution and density once crushed chalk moved past the tip and formed the annulus suggested large stress reductions. Considering these observations, a cavity expansion theory analysis was carried out using the applied pile head stresses and the XCT-derived void ratios. Results suggested that:

- The volumetric state of the chalk putty tended towards the CSL at the high-stress conditions neighbouring the pile tip shoulder, which highlighted the potential applicability of a critical state model for pile penetration.
- Convergence with the CSL was hindered at lower stresses levels and higher void ratios (i.e. inside the structure permitted space) by what were thought to be remnants of the original fabric analogous to the intact 1D boundary identified in the oedometer experiments.

6.5 Application of critical state framework to model pile shaft capacity

XCT images suggested low void ratios close to the pile shaft in all cases, but these were also found to increase with radial distance from the pile surface until matching far-field intact chalk values (Section 5.4). This qualitatively replicated independent field-scale observations and denoted the importance of densification under the path of the pile during drained penetration. However, it also hampered the selection of a void ratio profile to use with the critical state framework for interface friction derived from DSS testing (Eq. (16)), and the comparison with results from the pull-out tests. Furthermore, some of the model piles deflected during penetration, producing greater fracturing than what would have been expected of a vertically penetrating pile. This also led to gaps (macroscopic void space) within the chalk putty annulus. Therefore, various assumptions were examined to derive a void ratio profile input for the interface friction function and only annulus regions without gaps were considered in the analysis. However, none of the approaches were able to produce accurate estimations of shaft capacity, with estimates overpredicting shaft capacity by over 100%. Potential reasons for this discordancy were proposed to be that:

- XCT-derived void ratios implied substantially dense of critical conditions which may have precluded the mobilisation of critical state strengths due to strain localisation, as in the DSS tests.

- The constant interface thickness assumption used may not have been attained due to the relatively low lateral stiffness of fractured chalk and/or of the model piles. This implies that void ratios may have varied locally during shear, and thus, the pre-test void ratio input to the framework might not have been the critical state void ratio.
- XCT-derived void ratios might not be sufficiently accurate to be used in the highly void ratio-sensitive critical state interface friction function.

6.6 Small displacement pile engineering in chalk

Outcomes of the investigation of the mechanical behaviour of chalk and of pile penetration mechanisms were extrapolated to examine the processes associated with the installation of full-sized piles. The existing critical state model for pile penetration in chalk was adapted to qualitatively account for the role of penetration rates (Section 5.5). Based on this updated model, it was proposed that:

- Slow, drained penetration crushes the chalk but does not allow for pore pressure build-up. Volumetric contraction occurs instead, in a fashion resembling the scaled XCT tests presented in this Thesis. Thus, the annulus may be assumed to be in significantly dense of critical conditions at the end of fully-drained displacement pile installation, even more so if it takes place in series of steps or cycles, which could further densify the destructured chalk interface.
- High penetration rates like those resulting from impact driving takes place in largely undrained conditions involving large positive pore pressure developments as the chalk is crushed ahead of the pile tip. Very low shaft frictions are mobilised as a result of the high porosity and void ratio of the initially intact material, and of cyclic loading if the pile is being impact-driven. Constant volume, low effective stresses and high void ratios result in states close to the CSL.

A series of practical recommendations regarding the shaft capacity of small displacement piles were drawn considering this simplified model, the analysis of the experimental results of this Thesis, and independent pile test data:

- For pile driving at locations where the Chalk exhibits an average intact dry density (IDD) between 1.52 and 1.57 Mg/m^3, the critical state framework for interface friction proposed in this Thesis (Eq. (16)) may be used to preliminarily calculate average shaft friction and shaft capacity during and at the end of driving by using the intact void ratio as input parameter. For IDD < 1.52 Mg/m^3, the proposed framework posed no significant advantage to current CIRIA C574 guidelines. For IDD > 1.57 Mg/m^3, strain localisation might preclude the mobilisation of ultimate interface strength if shearing initiates from heavily dense of critical conditions, as observed in DSS testing and inferred for the XCT experiments.

- Pauses during driving and/or the end of installation are expected to lead to pore pressure dissipation and consolidation (i.e. void ratio reduction) of the chalk putty annulus, with associated increments in ultimate strength as per the critical state framework. This was proposed to be one of the most significant drivers of the pile set-up effect (i.e. the time-based increase in shaft capacity).
- Pore pressure dissipation and annulus densification may be completed before the end of installation when fully-drained penetration takes place and further densification is unlikely to occur thereafter. These post-installation heavy dense of critical conditions of the chalk putty annulus also preclude other ageing-related effects (e.g. secondary compression, creep-induced increases in stiffness). Thus, it was proposed that pile set-up effect is insignificant for ‘slowly’ jacked piles, a phenomenon that has been reported in the literature.

With regards to the pile set-up effect, drainage characteristics of chalk putty determined from the oedometer and triaxial tests and consolidation theory calculations suggested that (Section 5.5):

- The increase in critical strength of chalk putty during consolidation was quantitatively compatible with the magnitude of average shaft friction gains shortly after impact-driving reported in the literature. However, it was noted that volumetric contraction of the chalk putty annulus may be capped by the rigidity of the enclosing cemented chalk.
- The assessment of the ageing effect on chalk putty from triaxial experiments suggested that longer-term increments in chalk putty density (and, therefore, strength) and stiffness associated with creep and/or secondary compression could further magnify the set-up effect.
- Considering the difficulties in forecasting the thickness and void ratio of the chalk putty annulus at the end of installation and the magnitude of the effective stress changes occurring thereafter, it was concluded that the estimation of the set-up effect may have to rely on empirical correlations for the foreseeable future.

A small publicly available database of cone penetration tests (CPTs), which are qualitatively analogous to pile jacking, was used to further investigate pile penetration and shaft capacity mobilisation. It was found that the combined use of CPT data and the critical state framework could adequately characterise Chalk strength and stress sensitivity if the IDD profile is known. Furthermore, for short-term conditions and during pile installation, the applicability of design methods based on the CPT could be assessed based on the approximately comparable stress history of chalk and sand in the path of a jacked pile. The three key aspects of this stress history are the effect of the open-ended condition and partial/total plugging of tubular piles on effective radial stress levels ahead of the pile tip, the radial effective stress drop that takes place as the material is displaced by the pile tip, and the degradation of effective stress levels and shaft friction with increasing relative distance to the pile tip. Following widely-used industry guidelines for piles in sand, these aspects were introduced into a popular CPT design routine (UWA-05) as factors applied to the cone penetration resistance measurements, labelled A, B and c in the present Thesis, and were assessed using the small publicly available pile test and CPT database. From this analysis:

- Factor A was left unchanged from the current cavity expansion/contraction implementation.
- Factor B exhibited a similar range to values observed in extensive research pertaining piles in siliceous sands, suggesting that the unloading process occurring as the material flows past the pile tip is not significantly affected by the characteristics of Chalk.
- The magnitude of factor c ($\leq$ -1.0) indicated that driven piles in Chalk were at least as susceptible to friction fatigue than piles in carbonate and micaceous sands, likely due to the contractive behaviour of low-medium density chalk putty and the high lateral stiffness of the enclosing intact chalk.

Example calculations using data from full-scale test piles yielded comparable results to the recently presented CPT-based Chalk ICP-18 method, which suggested that CPT-based techniques are promising tools for shaft capacity estimation. However, extensive CPT and pile testing campaigns will be needed to verify and refine this approach.

6.7 Recommendations for future research

Considering the outcomes of this Thesis and of previous investigations, it is advised that future research on the shaft capacity of small displacement piles in Chalk focuses on:

- The use of the proposed critical state framework to further develop analytical approaches to pile penetration such as cavity expansion/contraction theory to rationally characterise pile installation and quantify pile set-up based on material characteristics to avoid the uncertainties of current purely empirical methods.

- Producing more high-quality field-scale pile test data involving chalk of different densities to further assess the link between intrinsic chalk putty strength and pile shaft capacity, as well as to validate recently proposed design routines based on the CPT.
- Quantifying the effect of chalk grade on shaft capacity, as this important parameter was outside the scope of this Thesis and is overlooked by most of recent research.

The work presented in the Thesis suggests that the first of these three tasks may benefit from the use of XCT and scaled models. Such approach would be substantially improved if model pile installation and testing was carried out 'in-situ' (i.e. simultaneously with XCT) while measuring local pile strains that can be traced to shaft-chalk load transfer. In this manner, stresses and XCT-derived strains/volumetric condition can be correlated in a truly time-resolved fashion.

Appendix A Oedometer, triaxial and simple shear test corrections

A.1 Oedometer compliance correction

Figure A1 presents the results of oedometer tests using dummy steel samples and the two experimental setups described in Section 4.3.1, including the porous discs and filter paper. The displacements measured at each vertical stress in this Figure, minus the elastic deformation of the steel dummy, were subtracted from the settlements recorded during the tests on chalk specimens.

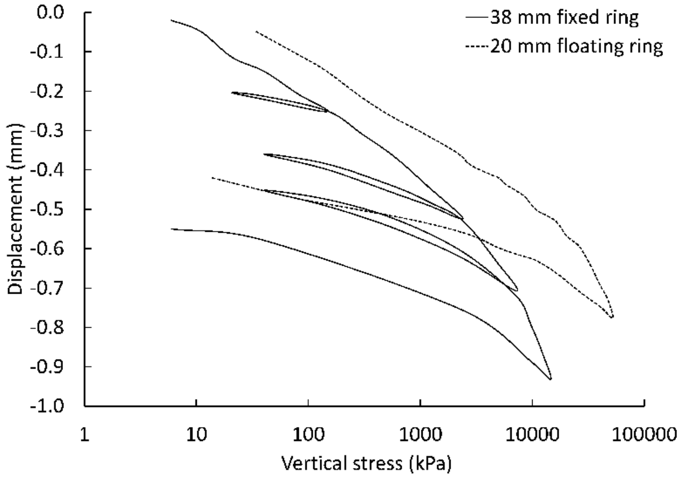

Figure A1. Oedometer apparatus compliance measurements.

A.2 Triaxial specimen cross-section area correction

Changes in specimen diameter during undrained triaxial compression were derived using the radial strain belt. When the linear range of the sensor was surpassed, specimen cross-section area corrections were applied. The idealised specimen deformation during a triaxial shear test is assumed to be that of a right cylinder (Bishop and Henkel 1962). However, some specimens were observed to significantly bulge into the shape of a barrel, as documented by Bishop and Green (1965) and others, with posterior development of multiple shear bands (Figure A2). The cross-section area correction for right cylinder-shaped deformation during undrained triaxial compression was assessed using (Head and Epps 2011):

$$\mathrm{A} = \frac{\mathrm{A_0}}{(1 - \varepsilon_{\mathrm{ax}})} \tag{24}$$

where A is the current (corrected) cross-section area, $\mathrm{A_0}$ is the cross-section area at the start of undrained compression and ε_{ax} is the axial strain in decimal units. Barrelling mode of deformation correction may be carried out by assuming full restraint at the specimen ends and thus, that the specimen developed a parabolic profile. The calculations to approximate the average area of the middle third of the specimen proposed by Zhang and Garga (1997) and Lade (2016) were evaluated, in each case, as:

$$\mathrm{A} = \left(\frac{\mathrm{A_0}}{12}\right)\left\{\left(\frac{11}{4}\right)\left[\frac{30}{(1 - \varepsilon_{\mathrm{ax}})} - 5\right]^{0.5} - 3.75\right\} \tag{25}$$

and

$$\mathrm{A} = \frac{\mathrm{A_0}}{(1 - \varepsilon_{\mathrm{ax}})}\left[2 - (1 - \varepsilon_{\mathrm{ax}})^{0.5}\right] \tag{26}$$

Figure A3 depicts two example applications of equations (24), (25) and (26) on ISO and 1D test data. These expressions have been plotted as continuations of the radial strain measurements. Also shown are the post-test average middle third cross-section areas derived from calliper measurements. As presented in this Figure, at least one of the area corrections qualitatively matched the radial strain belt trend and the post-test measurement. It was thus decided to use the correction function that provided the closest fit to the strain belt and post-test data.

Figure A2. Photograph of Test 8 at the end of the undrained shear stage.

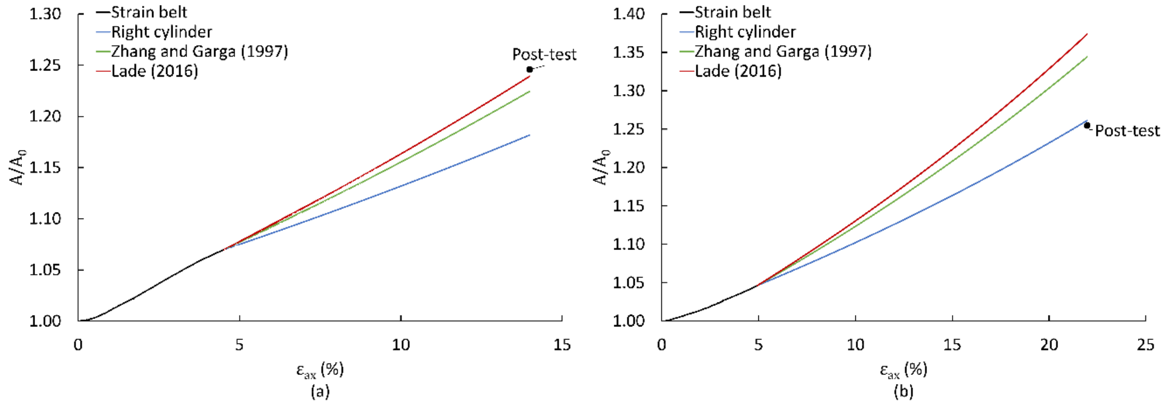

Figure A3. Results of the application of various triaxial area corrections in (a) Test 8 and (b) Test 9.

A.3 Triaxial membrane correction

The contribution of the strength of the latex membrane used to seal the triaxial specimens to the externally measured deviator stress is shown in Figure A4 for barrel-shaped deformation, as established in BS 1377-7:1990. Considering the magnitude of the ultimate strengths reported in Table 4.3, membrane-induced errors on this measurement were thought to be insignificant.

Errors in pore pressure and specimen volume change measurements due to membrane penetration into surface voids is deemed to be negligible in materials with d_{50}<0.1 mm (Head and Epps 2014), as is the case for chalk putty (Table 4.1). Therefore, corrections for these effects were not implemented.

Corrections for stress and volume/pore pressure errors resulting from membrane resistance and stretching during single-shear plane deformation were not applied because that this type of deformation was not observed.

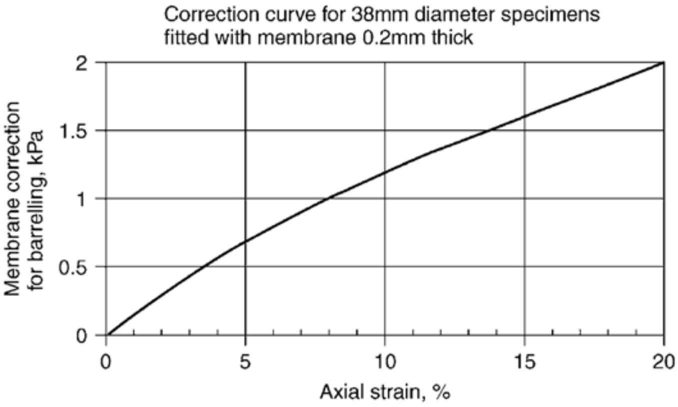

Figure A4. Deviatoric stress correction for the contribution of the latex membrane assuming barrelling-shaped deformation (t stands for thickness). From BS 1377-7:1990.

Errors due to water transfer through the membrane were similarly considered to be negligible, as Bishop and Henkel (1962) reported that volume errors are less than 0.02% per day of testing. Additionally, membranes were water-saturated for 24h prior to testing to further mitigate this effect (Head and Epps 2014).

A.4 EMDCSS apparatus membrane resistance and raceway friction

ASTM D6528-07 prescribes the measurement of the friction of the sliding plate on the lubricated raceways and the resistance against shear of the confinement hardware (i.e. ring stack and membrane). Thus, tests were performed without a soil sample. Stresses derived from the top and in-line load cells (by dividing load measurements by the internal cross-section area of the confinement rings) are shown in Figure A5. Also shown is the average of these two measurements. Considering the very small stress magnitudes evident in this Figure, no corrections were applied to the simple shear test data.

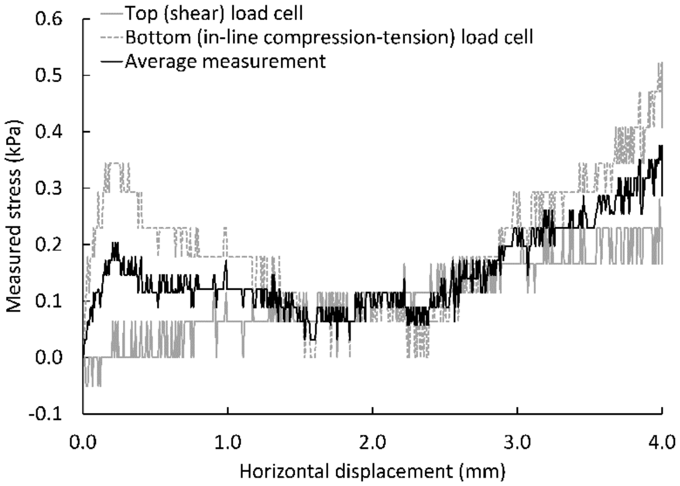

Figure A5. Raceway, membrane and ring confinement resistance to sliding.

Appendix B Initial operational stiffness of chalk putty in cyclic simple shear tests

In stress-controlled CSS testing, the GDS test control software requires a user input of the estimated stiffness of the specimen. However, detailed studies of the stiffness of chalk putty are scarce and exclusively pertain the use of dynamic probing (bender element testing) during triaxial experiments to derive very small strain ($\gamma \leq 0.001\%$; Jovičić 1997; Clayton 2011) shear moduli (G_0) along the vertical direction of the specimen (Alvarez-Borges et al. 2018; Bialowas et al. 2018). The operational shear modulus of the material during the CSS tests discussed in Section 4.4 and Section 5.3.2 is anticipated to concern strain levels beyond this strain range. Therefore, a series of DSS constant volume strain-controlled shear probes were performed to strain levels in the range of 0.015-0.025% on specimens C5 and C8 (Table 4.5) and on an additional SOM-A specimen not included in Section 4.4. Figure B1a presents the compression paths in volumetric space of these tests and denotes the e - σ'_{y0} states at which the probes were conducted. Figure B1b-d show the stress-strain results of these probe tests, which were carried out at 0.002% shear strain per minute. It may be noted from these graphs that the probes were performed at various initial σ'_{y0} levels and in either first-loading or overconsolidated conditions (the latter denoted by grey lines). The secant shear modulus (G) at $\gamma = 0.01\%$ was determined using each of the curves in Figure B1b-d. According to Vucetic (1994), this strain magnitude is the approximate threshold at which significant plastic strains occur in materials of the same plasticity index as chalk putty (6-9%; Table 4.1). Additionally, this is the approximate strain level at which G degrades at a constant log-linear rate, as depicted in Figure B2.

The commonly occurring tendency of increasing G with effective stress levels is shown in Figure B1e, which includes a function approximately defining G values corresponding to normally compressed conditions (G_{NC}). As presented by Viggiani and Atkinson (1995) and Jovičić and Coop (1997) for clays and sands, respectively, this function may be defined as:

$$\frac{G_{NC}}{p_{r1}} = A\left(\frac{\sigma'_{y0}}{p_{r2}}\right)^{n} \tag{27}$$

where A and n are material parameters and p_{r1} and p_{r2} are reference pressures used for dimensional consistency. For the data in Figure B1e: $A = 6$, $n = 0.295$, $p_{r1} = 1$ MPa and $p_{r2} = 1$ kPa.

To examine the effect of the volumetric state, Figure B1f compares σ'_{y0} normalised by the equivalent vertical effective stress on the 1D-NCL (Eq. (10)) at the current void ratio (σ'_{e}) with G divided by the G_{NC} value corresponding to normally-compressed conditions obtained using Eq.

(27). Despite the scatter, this Figure suggests that, unlike crushable sands (Jovičić and Coop 1997), the shear modulus of chalk putty is principally dependent on the current volumetric state rather than stress history. This notion had been put forward (with caveats) by Alvarez-Borges et al. (2018) concerning G_0, and suggests that fabric and stiffness are largely controlled by current density and effective stress conditions.

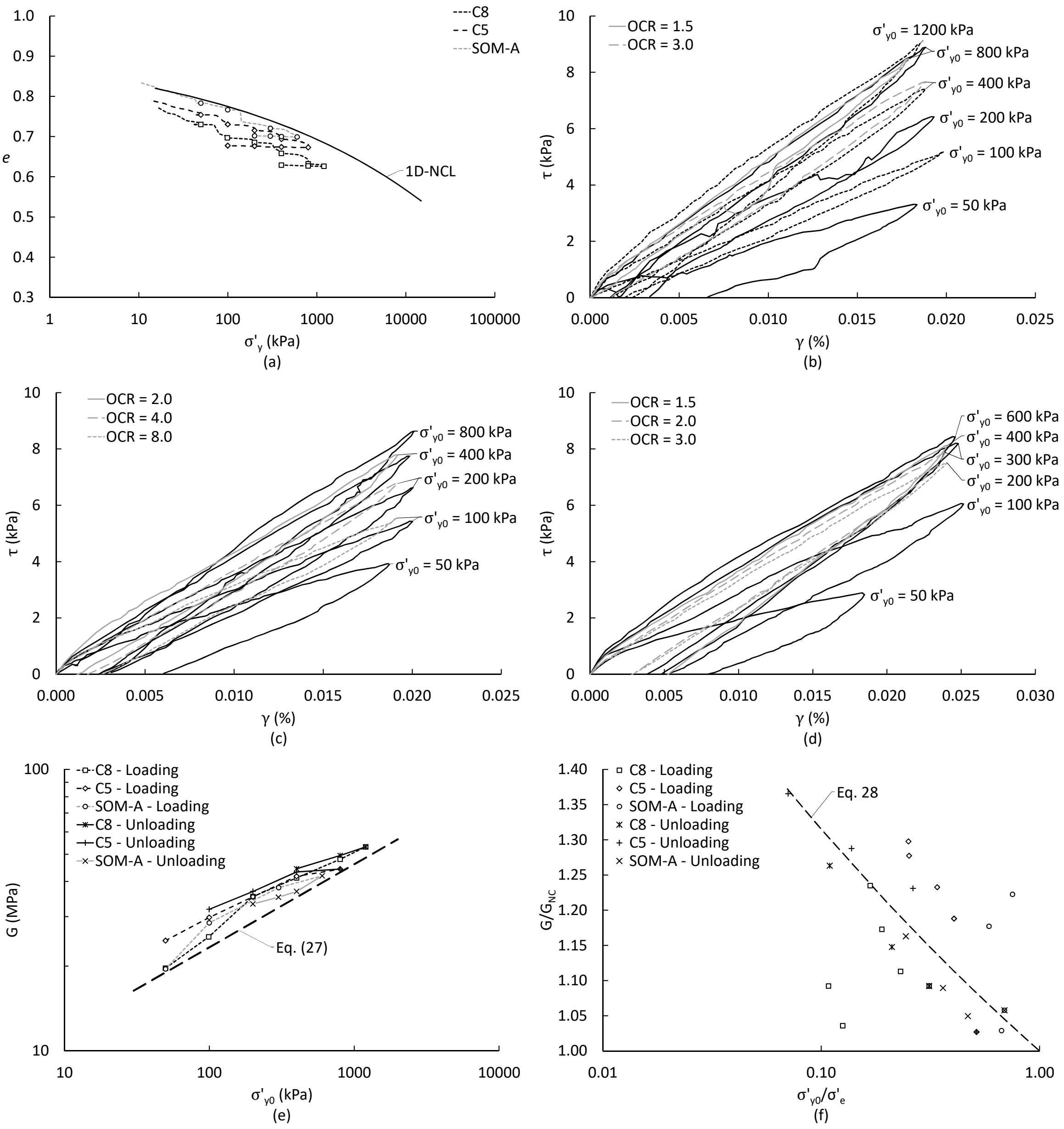

Figure B1. (a) Compression history of stress probe experiments (markers show stress probe locations); Stress probes for C8 (b), C9 (c), SOM-A (d); (e) Variability of G with σ'_{y0} (dotted lines denote probing during virgin compression); (d) Influence of volumetric state on G.

Following Coop and Jovičić (1999), the regression line shown in Figure B1f for the normalised data may be expressed as:

$$\frac{\mathrm{G}}{\mathrm{G_{NC}}} = \left(\frac{\sigma'_{\mathrm{e}}}{\sigma'_{\mathrm{y0}}}\right)^{m} \tag{28}$$

where m = 0.119.

The combination of Eqs. (27) and (28) leads to a similar general expression to that proposed by Rampello et al. (1995) for fine-grained soils:

$$\frac{\mathrm{G}}{\mathrm{p_{r1}}} = 6\left(\frac{\sigma'_{\mathrm{y0}}}{\mathrm{p_{r2}}}\right)^{0.295}\left(\frac{\sigma'_{\mathrm{e}}}{\sigma'_{\mathrm{y0}}}\right)^{0.119} \tag{29}$$

This equation was used to determine the initial shear modulus of chalk putty. A similar function to estimate $\mathrm{G_0}$ has been proposed by Bialowas et al. (2018).

The software-input estimated stiffness in kN/mm for CSS testing was calculated using the initial modulus derived using Eq. (29) and factorised by multiplying it by ≈0.1 to account for softening during testing. Figure 4.19c Figure 4.20c evidence that these stiffness predictions were adequate and resulted in the successful application of the intended sinusoidal time-domain strain regime throughout the stress-controlled test. Such performance was observed in all other CSS tests.

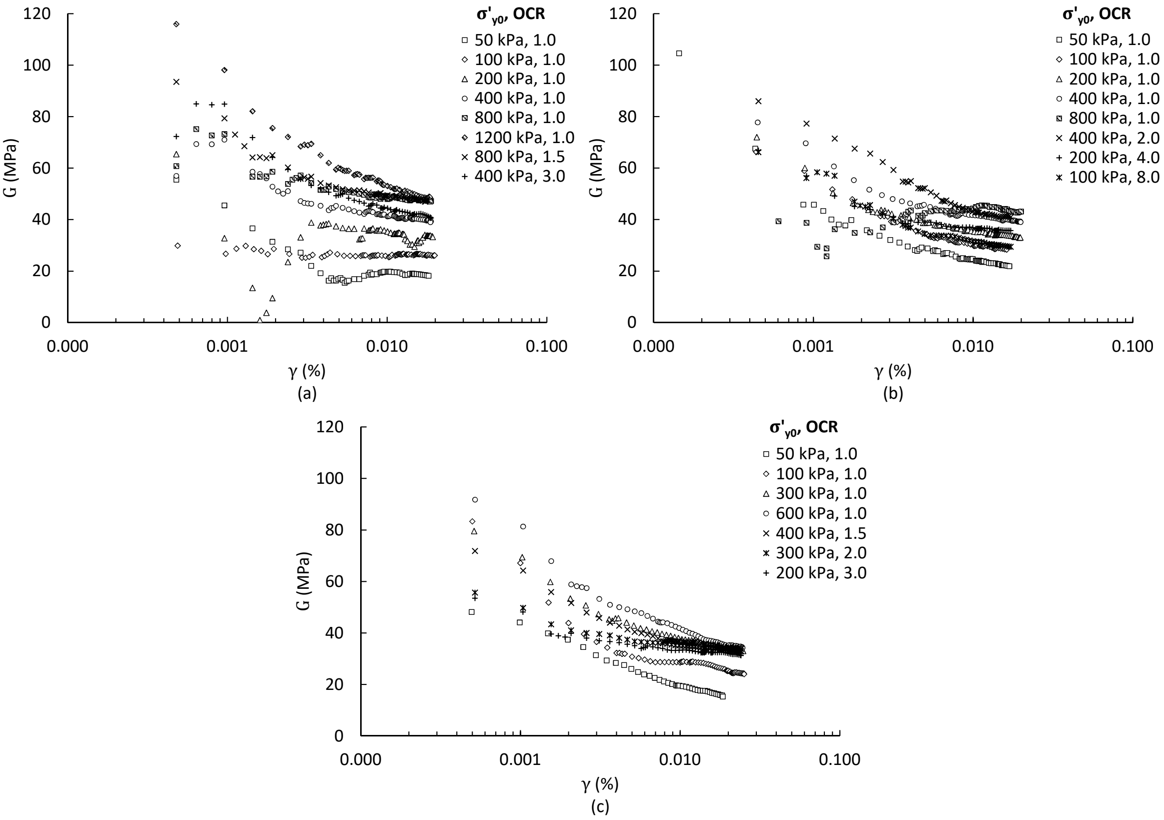

Figure B2. Stiffness degradation trends for stress probes of C8 (a), C5 (b) and SOM-A (c).

Appendix C Interpretation of simple shear test results

Simple shear test results cannot be directly analysed in terms of the principal stress invariants p' and q used to derive the CSL in Section 4.3, because the principal stress state cannot be fully defined by measuring solely σ'_y and τ_y as done in the EMDCSS (and in most devices; Muir Wood et al. 1980). Therefore, several interpretations have been drawn regarding specimen deformation and the attainment of critical state conditions during simple shear. Figure C1 shows the most commonly assumed modes of failure in simple shear, summarised as (after Airey et al., 1985):

- failure mode a, the horizontal plane is the plane of maximum stress obliquity,
- failure mode b, the horizontal plane is the plane of maximum shear stress, and
- failure mode c, maximum stress obliquity occurs first on a vertical plane.

The DSS test data interpretation method described by Oda and Konishi (1974), Oda (1975) and Muir Wood et al. (1980) is perhaps the most widely used (e.g. Airey et al. 1985, Budhu 1988, Lau 1988, and others). This method is based on the relationship between the angle of rotation of the major principal stress from the vertical axis (α) and the τ_y/σ'_y stress ratio at failure observed by Roscoe et al. (1967). This relationship is defined as:

$$\frac{\tau_y}{\sigma'_y} = k \tan \alpha \qquad (30)$$

where k was proposed by Oda and Konishi (1974) and Oda (1975) to be a material constant with similar meaning as the critical stress ratio M defined in Section 4.3.2. By assuming that $\tan \alpha = \tan 45° = 1$ in constant volume conditions at the critical state (when the direction of principal axes of stress and strain increment may be supposed to coincide), these authors state that:

$$\left(\frac{\tau_y}{\sigma'_y}\right)_c = k = \left(\frac{t}{s'}\right)_c = \sin \phi'_c \qquad (31)$$

where t and s' are the Massachusetts Institute of Technology (MIT) principal stress invariants $t = (1/2)(\sigma'_1 - \sigma'_3)$ and $s' = (1/2)(\sigma'_1 + \sigma'_3)$ and the subscript 'c' refers to critical state conditions. The use of MIT invariants instead of q and p' is preferred because the calculation of the intermediate principal stress, σ'_2, would require further empirical assumptions which may decrease the reliability of the method (Muir Wood et al. 1980; Airey et al. 1985).

Alternatively, Gutierrez et al. (2009) describes that $\tan \alpha$ in eq. (30) can be expressed in terms of 2α in the Mohr circle of stress, so that eq. (30) becomes:

$$\frac{\tau_y}{\sigma'_y} = k\left[\frac{\left(\sqrt{1+(\tan 2\alpha)^2}-1\right)}{\tan 2\alpha}\right] \tag{32}$$

Then substituting $\tan 2\alpha = 2\tau_y/(\sigma'_y - \sigma'_x)$ (see Figure 4.14) and rearranging:

$$\sigma'_x = \frac{\tau^2{}_y}{k\sigma'_y} + (1-k)\sigma'_y \tag{33}$$

At the end of consolidation but before shearing, the specimen is in one-dimensional compression and $\tau_y = 0$, therefore:

$$k = 1 - \frac{\sigma'_x}{\sigma'_y} = 1 - K_0 \tag{34}$$

which was also proposed by Muir Wood et al. (1980), and where the σ'_x/σ'_y stress ratio in one-dimensional compression is often determined using Jaky's relationship (Jaky 1944) $K_0 = 1 - \sin\phi'_{crit}$ for normally consolidated soils, thus returning to eq. (31).

However, the use of eq. (34) may lead to potential variability in k, as K_0 is likely to change with consolidation history. Furthermore, experimental data from Airey (1980), Dyvik and Zimmie (1983) and Airey et al. (1985) presented in Figure C2 shows that, for a variety of materials, there appears to be an offset in the $k = \sin\phi'_c$ correlation. To limit uncertainty, Muir Wood et al. (1980) and Airey et al. (1985) suggest the determination of k by measuring the angle of rotation of major principal strain increments at either peak or critical state conditions during a CNL simple shear test, when this value is expected to match α, according to the findings of Roscoe et al. (1967). They also note that any consistency of the k parameter for a given soil should be assumed to occur only when plastic flow has fully developed. This measurement procedure for k has been carried out using CNL Tests 11 and 12 (Table 4.4), and the outcomes are included in Figure C2. Results suggest that the $k = \sin\phi'_{crit}$ assumption is appropriate, though the data is obviously limited. Still, this evidence supports the use of the $k = \sin\phi'_{crit}$ correlation in the present Thesis.

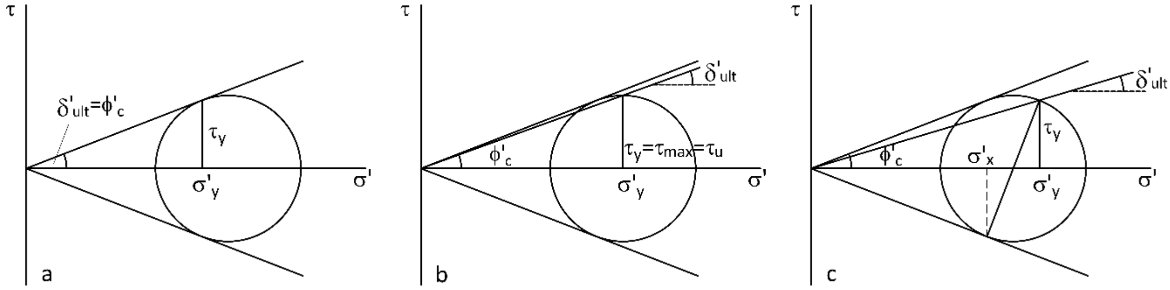

Figure C1. Common modes of failure assumed for simple shear conditions (redrawn from Airey et al., 1985 and Budhu, 1988).

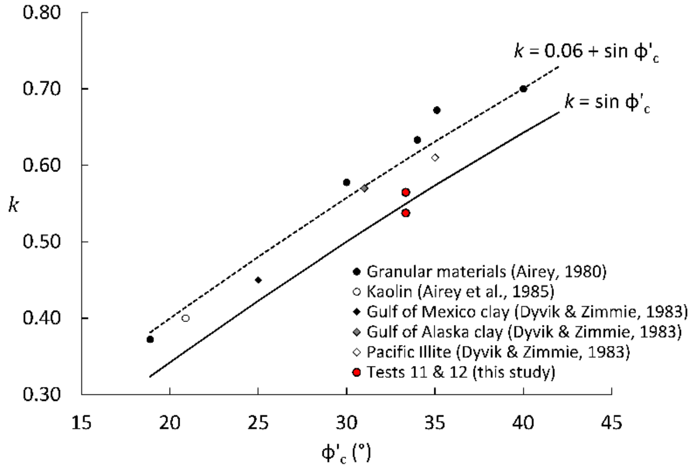

Figure C2. Correlation between *k* and ϕ'$_c$ in monotonic CNL DSS tests (based on Lau, 1988).

Appendix D Fundamentals of X-ray computed tomography

To perform cone beam XCT scans, X-rays are produced by the collision of an electron beam onto a metallic target. The electron beam is created by a large differential in electric potential (i.e. high voltage) between a filament (cathode), which emits electrons, and an anode, which accelerates them onto the target (Kruth et al. 2011). This hardware is placed inside a high-vacuum vessel ('X-ray tube') to avoid interaction with gas atoms present in air (Sun et al. 2012). During collision, most electrons in the beam impact and eject electrons from the outer orbitals of the atoms constituting the target, producing delta rays and heat (Figure D1a; Hsieh, 2015). A small portion of beam electrons may be abruptly decelerated and diverted by attraction to the nuclei of the target atoms (Figure D1c), or may crash onto one of the electrons on the inner orbitals of said atoms (Figure D1b). The former produces a continuous spectrum of X-rays known as Bremsstrahlung radiation; the latter produces a discrete spectrum of X-rays named characteristic radiation (Figure D2). The X-ray photons then exit the target and pass through a diaphragm as they depart the X-ray tube, thus producing a cone-shaped beam (Kruth et al. 2011; Sun et al. 2012).

X-rays are attenuated by the atoms composing the specimen principally by two phenomena: photoelectric interaction and Compton scattering (Hsieh 2015). The photoelectric interaction occurs when an X-ray photon collides with an inner orbital electron with sufficient energy to eject it as a photoelectron (Einstein 1905). The filling of the electron vacancy produces characteristic radiation, which in certain materials will be within the visible light spectrum (Figure D3a). The X-ray photon transfers all its energy to the electron during collision, thus disappearing. Compton scattering occurs when the X-ray photon collides with an electron from the outer shell of the atom and ejects it as a recoil electron (Compton 1923). The photon transfers some of its energy during the process and becomes deflected (i.e. scattered) but does not disappear (it becomes a 'Compton photon'; Figure D3b). Both phenomena are X-ray energy- and atomic number-dependent (Markowicz 2002; Kruth et al. 2011; Hsieh 2015). At energies in the range of 50-100 keV, the photoelectric effect is dominant and photon absorption is proportional to the atomic number (Z) of the specimen elevated to a power between 4 and 5. At energies above this range and up to 5-10 MeV, Compton scattering becomes dominant and proportional to Z. Therefore, the clear visualisation of materials exhibiting small differences in atomic number using XCT is often only practicable at low energies. However, low energies limit the capacity of the x-ray to penetrate matter and, consequently, restricts specimen size.

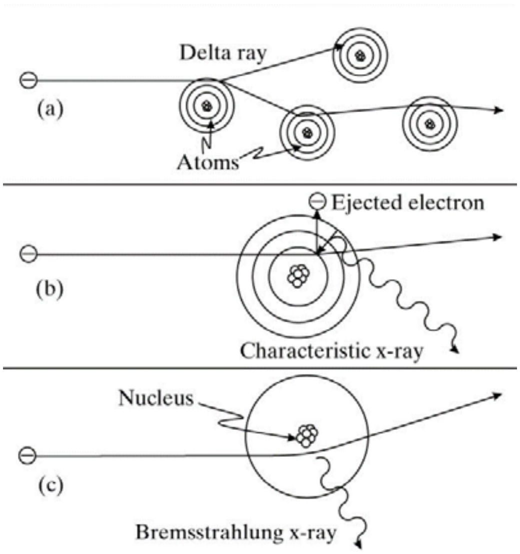

Figure D1. Beam electron interaction with atom target: (a) delta ray production; (b) characteristic interaction; (c) Bremsstrahlung interaction. From Kinahan (2016).

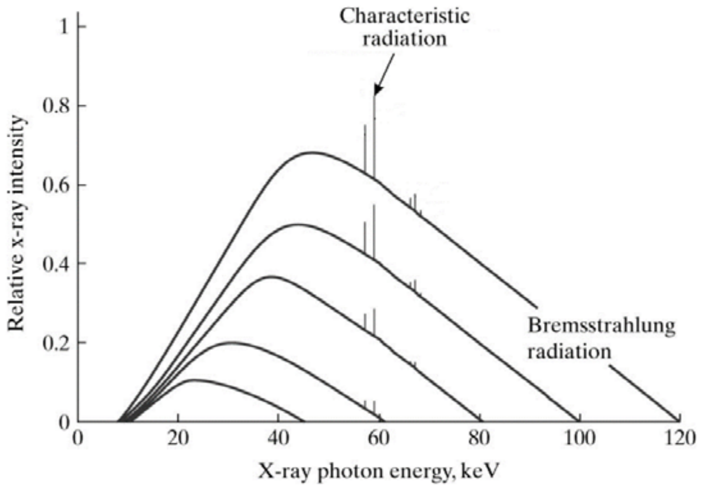

Figure D2. Energy spectrum of Bremsstrahlung and characteristic radiation at various intensities (edited from Kinahan, 2016).

Fundamental parameters of cone beam XCT scanning are (Kruth et al. 2011; Sun et al. 2012; Hsieh 2015):

- Voltage (or tension). The electric potential that accelerates electrons and produces the electron beam. Usually measured in kilovolts (kV).
- Electrical current. Electron flow rate supplied to the X-ray tube. Higher electrical current results in a larger number of electrons in the beam per unit of time, which produce more X-ray photons when the electrons collide with the target. Thus, current controls X-ray intensity, which is the number of photons delivered per unit area per unit of time to the

specimen and/or detector (i.e., X-ray flux or fluence). Electrical current is commonly measured in microamperes (µA).

- Photon energy. Energy of an X-ray photon produced by the interaction between an electron that has been accelerated by a given voltage and the target. Thus, higher voltages result in higher X-ray photon energies (and a higher energy spectrum), which in turn control the capacity of the X-ray to penetrate an object. Conventionally expressed in kiloelectronvolts (keV).
- Detector characteristics. Cone-beam scanners generally employ 2D flat panel detectors. Most flat panel detectors are an array of photodetector pixels covered by a matrix of scintillating amorphous silicon. Scintillating materials exhibit a strong photoelectric interaction with X-ray photons, which produces visible light (as described above). This light is sensed by the photodetector pixels, thus producing a signal. Detector size and position relative to the X-ray focal spot and the specimen controls scan magnification, as explained in Figure D4. Because the focal spot size cannot be infinitely small, there may be a trade-off between magnification and image quality, as shown in this Figure. Resolution is often estimated by dividing the width in mm of the specimen region within the field of view by the width in pixels of the detector.
- Focal spot size. This parameter results from the interaction between the breadth of the electron beam colliding with the target and the slope angle of the target, as shown in Figure D5. Micro-focus technologies make use of electromagnetic lenses to enforce sub-millimetre electron beam breadths. In addition to its abovementioned effect on scan resolution, a balance between focal spot size and detector cell size is often sought. If the focal spot is too large, incident photons are distributed in a large number of detector cells, reducing efficiency. Conversely, if the focal spot is too small, the reduced flux delivered to each cell may be masked by electrical (hardware) noise.

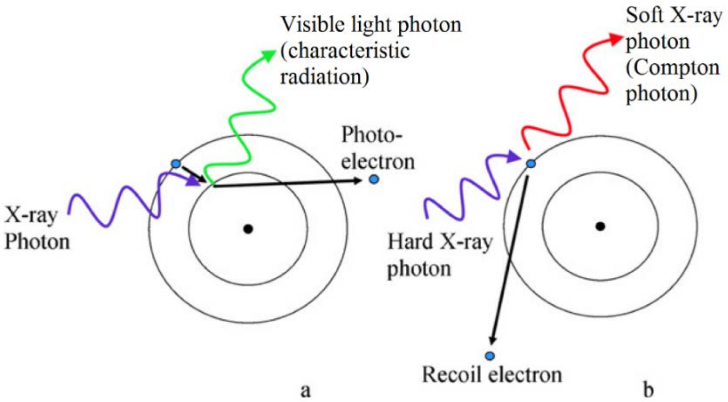

Figure D3. Principal X-ray attenuation (absorption) interactions (edited from Kruth et al., 2011).

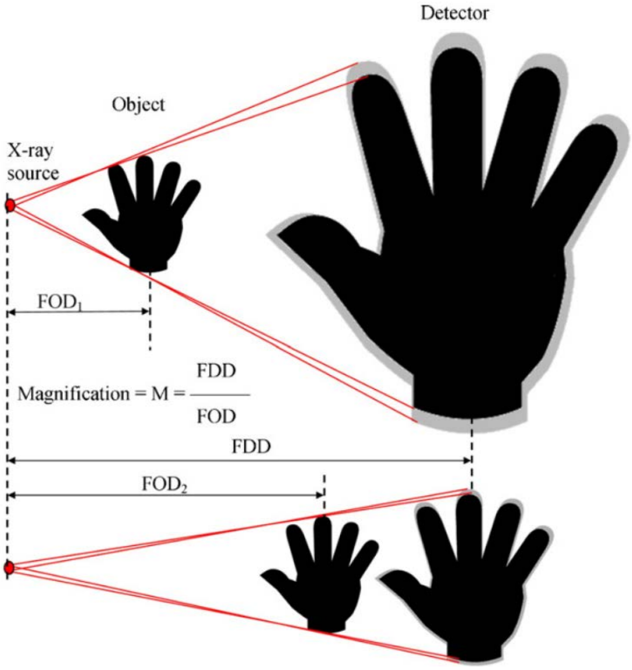

Figure D4. Estimation of scan magnification and trade-off between magnification and image blurriness (from Kruth et al., 2011).

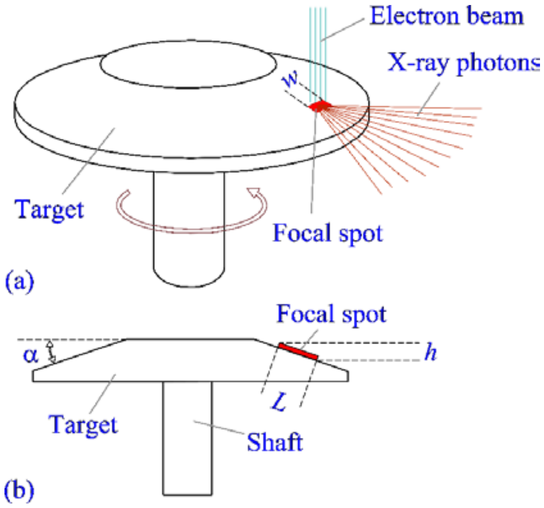

Figure D5. (a) Isometric schematic of rotating target, electron beam, focal spot and X-ray beam; (b) cross-section schematic of focal spot. Focal spot dimensions *w* = width; *L* = length; *h* = projected length. Re-drawn from Hsieh (2015).

Appendix E Model pile jacking-scanning rig

The testing-scanning hardware was designed to be able to attach the chalk specimen to the Instron machine and the XCT scanning stage. The device consists of the elements shown in Figure E1, labelled A to H. The characteristics and functions of each element are presented in Table E1, a cross-section view of the assembled rig is shown in Figure E2 and photographs of the device are given in Figure 4.25. Drawings for all hardware parts are provided in Figures E3-8.

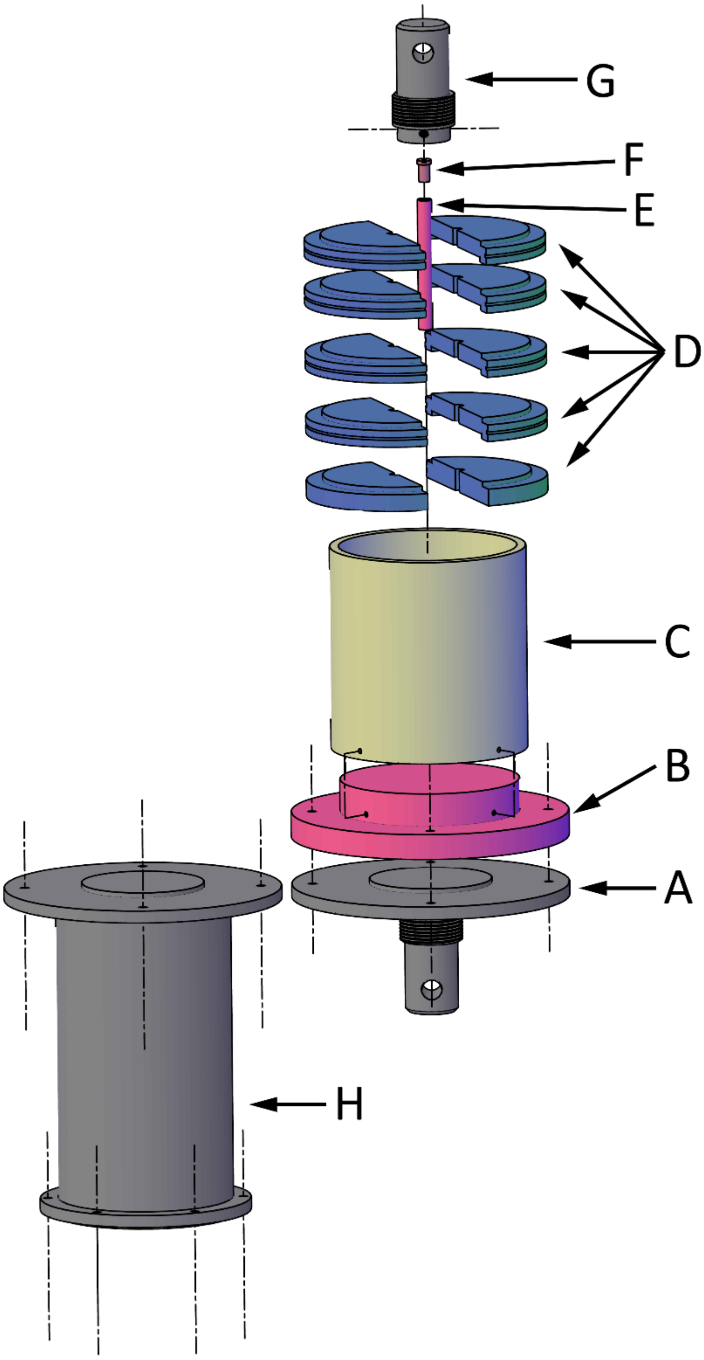

Figure E1. Assembly diagram of model pile testing-scanning rig (see text and Table E1 for part description).

Appendix E

Table E1. Jacking-scanning rig elements and functions.

Part	**Material**	**Function**
A – Instron compression-tension plate	EN1A Steel	Fixture attaching part B to the Instron test frame. Features a central seating ridge and 4 through holes to secure with part B and allow for tension loading. Figure E3.
B – Testing pedestal	2024 Aluminium	Base plate for chalk specimen. Attached to A by 4 nuts and bolts. Features a centred circular recess on bottom surface to improve coupling with parts A and H. Figure E4.
C – Specimen confinement	Perspex	125 mm diameter by 5 mm thick and 120 mm high pipe casing for chalk specimen. Attached to B by 4 screws. Figure E2.
D – Split-case pile confinement	6063 Aluminium	Mitigates pile buckling during installation. Formed by diametrically cut discs with a circumferential groove and a circular recess on the bottom surface. Sub-element D1 features no recess because it rests on the top flat surface of the chalk specimen. Assembled using cable ties and held in place by part C. Figure E5.
E – Model pile	Perspex/PEEK	Cylindrical solid bar or tubular element (see Table 4.6).
F – Pile head insert	EN1A Steel	Inserted at the head of tubular piles to prevent crushing damage by the grub-screw grip of element G. Features a longitudinal through-hole and a groove in the top surface to prevent air from being trapped inside the pile. Figure E6.
G – Pile head grip Instron fixture	EN1A Steel	Element attaching the pile head to the Instron test frame via 4 grub screws. Figure E7.
H – Scanning pedestal	6063 Aluminium	Replaces element A during XCT scanning. Features a central seating ridge. Attaches the rig via part B to the XCT scanner rotating stage while providing an offset distance from it to prevent image artefacts. Figure E8.

Elements A to G were employed during pile installation. Parts D, F and G were removed prior to XCT imaging, while element A was substituted with spacer element H. All parts used during XCT scanning (B, C, and E) were made from non-ferrous materials to minimise image artefacts.

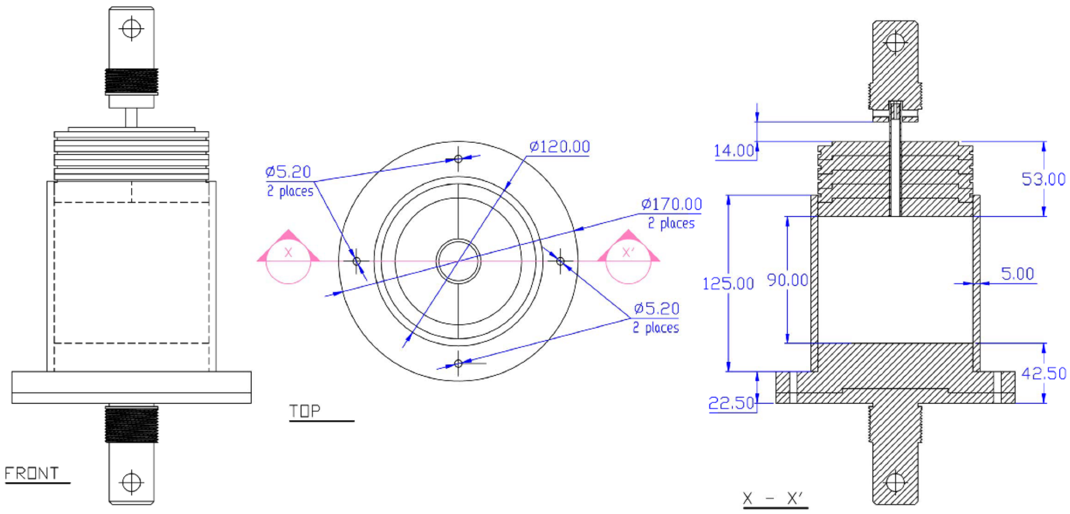

Figure E2. Front, top and cross-section view of jacking-scanning rig.

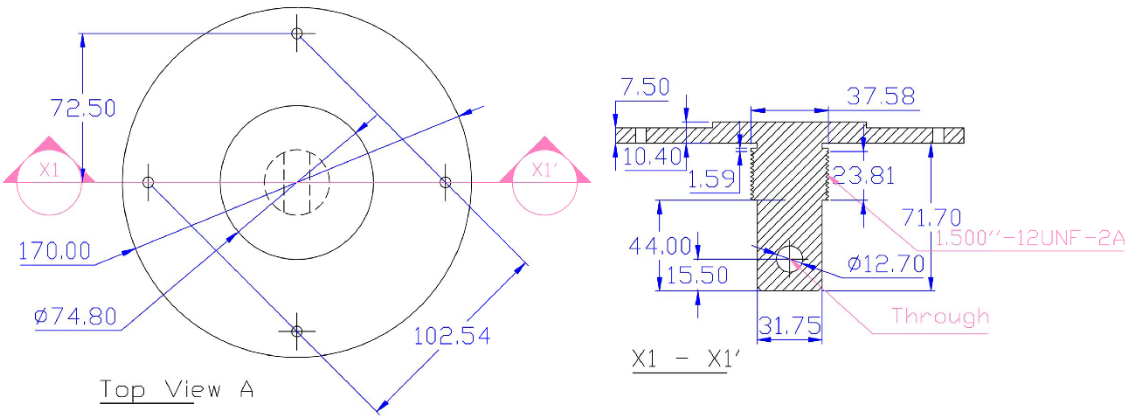

Figure E3. Top and cross-section view of part A.

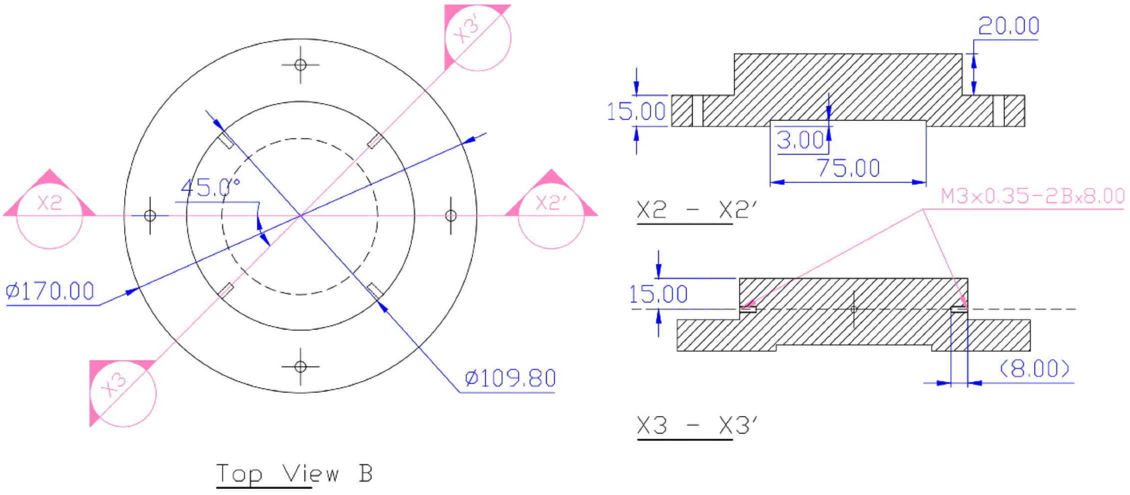

Figure E4. Top and cross-section views of part B.

Appendix E

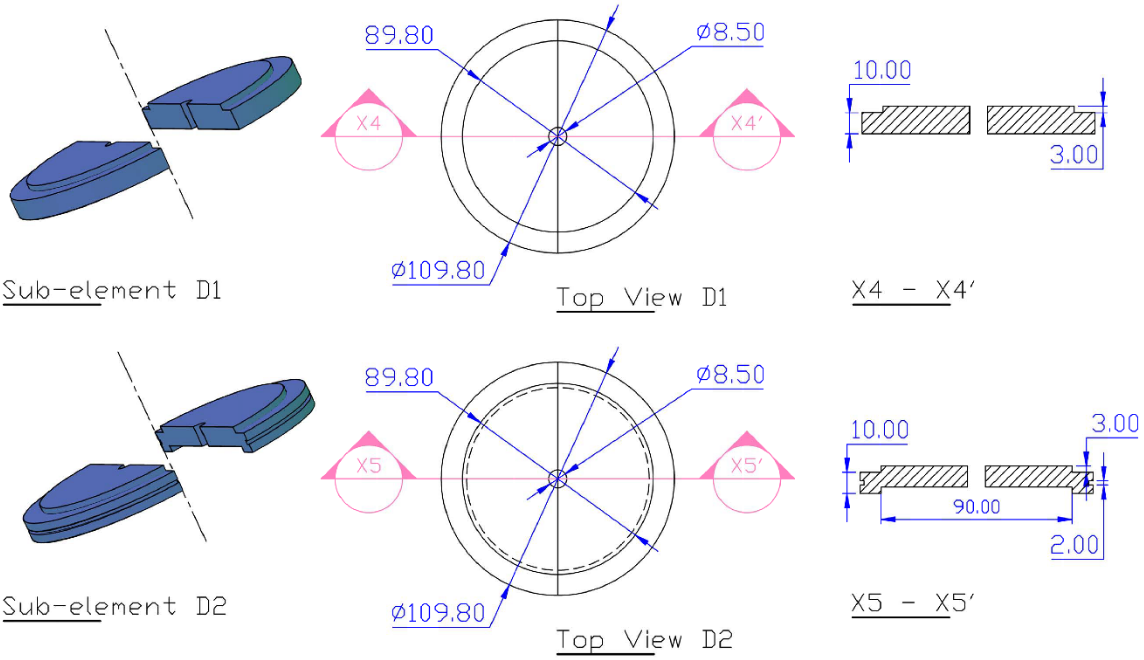

Figure E5. Isometric, top and cross-section views of part D.

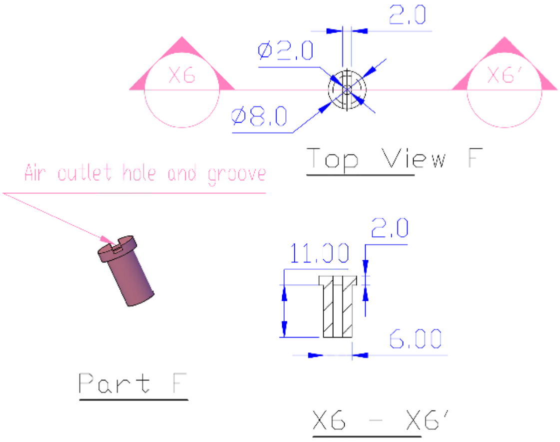

Figure E6. Isometric, top and cross-section views of part F.

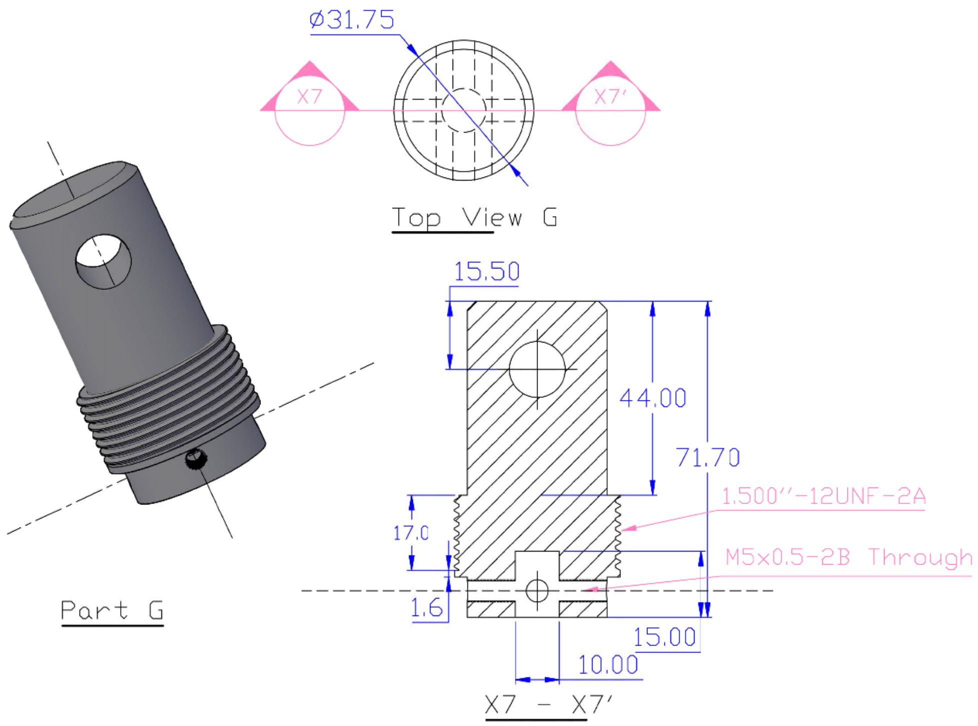

Figure E7. Isometric, top and cross-section views of part G.

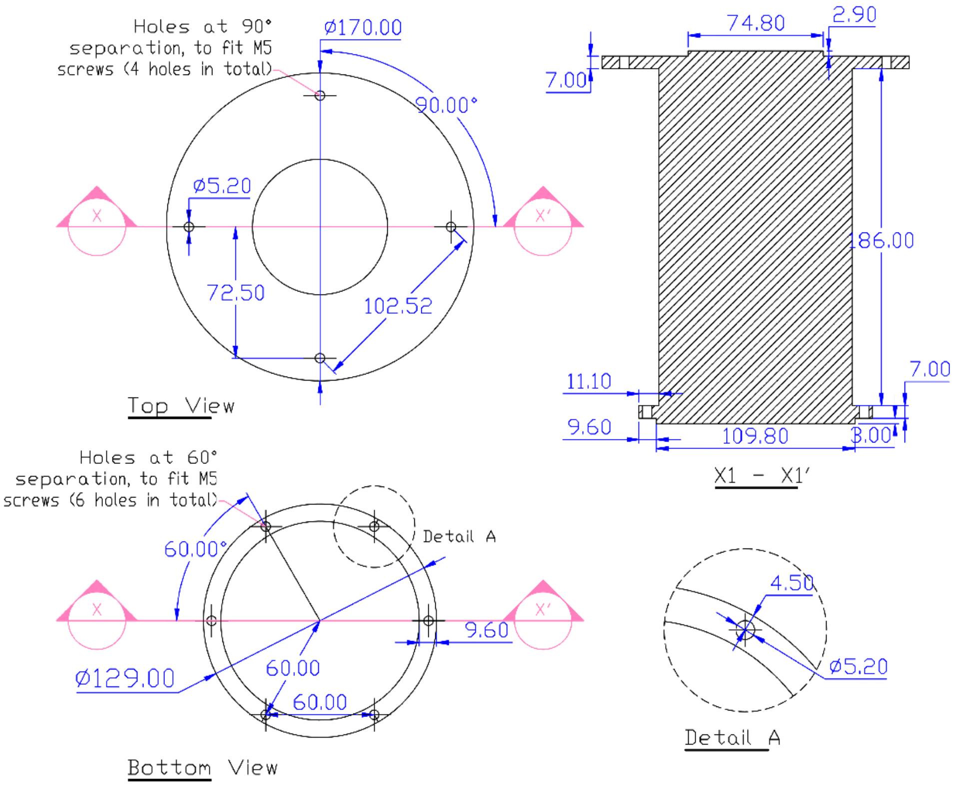

Figure E8. Top, bottom, cross-section and detail views of part H.

Appendix E

Appendix F Post-reconstruction conditioned XCT data

Figure F2a shows the raw Z-direction mean grey value profiles for experiments CT03 and CT04 corresponding to a 30x30 pixel window with the same cartesian coordinates than the one shown in Figure 4.27. Figure F2b depicts these same profiles after cropping out the top-hat effects and realigning and re-slicing the volumes as described in Section 4.5.4.3. Figure F2c presents the outcome of the application to CT03 and CT04 of the correction routine for the Z-direction non-uniformity in grey value profiles described in this Section. Likewise, the effect of shifting the global grey value range of the volumes is shown in Figure F2d. Finally, Figure F1 compares normalised IDD measurements with normalised raw (acquired) and ‘corrected’ Z-direction mean grey value profiles for the same region from where the IDD data was produced, for CT03-03 and CT04-04. This processed data was used to carry out the density measurements presented in Section 4.5.4.4 and the analysis of Section 5.4.

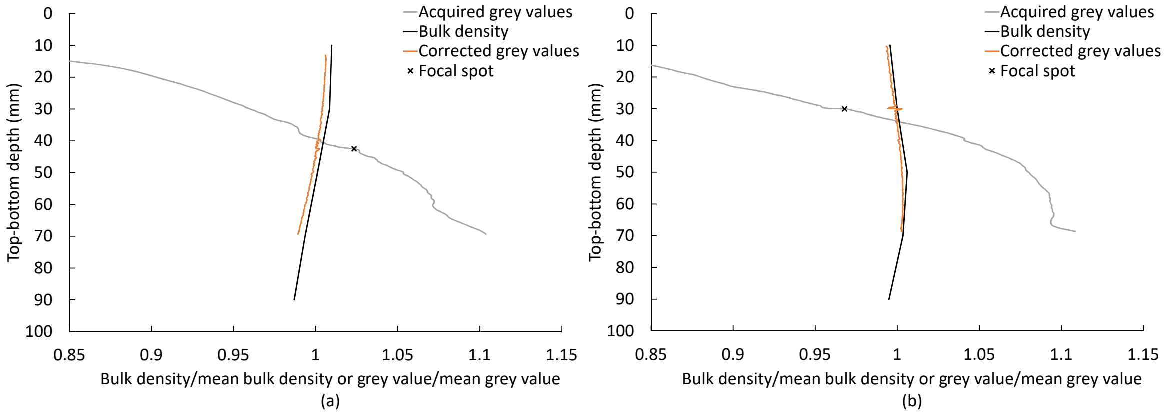

Figure F1. Top-bottom normalised intact bulk density and grey value profiles of the peripheral region shown in Figure 4.31b of CT03-03 (a) and CT04-02 (b).

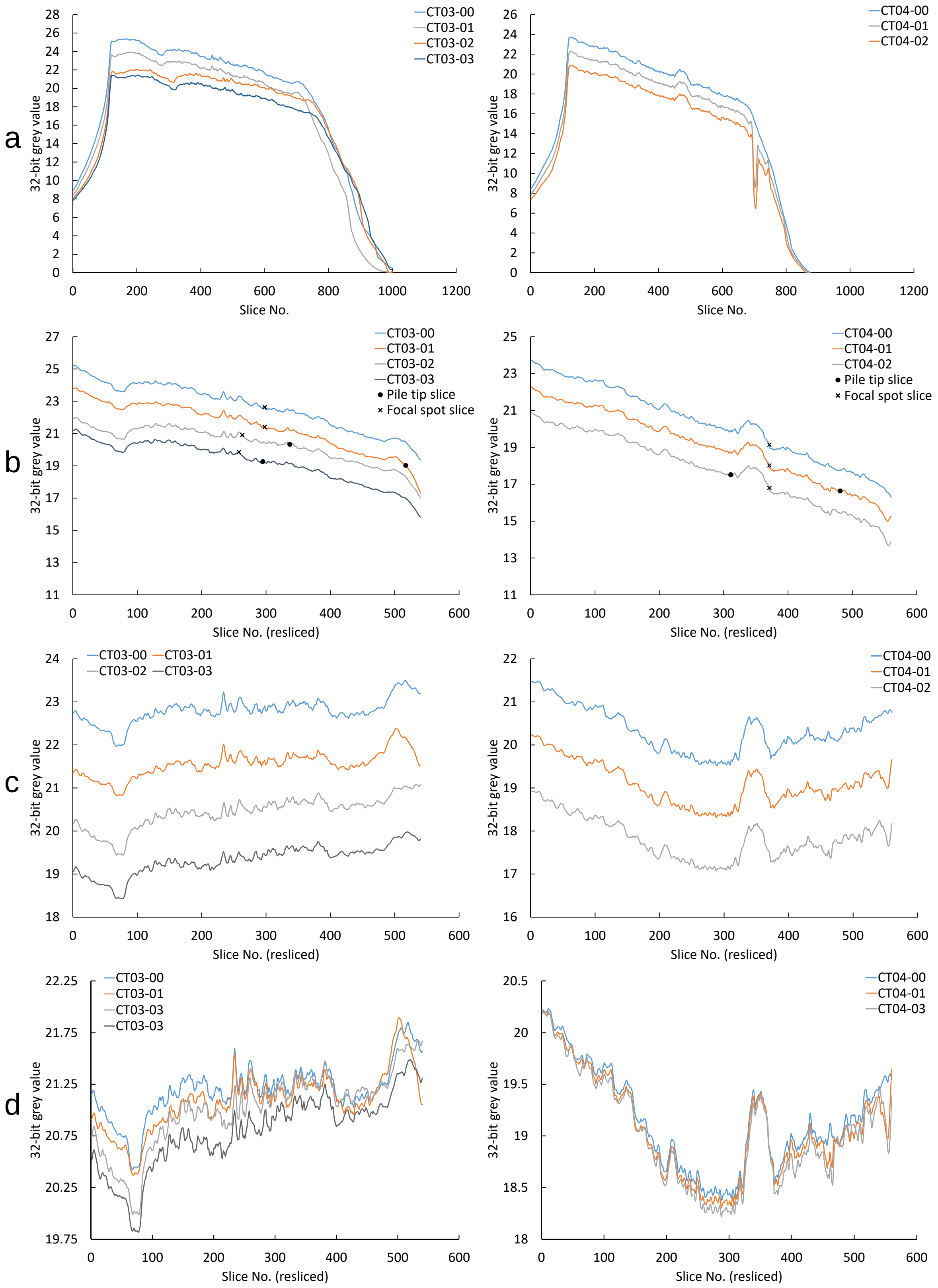

Figure F2. 30x30 pixel sampling window Z-direction mean grey value profiles of (a) unprocessed data, (b) cropped, realigned and re-sliced data, (c) non-uniformity corrected data and (d) data after shifting the global grey value range of tests CT03 and CT04.

List of References

Addis, M.A. 1987. Mechanisms of sediment compaction responsible for oil field subsidence. PhD Thesis, University of London, London, UK.

Addis, M.A. and Jones, M.E. 1990. Mechanical behaviour and strain rate dependance of high porosity chalk. *In* Chalk: Proceedings of the International Chalk Symposium. Thomas Telford Ltd, London, UK, pp. 239-244.

Aghakouchak, A., Sim, W.W. and Jardine, R.J. 2015. Stress-path laboratory tests to characterise the cyclic behaviour of piles driven in sands. Soils and Foundations, **55**(5): 917-928.

Airey, D.W. 1980. Soils in the cricular simple shear apparatus. MPhil Thesis, University of Cambridge, Cambridge, UK.

Airey, D.W. and Wood, D.M. 1987. An Evaluation of Direct Simple Shear Tests on Clay. Géotechnique, **37**(1): 25-35. doi: 10.1680/geot.1987.37.1.25

Airey, D.W., Budhu, M. and Muir Wood, D. 1985. Some aspects of the behaviour of soils in simple shear. *In* Developments in Soil Mechanics and Foundation Engineering. *Edited by* P.K. Banerjee and R. Butterfield. Elsevier Applied Science Publishers, London, UK. pp. 185-213.

Airey, D.W., Al-Douri, R. and Poulos, H.G. 1992. Estimation of Pile Friction Degradation from Shearbox Tests. Geotechnical Testing Journal, **15**(4): 388-392.

Alarcon-Guzman, A. and Leonards, G.A. 1988. Discussion of "Liquefaction Evaluation Procedure" by S.J. Poulos, G. Castro, and J.W. France (J Geotech Eng-Asce, 11(6)). Journal of Geotechnical Engineering-Asce, **114**(2): 232-236. doi: 10.1061/(ASCE)0733-9410(1988)114:2(232)

Aldiss, D.T., Farrant, A.R. and Hopson, P.M. 2012. Geological mapping of the Late Cretaceous Chalk Group of southern England: a specialised application of landform interpretation. Proceedings of the Geologists Association, **123**(5): 728-741. doi: 10.1016/j.pgeola.2012.06.005

Aldiss, D.T., Bloomfield, J.R., Buckley, D.K., Doran, S.K., Evans, D., Hopson, P., Royse, K.R. and Woods, M.A. (2004) *A Geological Model for the Chalk of East Kent. Volume 1 of 2: Report*. London (UK): British Geological Survey.

Altuhafi, F. and Jardine, R.J. 2011. Effect of particle breakage and strain path reversal on the properties of sands located near driven piles. *In* Deformation Characteristics of Geomaterials, Proceedings of the 5th International Sympsium. IOS Press, pp. 388-395.

Altuhafi, F.N. and Coop, M.R. 2011. Changes to particle characteristics associated with the compression of sands. Géotechnique, **61**(6): 459-471. doi: 10.1680/geot.9.P.114

Altuhafi, F.N., Coop, M.R. and Georgiannou, V.N. 2016. Effect of Particle Shape on the Mechanical Behavior of Natural Sands. Journal of Geotechnical and Geoenvironmental Engineering, **142**(12): doi: 10.1061/(Asce)Gt.1943-5606.0001569

Alvarez-Borges, F.J. 2014. The application of simple shear testing to evaluate the shaft resistance on piles driven in chalk. MSc Dissertation, University of Southampton, Southampton, UK.

Alvarez-Borges, F.J., Madhusudhan, B.N. and Richards, D.J. 2018. Stiffness of Destructured Weak Rock. *In* Micro to MACRO Mathematical Modelling in Soil Mechanics. Springer Nature, pp. 1-9. doi: 10.1007/978-3-319-99474-1_1

Andersen, K. 2009. Bearing capacity under cyclic loading — offshore, along the coast, and on land, The 21st Bjerrum Lecture. Canadian Geotechnical Journal, **46**(5): 513-535.

Andersen, K., Puech, A.A. and Jardine, R.J. 2013. Cyclic resistant geotechnical design and parameter selection for offshore engineering and other applications. *In* Design for Cyclic Loading: Piles and other Foundations, Proceedings of TC 209 Workshop of the 18th ICSMGE. Presses des Ponts, Paris (FR), pp. 9-44.

Anusic, I. 2018. Installation of Monopiles for Offshore Wind Turbine Foundations. PhD Thesis, Norwegian University of Science and Technology, Trondheim, NOR.

American Petroleum Institute 2000. API RP 2A-WSD: Recommended Practice for Planning, Designing and Constructing Fixed Offshore Platforms - Working Stress Design, 21st Edition. Washington DC (USA).

American Petroleum Institute 2014. ANSI/API RP2 GEO: Recommended Practice Geotechnical and Foundation Design Considerations. Washington DC (USA).

Arroyo, M., Butlanska, J., Gens, A., Calvetti, F. and Jamiolkowski, M. 2011. Cone penetration tests in a virtual calibration chamber. Géotechnique, **61**(6): 525-531. doi: 10.1680/geot.9.P.067

Arthur, J.R.F., Koenders, M. and Wong, R.K.S. 1986. Anisotropy in particle contacts associated with shearing in granular media. Acta Mechanica, **64**(1): 19-29.

American Society for Testing and Materials 2007. ASTM-D6528-07: Standard Test Method for Consolidated Undrained Direct Simple Shear Testing of Cohesive Soils. West Conshohocken, PA (USA).

Atkinson, J.H. 1993. An Introduction to the Mechanics of Soils and Foundations Through Critical State Soil Mechanics. McGraw-Hill Book Company Europe, Maidenhead, UK.

Augustesen, A.H., Leth, C.T., Østergaard, M.U., Møller, M., Dührkop, J. and Barbosa, P. 2015. Design methodology for cyclically and axially loaded piles in chalk for Wikinger OWF. *In* Frontiers in Offshore Geotechnics III. CRC Press/Balkema, London, UK, pp. 509-514.

Baek, J., Pineda, A.R. and Pelc, N.J. 2013. To bin or not to bin? The effect of CT system limiting resolution on noise and detectability. Physics in Medicine and Biology, **58**(5): 1433-1446.

Baligh, M.M. 1985. Strain Path Method. Journal of Geotechnical Engineering-Asce, **111**(9): 1108-1138. doi: 10.1061/(Asce)0733-9410(1985)111:9(1108)

Baligh, M.M., Azzouz, A.S. and Chin, C.T. 1987. Disturbances Due to Ideal Tube Sampling. Journal of Geotechnical Engineering-Asce, **113**(7): 739-757. doi: 10.1061/(Asce)0733-9410(1987)113:7(739)

Barbosa, P., Geduhn, M., Jardine, R.J., Schroeder, F. and Horn, M. 2015a. Full scale offshore verification of axial pile design in chalk. *In* Frontiers in Offshore Geotechnics III. CRC Press/Balkema, pp. 515-520.

Barbosa, P., Geduhn, M., Jardine, R.J., Schroeder, F. and Horn, M. 2015b. Offshore pile load tests in chalk. *In* Proceedings of the 16th European Conference on Soil Mechanics and Geotechnical Engineering. Institution of Civil Engineers (ICE) - Thomas Telford, pp. 2885-2890.

Barnes, G.E. 2013. The Plastic Limit and Workability of Soils. PhD Thesis, University of Manchester, Manchester, UK.

Barton, N.R. 1986. Deformation phenomena in jointed rock, The 8th Laurits Bjerrum Memorial Lecture. Géotechnique, **36**(2): 147-167. doi: 10.1680/geot.1986.36.2.147

BCP 1971. Field tests on piles in sand. Soils and Foundations, **11**(2): 29-49.

Been, K. and Jefferies, M.G. 1985. A State Parameter for Sands. Géotechnique, **35**(2): 99-112. doi: 10.1680/geot.1985.35.2.99

Been, K., Jefferies, M.G. and Hachey, J. 1991. The critical state of sands. Géotechnique, **41**(3): 365-381. doi: 10.1680/geot.1991.41.3.365

Bell, F.G., Culshaw, M.G. and Cripps, J.C. 1999. A review of selected engineering geological characteristics of English Chalk. Engineering Geology, **54**(3-4): 237-269. doi: 10.1016/S0013-7952(99)00043-5

Bialowas, G. 2017. Time and Stress Dependent Mechanical Properties of Reconstituted Chalk. PhD Thesis, University of Bristol, Bristol, UK.

Bialowas, G. and Diambra, A. 2018. Time and stress dependent strength and stiffness of reconstituted chalk. *In* Engineering in Chalk, Proceedings of the Chalk 2018 Conference. ICE Publishing, pp. 503-508.

Bialowas, G.A., Diambra, A. and Nash, D.F.T. 2018. Stress and time-dependent properties of crushed chalk. Proceedings of the Institution of Civil Engineers-Geotechnical Engineering, **171**(6): 530-544. doi: 10.1680/jgeen.17.00168

Birnbacher, L., Willner, M., Marschner, M., Pfeiffer, D., Pfeiffer, F. and Herzen, J. 2018. Accurate effective atomic number determination with polychromatic grating-based phase-contrast computed tomography. Optics Express, **26**(12): 15153-15166. 10.1364/Oe.26.015153

Bishop, A.W. and Henkel, D.J. 1962. The Measurement of Soil Properties in the Triaxial Test. (Second Edition Edition), Edward Arnold, London, UK.

Bishop, A.W. and Green, G.E. 1965. The influence of end restraint on the compression strength of a cohesionless soil. Géotechnique, **15**(3): 243-266. doi: 10.1680/geot.1965.15.3.243

Blumenthal, W.R., Cady, C.M., Lopez, M.F., Gray, G.T. and Idar, D.J. 2002. Influence of temperature and strain rate on the compressive behavior of PMMA and polycarbonate polymers. *In* Shock Compression of Condensed Matter-2001, Proceedings. AIP Publishing, pp. 665-668. doi: 10.1063/1.1483626

Bond, A.J., Jardine, R.J. and Dalton, J. 1991. Design and performance of the imperial college instrumented pile. Geotechnical Testing Journal, **14**(4): 413-424.

Boulanger, R.W. and Idriss, I.M. 2006. Liquefaction susceptibility criteria for silts and clays. Journal of Geotechnical and Geoenvironmental Engineering, **132**(11): 1413-1426. doi: 10.1061/(Asce)1090-0241(2006)132:11(1413)

Boulon, M. and Foray, P. 1986. Physical and numerical simulation of lateral shaft friction along offshore piles in sand. *In* Numerical Methods in Offshore Piling. *Edited*. Institut Français du Pétrole - Laboratoire Central Des Ponts et Chaussées - Technip, Saint-Just-la-Pendue, FR. pp. 127-148.

Braun, H., Kyriakou, Y., Kachelriss, M. and Kalender, W.A. 2010. The influence of the heel effect in cone-beam computed tomography: artifacts in standard and novel geometries and their correction. Physics in Medicine and Biology, **55**(19): 6005-6021. doi: 10.1088/0031-9155/55/19/024

Bristow, R., Mortimore, R. and Wood, C. 1997. Lithostratigraphy for mapping the Chalk of southern England. Proceedings of the Geologists Association, **108**(4): 293-315. Doi: 10.1016/S0016-7878(97)80014-4

Brucy, F., Meunier, J. and Nauroy, J.F. 1991. Behaviour of pile plug in sandy soils during and after driving. *In* 23rd Offshore Technology Conference. OTC, pp. 145-152.

British Standards Institution 2009. 13320:2009. Particle size analysis - Laser diffraction methods. London, UK.

British Standards Institution (BSI) 1998a. 1377-5:1990. Methods of test for soils for civil engineering purposes - Part 5: Compressibility, permeability and durability tests. London, UK.

British Standards Institution (BSI) 1998b. 1377-2:1990. Methods of test for soils for civil engineering purposes - Part 2: Classification tests. London, UK.

British Standards Institution (BSI) 1998c. 1377-7:1990 Methods of tests for soils for civil engineering purposes - Part 7: Shear strength tests (total stress). London, UK.

Buckley, R.M. 2018. The axial behaviour of displacement piles in chalk. PhD Thesis, Imperial College London, London (UK).

Buckley, R.M., Jardine, R.J., Kontoe, S. and Lehane, B.M. 2018a. Effective stress regime around a jacked steel pile during installation ageing and load testing in chalk. Canadian Geotechnical Journal, **55**(11): 1577-1591. doi: 10.1139/cgj-2017-0145

Buckley, R.M., Jardine, R.J., Kontoe, S., Parker, D. and Schroeder, F.C. 2018b. Ageing and cyclic behaviour of axially loaded piles driven in chalk. Géotechnique, **68**(2): 146-161. doi: 10.1680/jgeot.17.P.012

Budhu, M. 1988. Failure State of a Sand in Simple Shear. Canadian Geotechnical Journal, **25**(2): 395-400. doi: 10.1139/t88-041

Bundy, S.P.S. 2013. Geotechnical properties of chalk putties. PhD Thesis, University of Portsmouth, Portsmouth, UK.

Burland, J.B. 1990a. On the compressibility and shear strength of natural clays, The 30th Rankine Lecture. Géotechnique, **40**(3): 329-378. doi: 10.1680/geot.1990.40.3.329

Burland, J.B. 1990b. Preface. *In* Chalk: Proceedings of the International Chalk Symposium. Thomas Telford, London, UK, pp. 1-4.

Burland, J.B. and Bayliss, F.V.S. 1990. Settlement and yielding of upper chalk supporting the foundations for a silo complex. *In* Chalk: Proceedings of the International Chalk Symposium. Thomas Telford, London, UK, pp. 365-374.

Burland, J.B. and French, D.J. 1990. Results of trials in weathered chalk of a novel piling system - the wedge-pile. *In* Chalk: Proceedings of the International Chalk Symposium. Thomas Telford Ltd, pp. 375-383.

Burland, J.B., Hancock, R.J. and May, J. 1983. A case history of a foundation problem in soft chalk. Géotechnique, **33**(4): 385-395.

Byrne, B.W. 1994. Driven Pipe piles in Dense Sand. Honours thesis, University of Western Australia, Perth, AU.

Cancelli, A., Guadagnini, R. and Pellegrini, M. 1982. Friction –cone– penetration testing in alluvial soils. *In* Proceedings of the 2nd European Symposium on Penetration Testing. AA Balkema, pp. 513-518.

Canny, J. 1986. A Computational Approach to Edge Detection. IEEE Transactions on Pattern Analysis and Machine Intelligence, **8**(6): 679-698.

Carotenuto, P., Meyer, V.M., Strøm, P.J., Cabarkapa, Z., St John, H. and Jardine, R. 2018. Installation and axial capacity of the Sheringham Shoal offhsore wind farm monopiles - a case history. *In* Engineering in Chalk, Proceedings of the Chalk 2018 Conference. ICE Publishing, pp. 117-122.

Carrera, A., Coop, M. and Lancellotta, R. 2011. Influence of grading on the mechanical behaviour of Stava tailings. Géotechnique, **61**(11): 935-946. doi: 10.1680/geot.9.P.009

Carrington, T.M., Li, G. and Rattley, M.J. 2011. A new assessment of ultimate unit friction for driven piles in low to medium density chalk. *In* Proceedings of the 15th European Conference on Soil Mechanics and Geotechnical Engineering. IOS Press, Amsterdam, NL, pp. 825-830. DOI 10.3233/978-1-60750-801-4-825

Carter, J.P., Airey, D.W. and Fahey, M. 2000. A review of laboratory testing of calcareous soils. *In* Proceedings of the 2nd International Conference on Engineering for Calcareous Sediments. AA Balkema, Rotterdam, NL, pp. 401-431.

Casagrande, A. 1936. Characteristics of cohesionless soils affecting the stability of slopes and earth fills. Journal of the Boston Society of Civil Engineers, **23**(1): 13-32.

Castro, G. 1969. Liquefaction of sands. PhD Thesis, Harvard University, Cambridge, USA.

Castro, G. and Poulos, S.J. 1977. Factors affecting liquefaction and cyclic mobility. Journal of the Geotechnical Engineering Division-Asce, **103**(GT6): 501-516.

Chan, D.L.H., Buckley, R.M., Liu, T. and Jardine, R.J. 2019. Laboratory investigation of interface shearing in chalk. *In* 7th International Symposium on Deformation Characteristics of Geomaterials. EDP Sciences, pp. Article No. 13009. doi: 10.1051/e3sconf/20199213009

Chow, F.C. 1997. Investigations into the Behaviour of Displacement Pile for Offshore Foundations. PhD Thesis, University of London (Imperial College), London, UK.

Ciavaglia, F., Carey, J. and Diambra, A. 2017a. Time-dependent uplift capacity of driven piles in low to medium density chalk. Géotechnique Letters, **7**(1): 90-96. doi: 10.1680/jgele.16.00162

Ciavaglia, F., Carey, J. and Diambra, A. 2017b. Monotonic and cyclic lateral tests on driven piles in Chalk. Proceedings of the Institution of Civil Engineers-Geotechnical Engineering, **170**(4): 353-366. doi: 10.1680/jgeen.16.00113

Clausen, C.J.F., Aas, P.M. and Karlsrud, K. 2005. Bearing capacity of driven piles in sand, the NGI approach. *In* Frontiers in Offshore Geotechnics. Taylor & Francis, London (UK), pp. 677-682.

Clayton, C.J. 1986. The chemical environment of flint formation in Upper Cretaceous chalks. *In* Proceedings of the 4th International Flint Symposium. Cambridge University Press, Cambridge, UK, pp. 43-54.

Clayton, C.R.I. 1978. Chalk as fill. PhD Thesis, University of Surrey, Guildford, UK.

Clayton, C.R.I. 1983. The Influence of Diagenesis on Some Index Properties of Chalk in England. Géotechnique, **33**(3): 225-241. doi: 10.1680/geot.1983.33.3.225

Clayton, C.R.I. 1990. The mechanical properties of the Chalk. *In* Chalk: Proceedings of the International Chalk Symposium. Thomas Telford, London, UK, pp. 213-232.

Clayton, C.R.I. 2011. Stiffness at small strain: research and practice, The 50th Rankine Lecture. Géotechnique, **61**(1): 5-37.

Clayton, C.R.I. and Matthews, M.C. 1987. Deformation, diagenesis and the mechanical behaviour of chalk. *In* Deformation of Sediments and Sedimentary Rocks. *Edited by* M. Jones and R.M.F. Preston. Blackwell Scientific Publications, London, UK. pp. 55-62.

Clayton, C.R.I. and Serratrice, J.F. 1997. General report session 2: The mechanical properties and behaviour of hard soils and soft rocks. *In* Proceedings of an International Symposium on Geotechnical Engineering of Hard Soils - Soft Rocks. AA Balkema, Rotterdam, NL, pp. 1839-1877.

Clayton, C.R.I. and Heymann, G. 2001. Stiffness of geomaterials at very small strains. Géotechnique, **51**(3): 245-255. doi: 10.1680/geot.51.3.245.39363

Clayton, C.R.I., Matthews, M.C. and Heymann, G. 2003. The Chalk. *In* Characterisation and Engineering Properties of Natural Soils. *Edited by* T.S. Tan, K.K. Phoon, D.W. Hight and S. Leroueil. A.A. Balkema, Lisse, NL. pp. 1402-1434.

Cnudde, V. and Boone, M.N. 2013. High-resolution X-ray computed tomography in geosciences: A review of the current technology and applications. Earth-Science Reviews, **123**(1-17. doi: 10.1016/j.earscirev.2013.04.003

Collins, I.F., Pender, M.J. and Wang, Y. 1992. Cavity Expansion in Sands under Drained Loading Conditions. International Journal for Numerical and Analytical Methods in Geomechanics, **16**(1): 3-23. DOI 10.1002/nag.1610160103

Compton, A.H. 1923. A Quantum Theory of the Scattering of X-rays by Light Elements. Physical Review, **21**(5): 483-502.

Coop, M.R. 1990. The mechanics of uncemented carbonate sands. Géotechnique, **40**(4): 607-626. doi: 10.1680/geot.1990.40.4.607

Coop, M.R. and Lee, I.K. 1993. The behaviour of granular soils at elevated stresses. *In* Predictive Soil Mechanics, Proceedings of the Wroth Memorial Symposium. Thomas Telford, London, UK, pp. 186-198.

Coop, M.R. and Jovičić, V. 1999. The influence of state on the very small strain stiffness of sands. *In* Pre-failure Deformation Characteristics of Geomaterials, Proceedings of the 2nd International Symposium. AA Balkema, Rotterdam (NL), pp. 175-181.

Coop, M.R., Sorensen, K.K., Freitas, T.B. and Georgoutsos, G. 2004. Particle breakage during shearing of carbonate sand. Géotechnique, **54**(3): 157-163. doi: 10.1680/geot.2004.54.3.157

Cotecchia, F. and Chandler, R.J. 1997. The influence of structure on the pre-failure behaviour of a natural clay. Géotechnique, **47**(3): 523-544. doi: 10.1680/geot.1997.47.3.523

Cotecchia, F. and Chandler, R.J. 2000. A general framework for the mechanical behaviour of clays. Géotechnique, **50**(4): 431-447. doi: 10.1680/geot.2000.50.4.431

Coyne, D.L., Rattley, M.J., Houlston, P., Alobaidi, I., Benson, A. and Russell, C. 2015. Cyclic laboratory testing of chalk to improve the reliability of piled foundation design. *In* Frontiers in Offshore Geotechnics III. CRC Press/Balkema, London, UK, pp. 1185-1190.

Cuccovillo, T. and Coop, M.R. 1993. The influence of bond strength on the mechanics of carbonate soft rocks. *In* Proceedings of an International Symposium on Geotechnical Engineering of Hard Soils - Soft Rocks. AA Balkema, Rotterdam, NL, pp. 447-455.

Cuccovillo, T. and Coop, M.R. 1999. On the mechanics of structured sands. Géotechnique, **49**(6): 741-760. doi: 10.1680/geot.1999.49.6.741

Dahou, A., Shao, J.F. and Bederiat, M. 1995. Experimental and Numerical Investigations on Transient Creep of Porous Chalk. Mechanics of Materials, **21**(2): 147-158. doi: 10.1016/0167-6636(95)00004-6

De Alba, P., Seed, H.B. and Chan, C.K. 1978. Sand Liquefaction in Large-Scale Simple Shear Tests. Journal of the Geotechnical Engineering Division-Asce, **104**(2): 291-292.

De Nicola, A. and Randolph, M.F. 1999. Centrifuge modelling of pipe piles in sand under axial loads. Géotechnique, **49**(3): 295-318.

DeJong, J.T. and Westgate, Z.J. 2009. Role of Initial State, Material Properties, and Confinement Condition on Local and Global Soil-Structure Interface Behavior. Journal of Geotechnical and Geoenvironmental Engineering, **135**(11): 1646-1660. doi: 10.1061/(Asce)1090-0241(2009)135:11(1646)

Desrues, J. 2004. Tracking strain localisation in geomaterials using computerized tomography. *In* X-ray CT for Geomaterials: Soils, Concrete, Rocks, Proceedings of the International Workshop on X-ray CT for Geomaterials. A.A. Balkema, Lisse (NL), pp. 15-42.

Desrues, J. and Viggiani, G. 2004. Strain localization in sand: an overview of the experimental results obtained in Grenoble using stereophotogrammetry. International Journal for Numerical and Analytical Methods in Geomechanics, **28**(4): 279-321. 10.1002/nag.338

Desrues, J. and Ando, E. 2015. Strain localisation in granular media. Comptes Rendus Physique, **16**(1): 26-36. 10.1016/j.crhy.2015.01.001

Diambra, A., Ciavaglia, F., Harman, A., Dimelow, C., Carey, J. and Nash, D.F.T. 2014. Performance of cyclic cone penetration tests in chalk. Géotechnique Letters, **4**(3): 230-237. doi: 10.1680/geolett.14.00050

Dijkstra, J. 2009. On the Modelling of Pile Installation. PhD Thesis, Delft University of Technology, Zutphen, NL.

Dobry, R., Ladd, R.S., Yokel, F.Y., Chung, R.M. and Powell, D. 1982. Prediction of Pore Water Pressure Buildup and Liquefaction of Sands During Earthquakes by the Cyclic Strain Method. National Bureau of Standards, Washington DC (USA).

Doreau-Malioche, J., Combe, G., Viggiani, G. and Toni, J.B. 2018. Shaft friction changes for cyclically loaded displacement piles: an X-ray investigation. Géotechnique Letters, **8**(1-7.

Doughty, L. 2016. Laboratory Testing of Chalk. MSc Dissertation, Imperial College London, London, UK.

Doughty, L., Buckley, R.M. and Jardine, R.J. 2018. Investigating the effect of ageing on the behaviour of chalk putty. *In* Engineering in Chalk, Proceedings of the Chalk 2018 Conference. ICE Publishing, pp. 695-701. doi: 10.1680/eiccf.64072.695

Drnevich, V.P., Gorman, C.T. and Hopkins, T.C. 1974. Shear strength of cohesive soils and friction sleeve resistance. *In* Proceedings of the European Symposium on Penetration Testing. National Swedish Building Research, pp. 129-133.

du Plessis, A., Meincken, M. and Seifert, T. 2013. Quantitative Determination of Density and Mass of Polymeric Materials Using Microfocus Computed Tomography. Journal of Nondestructive Evaluation, **32**(4): 413-417. doi: 10.1007/s10921-013-0195-7

Dührkop, J., Augustesen, A.H. and Barbosa, P. 2015. Cyclic pile load tests combined with laboratory results to design offshore wind turbine foundations in chalk. *In* Frontiers in Offshore Geotechnics III. CRC Press/Balkema, London, UK, pp. 533-538.

Dührkop, J., Maretzki, S. and Rieser, J. 2017. Re-evaluation of pile driveability in chalk. *In* Proceedings of the 8th International Conference on Offshore Site Investigation and Geotechnics. Society for Underwater Technology, pp. 666-673.

Dyvik, R. and Zimmie, T.F. (1983) Publication No. 149: Lateral stress measurements during static and cyclic simple shear testing. Oslo, NOR: Norwegian Geotechnical Institute

Dyvik, R., Berre, T., Lacasse, S. and Raadim, B. 1987. Comparison of Truly Undrained and Constant Volume Direct Simple Shear Tests. Géotechnique, **37**(1): 3-10. doi: 10.1680/geot.1987.37.1.3

Einav, I. and Randolph, M.F. 2005. Combining upper bound and strain path methods for evaluating penetration resistance. International Journal for Numerical Methods in Engineering, **63**(14): 1991-2016. doi: 10.1002/nme.1350

Einstein, A. 1905. Über einen die Erzeugung und Verwandlung des Lichtes betreffenden heuristischen Gesichtspunkt. Annalen der Physik, **17**(6): 132-148.

Fakharian, K. and Evgin, E. 1997. Cyclic simple-shear behavior of sand-steel interfaces under constant normal stiffness condition. Journal of Geotechnical and Geoenvironmental Engineering, **123**(12): 1096-1105. doi: 10.1061/(Asce)1090-0241(1997)123:12(1096)

Fearon, R.E. and Coop, M.R. 2000. Reconstitution: what makes an appropriate reference material? Géotechnique, **50**(4): 471-477. doi: 10.1680/geot.2000.50.4.471

Feldkamp, L.A., Davis, L.C. and Kress, J.W. 1984. Practical Cone-Beam Algorithm. Journal of the Optical Society of America a-Optics Image Science and Vision, **1**(6): 612-619. doi: 10.1364/Josaa.1.000612

Fellenius, B.H. 2015. Static tests on instrumented piles affected by residual load. Journal of the Deep Foundations Institute, **9**(1): 11-20.

Finno, R.J., Harris, W.W., Mooney, M.A. and Viggiani, G. 1996. Strain localization and undrained steady state of sand. Journal of Geotechnical Engineering-Asce, **122**(6): 462-473. doi: 10.1061/(Asce)0733-9410(1996)122:6(462)

Flay, N. 2016. An investigation of the factors associated with the X-ray tube and their influence on dimensional measurement in micro-focus cone-beam industrial X-ray computed tomography systems. PhD Thesis, University of Southampton, Southampton (UK).

Fleming, K., Weltman, A., Randolph, M.F. and Elson, K. 2009. Piling Engineering. Taylor & Francis, Chippenham, UK.

Gavin, K., Igoe, D. and Doherty, P. 2011. Piles for offshore wind turbines: a state-of-the-art review. Proceedings of the Institution of Civil Engineers-Geotechnical Engineering, **164**(4): 245-256. doi: 10.1680/geng.2011.164.4.245

Gavin, K.G. and Lehane, B.M. 2003. The shaft capacity of pipe piles in sand. Canadian Geotechnical Journal, **40**(1): 36-45. doi: 10.1139/T02-093

Gavin, K.G. and Lehane, B.M. 2005. Estimating the end bearing resistance of pipe piles in sand using the Final Filling Ratio. *In* Frontiers in Offshore Geotechnics. Taylor & Francis, pp. 717-723.

Gavin, K.G. and O'Kelly, B.C. 2007. Effect of friction fatigue on pile capacity in dense sand. Journal of Geotechnical and Geoenvironmental Engineering, **133**(1): 63-71. doi: 10.1061/(Asce)1090-0241(2007)133:1(63)

Gavin, K.G., Jardine, R.J., Karlsrud, K. and Lehane, B.M. 2015. The effects of pile ageing on the shaft capacity of offshore piles in sand. *In* Frontiers in Offshore Geotechnics III. CRC Press/Balkema, London, UK, pp. 129-151.

GDS Instruments 2014. Electromechanical Dynamic Cyclic Simple Shear Datasheet. [online]. Available from: http://www.gdsinstruments.com/__assets__/products/000028/EMDCSS_Datasheet.pdf [cited 29/04/2018].

Geduhn, M., Barbosa, P. and Dührkop, J. 2018a. Offshore static and dynamic pile load tests results in low density chalk Grade A1/A2 to optimize the foundation design of jacket piles. *In* Engineering in Chalk, Proceedings of the Chalk 2018 Conference. ICE Publishing, pp. 403-407.

Geduhn, M., Barbosa, P., Dührkop, J., Augustesen, A.H., Østergaard, M.U. and Steenfelt, J.S. 2018b. Offshore pile load tests in Chalk to support the design of jacket foundations. Proceedings of the Institution of Civil Engineers-Geotechnical Engineering, **171**(6): 508-517. doi: 10.1680/jgeen.17.00217

Gennaro, V.D., Delage, P., Cui, Y.J., Schroeder, C.H. and Collin, F. 2003. Time-Dependent Behaviour of Oil Reservoir Chalk: A Multiphase Approach. Soils and Foundations, **43**(4): 131-147. doi: 10.3208/sandf.43.4_131

Gibson, R.E. and Henkel, D.J. 1954. Influence of Duration of tests at Constant Rate of Strain on Measured “Drained” Strength. Géotechnique, **4**(1): 6-15. doi: 10.1680/geot.1954.4.1.6

Golightly, C.R. 1988. Engineering Properties of Carbonate Sands. PhD Thesis, University of Bradford, Bradford, UK.

Grennan, J.T. 2010. Characterization of a Reconstituted Low Plasticity Silt. MSc Thesis, Massachusetts Institute of Technology, Boston MA, USA.

Gutierrez, M., Wang, J. and Yoshimine, M. 2009. Modeling of the simple shear deformation of sand: effects of principal stress rotation. Acta Geotechnica, **4**(3): 193-201. doi: 10.1007/s11440-009-0094-3

Haigh, S.K., Vardanega, P.J. and Bolton, M.D. 2013. The plastic limit of clays. Géotechnique, **63**(6): 435-440. doi: 10.1680/geot.11.P.123

Hancock, J.M. 1975. The petrology of chalk. Proceedings of the Geologists' Association, **86**(4): 499-535. doi: 10.1016/S0016-7878(75)80061-7

Hardin, B.O. 1985. Crushing of soil particles. Journal of Geotechnical Engineering-Asce, **111**(10): 1177-1192. doi: 10.1061/(Asce)0733-9410(1985)111:10(1177)

Head, K.H. and Epps, R.J. 2011. Manual of Soil Laboratory Testing, Volume 2: Permeability, Shear Strength and Compressibility tests. (3rd Edition), Whittles Publishing, Dunbeath, UK.

Head, K.H. and Epps, R.J. 2014. Manual of Soil Laboratory Testing, Volume 3: Effective Stress tests. (3rd Edition), Whittles Publishing, Dunbeath, UK.

Heerema, E.P. 1980. Predicting pile driveability: heather as an illustration of the friction fatigue theory. Ground Engineering, **13**(15-37.

Henke, S. and Grabe, J. 2013. Field measurements regarding the influence of the installation method on soil plugging in tubular piles. Acta Geotechnica, **8**(3): 335-352. doi: 10.1007/s11440-012-0191-6

Herle, I. and Gudehus, G. 1999. Determination of parameters of a hypoplastic constitutive model from properties of grain assemblies. Mechanics of Cohesive-Frictional Materials, **4**(5): 461-486.

Heymann, G. 1998. The Stiffness of Soils and Weak Rocks at Very Small Strains. PhD thesis, University of Surrey, Guilford, UK.

Hobbs, N.B. and Robins, P. 1976. Compression and Tension Tests on Driven Piles in Chalk. Géotechnique, **26**(1): 33-46. doi: 10.1680/geot.1976.26.1.33

Hobbs, N.B. and Healy, P.R. 1979. CIRIA Report PG6: Piling in Chalk. Construction Industry Research and Information Association (CIRIA), London, UK.

Hobbs, N.B. and Atkinson, M.S. 1993. Compression and tension tests on an open ended tube pile in chalk. Ground Engineering, **26**(3): 30-34.

Hoek, E. (2007) *Practical Rock Engineering*. Vancouver, CAN Available from: https://www.rocscience.com/assets/resources/learning/hoek/Practical-Rock-Engineering-Full-Text.pdf [Accessed 29/10/2018]

Hoek, E. and Diederichs, M.S. 2006. Empirical estimation of rock mass modulus. International Journal of Rock Mechanics and Mining Sciences, **43**(2): 203-215. doi: 10.1016/j.ijrmms.2005.06.005

Holeyman, A. and Legrand, C. 1997. Soil-structure interaction during pile vibratory driving. *In* Proceedings of the XIV International Conference on Soil Mechanics and Foundation Engineering. AA Balkema, pp. 817-822.

Holloway-Strong, M. 1998. A study of the factors which govern the compressibility of chalk. PhD Thesis, University of Surrey, Guildford, UK.

Holloway-Strong, M. and Hughes, S.J. 2001. The influence of contact area on the deformation of chalk. Quarterly Journal of Engineering Geology and Hydrogeology, **34**(1): 99-110. doi: 10.1144/qjegh.34.1.99

Holloway-Strong, M.U., Hughes, S.J. and Hellawell, E.E. 2007. Stress-Deformation Behavior of Chalk. International Journal of Geomechanics, **7**(6): 403-409. doi: 10.1061/(asce)1532-3641(2007)7:6(403)

Homand, S. and Shao, J.F. 2000. Mechanical behaviour of a porous chalk and effect of saturating fluid. Mechanics of Cohesive-Frictional Materials, **5**(7): 583-606. doi: 10.1002/1099-1484(200010)5:7<583::Aid-Cfm110>3.0.Co;2-J

Hopson, P. 2005. A stratigraphical framework for the Upper Cretaceous Chalk of England and Scotland with statements on the Chalk of Northern Ireland and the UK offshore sector - Research Report. British Geological Survey, Keyworth, UK.

Hsieh, J. 2015. Computed Tomography: Principles, Design, Artifacts, and Recent Advances. (3rd Edition), Society of Photo-Optical Instrumentation Engineers (SPIE), Bellingham, WA, USA.

Hyde, A.F.L., Higuchi, T. and Yasuhara, K. 2006. Liquefaction, Cyclic Mobility, and Failure of Silt. Journal of Geotechnical and Geoenvironmental Engineering, **132**(6): 716-735. doi: 10.1061/(Asce)1090-0241(2006)132:6(716)

Ishihara, K. 1993. Liquefaction and flow failure during earthquakes, The 33rd Rankine Lecture. Géotechnique, **43**(3): 351-415. doi: 10.1680/geot.1993.43.3.351

Ishihara, K., Tatsuoka, F. and Yasua, S. 1975. Undrained deformation and liquefaction of sand under cyclic stresses. Soils and Foundations, **15**(1): 29-44. doi: 10.3208/sandf1972.15.29

Iskander, M. 2010. Review of Design Guidelines for Piles in Sand. *In* Behavior of Pipe Piles in Sand. Springer Series in Geomechanics and Geoengineering. *Edited by* W. Wu and R.I. Borja. Springer, Berlin (GER). pp. 7-23.

Iwashita, K. and Oda, M. 2000. Micro-deformation mechanism of shear banding process based on modified distinct element method. Powder Technology, **109**(1-3): 192-205. doi: 10.1016/S0032-5910(99)00236-3

Jaky, J. 1944. The coefficient of earth pressure at rest (In Hungarian: A nyugalmi nyomas tenyezoje). Journal of the Society of Hungarian Engineers Architects (In Hungarian: Magyar Mernok es Epitesz-Egylet Kozlonye), 355-358.

Jardine, R.J. 1992. Some observations on the kinematic nature of soil stiffness. Soils and Foundations, **32**(2): 111-124. doi: 10.3208/sandf1972.32.2_111

Jardine, R.J. and Chow, F.C. 1996. New Design Methods for Offshore Piles. The Marine Technology Directorate Ltd, London (UK).

Jardine, R.J. and Chow, F.C. 2007. Some recent developments in offshore pile design. *In* Offshore Site Investigation and Geotechnics, Proceedings of the 6th International Conference. Society for Underwater Technology, London (UK), pp. 303-332.

Jardine, R.J., Symes, M.J. and Burland, J.B. 1984. The measurement of soil stiffness in the triaxial apparatus. Géotechnique, **34**(3): 323-340. doi: 10.1680/geot.1984.34.3.323

Jardine, R.J., Lehane, B.M. and Everton, S.J. 1993. Friction coefficients for piles in sands and silts. *In* Offshore Site Investigation and Foundation Behaviour. *Edited by* D.A. Ardus, D. Clare, A. Hill, R. Hobbs, R.J. Jardine and J.M. Squire. Springer Science+Business Media, B.V., Dordrecht (NL). pp. 661-677.

Jardine, R.J., Standing, J.R. and Chow, F.C. 2006. Some observations of the effects of time on the capacity of piles driven in sand. Géotechnique, **56**(4): 227-244. doi: 10.1680/geot.2006.56.4.227

Jardine, R.J., Chow, F.C., Overy, R. and Standing, J. 2005. ICP design methods for driven piles in sands and clays. Thomas Telford, London, UK.

Jardine, R.J., Zhu, B.T., Foray, P. and Yang, Z.X. 2013a. Measurement of stresses around close-ended displacement piles in sand. Géotechnique, **63**(1): 1-17.

Jardine, R.J., Zhu, B.T., Foray, P. and Yang, Z.X. 2013b. Interpretation of stress measurements made around closed-ended displacement piles in sand. Géotechnique, **63**(8): 613-627. doi: 10.1680/geot.9.P.138

Jardine, R.J., Thomsen, N.V., Mygind, M., Liingaard, M.A. and Thilsted, C.L. 2015. Axial capacity design practice for North European wind-turbine projects. *In* Frontiers in Offshore Geotechnics III. CRC Press/Balkema, pp. 581-586.

Jardine, R.J., Buckley, R.M., Kontoe, S., Barbosa, P. and Schroeder, F.C. 2018. Behaviour of piles in driven chalk. *In* Engineering in Chalk, Proceedings of the Chalk 2018 Conference. ICE Publishing, pp. 33-51. DOI 10.1680/eiccf.64072.033

Jefferies, M. and Been, K. 2000. Implications for critical state theory from isotropic compression of sand. Géotechnique, **50**(4): 419-429. doi: 10.1680/geot.2000.50.4.419

Jefferies, M. and Been, K. 2016. Soil Liquefaction: A Critical State Approach. CRC Press, London, UK.

Jiang, M.J. and Sun, Y.G. 2012. Cavity expansion analyses of crushable granular materials with state-dependent dilatancy. International Journal for Numerical and Analytical Methods in Geomechanics, **36**(6): 723-742. doi: 10.1002/nag.1027

Johnson, J.P., Rhett, D.W. and Siemers, W.T. 1988. Rock mechanics of the Ekofisk Reservoir in the evaluation of subsidence. *In* Proceedings of the 20th Offshore Technology Conference. Offshore Technology Conference, Richardson TX, USA, pp. 39-51.

Johnston, I.W., Lam, T.S.K. and Williams, A.F. 1987. Constant Normal Stiffness Direct Shear Testing for Socketed Pile Design in Weak Rock. Géotechnique, **37**(1): 83-89. doi: 10.1680/geot.1987.37.1.83

Jovičić, V. 1997. The measurement and interpretation of small strain stiffness of soils. PhD Thesis, City University of London, London, UK.

Jovičić, V. and Coop, M.R. 1997. Stiffness of coarse-grained soils at small strains. Géotechnique, **47**(3): 545-561.

Kågeson-Loe, N.M., Jones, M.E., Petley, D.N. and Leddra, M.J. 1993. Fabric Evolution During the Deformation of Chalk. International Journal of Rock Mechanics and Mining Sciences & Geomechanics Abstracts, **30**(7): 739-745. doi: 10.1016/0148-9062(93)90016-7

Kallehave, D., Byrne, B.W., LeBlanc, T.C. and Mikkelsen, K.K. 2015. Optimization of monopiles for offshore wind turbines. Philosophical Transactions of the Royal Society of London A, **373**(2035): doi: 10.1098/rsta.2014.0100

Katsaros, K.I. 2008. The long-term stress-strain behaviour of chalk. PhD Thesis, University of Brighton, Brighton, UK.

Kennedy, W.J. and Garrison, R.E. 1975. Morphology and genesis of nodular chalks and hardgrounds in the Upper Cretaceous of southern England. Sedimentology, **22**(3): 311-386. DOI 10.1111/j.1365-3091.1975.tb01637.x

Ketcham, R.A. and Carlson, W.D. 2001. Acquisition, optimization and interpretation of X-ray computed tomographic imagery: applications to the geosciences. Computers & Geosciences, **27**(4): 381-400. doi: 10.1016/S0098-3004(00)00116-3

Kinahan, P. 2016. Imaging Detectors for Medical and Healdth Sciences [online]. Available from: http://courses.washington.edu/phys428/ [cited 25 October 2018].

Kishida, H. and Uesugi, M. 1987. Tests of the Interface between Sand and Steel in the Simple Shear Apparatus. Géotechnique, **37**(1): 45-52. doi: 10.1680/geot.1987.37.1.45

Kolk, H.J., Baaijens, A.E. and Senders, M. 2005. Design criteria for pipe piles in silica sands. *In* Frontiers in Offshore Geotechnics. Taylor & Francis, London (UK), pp. 711-716.

Kraft, L.M. 1991. Performance of Axially Loaded Pipe Piles in Sand. Journal of Geotechnical Engineering-Asce, **117**(2): 272-296. doi: 10.1061/(Asce)0733-9410(1991)117:2(272)

Kruth, J.P., Bartscher, M., Carmignato, S., Schmitt, R., De Chiffre, L. and Weckenmann, A. 2011. Computed tomography for dimensional metrology. Cirp Annals-Manufacturing Technology, **60**(2): 821-842. doi: 10.1016/j.cirp.2011.05.006

Kuwajima, K., Hyodo, M. and Hyde, F.L. 2009. Pile bearing capacity factors and soil crushability. Journal of Geotechnical and Geoenvironmental Engineering, **135**(7): 901-913.

Kuwano, R. and Jardine, R.J. 2002. On measuring creep behaviour in granular materials through triaxial testing. Canadian Geotechnical Journal, **39**(5): 1061-1074. doi: 10.1139/T02-059

Lade, P.V. 2016. Triaxial Testing of Soils. John Wiley & Sons, Chichester, UK.

Lake, L.M. 1975. Engineering Properties of Chalk with Special Reference to Foundation Design and Performance. PhD Thesis, University of Surrey, Guilford, UK.

Lake, L.M. 1990. Underground excavations in Chalk. *In* Chalk: Proceedings of the International Chalk Symposium. Thomas Telford, London, UK, pp. 461-467.

Lambe, T.W. 1951. Soil testing for engineers. Wiley, New York, USA.

Lambe, T.W. and Whitman, R.V. 1979. Soil Mechanics, SI Version. John Wiley and Sons, New York, USA.

Landis, E.N. and Keane, D.T. 2010. X-ray microtomography. Materials Characterization, **61**(12): 1305-1316. doi: 10.1016/j.matchar.2010.09.012

Lau, W.H.W. 1988. The behaviour of clay in simple shear and triaxial tests. PhD Thesis, City University London, London (UK).

Lautridou, J.P. and Ozouf, J.C. 1982. Experimental frost shattering: 15 years of research at the Centre de Géomorphologie du CNRS. Progress in Physical Geography: Earth and Environment, **6**(2): 215-232. doi: 10.1177/030913338200600202

Le Tirant, P. and Nauroy, J.F. (eds) 1994. Foundations in carbonate soils. Paris (France): Editions Technip

Leddra, M.J. 1989. Deformation of chalk through compaction and flow. PhD Thesis, University of London (University College London), London, UK.

Leddra, M.J. and Jones, M.E. 1990. Steady-state flow during undrained loading of chalk. *In* Chalk: Proceedings of the International Chalk Symposium. Thomas Telford Ltd, London, UK, pp. 245-252.

Lehane, B.M. and Gavin, K.G. 2001. Base resistance of jacked pipe piles in sand. Journal of Geotechnical and Geoenvironmental Engineering, **127**(6): 473-480. doi: 10.1061/(Asce)1090-0241(2001)127:6(473)

Lehane, B.M. and White, D.J. 2005. Lateral stress changes and shaft friction for model displacement piles in sand. Canadian Geotechnical Journal, **42**(4): 1039-1052. doi: 10.1139/T05-023

Lehane, B.M., Schneider, J.A. and Xu, X. 2005a. A review of design methods for offshore driven piles in siliceous sand. University of Western Australia, Perth (Australia).

Lehane, B.M., Schneider, J.A. and Xu, X. 2005b. The UWA-05 method for prediction of axial capacity of driven piles in sand. *In* Frontiers in Offshore Geotechnics. Taylor & Francis, pp. 683-689.

Lehane, B.M., Schneider, J.A. and Xu, X. 2008. Design of displacement piles in siliceous sands using the CPT. Australian Geomechanics, **43**(2):

Lehane, B.M., Jardine, R.J., Bond, A.J. and Frank, R. 1993. Mechanisms of Shaft Friction in Sand from Instrumented Pile Tests. Journal of Geotechnical Engineering-Asce, **119**(1): 19-35. doi: 10.1061/(Asce)0733-9410(1993)119:1(19)

Lehane, B.M., Schneider, J.A., Lim, J.K. and Mortara, G. 2012. Shaft Friction from Instrumented Displacement Piles in an Uncemented Calcareous Sand. Journal of Geotechnical and Geoenvironmental Engineering, **138**(11): 1357-1368. doi: 10.1061/(Asce)Gt.1943-5606.0000712

Leonards, G.A. and Girault, P. 1961. A study of the one-dimensional consolidation test. *In* Proceedings of the 5th International Conference on Soil Mechanics and Foundation Engineering. Dunold, Paris, FR, pp. 213-218.

Leroueil, S. and Vaughan, P.R. 1990. The general and congruent effects of structure in natural soils and weak rocks. Géotechnique, **40**(3): 467-488. doi: 10.1680/geot.1990.40.3.467

Leroueil, S., Tavenas, F. and Locat, J. 1985. Discussion: Correlations between index tests and the properties of remoulded clays by W.D. Carrier III & J.F. Beckman (Géotechnique 34 (2)). Géotechnique, **35**(2): 223-229. doi: 10.1680/geot.1985.35.2.223

Li, X.S. and Wang, Y. 1998. Linear representation of steady-state line for sand. Journal of Geotechnical and Geoenvironmental Engineering, **124**(12): 1215-1217. doi: 10.1061/(Asce)1090-0241(1998)124:12(1215)

Lim, J.K. and Lehane, B. 2015a. Shearing resistance during pile installation in sand. Proceedings of the Institution of Civil Engineers-Geotechnical Engineering, **168**(3): 227-235. doi: 10.1680/geng.14.00066

Lim, J.K. and Lehane, B. 2015b. Time effects on shaft capacity of jacked piles in sand. Canadian Geotechnical Journal, **52**(11): 1830-1838. doi: 10.1139/cgj-2014-0463

Lobo-Guerrero, S. and Vallejo, L.E. 2007. Influence of pile shape and pile interaction on the crushable behavior of granular materials around driven piles: DEM analyses. Granular Matter, **9**(3-4): 241-250. doi: 10.1007/s10035-007-0037-3

Longworth, T.I. and Driscoll, R.M.C. 1991. Observations and analysis of ground deformation adjacent to a deep road cutting in chalk. *In* Proceedings of the X European Conference on Soil Mechanics and Foundation Engineering. AA Balkema, Rotterdam, NL, pp. 819-824.

López-Querol, S. 2009. Dicussion: Undrained monotonic and cyclic simple shear behaviour of carbonate sand by D. Porcino, G. Caridi and V. N. Ghionna (Géotechnique 58(8)). Géotechnique, **60**(4): 303-305. doi: 10.1680/geot.8.D.021

Lord, J.A. and Davies, J.A.G. 1979. Lateral loading and tension tests on a driven cased pile in chalk. *In* Recent developments in the design and construction of piles. *Edited*. Institution of Civil Engineers, London (UK). pp. 113-120.

Lord, J.A., Twine, D.P. and Yeow, H. 1994. CIRIA Project Report 11: Foundations in chalk. Construction Industry Research and Information Association (CIRIA), London, UK.

Lord, J.A., Clayton, C.R.I. and Mortimore, R.N. 2002. CIRIA Report C 574: Engineering in Chalk. Construction Industry Research and Information Association (CIRIA), London, UK.

Louis, L., Baud, P. and Wong, T.F. 2007. Characterization of pore-space heterogeneity in sandstone by X-ray computed tomography. Rock Physics and Geomechanics in the Study of Reservoirs and Repositories, **284**(127-146. 10.1144/Sp284.9

Luck, F., Kolditz, D., Hupfer, M. and Kalender, W.A. 2013. Effect of shaped filter design on dose and image quality in breast CT. Physics in Medicine and Biology, **58**(12): 4205-4223. doi: 10.1088/0031-9155/58/12/4205

Lunne, T., Robertson, P.K. and Powell, J.J.M. 1997. Cone penetration testing in geotechnical practice. Spon Press, Abingdon (UK).

Luong, M.P. 1980. Stress-strain aspects of cohesionless soils under cyclic and transient loading. *In* Proceedings of the International Symposium on Soils Under Cyclic and Transient Loading. A. A. Balkema, Leiden, NL, pp. 315-324.

Madhusudhan, B.N. and Baudet, B.A. 2014. Influence of reconstitution method on the behaviour of completely decomposed granite. Géotechnique, **64**(7): 540-550. doi: 10.1680/geot.13.P.159

Mahanta, R., Ghanekar, R.K. and Kumar, K. 2015. CPT-based pile shaft friction in calcareous sands of western Indian offshore. *In* Frontiers in Offshore Geotechnics III. CRC Press/Balkema, London (UK), pp. 619-624.

Mail, N., Moseley, D.J., Siewerdsem, J.H. and Jaffray, D.A. 2009. The influence of bowtie filtration on cone-beam CT image quality. Medical Physics, **36**(1): 22-32. doi: 10.1118/1.3017470

Maranini, E. and Brignoli, M. 1999. Creep behaviour of a weak rock: experimental characterization. International Journal of Rock Mechanics and Mining Sciences, **36**(1): 127-138. doi: 10.1016/S0148-9062(98)00171-5

Markins, S.R. 2014. Artifacts Interfering with Interpretation of Cone Beam Computed Tomography Images. Dental Clinics of North America, **58**(3): 485-495. doi: 10.1016/j.cden.2014.04.007

Markowicz, A.A. 2002. X-ray Physics. *In* Handbook of X-Ray Spectrometry. *Edited by* R.E. Van Grieken and A.A. Markowicz. Marcel Dekker Inc., New York City, NY (USA). pp. 1-94.

Matthews, M.C. 1993. The mass compressibility of fractured chalk. PhD Thesis, University of Surrey, Guilford, UK.

Matthews, M.C. and Clayton, C.R.I. 1992. Compressibility of jointed rock massess with specific reference to the chalk. *In* International Society of Rock Mechanics Symposium: Eurock '92. Thomas Telford, London, UK, pp. 445-450.

Matthews, M.C. and Clayton, C.R.I. 1993. Influence of the intact porosity on the engineering properties of a weak rock. *In* Proceedings of an International Symposium on Geotechnical Engineering of Hard Soils - Soft Rocks. A. A. Balkema, Rotterdam, NL, pp. 693-702.

Matthews, M.C. and Clayton, C.R.I. 2004. Large diameter plate tests on weathered in-situ Chalk. Quarterly Journal of Engineering Geology and Hydrogeology, **37**(61-72. doi: 10.1144/1470-9236/03-033

Mesri, G. 1973. Coefficient of Secondary Compression. Journal of the Soil Mechanics and Foundations Division-ASCE, **99**(1): 123-137.

Mesri, G. and Vardhanabhuti, B. 2009. Compression of granular materials. Canadian Geotechnical Journal, **46**(4): 369-392. doi: 10.1139/T08-123

Michalowski, R.L. 2005. Coefficient of Earth Pressure at Rest. Journal of Geotechnical and Geoenvironmental Engineering, **131**(11): 1429-1433. doi: 10.1061/(ASCE)1090-0241(2005)131:11(1429)

Millar, M.J. 2000. The stress-strain behaviour of jointed chalk. PhD Thesis, University of Brighton, Brighton, UK.

Mitchell, J.K. and Soga, K. 2005. Fundamentals of Soil Behavior. John Wiley & Sons, Inc., Hoboken NJ, USA.

Mortimore, R.N. 1983. The stratigraphy and sedimentation of the Turonian-Campanian in the Southern Province of England. Zitteliana, **10**(27-41.

Mortimore, R.N. 1986. Stratigraphy of the upper cretaceous white chalk of Sussex. Proceedings of the Geologists' Association, **97**(2): 97-139. doi: 10.1016/s0016-7878(86)80065-7

Mortimore, R.N. 1990. Chalk or chalk? *In* Chalk: Proceedings of the International Chalk Symposium. Thomas Telford, London, UK, pp. 15-45.

Mortimore, R.N. 2012. Making sense of Chalk: a total-rock approach to its Engineering Geology (11th Glossop Lecture). Quarterly Journal of Engineering Geology and Hydrogeology, **45**(252-334.

Mortimore, R.N. and Fielding, P.M. 1990. The relationship between texture, density and strength of chalk. *In* Chalk: Proceedings of the International Chalk Symposium. Thomas Telford, London, UK, pp. 109-132.

Mortimore, R.N. and Pomerol, B. 1997. Upper Cretaceous tectonic phases and end Cretaceous inversion in the Chalk of the Anglo-Paris Basin. Proceedings of the Geologists Association, **108**(3): 231-255. doi: 10.1016/S0016-7878(97)80031-4

Mortimore, R.N., Pomerol, B. and Foord, J. 1990. Engineering stratigraphy and palaeogeography for the Chalk of the Anglo-Paris basin. *In* Chalk: Proceedings of the International Chalk Symposium. Thomas Telford, London, UK, pp. 47-62.

Muir Wood, A., Mackenzie, B., Burbury, D., Rattley, M.J., Clayton, C.R.I., Mygind, M., Wessel Andersen, K., LeBlanc Thilsted, C. and Albjerg Liingaard, M. 2015. Design of large diameter monopiles in chalk at Westermost Rough offshore wind farm. *In* Frontiers in Offshore Geotechnics III. CRC Press/Balkema, London, UK, pp. 723-728.

Muir Wood, D. 1994. Soil Behaviour and Critical State Soil Mechanics. Cambridge University Press, Cambridge, UK.

Muir Wood, D., Drescher, A. and Budhu, M. 1980. On the determination of stress state in the simple shear apparatus. Geotechnical Testing Journal, **2**(4): 211-222.

Mull, R.T. 1984. Mass Estimates by Computed-Tomography - Physical Density from Ct Numbers. American Journal of Roentgenology, **143**(5): 1101-1104. DOI 10.2214/ajr.143.5.1101

Murff, J.D. 1987. Pile Capacity in Calcareous Sands - State-of-the-Art. Journal of Geotechnical Engineering-Asce, **113**(5): 490-507. doi: 10.1061/(Asce)0733-9410(1987)113:5(490)

Murton, J.B. 2018. Frost weathering of chalk. *In* Engineering in Chalk, Proceedings of the Chalk 2018 Conference. ICE Publishing, pp. 497-502. DOI 10.1680/eiccf.64072.497

Newbury, D.E., Joy, D.C., Echlin, P., Fiori, C.E. and Goldstein, J.I. 1986. Advanced Scanning Electron Microscopy and X-Ray Microanalysis. Springer Science+Business Media, New York NY, USA.

Ngan-Tillard, D., Cheng, X.H., Van Nes, J.H.G. and Zitha, P.L.J. 2005. Application of x-ray computed tomography to cone penetration tests in sand. *In* Geo-Frontiers 2005 Congress. American Society of Civil Engineers, pp. 1-12.

Nocilla, A., Coop, M.R. and Colleselli, F. 2006. The mechanics of an Italian silt: an example of 'transitional' behaviour. Géotechnique, **56**(4): 261-271. doi: 10.1680/geot.2006.56.4.261

Nowak, P.A. and Thijssen, R. 2018. Ipswich barrier: design of pile foundations for the main barrier structure. *In* Engineering in Chalk, Proceedings of the Chalk 2018 Conference. ICE Publishing, pp. 235-240. DOI 10.1680/eiccf.64072.235

O'Neill, M.W., Vipulanandan, C. and Wong, D. 1990. Laboratory Modelling of Vibro-Driven Piles. Journal of Geotechnical Engineering, **116**(8): 1190-1209.

Oda, M. 1975. On the relation $\tau/\sigma_N=\kappa \tan\psi$ in the simple shear test. Soils and Foundations, **15**(4): 35-41.

Oda, M. and Konishi, J. 1974. Rotation of principal stresses in granular material during simple shear. Soils and Foundations, **14**(4): 39-53.

Otani, J., Watanabe, Y. and Chevalier, B. 2010. Introduction of X-ray CT application in geotechnical engineering - theory and practice. *In* 9th World Congress on Computational Mechanics and 4th Asian Pacific Congress on Computational Mechanics. pp. 1-10. doi: 10.1088/1757-899x/10/1/012089

Otter, L. 2011. The influence of suction changes on the stiffness of the railway foundation. PhD Thesis, University of Southampton,

Paik, K., Salgado, R., Lee, J. and Kim, B. 2003. Behavior of open- and closed-ended piles driven into sands. Journal of Geotechnical and Geoenvironmental Engineering, **129**(4): 296-306. doi: 10.1061/(Asce)1090-0241(2003)129:4(296)

Peck, R.B. 1979. Liquefaction Potential: Science Versus Practice. Journal of the Geotechnical Engineering Division-Asce, **105**(3): 393-398.

Pestana, J.M. and Whittle, A.J. 1995. Compression model for cohesionless soils. Géotechnique, **45**(4): 611-631. doi: 10.1680/geot.1995.45.4.611

Petley, D., Jones, M.E., Fan, C., Stafford, C., Leddra, M.J. and Kageson-Loe, N. 1993. Deformation and fabric changes in weak fine-grained rocks during high pressure consolidation and shear. *In* Proceedings of an International Symposium on Geotechnical Engineering of Hard Soils - Soft Rocks. Balkema, Rotterdam, NL, pp. 737-743.

Phillips, D.H. and Lannutti, J.J. 1997. Measuring physical density with X-ray computed tomography. Ndt & E International, **30**(6): 339-350. doi: 10.1016/S0963-8695(97)00020-0

Porcino, D., Caridi, G. and Ghionna, V.N. 2008. Undrained monotonic and cyclic simple shear behaviour of carbonate sand. Géotechnique, **58**(8): 635-644. doi: 10.1680/geot.2007.00036

Poulos, S.J. 1981. The steady state deformation. Journal of the Geotechnical Engineering Division-Asce, **107**(5): 553-562.

Powell, J.J.M. 1990. Discussion on foundations. *In* Chalk: Proceedings of the International Chalk Symposium. Thomas Telford Ltd, London, UK, pp. 416-417.

Powrie, W. 2014. Soil Mechanics Concepts and Applications. Taylor & Francis, Boca Raton, FL (USA).

Puig, J. 1973. Problemes de terrassement dans la craie. Bulletin de Liaison des Laboratoires des Ponts et Chaussees, **63**(1): 56-72.

Rae, P.J., Brown, E.N. and Orler, E.B. 2007. The mechanical properties of poly(ether-ether-ketone) (PEEK) with emphasis on the large compressive strain response. Polymer, **48**(2): 598-615. doi: 10.1016/j.polymer.2006.11.032

Rampello, S., Georgiannou, V.N. and Viggiani, G. 1995. The dependence of small strain stiffness on stress state and history for fine grained soils: the example of Vallericca clay. *In* Pre-failure Deformation of Geomaterials, Proceedings of the International Symposium. A.A. Balkema, Rotterdam, NL, pp. 273-278.

Randolph, M.F. 2003. Science and empiricism in pile foundation design, The 43rd Rankine Lecture. Géotechnique, **53**(10): 847-875.

Randolph, M.F. 2008. IMPACT - Dynamic analysis of pile driving. Manual.

Randolph, M.F. and Wroth, C.P. 1981. Application of the Failure State in Undrained Simple Shear to the Shaft Capacity of Driven Piles. Géotechnique, **31**(1): 143-157. doi: 10.1680/geot.1981.31.1.143

Randolph, M.F. and Gourvenec, S. 2011. Offshore Geotechnical Engineering. Spon Press, Abingdon (UK).

Randolph, M.F., Carter, J.P. and Wroth, C.P. 1979. Driven piles in clay - the effects of installation and subsequent consolidation. Géotechnique, **29**(4): 361-393.

Randolph, M.F., Dolwin, J. and Beck, R. 1994. Design of Driven Piles in Sand. Géotechnique, **44**(3): 427-448. doi: 10.1680/geot.1994.44.3.427

Rat, M. and Schaeffner, M. 1990. Classification of chalks and conditions of use in embankments. *In* Chalk: Proceedings of the International Chalk Symposium. Thomas Telford, London, UK, pp. 425-428.

Razoaki, R.N. 2000. Effect of ageing on mechanics of chalk slurries. PhD Thesis, University of Portsmouth, Portsmouth, UK.

Rimoy, S. 2013. Ageing and axial loading studies of displacement piles in sand. PhD Thesis, Imperial College London,

Risnes, R. 2001. Deformation and Yield in High Porosity Outcrop Chalk. Physics and Chemistry of the Earth Part a-Solid Earth and Geodesy, **26**(1-2): 53-57. doi: 10.1016/S1464-1895(01)00022-9

Robertson, P.K. and Fear, C.E. 1997. Liquefaction of sands and its evaluation. *In* First International Conference on Earthquake Geotechnical Engineering. A.A. Balkema, Rotterdam, NL, pp. 1253-1287.

Robertson, P.K. and Wride, C.E. 1998. Evaluating cyclic liquefaction potential using the cone penetration test. Canadian Geotechnical Journal, **35**(3): 442-459. doi: 10.1139/cgj-35-3-442

Roscoe, K.H., Schofield, A.N. and Wroth, C.P. 1958. On The Yielding of Soils. Géotechnique, **8**(1): 22-52. doi: 10.1680/geot.1958.8.1.22

Roscoe, K.H., Bassett, R.H. and Cole, E.R.L. (1967) Principal Axes Observed during Simple Shear of a Sand. Paper presented at Proceedings of the Geotechnical Conference on Shear Strength Properties of Natural Soils and Rocks Oslo (Norway)

Russell, A.R. and Khalili, N. 2002. Drained cavity expansion in sands exhibiting particle crushing. International Journal for Numerical and Analytical Methods in Geomechanics, **26**(4): 323-340. doi: 10.1002/nag.203

Saleem, Z. 2011. Alternatives and modifications of Monopile foundation or its installation technique for noise mitigation. MSc Thesis, Delft University of Technology, Delft, NL.

Salgado, R., Mitchell, J.K. and Jamiolkowski, M. 1997. Cavity expansion and penetration resistance in sand. Journal of Geotechnical and Geoenvironmental Engineering, **123**(4): 344-354. doi: 10.1061/(Asce)1090-0241(1997)123:4(344)

Schneider, J.A. 2008. Analysis of piezocone data for displacement pile design. PhD Thesis, University of Western Australia, Crawley, WA (Australia).

Schneider, J.A., White, D.J. and Lehane, B.M. 2007. Shaft friction of piles in siliceous, calcareous and micaceous sands. *In* Offshore Site Investigation and Geotechnics: Confronting New Challenges and Sharing Knowledge. *Edited by* M. Pourshoushtari. Society for Underwater Technology, London (UK). pp. 367-382.

Schneider, J.A., Xu, X.T. and Lehane, B.M. 2008. Database assessment of CPT-based design methods for axial capacity of driven piles in siliceous sands. Journal of Geotechnical and Geoenvironmental Engineering, **134**(9): 1227-1244. doi: 10.1061/(Asce)1090-0241(2008)134:9(1227)

Schofield, A. and Wroth, C.P. 1968. Critical State Soil Mechanics. McGraw-Hill, New York City, USA.

Schroeder, C. 2002. Du coccolithe au réservoir pétrolier: Approche phénoménologique du comportement mécanique de la craie en vue de sa modélisation à différentes échelles. PhD Thesis, Université de Liège, Liège, BE.

Schulze, R., Heil, U., Groβ, D., Bruellmann, D.D., Dranischnikow, E., Schwanecke, U. and Schoemer, E. 2011. Artefacts in CBCT: a review. Dentomaxillofacial Radiology, **40**(5): 265-273. doi: 10.1259/dmfr/30642039

Seed, H.B. 1979. Soil Liquefaction and Cyclic Mobility Evaluation for Level Ground during Earthquakes. Journal of the Geotechnical Engineering Division-Asce, **105**(2): 201-255.

Shajarati, A., Sørensen, K.W., Nielsen, S.K. and Ibsen, L.B. (2012) Behaviour of Cohesionless Soils During Cyclic Loading. Aalborg, DK: Department of Civil Engineering, Aalborg University

Sharma, S.S. and Fahey, M. 2003a. Evaluation of cyclic shear strength of two cemented calcareous soils. Journal of Geotechnical and Geoenvironmental Engineering, **129**(7): 608-618. 10.1061/(Asce)1090-0241(2003)129:7(608)

Sharma, S.S. and Fahey, M. 2003b. Degradation of stiffness of cemented calcareous soil in cyclic triaxial tests. Journal of Geotechnical and Geoenvironmental Engineering, **129**(7): 619-629. 10.1061/(Asce)1090-0241(2003)129:7(619)

Sheng, D.C., Eigenbrod, K.D. and Wriggers, P. 2005. Finite element analysis of pile installation using large-slip frictional contact. Computers and Geotechnics, **32**(1): 17-26. doi: 10.1016/j.compgeo.2004.10.004

Shipton, B. and Coop, M.R. 2012. On the compression behaviour of reconstituted soils. Soils and Foundations, **52**(4): 668-681. doi: 10.1016/j.sandf.2012.07.008

Shipton, B., Coop, M.R. and Nocilla, A. 2006. Particle breakage in transitional soils. *In* Proceedings of the International Symposium on Geomechanics and Geotechnics of Particulate Media. CRC Press, London, UK, pp. 143-147.

Skempton, A.W. 1984. The Colloidal "Activity" of Clays. *In* Selected Papers on Soil Mechanics *Edited by* A.W. Skempton. Thomas Telford Ltd, London, UK. pp. 62-64.

Stone, K.J.L. and Katsaros, K.I. 2011. An investigation of the long-term engineering response of intact chalk. *In* Proceedings of the 15th European Conference on Soil Mechanics and Geotechnical Engineering. IOS Press, Amsterdam, NL, pp. 287-292.

Stroud, M.A. 1971. the behaviour of sand at low stress levels in the simple-shear apparatus. PhD Thesis, University of Cambridge, Cambridge, UK.

Sun, W., Brown, S.B. and Leach, R.K. (2012) NPL REPORT ENG 32: An overview of industrial X-ray computed tomography. Teddington, UK: National Physical Laboratory

Svinkin, M.R. 2004. Some uncertainties in high-strain dynamic pile testing. Geotechnical Engineering for Transportation Projects, Vol 1, 126): 705-714.

Teh, C.I. and Houlsby, G.T. 1991. An Analytical Study of the Cone Penetration Test in Clay. Géotechnique, **41**(1): 17-34. doi: 10.1680/geot.1991.41.1.17

Ter-Stepanian, G. 1992. Mechanics of soil creep during shear. *In* Geomechanics and water engineering in environmental management. *Edited by* R.N. Chowdhury. AA Balkema, Rotterdam (NL). pp. 529-557.

Thompson, G.W. and Jardine, R.J. 1998. The applicability of the new Imperial College Pile design method to calcareous sands. *In* Offshore site investigation and foundation behaviour, Proceedings of an International Conference. Society for Underwater Technology, pp. 383-400.

Tsuha, C.H.C., Foray, P.Y., Jardine, R.J., Yang, Z.X., Silva, M. and Rimoy, S. 2012. Behaviour of displacement piles in sand under cyclic axial loading. Soils and Foundations, **52**(3): 393-410. doi: 10.1016/j.sandf.2012.05.002

Vaughan, P.R. 1997. Engineering behaviour of weak rocks: Some answers and some questions. *In* Proceedings of an International Symposium on Geotechnical Engineering of Hard Soils - Soft Rocks. AA Balkema, Rotterdam, NL, pp. 1741-1765.

Vaughan, P.R., Maccarini, M. and Mokhtar, S.M. 1988. Indexing the engineering properties of residual soil. Quarterly Journal of Engineering Geology, **21**(1): 69-84. doi: 10.1144/Gsl.Qjeg.1988.021.01.05

Verdugo, R. and Ishihara, K. 1996. The steady state of sandy soils. Soils and Foundations, **36**(2): 81-91. doi: 10.3208/sandf.36.2_81

Viggiani, G. and Atkinson, J.H. 1995. Stiffness of fine-grained soil at very small strains. Géotechnique, **45**(2): 249-265.

Viggiani, G., Finno, R.J. and Harris, W.W. 1994. Experimental Observations of Strain Localisation in Plane Strain Compression of a Stiff Clay. *In* Proceedings of the 3rd International Workshop on Localisation and Bifurcation Theory for Soils and Rocks. AA Balkema, Rotterdam, NL, pp. 189-198.

Vijayvergiya, V.N., Cheng, A.P. and Kolk, H.J. 1977. Effect of Soil Set up on Pile Driveability in Chalk. Journal of the Geotechnical Engineering Division-Asce, **103**(10): 1069-1082.

Viking, K. 2006. The vibratory pile installation technique. *In* Proceedings of the International Conference on Vibratory Pile Driving and Deep Soil Compaction. Editions du LCPC, pp. 65-82.

Vucetic, M. 1994. Cyclic Threshold Shear Strains in Soils. Journal of Geotechnical Engineering-Asce, **120**(12): 2208-2228. doi: 10.1061/(Asce)0733-9410(1994)120:12(2208)

Wakeling, T.R.M. 1966. Foundations on chalk. *In* Proceedings of the Symposium on Chalk in Earthworks and Foundations. Institution of Civil Engineers (ICE), London, UK, pp. 15-23.

Wakeling, T.R.M. 1970. A comparison of the results of standard site investigation methods against the results of detailed geotechnical investigation in Middle Chalk at Mundford, Norfolk. *In* In situ investigations in soils and rocks, Proceedings of the Conference Organized by the British Geotechnical Society. British Geotechnical Society, London, UK, pp. 17-22.

Wang, Z.L., Dafalias, Y.F. and Shen, C.K. 1990. Bounding surface hypoplasticity model for sand. Journal of Engineering Mechanics-Asce, **116**(5): 983-1001. Doi 10.1061/(Asce)0733-9399(1990)116:5(983)

Ward, W.H., Burland, J.B. and Gallois, R.W. 1968. Geotechnical assessment of a site at Mundford, Norfolk, for a large proton accelerator. Géotechnique, **18**(4): 399-341. doi: 10.1680/geot.1968.18.4.399

White, D.J. 2005. A general framework for shaft resistance on displacement piles in sand. *In* Frontiers in Offshore Geotechnics. Taylor & Francis, pp. 697-703.

White, D.J. and Bolton, M.D. 2002. Observing friction fatigue on a jacked pile. *In* Constitutive and Centrifuge Modelling: Two Extremes. *Edited by* S. Springman. A. A. Balkema, Lisse (NL). pp. 347-354.

White, D.J. and Bolton, M.D. 2004. Displacement and strain paths during plane-strain model pile installation in sand. Géotechnique, **54**(6): 375-397. doi: 10.1680/geot.2004.54.6.375

White, D.J. and Lehane, B.M. 2004. Friction fatigue on displacement piles in sand. Géotechnique, **54**(10): 645-658. doi: 10.1680/geot.54.10.645.56344

White, D.J. and Deeks, A.D. 2007. Recent research into the behaviour of jacked foundation piles. *In* Proceedings of the International Workshop of Recent Advances of Deep Foundations. Taylor & Francis Group, London, UK, pp. 3-26.

White, D.J., Schneider, J.A. and Lehane, B.M. 2005. The influence of the effective area ratio on shaft friction of displacement piles in sand. *In* Frontiers in Offshore Geotechnics. Taylor & Francis, London (UK), pp. 741-747.

White, D.J., Finlay, T., Bolton, M.D. and Bearss, G. 2002. Press-in piling: Ground vibration and noise during piling installation. *In* Proceedings of the International Deep Foundations Congress. American Society of Civil Engineers, pp. 363-371.

Wong, D., Oneill, M.W. and Vipulanandan, C. 1992. Modeling of Vibratory Pile Driving in Sand. International Journal for Numerical and Analytical Methods in Geomechanics, **16**(3): 189-210. doi: 10.1002/nag.1610160303

Yang, Z.X., Jardine, R.J., Zhu, B.T. and Rimoy, S. 2014. Stresses Developed around Displacement Piles Penetration in Sand. Journal of Geotechnical and Geoenvironmental Engineering, **140**(3): doi: 10.1061/(Asce)Gt.1943-5606.0001022

Yang, Z.X., Guo, W.B., Jardine, R.J. and Chow, F. 2017. Design method reliability assessment from an extended database of axial load tests on piles driven in sand. Canadian Geotechnical Journal, **54**(1): 59-74. doi: 10.1139/cgj-2015-0518

Yang, Z.X., Jardine, R.J., Zhu, B.T., Foray, P. and Tsuha, C.H.C. 2010. Sand grain crushing and interface shearing during displacement pile installation in sand. Géotechnique, **60**(6): 469-482. doi: 10.1680/geot.2010.60.6.469

Yoshimi, Y. and Oh-Oka, H. 1975. Influence of degree of shear stress reversal on the liquefaction potential of saturated sand. Soils and Foundations, **15**(3): 27-40. doi: 10.3208/sandf1972.15.3_27

Yoshimine, M. and Ishihara, K. 1998. Flow potential of sand during liquefaction. Soils and Foundations, **38**(3): 189-198. doi: 10.3208/sandf.38.3_189

Yoshimine, M., Robertson, P.K. and Wride, C.E. 1999. Undrained shear strength of clean sands to trigger flow liquefaction. Canadian Geotechnical Journal, **36**(5): 891-906. doi: 10.1139/cgj-36-5-891

Youd, T.L., Idriss, I.M., Andrus, R.D., Arango, I., Castro, G., Christian, J.T., Dobry, R., Finn, W.D.L., Harder, L.F., Hynes, M.E., Ishihara, K., Koester, J.P., Liao, S.S.C., Marcuson, W.F., Martin, G.R., Mitchell, J.K., Morikawi, Y., Power, M.S., Robertson, P.K., Seed, R.B. and Stokoe, K.H. 2001. Liquefaction Resistance of Soils: Summary Report from the 1996 NCEER and 1998 NCEER/NSF Workshops on Evaluation of Liquefaction Resistance of Soils. Journal of Geotechnical and Geoenvironmental Engineering, **127**(10): 817-833. doi: 10.1061/(ASCE)1090-0241(2001)127:10(817)

Yu, H.S. and Houlsby, G.T. 1991. Finite Cavity Expansion in Dilatant Soils - Loading Analysis. Géotechnique, **41**(2): 173-183. doi: 10.1680/geot.1991.41.2.173

Zhang, G., Marshall, N., Jacobs, R., Liu, Q. and Bosmans, H. 2013. Bowtie filtration for dedicated cone beam CT of the head and neck: a simulation study. The British Journal of Radiology, **86**(1028): doi: 10.1259/bjr.20130002

Zhang, H. and Garga, V.K. 1997. Quasi-steady state: a real behaviour? Canadian Geotechnical Journal, **34**(5): 749-761. doi: 10.1139/t97-046

Zhang, Z. and Wang, Y.H. 2015. Examining Setup Mechanisms of Driven Piles in Sand Using Laboratory Model Pile Tests. Journal of Geotechnical and Geoenvironmental Engineering, **141**(3): doi: Unsp 04014114 10.1061/(Asce)Gt.1943-5606.0001252

Ziogos, A., Brown, M., Ivanovic, A. and Morgan, N. 2017. Chalk-steel interface testing for marine energy foundations. Proceedings of the Institution of Civil Engineers-Geotechnical Engineering, **170**(3): 285-298. doi: 10.1680/jgeen.16.00112